A study of insulating liquids properties for encapsulation of power electronics substrates

Chencho Dorji

THESE

Pour optenir le grade de

DOCTEUR DE L'UNIVERSITE GRENOBLE ALPES

Ecole doctoral : Electronique, Automatique, Traitement du Signal (EEATS)

Etude des propriétés des isolants liquides pour l'encapsulation des substrats d'électronique de puissance

A study of insulating liquids properties for encapsulation of power electronics substrates

Présentée par :

Chencho DORJI

Direction de thèse

Olivier LESAINT — Directeur de thèse
Directeur de recherche, CNRS

Rachelle HANNA — Co-encadrante de thèse
Maître de conférences, Grenoble INP

Thèse soutenue publiquement le 20/03/2024

Devant le jury composé de :

Sombel DIAHAM — Rapporteur
Maître de conférences HDR, Université de Toulouse
Laboratoire Laplace

Christophe LOUSTE — Rapporteur
Professeur, Université de Poitiers
Laboratoire Pprime

Serge ANGEL — Examinateur
Professeur, Université de Montpellier
Laboratoire IES

Etienne GHEERAERT — President du jury
Professeur, Université Grenoble Alpes
Laboratoire Institut Néel

Remerciements

Ce travail a été réalisé sous la supervision de M. Olivier LESAINT, Directeur de Recherche au CNRS dans l'équipe Matériaux Diélectriques et Electrostatique (MDE) du laboratoire G2ELab. Je tiens à lui exprimer ma profonde gratitude pour son aide et ses conseils continus dans tous les travaux expérimentaux, la rédaction scientifique et surtout pour avoir partagé ses connaissances approfondies dans le domaine des matériaux diélectriques.

J'aimerais également remercier Mme Rachelle HANNA, Maître de Conférences à Grenoble INP-G2Elab, pour avoir co-supervisé ma thèse. Son soutien et ses encouragements m'ont guidé tout au long de ce travail.

Un grand merci à M. Rabih KHAZAKA, Ingénieur de recherche chez Safran, pour m'avoir fourni des échantillons de substrat céramique et de liquides. Je le remercie également pour sa contribution au suivi et à la réalisation des expériences.

Je tiens également à remercier Mme Oumayma DIKI pour son travail sur l'étude du vieillissement thermique de différents liquides isolants dans le cadre de son stage. Un résumé de ses travaux se trouve en annexe.

Je voudrais également remercier tout le personnel de G2elab, particulièrement Mme Nelly BONIFACI et Mme Afef LEBOUC pour avoir été membre du CSI (Comité de suivi individuel) et m'avoir donné de précieux conseils et commentaires pour l'avancement de ce travail, Mrs. Christophe POLLET, Jean-Luc PALENZUELA, Sébastien FLURY pour m'avoir aidé à construire des cellules de test, des échantillons et des systèmes expérimentaux. Je remercie également tous les collègues doctorants de l'équipe MDE pour le temps précieux qu'ils m'ont consacré (Igor, Simon, Gween, Francis, Enrique…).

Je suis également très reconnaissant au Gouvernement Français d'avoir financé ce travail pendant trois ans, ainsi qu'au G2ELab pour avoir financé et fourni l'équipement et les plates-formes nécessaires à la réalisation des expériences, ainsi que pour la possibilité de participer à plusieurs conférences internationales.

Merci à la société ARKEMA pour son soutien tout au long de la thèse, en particulier en fournissant les liquides DBT et BT06 qui ont été très utiles pour cette étude.

Enfin, je tiens à remercier mon épouse, Mélanie, pour son soutien moral tout au long de cette thèse.

Table of Content

Figure List

Table List

Abbreviations

AC	:	Alternating Current
Al_2O_3	:	Aluminium Oxide (Alumina)
AlN	:	Aluminium Nitride
BD	:	Breakdown
BDV	:	Breakdown Voltage
BNC	:	Bayonet Neill-Concelman
BT06	:	Benzyltoluene Zero Six
CCD	:	Charge Coupled Device
CTE	:	Coefficient of Thermal Expansion
DBC	:	Direct bonded copper substrate
DBT	:	Di-benzyltoluene
DC	:	Direct Current
EHD	:	Electrohydrodynamic
FEA	:	Finite Element Analysis
FTIR	:	Fourier Transform Infrared Ray
GaAs	:	Gallium Arsenide
GaN	:	Gallium Nitride
Ge	:	Germanium
HT	:	High Temperature
HV	:	High Voltage
IGBT	:	Insulated Gate Bipolar Transistor
Ipd	:	Partial Discharge Current
Ipm	:	Photomultiplier Current
MJO	:	Mobil Jet Oil
MOSFET	:	Metal Oxide Semiconductor Field Effect Transistor
PD	:	Partial Discharge
PDIV	:	Partial Discharge Inception Voltage
PM	:	Photomultiplier
PRPD	:	Phase Resolved Partial Discharge
RT	:	Room Temperature
Rm	:	Measurement Resistor
SC	:	Semi-conductor
SCLC	:	Space Charge Limitted Current
SE	:	Synthetic Ester
SF6	:	Sulphur Hexafluoride
S.Gel	:	Silicone gel
Si	:	Silicone
Si_3N_4	:	Silicone Nitride
SiC	:	Silicone Carbide
S.Oil	:	Silicone Oil
ToF	:	Time of Flight
tr	:	Impulse voltage rise time
TRLM	:	Time Resolved Light Measurement
V_{BI}	:	Bipolar Impulse Voltage
V_{DC}	:	Direct Current Voltage
V_{UI}	:	Unipolar Impulse Voltage
Z_m	:	Measurement Impedance

Introduction

Modern power electronics are mainly based on semiconductor devices (i.e., diodes, IGBTs, MOSFETS, etc) and are basically used for control and conversion of electrical power for wide range of applications. For low power and low voltage applications (such as mobile charger, cell phones, computers, etc), the semiconductor devices are simply mounted on a circuit board and does not require special material design for electrical isolation or thermal management. However, a compact single unit power conversion device generally termed as 'power module' is used for high voltage and high-power applications. These power modules are required to handle tens of megawatts and several kilovolts (such as in high voltage AC-DC converters, rail way traction system, industrial drives, etc). Therefore, semiconductor devices are mounted on metalized ceramic substrates and embedded in insulating material called encapsulation.

Most classical power modules are based on silicone (Si) semiconductor (SC) devices with maximum operating temperature of 150°C. More recently, the Si based semiconductor devices are getting replaced by wide band gap materials such as Silicone Carbide (SiC) or Gallium Nitride (GaN). These wide band gap SC devices can be used at high theoretical temperatures up to 500°C and voltages up to 10kV. However, silicone gel, the most commonly used encapsulant material develops thermal cracking at temperatures above 200°C. Moreover, increased risk of permanent degradation of silicone gel due to partial discharge and electrical breakdowns are expected for wide band gap power modules. As a result, all the wide band gap-based power modules are limited to practical temperatures below 175°C and maximum blocking voltage of 6kV, similar to Si based power modules. Finding an alternative encapsulant material suitable to operate at high temperature (>200°C) and high voltage (> 10kV) is a key to enable the potential of wide band gap power modules in future.

One of the potential alternative encapsulant materials are dielectric liquids. They are known to have excellent self-healing properties against partial discharge and electrical breakdowns and are widely used in power transformers, circuit breakers, high voltage cable joints, capacitors, etc. Several dielectric liquids are also used as heat transfer liquids in industries due to their low viscosity and high specific heat capacity. These features of dielectric liquids are interesting to be used as an alternative encapsulant in power modules. However, very limited information is available regarding applicability of dielectric liquids in power module packaging. The objective of this thesis is to evaluate several aspects of dielectric liquids as alternative high temperature encapsulants in power modules. In addition to dielectric properties, the possible contribution of liquids to cooling of modules, taking advantage of the Electro-Hydro-Dynamic (EHD) motion under high electric field, will be evaluated. Also, the optical detection of partial discharges via optical measurements, made possible thanks to the transparency of liquids, will be investigated since it may help to better understand the PD behaviour of encapsulated substrates under realistic fast-rise impulse voltage.

In this work, we will make comparisons between different liquids by measuring first their dielectric properties. Variations of electrical conductivity with electric field up to 30kV/mm and temperature up to 300°C will be investigated. These results will be used to develop a finite element analysis (FEA) model to study the electric field evolution at triple point when a ceramic substrate is embedded in dielectric liquid. These simulation results would contribute to better understand partial discharge activity under impulse voltage with different rise times, ac and dc. We will also design a test system to study the EHD heat transfer enhancement in dielectric liquids, and evaluate its practical contribution to cooling of power devices. Some preliminary

studies on accelerated thermal aging of different liquids will also be investigated and reported as an Annex.

1 Review on potential encapsulant and substrates materials for wide band gap power electronic modules

The history of power electronics begun in early 1900s when Peter Cooper Hewitt invented the mercury arc rectifier [1] to convert alternating current (AC) to direct current (DC). The invention of semiconductor (SC) device, bipolar junction transistors (BJT) in mid 1900s enabled higher voltage operation but limited operation at low frequencies. A breakthrough in power electronics came with the invention of metal oxide field effect transistor (MOSFET) at Bell Labs in 1959. It enabled higher frequency operation than BJT but was limited to low voltage applications. Later in 1980s, insulated gate bipolar transistor (IGBT) was invented. IGBTs inherited the features of BJT to handle high voltage operation and high frequency operation capability of MOSFET. Since then, the development of power devices has continued to evolve towards more efficient, robust, cheaper and faster switching devices.

To support the growing field of power electronics, a fully integrated power conversion device, usually called “power module”, was developed simultaneously. Compared to the assembly of low voltage semiconductor devices where components are mounted on a printed circuit board, the power module provides better thermal management and electrical isolation of semiconductor chips, for applications requiring high voltage and high switching frequency. The first power module was manufactured by Semikron in 1974. Following that, numerous other manufacturers have been focusing on increasing its efficiency, while reducing its size and cost. Prior to 2008, most of power modules were based on classical Silicon (Si) chips. This material is characterized by rather high switching and conduction losses, and is limited to maximum junction temperature of 175°C. Later, semiconductor devices based on Wide Band Gap (WBG) materials have emerged by early 2000’s [2].These WBG materials, such as Silicone Carbide (SiC) and Gallium Nitride (GaN) allow higher switching frequency (~ 200kHz) with lower losses, higher junction temperature (>200°C), and higher voltage operation (blocking voltage > 10kV) [3]. Ultra-wide band-gap semiconductors such as Ga_2O_3, AlGaN or Diamond offer even better performances but the technology still remains immature [4]. In 2008, a hybrid power module with Si IGBT and SiC Schottky diode became commercially available. Today, almost all Si power devices are getting replaced by SiC power devices. However, the large theoretical potential of WBG materials remains under-used in practice since several materials used for packaging semiconductor chips, such as encapsulant (silicone gel), solder, and substrate, show several limitations at high temperature and high voltage. Accordingly, SiC power modules unfortunately remain limited in applications to maximum temperature of 175°C and blocking voltage of 6.5 kV, i.e., similar to Si power modules. Research in the field of packaging technologies remains therefore essential to fully benefit from the potential advantages of WBG semiconductors.

This chapter consists of a brief description of a conventional power module structure, followed by a more detailed discussion on trends, challenges and options regarding semiconductors devices and encapsulants. A review on previous studies dealing with electrical characterization of different encapsulant materials in interface with various substrate materials

will be presented, especially for high temperature and high voltage applications. Finally, the objective of this PhD will be outlined.

1.1. Structure of a power module

A power module consists of semiconductor switching devices properly connected to perform electrical power conversion for various applications. Depending upon the type of applications and technological advances, power modules come in large varieties of structures. A conventional structure is shown in Fig 1.1. Materials and functions of each power module components are described below:

- *Semiconductor die* – Classical or WBG semiconductor chips (i.e., IGBT, MOSFET, Thyristor, diodes). Power conversion is achieved by these active devices.
- *Substrate* – Usually made of ceramic-based materials, showing high thermal conduction, low electrical conductivity, and high breakdown voltage. Sintered ceramic materials such as Alumina (Al_2O_3), Aluminium Nitride (AlN), Silicone Nitride (Si_3N_4) are the most commonly used substrate in power modules. Thick metallization is present on both surfaces, usually made of Copper or Aluminium (with finish layer such as Nickel/Gold/Silver).
- *Baseplate* – It serves as heat transfer medium and provides mechanical support, and is usually done with copper or copper composites, carbon reinforced composites, Aluminium Silicon Carbide (AlSiC).
- *Bonding materials* – They are used to attach the die and the connectors to substrate, and made typically from lead-based soft solder, lead free solder, etc. It plays a critical role in the reliability of the power module.
- *Encapsulation* – Insulating material embedding all the semiconductor devices, wires and substrate. It is used to increase the dielectric strength of power modules by supressing partial discharges around the semiconductor die and substrate metallisation. In addition, it provides some mechanical soft support of fragile components such as bonding wires, and protect the devices from external aggressions (contamination, moisture, corrosion …). It must withstand high local electric field and sometimes high temperature. Silicone gel is most commonly used.
- *Thermal interface* – It improves the thermal contact to increase heat transfer from base plate to heat sink.
- *Heat sink* – Cooling of power module

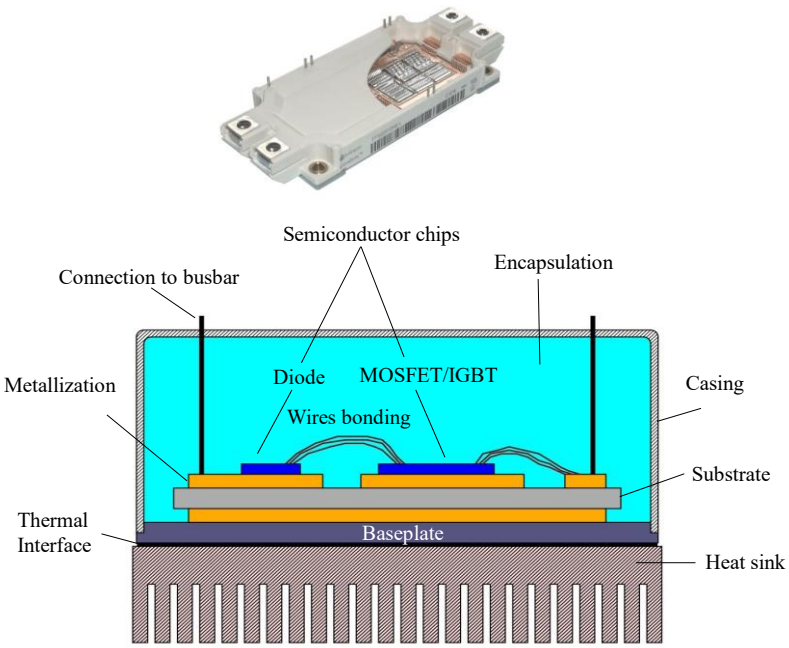

Fig 1.1. Conventional structure of power module (not to scale)

1.2. New semiconductor materials for power devices

The wide bandgap (WBG) semiconductors are developed to increase power density with reduced conduction and switching losses. The Si based power devices are limited to maximum blocking voltage of 6.5kV and maximum junction temperature of 175°C [5, 6]. Therefore, WBG semiconductors are developed to withstand higher blocking voltage higher than 10kV and junction temperature exceeding 350°C. A comparison of different semiconductor materials is shown in Table 1.1. Nowadays, semiconductor devices based on SiC and GaN are commercially available.

Table 1.1. Intrinsic properties of semiconductor materials at 300K

Properties	Classical semiconductors		Wide band gap Semiconductors			
	Si	GaAs	4H-SiC	GaN	Ga_2O_3	Diamond
Band gap energy (eV)	1.12	1.4	3.26	3.4	4.8	5.5
Breakdown field ($V\ cm^{-1}$) x 10^6	0.3	0.4	3.0	3.5	8	10
Electron mobility ($cm^2\ V^{-1}\ s^{-1}$)	1420	8500	1000	2000	400	2200
Hole mobility ($cm^2\ V^{-1}\ s^{-1}$)	600	400	100	200	100	850
Electron saturation velocity ($cm\ s^{-1}$) x 10^6	10	20	22	25	20	27
Relative permittivity	11.8	12.9	9.7	9.5	10-15	5.5 - 10
Thermal conductivity ($W\ cm^{-1}\ K^{-1}$)	1.3	0.54	4.9	1.3	0.2	22

There are several advantages of WBG, that make them superior to Si semiconductor:

i. *High voltage operation* - 4H-SiC is the most commercially available WBG material today, showing high intrinsic breakdown strength of 300kV/mm, compared to Si with breakdown strength of 30kV/mm. This allows thinner drift region, which in turn results in much lower specific on-resistance (R_{on}), thus reducing conduction losses, Fig 1.2 [7]. A graph showing the trade-off between maximum blocking voltage and R_{on} of various semiconductor devices for different materials is shown in Fig 1.3. The best material with the highest breakdown voltage and minimum specific on-resistance is diamond (see Fig 1.3). However, diamond semiconductor devices are still at an early stage of development, and require a reduction in defects density to become commercially available.

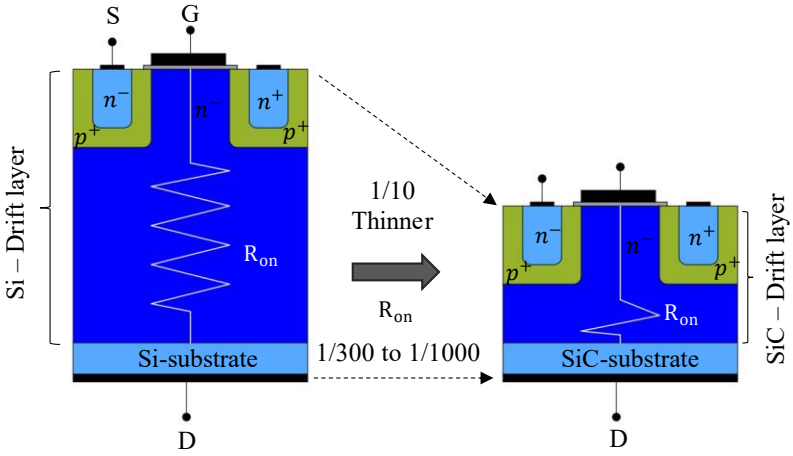

Fig 1.2. Illustration of reduction in drift layer (voltage isolation layer) in SiC-MOSFET compared to Si – MOSFET *[7]*

ii. *High switching frequency* – Because of the high voltage drop across the drift region (consequence of high R_{on}), Si-MOSFETs are not used for high voltage application, although they do offer fast switching capabilities. Only Si-IGBTs are used for high voltage applications [8]. However, low R_{on} combined to the high mobility of majority charge carrier of unipolar SiC devices (such as SiC MOSFET and SiC Schottky diodes) outweighs the usefulness of Si-IGBT and PIN diodes. This allows very fast switching (>200kHz) [8] with comparatively very low switching losses. The high switching frequency results in smaller and less expensive passive components required for power conversion, such as filters, capacitors and inductors. A comparison of efficiency based on switching losses in Si-IGBT and SiC-MOSFET power modules was done in [9] as shown in Fig 1.4.

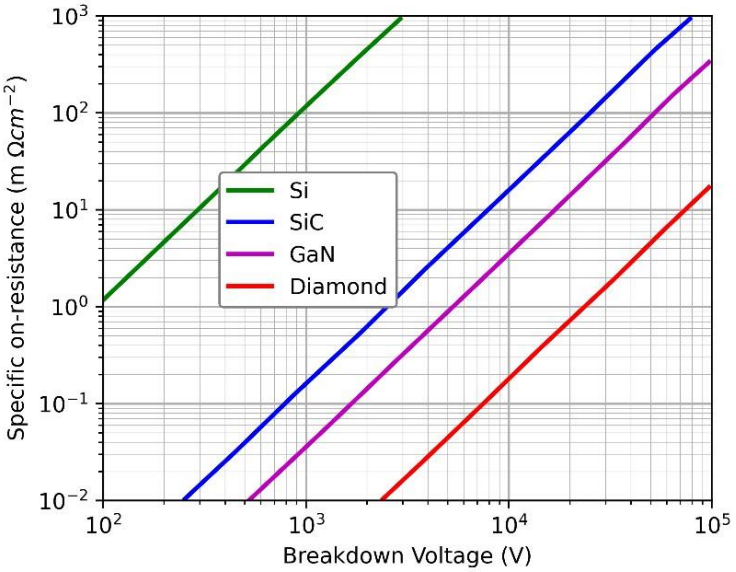

Fig 1.3. Theoretical specific on-resistance and breakdown voltage for various semiconductor materials *[6]*

iii. *High junction temperature* – large band gap energy in WBG semiconductors (see Table 1.1) results in low intrinsic charge concentration. Thus, WBG devices are suitable to operate at much higher junction temperature than classical Si devices. A calculation of maximum theoretical junction temperature (thermal run-away temperature) at different breakdown voltage was done in [9] (see Fig 1.5). Theoretically, WBG material such as SiC could be operated at a junction temperature as high as 1000°C, as compared to typical maximum junction temperature of 175°C in Si. Moreover, the high thermal conductivity of SiC (4 times higher than Si) reduces the thermal resistance of the chip, thus allowing better heat transfer up to the baseplate. This increased operating temperature of SiC devices enables more compact and high-power density modules, with reduced complexity of thermal management.

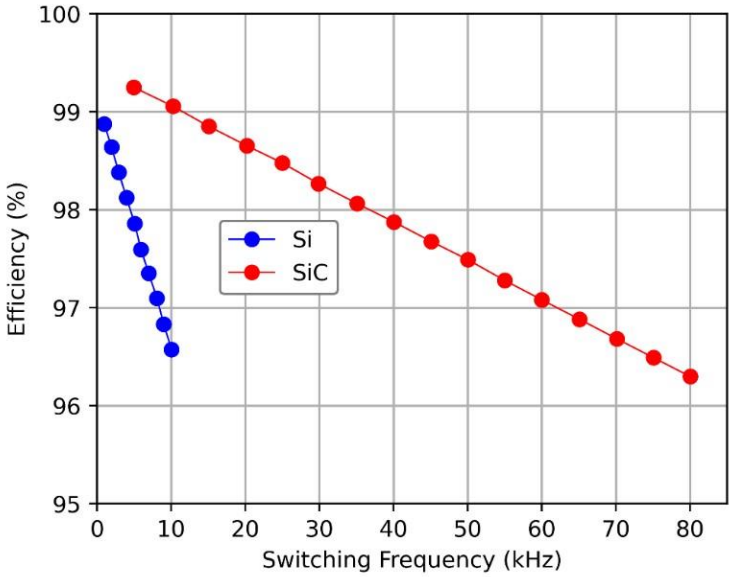

Fig 1.4. Switching efficiency comparison of Si IGBT and SiC MOSFET power module *[8]*

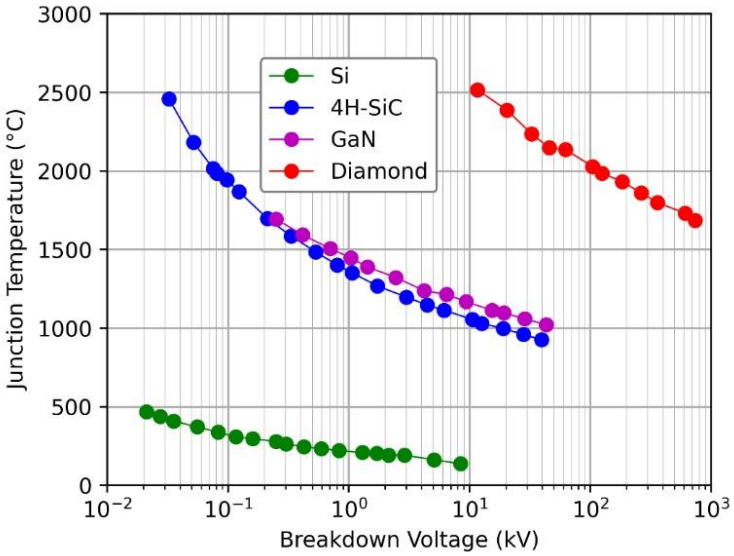

Fig 1.5. Theoretical runaway temperature as a function of breakdown voltage for different semiconductor materials *[8]*

1.3. Power module encapsulation: limitations and alternatives

The basic purpose of encapsulation is to protect the power chip and assembled components from hostile environments, such as moisture, dust, and chemicals. Since dielectric materials used for encapsulation show much higher breakdown fields compared to atmospheric air, they also provide a very efficient protection against breakdown between conductors, and also suppress very efficiently localized partial discharges that may occur in high field areas, typically around triple junctions between ceramic, metallization, and encapsulating material. Several material characteristics have to be taken into account for future WBG power modules encapsulation:

- High purity – for direct contact with semiconductor chips
- Better partial discharge suppression
- Low moisture absorption and gas permeability
- Maximum operating temperature > 250°C
- High dielectric strength (>20kV/mm)
- High electrical resistivity (>10^{13} Ω cm)
- Coefficient of thermal expansion (CTE) close to that of the substrate in use

1.3.1. Limitations of silicone gel

Silicone gel is widely used as encapsulant in both Si and SiC-based power modules, operating at temperature below 175°C. It offers excellent features including high purity, low toxicity and softness (it absorbs mechanical stress caused by thermal expansion of surrounding materials). Unfortunately, it is not suitable for higher temperature and higher voltage applications due to two reasons:

i. *Thermal cracking at high temperature* – Silicone gel is limited to operate at maximum temperature of 200°C (Fig 1.6), which is lower compared to the maximum temperature limits of other components present in a power module. Thermal cracks start to develop in gel when exposed to prolonged high temperature, due to hardening process and/or mismatch of CTEs under high temperature gradient [10, 11]. Therefore, WBG power modules using silicone

gel as encapsulant are currently rated below 200°C, despite their potential to handle higher temperatures.

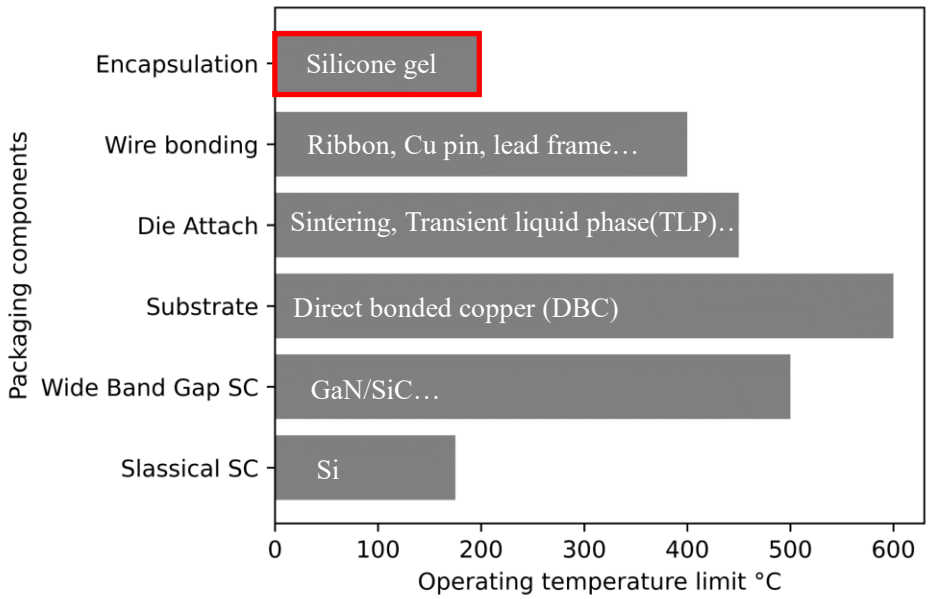

Fig 1.6. Maximum operating temperatures of different components of a power module

ii. *Degradation by partial discharges under increased voltage level* – In the case of high voltage power modules (e.g., 4H-SiC IGBTs offering blocking voltage > 10kV), the enhanced local electric field around metallized tracks (triple junction) is reported to exceed 100kV/mm [12]. This strongly promotes the occurrence of partial discharge (PD) in this region, and also increases the risk of breakdown (BD) that may occur at different locations: in the gel, in the substrate material, or at their interface (Fig 1.7). The occurrence of PDs or BD in silicone gel results in irreversible damage.

iii. *Poor thermal management* – Heat dissipation from the semiconductor chips is limited by the low thermal conductivity of silicone gel (0.2 W/m.K). Therefore, most heat is extracted via the baseplate attached to bulky heat sink components.

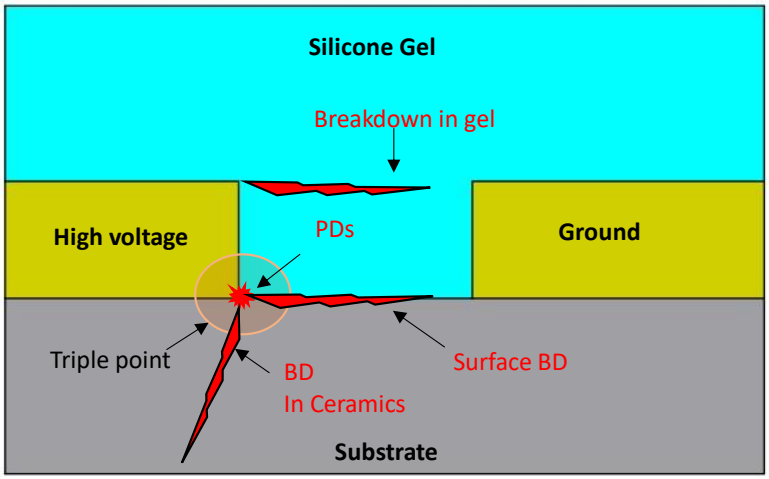

Fig 1.7. Typical regions in a power module where PDs and BD may occur

1.3.2. Alternative materials for high temperature encapsulation

At present, the encapsulation material (Silicone gel) induces a limitation for operating WBG power modules at higher temperature and higher voltage. It is therefore of great interest

to identify other insulating materials more compatible with applications at higher temperature and higher voltage. These materials should have following desirable electrical, thermal and mechanical properties:

- Continuous operating temperature much higher than 200°C
- High electrical resistivity (more than typically 10^{-13} Ωcm)
- Dielectric strength larger than 20kV/mm
- High thermal conductivity and good matching of CTE with substrate material (usable temperature -60°C to 350°C)
- High chemical resistance
- High purity for direct contact with semiconductor chips
- Low gas permeability
- Long pot life (ideally ~30 minutes) with low curing temperature
- Non-toxicity and environmental friendliness

Presently, no single material that can satisfy all the requirement listed. Besides silicone gel, several high temperature encapsulation materials do exist:

- *Glass encapsulation*: lead glass insulators show melting point of 500°C and glass transition temperature higher than 300°C (transition from rigid to flexible state). However, when used as power module encapsulant, it showed inferior PD properties [13, 14]. Moreover, high potting temperature (500°C or above) cause damage to bonding wires and semiconductor chips. They are also susceptible to thermal cracking due to its brittle nature.

- *Cements*: Cement insulators have high operating temperature up to 1000°C. However, the sintering process need high temperature (>300°C) [14] which can potentially cause damage to other packaging components. It also suffers from high Young Modulus (>100GPa) and a CTE between 3 to 6 ppm/°C. These properties induce high mechanical stress and could lead to fractures.

- *Epoxy resins*: These materials are widely used in electronic packaging for decades due to their superior performance in adhesion strength, elastic modulus and chemical resistance. However, when used for high temperature encapsulation, the glass transition temperature is limited to 200°C and eventually inhibit the usability of WBG power module for high temperature applications. Novel epoxy resin with both low viscosity and higher glass transition temperature are currently being developed.

- *Insulating liquids*: There exists several non-polar liquids showing both good dielectric properties, and interesting high temperature properties: some of them are used in industry for heat transfer applications at operating temperature > 300°C. Compared to gel or solid encapsulation, liquid insulation would tentatively show several advantages and drawbacks:

  Advantages:

  (a) There is no issue with CTE mismatch with other packaging components;
  (b) liquids usually show good self-healing properties: they can be quickly reusable after breakdown or partial discharge, provided that their degradation is limited;
  (c) several liquids are known to provide excellent PD suppression properties under ac, such as liquids used to impregnate power capacitors or high voltage cables, where PD constitute a critical issue;

(d) liquids can be easily circulated and replaced.

In addition, dielectric liquids may also contribute to cool modules, taking advantage of convective heat transfer such as in power transformers. Moreover, if EHD (Electro-Hydro-Dynamic) motion takes place due to high local electric fields, convective heat transfer could be in turn strongly enhanced.

Drawbacks:

Use of liquids would induce an increased complexity of module structure, requiring tightness and means to accommodate the increase of pressure at high temperature. In this regard, liquids with a low vapour pressure and high boiling temperature would be required. Liquid insulation is also known to be affected by solid particles able to trigger breakdown. The presence of gas bubbles (air, vapour), of much lower dielectric strength compared to the liquid, should also be avoided.

Today, there are still no practical applications of dielectric liquids for the insulation of power electronics modules. Several PhD studies and papers were devoted to this prospective subject [15, 16, 17]. Concerning electrical properties of liquids at high temperature and suitability of liquids as encapsulant materials, the most significant study addressing these issues to date is J. Muslim's PhD [17]. The present work constitutes a follow-up of this work, taking advantage of several investigation techniques previously developed in this study (such as high temperature dielectric test cells).
A summary of previous works is provided in the following section. Afterwards, the remaining questions and the objectives of this thesis will be outlined.

1.4. Potential dielectric liquids suitable for high temperature encapsulation

Several liquids can be considered based on their thermal properties provided by the manufacturers. Some of these liquids are primarily intended to industrial heat transfer, and their dielectric properties are therefore not indicated in the datasheet. Some of them were previously investigated at high temperature, especially in [17], and others not yet. Therefore, the characterization of dielectric properties for wide range of temperature and electric field remains essential to evaluate their applicability in power module packaging.

i. *Benzyltoluene-based liquids*: mono-benzyltoluene (Jarytherm® BT06) [18] and di-benzyltoluene (Jarytherm® DBT) [19] are synthetic hydrocarbon liquids manufactured and supplied by Arkema. Low viscosity and excellent thermal stability of Jarytherm® BT06 makes it suitable for cooling-heating processes in chemical industries. It is used in temperature environment up to 290°C at atmospheric pressure and up to 350°C under pressurized conditions. Jarytherm® DBT (simply called "DBT" in the following text) is primarily used in chemical and plastic industries as heat transfer liquid. The maximum operating temperature in use is 350°C at atmospheric pressure. These non-polar liquids have a chemical composition quite close to the Jarylec® [20] based on a mixture of mono- and di-benzyltoluene. Jarylec® is used to impregnate capacitors, and shows excellent PD suppression and gas-absorbing properties. Conductivity and breakdown properties of DBT were previously investigated up to 350 °C [17] as detailed in next sections, as well as PD and breakdown on embedded substrates. No such data were obtained in BT06.

ii. *Ester liquids*: Synthetic ester oil (MIDEL® 7131) [21], simply called "Midel" in the following text is used as transformer oil up to 433 kV. It has very low pour point (-56°C) and high moisture tolerance. Its resistance to high temperatures is lower compared to

benzyltoluene (< 200 °C, according to the manufacturer). Dielectric characterization was also obtained in [17]. Another ester-based liquid, Mobil Jet^{TM} Oil II [22], referred as 'Jet oil' in the following text is mostly used as lubricant in air-craft gas turbines, constitutes another interesting liquid to investigate, since it shows excellent thermal and oxidation stability. No dielectric characterization is available today.

iii. *Silicone oil*: This liquid can be found in wide range of viscosities to suit the needs of the application. It has a wide range of applications such as lubricants, cosmetics, heating / cooling fluids (up to 200°C), high temperature dielectric liquids (e.g., in high-speed train transformers), etc. Silicone oil is known for its stability against oxidation and thermal cycles.

Table 1.2 provides a summary of the basic characteristics of these liquids. The results of dielectric characterization already obtained at high temperature in some liquids will be discussed in the following sections.

Table 1.2. General properties of potential liquids for high temperature application

Properties	Benzyltoluene		Esters		Silicone Oil
	Jarytherm® DBT	Jarytherm® BT06	MIDEL® 7131	Mobil Jet^{TM} Oil II	Rhodhosil®Oil 47V50
Kinematic viscosity 25°C [mm^2/s]	50	5.9	29	27.6	50
Density 25°C [kg/m^3]	1044	1008	970	1003	960
Boiling point [°C]	390	290	250	-	-
Fire point [°C]	230	155	316	285	340
Pour point [°C]	-34	-57	-56	-59	-50
Self-ignition [°C]	470	490	260	404	300
Flash point [°C]	200°C	370	260	270	240
Thermal conductivity [W/m°C]	0.126	0.130	0.147	-	0.16
Specific Heat [kJ/mK]	1.58	1.61	1.9	-	1.46

1.4.1. Dielectric properties of DBT and Midel under high temperature

The dielectric properties of liquids at high temperature were rarely investigated in the past, mainly because most applications of insulating liquids (e.g., power transformers, capacitors, cables) operate at moderate maximum temperatures < 100 °C, in order to mitigate ageing of these devices. Quite few applications use liquids at temperatures far exceeding 100°C. A typical example is found with high-speed train powers transformers, requiring high power (> 5 MW) together with compact size and light weight. Such transformers typically use esters or silicon oil. The only available study of dielectric properties at much higher temperatures (up to 350 °C in DBT) is the J. Muslim's PhD [17].

Several different methods can be used to characterize dielectric properties. Dielectric spectroscopy is a widely used method to obtain dielectric properties versus frequency. Its principle will be discussed in section 2.1.1. It provides useful information such as dc electrical

conductivity (σ_{dc}), permittivity (ϵ', ϵ''), dissipation factor ($\tan\delta$), etc. Previous studies [17, 23] used a broadband dielectric spectrometer Novocontrol Alpha-A, with a special coaxial cylindrical text cell developed to allow measurements up to 350°C. Experimental setup and procedures are detailed in [23]. The objective was primarily to investigate the influence of temperature on dielectric properties of Jarytherm® DBT (up to 350°C) and MIDEL® 7131 (up to 200°C), and compare them with the properties of silicone gel. A summary of this study can be seen in Fig 1.8.

It was observed that temperature varied over a large range has large influence on the dielectric properties of liquids. An increase of low-field dc conductivity (σ_{dc}, measured at a field of 1V/mm) and loss factor tanδ by more than 4 decades was observed in Jarytherm® DBT, when temperature increases from 20°C to 350°C. Similar observations were also made with Midel. The increase of low-field conductivity, typical in many insulating liquids, is mainly caused by the increase in charge carrier mobility (ions), induced by the decrease of viscosity versus temperature. In DBT, an increase of conductivity by about 3 decades over the same temperature range can be attributed to enhanced mobility, and the total increase of conductivity also involves some increase of available ion density resulting from modified dissociation / recombination equilibrium.

A classical decrease of permittivity ε' was also observed in both liquids and in silicone gel, mostly related to the decrease in the density. Over the whole temperature range, ε' in DBT dropped from 2.65 to 2.2 (- 20%), which is comparable to the drop in density (- 24%). The values of ε' in DBT confirm that this liquid is non-polar, while MIDEL7131 (ε' between 3 to 4) is slightly polar.

During several temperature cycles up to 350°C in DBT in non-oxidating conditions (N_2 atmosphere), the conductivity remained fairly stable, ranging from 1.89×10^{-14} S/cm up (fresh liquid) to 2.98 $x10^{-14}$ S/cm (at the end of measurements). This suggests a quite good stability of the liquid at high temperature. DBT shows a lower conductivity, permittivity and dielectric loss than Midel. Moreover, it has been used at unrivalled high temperatures up to 350°C in industry for heat transfer applications. DBT therefore shows both good insulating properties typical of non-polar liquids, and excellent high temperature stability, it was thus the centre of interest in the J. Muslim's PhD [17].

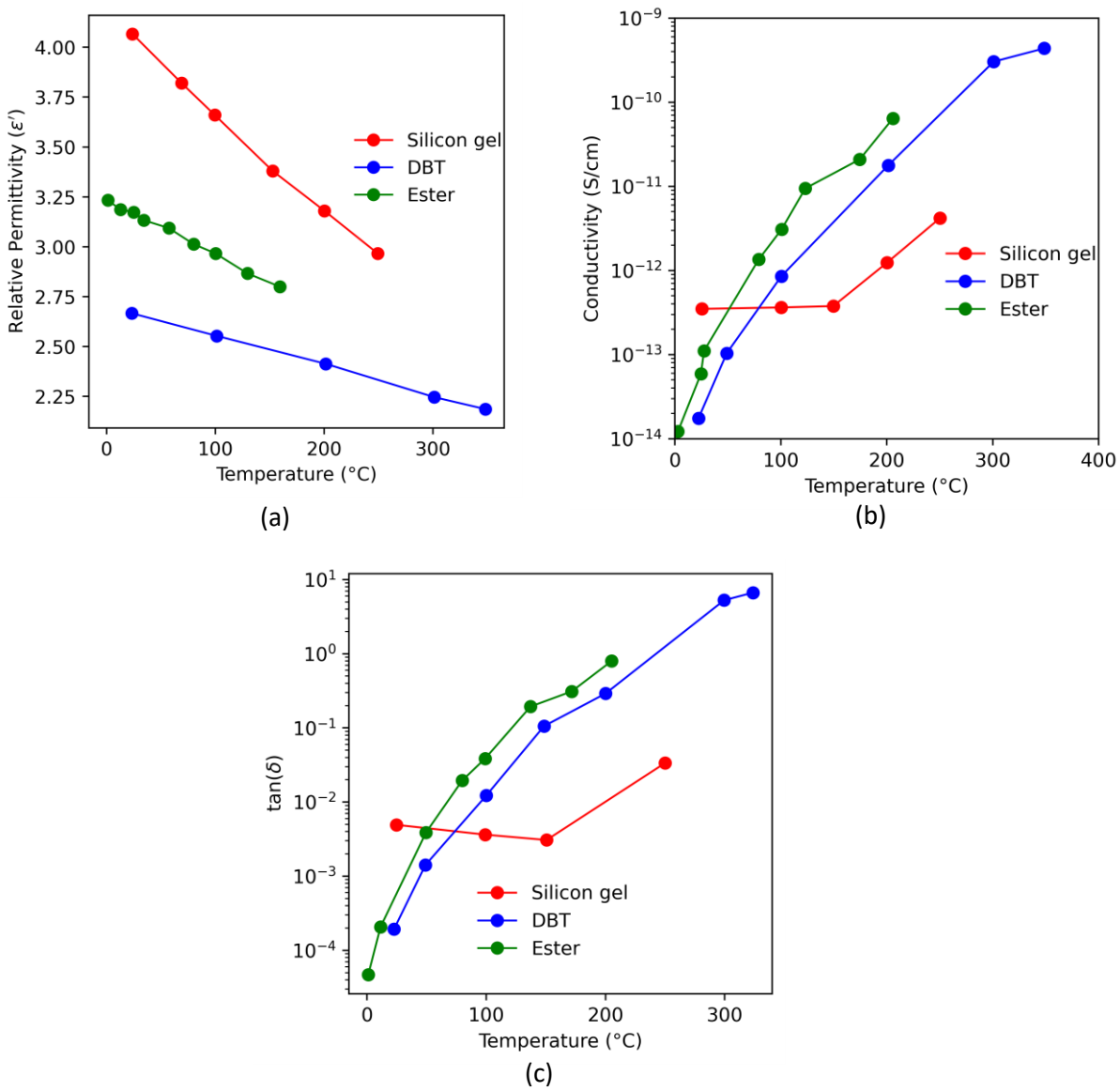

Fig 1.8. Dielectric properties of DBT and Midel (Ester) compared with silicone gel (a) Permittivity at 0.5MHz (b) Conductivity at 0.1Hz (c) Loss factor at 100Hz *[17]*

1.4.2. Partial discharges evolution versus temperature

Partial discharge (PD) characteristics of materials are important for HV applications, since they indicate practical maximum limits in terms of electric field or voltage, and also demonstrate how the material behaves when PD occur. In dielectric liquids, PDs usually start from high field regions such as sharp electrode edges where the electric field is enhanced. The pollution by solid particles and the presence of bubbles may also induce PDs, but such cases will not be considered in the present study. To replicate PD inception induced by a high local electric field, PD measurements were carried out using a point-plane geometry with tip radius of curvature 2.0 µm and point-plane distance 10 mm [24]. Two main information were derived from PD measurements under AC:

i. *Partial discharge inception voltage (PDIV)* – The number of PDs usually increases exponentially versus voltage. In this study, PDIV was arbitrarily defined as the voltage level at which an average 10 PDs per minute occurred, with a threshold PD detection level of 0.3 pC.

ii. *Phase resolved partial discharge (PRPD)* – PDs under ac are often phase-shifted compared to applied voltage, and their statistical distribution and amplitude are usually different during positive and negative half-waves. Therefore, PRPD provides interesting information related to the nature and origin of PDs.

In DBT, PDs occurred mostly in negative polarity with a very low amplitude, a few pC. Further analysis showed that such PDs correspond to the inception of slow "1st mode" pre-breakdown streamers at the point [25], constituted by small cavities that does not propagate very far (a few µm). These small PDs are further suppressed with increasing temperature (Fig 1.9). A significant increase in PDIV with temperature was also reported in [17, 24].

In MIDEL® 7131, PDs occurred mostly during positive phase with much higher amplitude (up to some nC) [17, 24], corresponding to filamentary "2nd mode" streamers of much greater size [25, 26]. In contrast to Jarytherm®DBT, the PDIV was reported to decrease with increasing temperature in Midel. In Fig 1.*9*, it is significant to observe that at 80°C only a few PDs about 1 pC in amplitude are recorded in DBT @ 20 kV, whereas PDs > 2 nC already existed @ 17 kV in Midel. Therefore, it was concluded in that DBT shows superior PD suppression properties compared to Midel, especially at high temperatures (Fig 1.*10*).

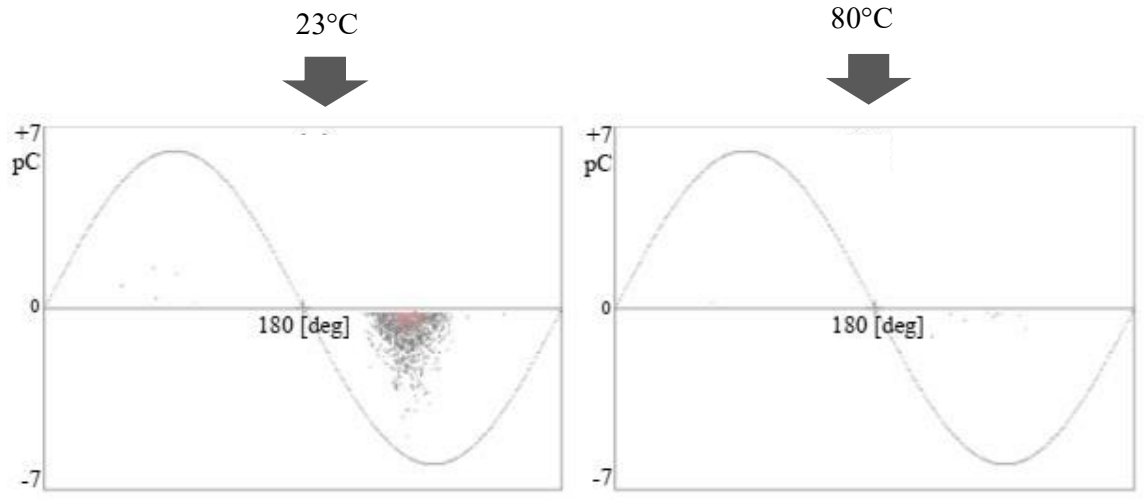

(a)

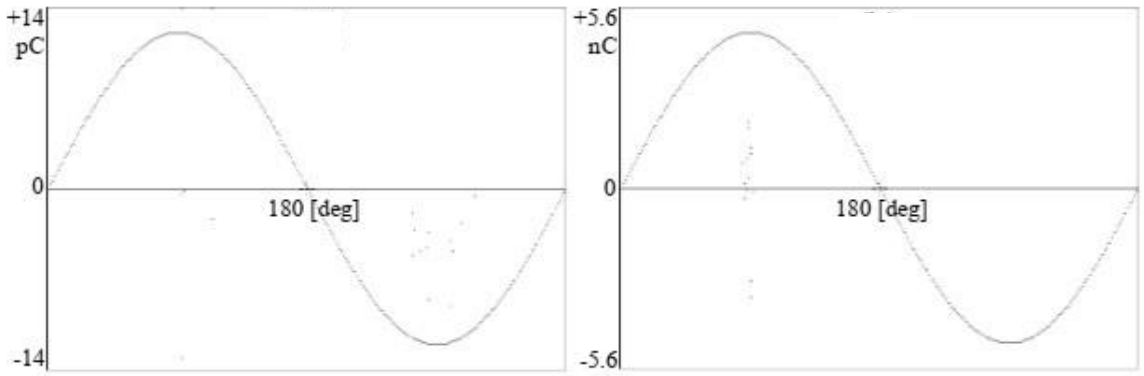

(b)

Fig 1.9. Typical PRPD pattern at temperatures 23°C and 80°C in (a) DBT at 20kV (b) Midel at 17kV *[17, 26]*

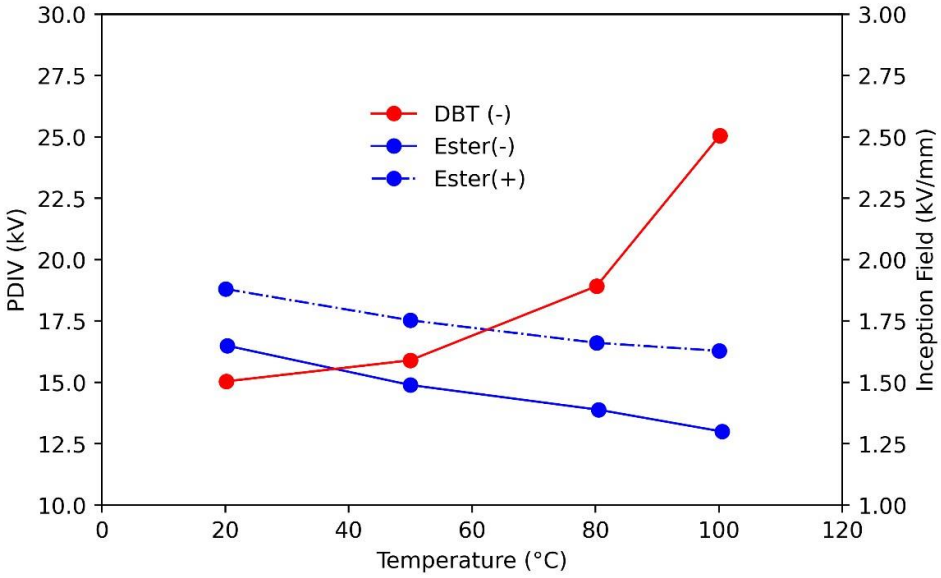

Fig 1.10. PDIV in DBT and Midel *[17]*

1.4.3. Breakdown measurements at high temperatures

Breakdown strength constitutes a fundamental dielectric property of insulating material. The voltage at which an electric arc establishes through the insulator between two electrodes is called Breakdown Voltage (BDV). The BDV does not constitute an intrinsic property, since it strongly depends on many parameters: presence of impurities (moisture, additives, particles), defects or bubbles, shape/surface of electrodes, type of voltage (ac, dc, impulses), etc. However, measurement of BDV in identical conditions (e.g., following the IEC 60156 standard method [27]) can be useful to compare liquids. Dielectric breakdown usually induces a permanent defect in solid and gel insulating materials. However, in liquid the non-permanent defect induced (bubble, by-products and carbonised particles) quickly disappears in the liquid (self-healing). This allows the fluid to be reusable after several repetitive breakdowns.

Both AC and DC breakdown measurements were previously made with DBT at temperatures up to 350°C, and in Midel (temperature up to 250°C) [17, 28]. The method was derived from the standard IEC 60156 (sphere-sphere breakdown gap), with a shorter gap distance reduced to 0.4 mm instead of 2.5 mm in the standard test, in order to limit the voltage below the limit of the high temperature test cell (30 kV). The rate of voltage rise (ramp) was 1kV/s for both AC and DC. For each liquid, 20 repetitive breakdown measurements were obtained at each temperature, with a low energy (< 100 mJ) in order to minimize the influence of degradation by-products on measurements.

The breakdown voltage for both liquids at different temperatures are summarized in the Fig 1.11. At temperatures below 250°C, Midel showed slightly higher breakdown strength compared to DBT. In both liquids, the breakdown field (E_{BD}) is significantly reduced with increasing temperature. E_{BD} in DBT even at very high temperature (350°C) remained quite high (> 35 kV/mm), superior to quoted values in silicone gels or ceramics where E_{BD} is usually less than 20 kV/mm at room temperature.

In the same study [28], a significant reduction of E_{BD} was also reported with the reduction of liquid pressure (1kPa to 200kPa). Both effects of temperature and pressure were attributed to the easier liquid / vapour phase transition occurring at high temperature and / or low pressure: the thermal energy required to boil the liquid is reduced. Since the creation of an initial vapour

cavity is the first fast step involved in the development of pre-breakdown phenomena in liquids, the breakdown voltage is accordingly reduced.

Both DBT and Midel liquids studied show promising electrical properties under high voltage and high temperature. To further investigate the possibility of using liquid as encapsulant, several partial discharge and breakdown measurements were done to test their performance when used with ceramic substrates, in comparison with silicone gel. A summary of previous work on characterization of different ceramic substrate embedded in various liquids and silicone gel will be discussed in the following sections.

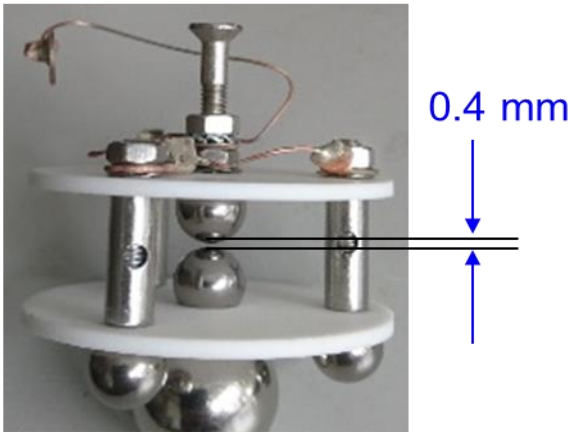

(a)

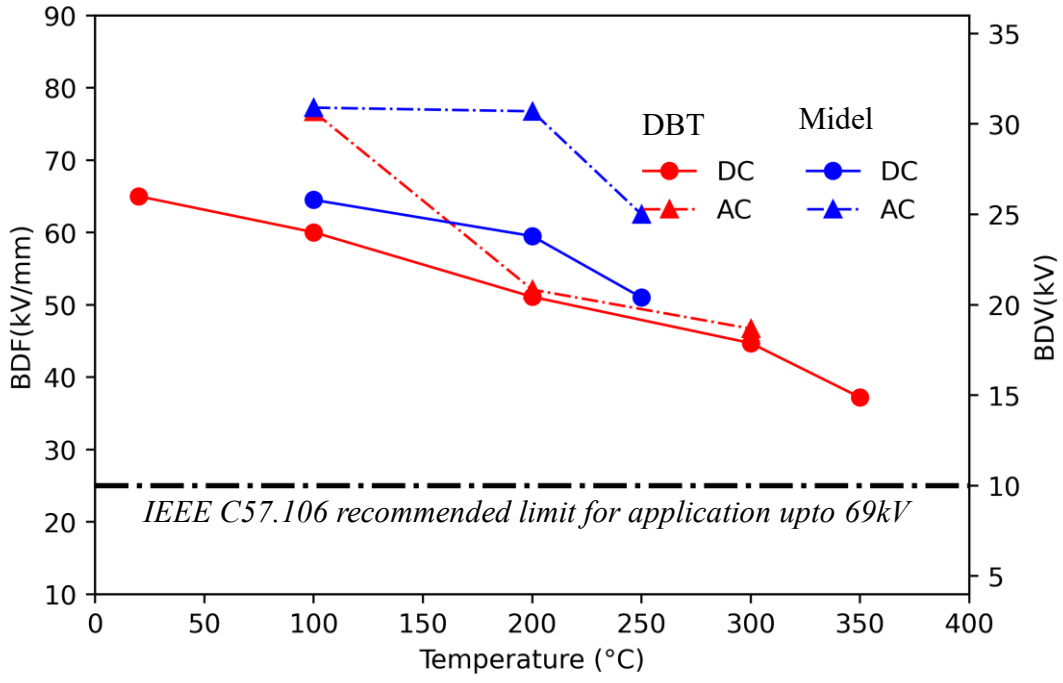

(b)

Fig 1.11. (a). Electrode assembly for breakdown measurement in liquids at high temperature. (b) AC and DC breakdown field EBD in DBT and Midel in a sphere-sphere electrode assembly *[28]*

1.5. Characterization of power electronic substrates embedded in liquid dielectrics and silicone gel

As discussed in section 1.3.1, increasing the voltage level in WBG power modules increases the risk of partial discharge and breakdown either in the encapsulation, in the ceramic substrate or at their interface. Therefore, it is essential to evaluate their occurrence with various ceramic substrate embedded in different liquids. The following sections discuss and summarise previous studies carried out with liquids and silicone gel.

1.5.1. Surface breakdown measurements

Two commonly used ceramic substrate materials, Aluminium Nitride (AlN) and Alumina (Al_2O_3), were chosen for surface breakdown studies under DC and impulse voltages, and tests were also made with fiberglass reinforced Epoxy for comparison (Fig 1.12) [17]. The electrode gap between the high voltage electrode (HV) and ground electrode varied from 0.3 mm to 1.2 mm. Although the field is non-uniform, breakdown measurements in the following are simply quoted as the average mean field (E_{BD} = breakdown voltage / gap distance).

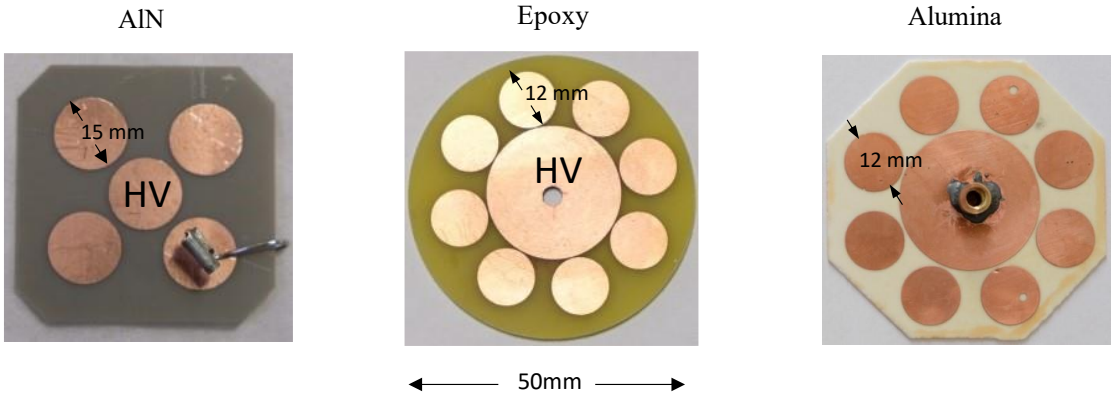

Fig 1.12. Different substrate samples used for testing breakdown between metallized tracks encapsulated with liquids and silicone gel *[17]*

Alumina and Epoxy substrates were mostly used to compare the breakdown performance between silicone gel and DBT in [29]. With epoxy, for each electrode gap distance, 20 repetitive DC breakdowns (ramp of 1kV/s) were recorded when DBT was used. No apparent drop in E_{BD} and no observable degradation were observed in the epoxy for short gaps of 0.2mm, indicating that the breakdown occurred in the liquid, allowing quick recovery to initial properties (self-healing character). However, for gaps larger than 0.5 mm, a progressive reduction of E_{BD} was reported [17, 29]. At larger gaps of 1mm, a permanent "crack" developed over the epoxy substrate, inducing irreversible degradation. When tested with Silicone gel, irreversible degradation of the gel due to breakdown occurred since the first breakdown test, irrespective of the electrode gap.

E_{BD} with DBT encapsulant was reported to be slightly higher with alumina substrate at 45kV/mm, against 32kV/mm with Epoxy. Unlike in Epoxy, breakdown always occurred in the alumina ceramics, irrespective of the electrode gap when DBT was used. This irreversible degradation of the substrate resulted in a rapid reduction of E_{BD} when repetitive tests were done with a single substrate sample.

With Alumina as substrate, silicone gel showed higher E_{BD} (69kV/mm) than with DBT (45kV/mm) at room temperature, Fig 1.13. However, as in the case of Epoxy, irreversible degradation of the gel since the 1st voltage shot resulted in large reduction of E_{BD}, down to nearly 1kV/mm. This is illustrated by the very large drop of E_{BD} between first shot, and subsequent shots in Fig 1.13. No large variation of E_{BD} was recorded versus gap distance, i.e., the breakdown voltage was roughly proportional to distance. E_{BD} was reported to reduce with increase in temperature, such as in Fig 1.13. Although DBT and alumina can withstand higher temperatures, surface breakdown experiments were limited to 200 °C due to experimental limitations. No breakdown data are available to date at higher temperatures, and with other substrate material such as AlN. Only a few preliminary experiments indicated a slightly lower breakdown voltages with AlN, compared to alumina.

In the same study [17, 29], repetitive unipolar impulse voltage (duration: 60 µs at half value, rise time: 50ns, frequency: 100Hz) was also used to compare the performance of Jarytherm® DBT against silicone gel with alumina substrate. Repetitive unipolar impulses with fast rise time were used to represent conditions more relevant to actual modules during switching, than DC. The fast dV/dt used, close to 1 kV/ns, is also representative of faster switching occurring with wide bandgap semiconductors.

A significant drop of E_{BD} was observed in gel under impulse, while no clear differences were observed between impulse and DC breakdown when DBT was used (Fig 1.14). Whatever the conditions used, slightly higher E_{BD} were recorded in silicone gel, compared to DBT (about + 25 %). These conclusions, obtained with a limited number of samples, should be however further confirmed by a more thorough investigation involving a larger number of samples, and statistical analysis such as Weibull.

As a main conclusion, the favourable self-healing breakdown property of liquids unfortunately could not be observed in the case of surface breakdown discharges with ceramic substrates. The ceramic constitutes the weakest material regarding breakdown properties, and provides the preferred path for the breakdown arc between metallized tracks. This agrees with the fact that the liquid alone shows a higher breakdown field compared to ceramic materials, although this property was observed in different conditions (quasi-uniform field).

However, DBT showed interesting breakdown properties when associated with ceramic substrates, although slightly inferior to silicone gel at temperatures up to 200 °C. This could easily be compensated by using slightly larger distances between metallized tracks. In addition, breakdown measurements in the liquid alone show that it may be used at much higher temperatures, contrary to silicone gel. Further surface breakdown experiments at higher temperatures and with a large number of samples remain however necessary to fully assess the potential of such liquid for encapsulation of high temperature / high voltage power modules.

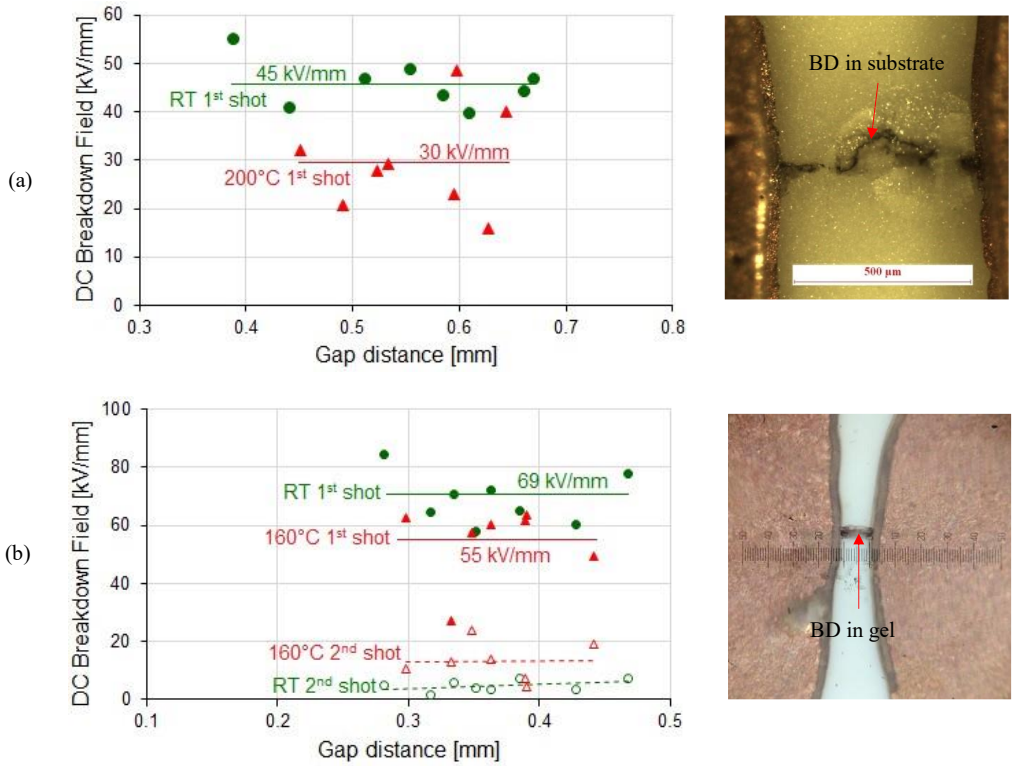

Fig 1.13. DC breakdown measurements at different temperatures with alumina substrate embedded in (a) DBT and (b) Silicone Gel *[17, 29]*

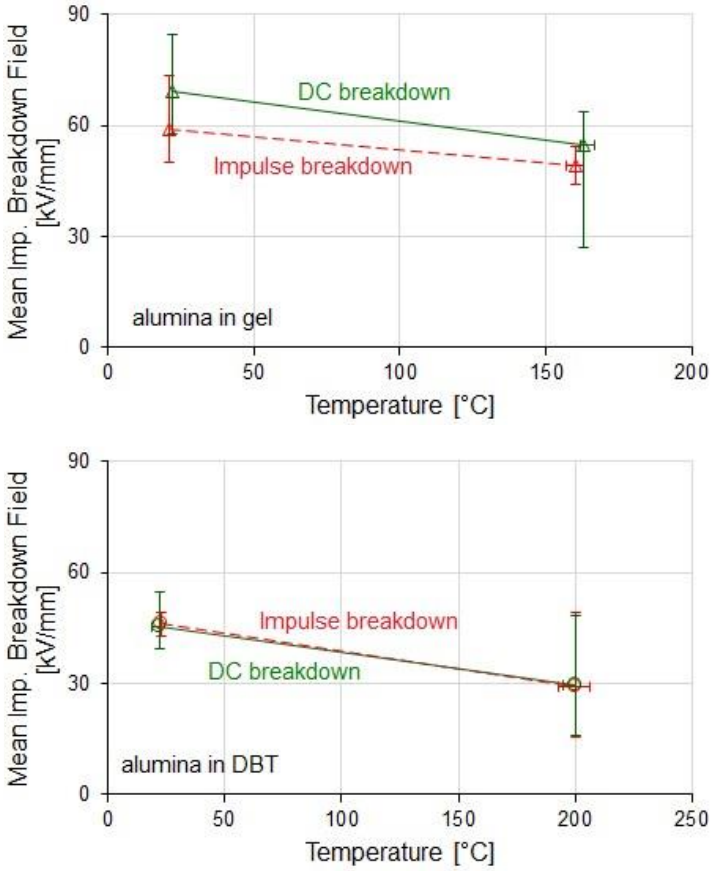

Fig 1.14. Comparison of surface breakdown over alumina substrate embedded in silicone gel and DBT *[17]*

1.5.2. Partial discharge characterization of liquids and substrates

The substrate and encapsulation materials in power module are exposed to DC or repetitive impulse voltages. Standard electrical measurement methods and tools are well established to detect PD activity under AC (see details in Chapter 3). However, these electrical methods are not suitable for fast rise impulse voltage, commonly found in SiC power modules with fast slew rate (dV/dt) up to 100kV/µs [30] . Several previous studies [29 -35] tried to use an optical detection method, to study PD activity for fast rise impulse voltage. The optical method uses a sensitive and fast light detector (photomultiplier, PM) to detect the light emitted by PDs (detail in Chapter 4), taking advantage of the transparency of encapsulating materials (silicone gel, liquids).

This method could tentatively be very useful, since it shows both high sensitivity (below 1 pC) and fast time resolution (about 1 ns), and can also be used whatever the voltage shape, contrary to conventional electrical detection. However, it's use can be limited for opaque materials, and also for materials that emit light due to other mechanisms than PD when stressed with electric field (also called "electroluminescent" material). The interpretation of light measurements can thus be misleading, may vary according to the nature of materials (substrate, encapsulant), and must be done with great care.

Previous works on PD detection in power electronic substrates embedded in liquids and gels using both electrical and optical methods will be summarised in this section. In all these experiments, metallized substrates were chemically etched and cut in desired samples to be tested in a typical test cell arrangement as shown in Fig 1.15 [31].

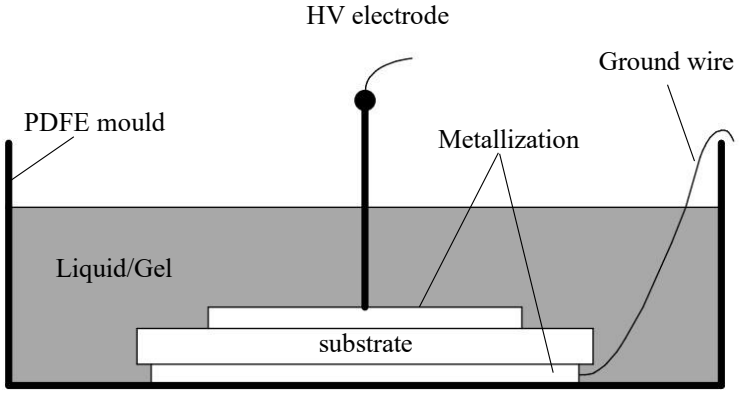

Fig 1.15. Sample geometry used for PD measurement with substrates embedded in liquids and gel *[31]*.

1.5.2.1. Partial discharges measured with standard electrical detection under AC

PD measurements with ceramic substrates made of alumina (Al_2O_3) and Aluminium Nitride (AlN) embedded in liquid (Jarytherm® DBT) and Silicone gel were reported in [17]. Very intensive PD activity was detected in both substrates without encapsulation in open air, with high PD charge (several nC) and low PDIV (~1 kV) (Fig 1.16).

When these substrates are immersed in liquids, a very large reduction of PD charge (down to a few pC) and increase of PDIV occurred [17]. In Al_2O_3, the PDIV with DBT increased to 4 kV and becomes higher than with silicone gel, and in AlN to 2.6 kV (Fig 1.15 - Fig 1.17). This demonstrates the high efficiency of DBT to supress PDs on substrates, equivalent or even superior to silicone gel.

The PD activity was observed to be symmetrical during positive and negative half waves in both Al_2O_3 and AlN substrates embedded in Jarytherm® DBT. Such patterns were surprisingly very different from PDs measured in the liquid alone using a point-plane gap [32]. Also, the number of PDs were reported to be fairly reproducible. A quite stable PD regime was obtained above PDIV, and the voltage can be nearly doubled without breakdown. Thus, it was concluded in [17] that PDs recorded with embedded ceramic substrates do not occur in the liquid, but within the Al_2O_3 and AlN ceramic material. These ceramic materials are elaborated by sintering powders and contain pores of µm size, which may explain the occurrence of internal PDs, contrary to polymers such as epoxy. With silicone oil encapsulation, PDs were also reported to originate from substrates (Al_2O_3 and AlN) with PDIV of 5kV in AlN and 3.5 kV in Al_2O_3 [31].

The influence of temperature on PD activity was investigated in [15, 17, 33]. A significant reduction of PD activity was reported when substrates are embeded in liquid (Fig 1.16 – Fig 1.18). The AlN exhibited inferior performance at very high temperatures (lower PDIV, large dielectric losses and thermal cracking at 350°C) compared to Al_2O_3 substrate [17]. With Silicone gel, some decrease of PDIV and increase of average PD current was reported when temperature is increased [17, 33]. These results suggested that liquid encapsulation has better PD suppression property at high temperature than Silicone gel. However, these results were obtained under ac voltage, and are therefore not directly representative of actual conditions within power modules. The question of PDs under fast impulses remains an open question.

The recording of PDs with epoxy substrates (non-ceramic) with silicone oil was much more difficult to achieve [33]. In most experiments, once PDs appeared they were very instable compared to sintered ceramic materials, and breakdown of the epoxy substrate occurred very rapidly. Thus, few measurements were obtained with epoxy substrates. The PDIV was about 7 kV, characterized by marked asymmetry in the PRPD pattern and much smaller average PD current (Ipd) compared to ceramic substrates. PDs are more numerous during the negative half wave, such as in measurements with point-plane electrode in liquid alone. This suggested that with Epoxy substrates, PDs originate in the liquid in a comparable way as in point-plane gap.

In conclusion, from the experiments in [17], Jarytherm® DBT encapsulation with Al_2O_3 substrate has shown promising combination for future high voltage and high temperature applications. Other liquid such as Silicone oil also exhibited promising partial discharge properties [31] which could potentially be used for high voltage applications. However, use of silicone oil for temperatures higher than 200°C has not been reported.

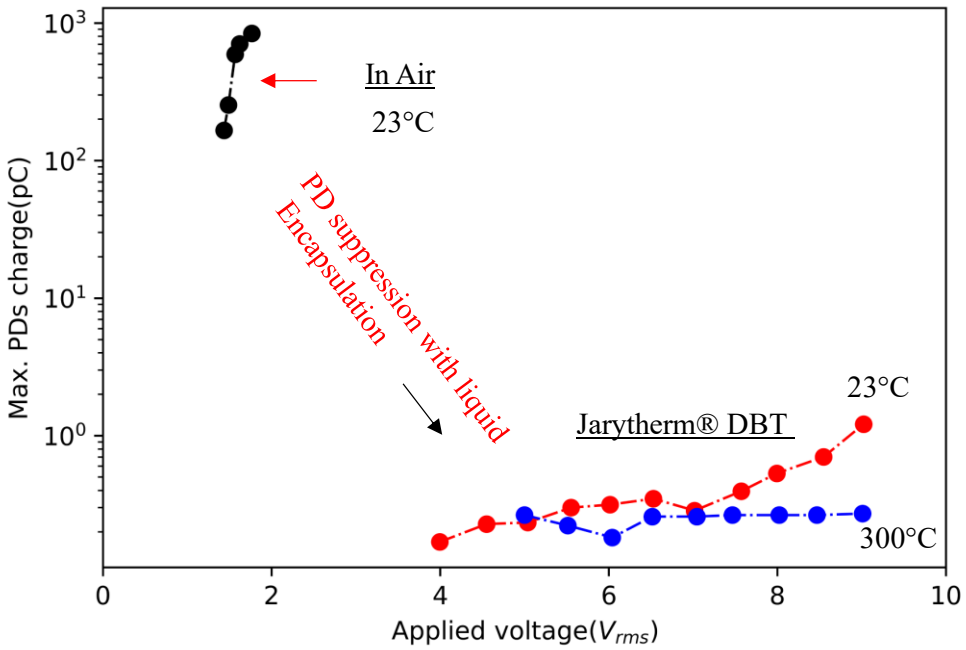

Fig 1.16. Comparison of PDs in Al_2O_3 substrate in open air versus when embedded in DBT *[17]*

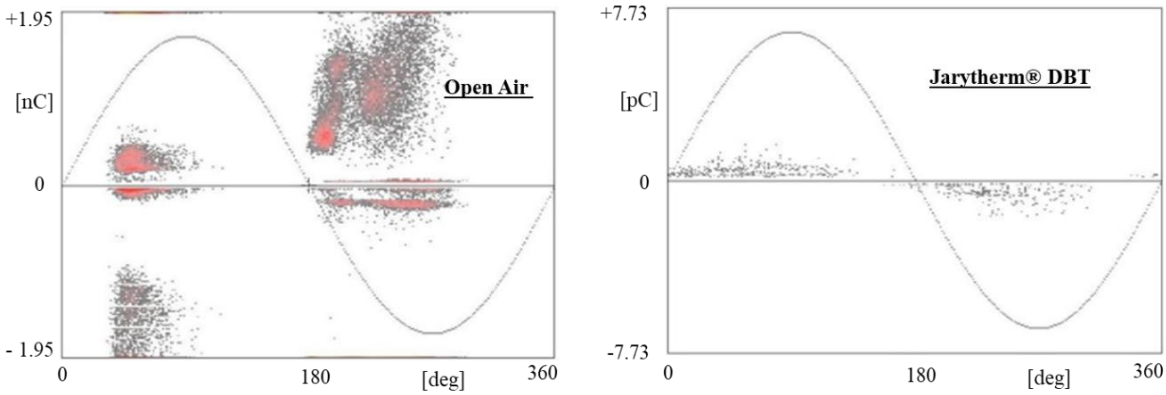

Fig 1.17. Typical phase resolved partial discharge (PRPD) in Al_2O_3 substrate measured in open air compared to when embedded in DBT *[17]*

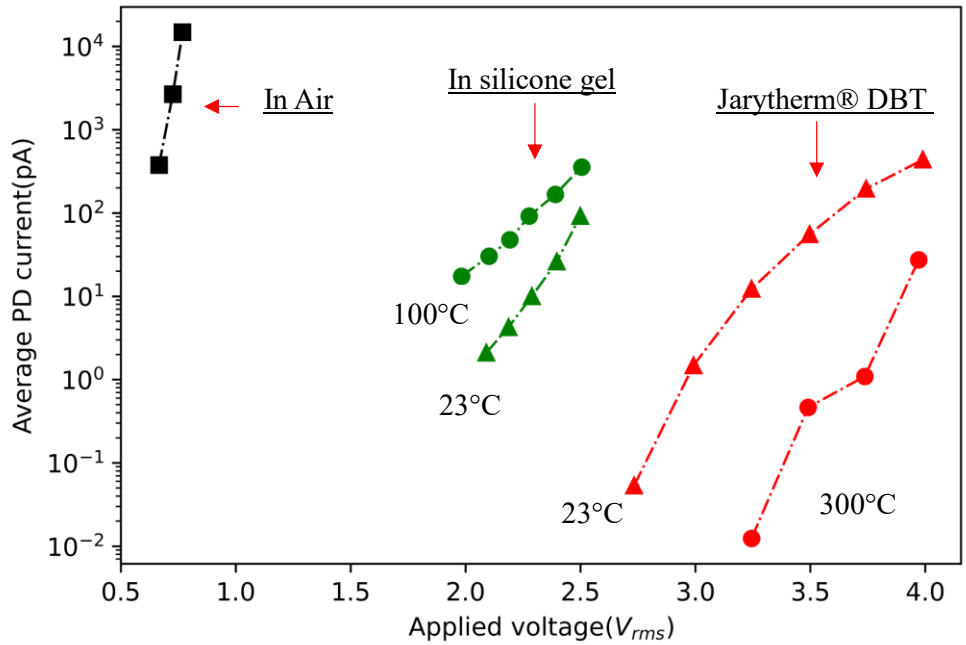

Fig 1.18. Comparison of PDs in AlN substrate in open air versus when embedded in DBT/Silicone gel *[17]*

1.5.2.2. Partial discharge detection with Optical measurements under AC and Impulse voltages

PD detection using optical methods in power electronics substrates embedded in various encapsulants has been reported in several publications [30 - 35]. Since optical PD detection method can be perturbed by other light emission processes such as electroluminescence originating from the liquid or substrates, authors in [15, 31, 34, 35] studied the correlation between light measured using optical method and PDs detected using electrical method under AC. The substrates and liquid that does not show electroluminescence were then used for PD detection under impulse voltages.

Silicone oil and silicone gel are reported to be non-electroluminescent [15, 31]. Silicone gel is rapidly destroyed by PDs and hard to remove from the test cell, therefore silicone oil was mostly used as encapsulant material in these studies.

The time resolved light recording of photomultiplier light with AlN substrate showed poor correlations with PD recording, Fig 1.19. The light emission under ac was reported to be highly dissymmetric, with very low light during positive cycle and large light intensity during negative cycle, also showing a large phase shift with voltage. In contrast, as already explained PD patterns are nearly symmetric.

Another way to compare the electrical and optical measurement methods was to check the correlation between average PD current (Ipd) with the total integrated light from PM (Ipm). The average PD current was calculated by summing all recorded PDs during a long-time duration (typically 1 minute). In AlN, Ipm was detected at voltages as low as 2.5 kVrms even though PDs started occurring at PDIV = 5kV (Fig 1.20). This large discrepancy indicated that light at low voltages is due to electroluminescence from the AlN substrate. It was also reported that AlN substrates also show photo-luminescence when exposed to light, and thermo-luminescence when exposed to high temperatures, which further complicated the PD detection

using optical methods. However, PD measurement in AlN using optical method was reported in papers such as [36], with no attention paid to its electroluminescence, which casts doubts on conclusions obtained.

In contrast with AlN, the time resolved light recording with Al_2O_3 exhibited good correlation with PD recording under AC [15, 31]. The light intensity during positive and negative voltage cycles were nearly symmetrical and slightly phase shifted, similar to PRPD recordings obtained using electrical measurement.

The variations of Ipm and Ipd can be compared, with a nearly exponential increase in both cases. The PDIV derived from optical measurements was reported to be slightly lower than PDIV recorded with electrical measurement. This was expected to result from higher sensitivity of the PM detection. Therefore, in [31, 33] only Al_2O_3 substrate embedded in silicone oil were used for evaluating PD activity under impulse voltage.

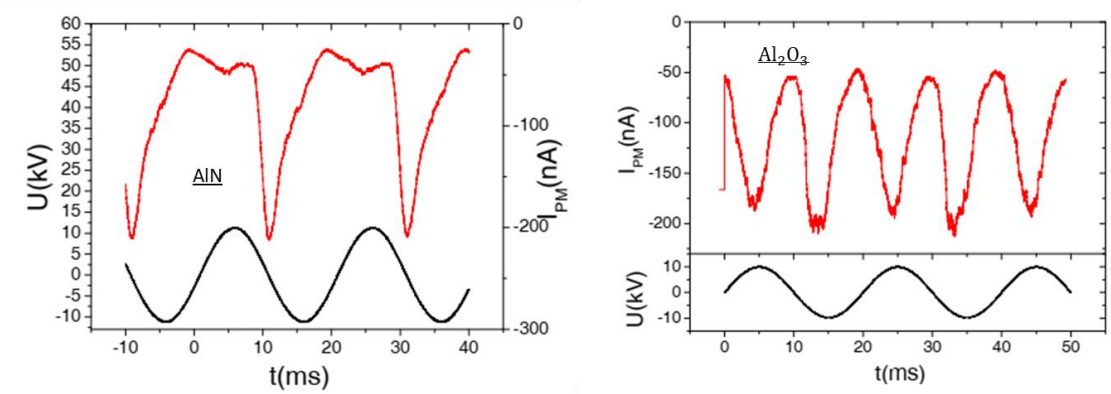

Fig 1.19. Time-resolved recording of the light emission (photomultiplier current Ipm) with AlN and Al_2O_3 substrates embedded in silicone oil under 50 Hz at room temperature (applied voltage: 8 kV rms) *[31]*

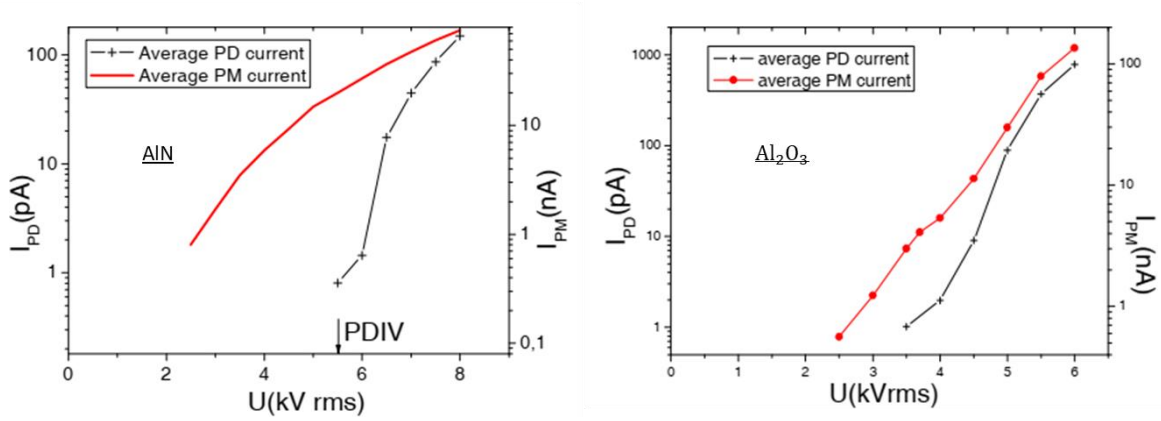

Fig 1.20. Average light intensity (Ipm) and PD current (Ipd) recorded with AlN and Al_2O_3 *[31]*

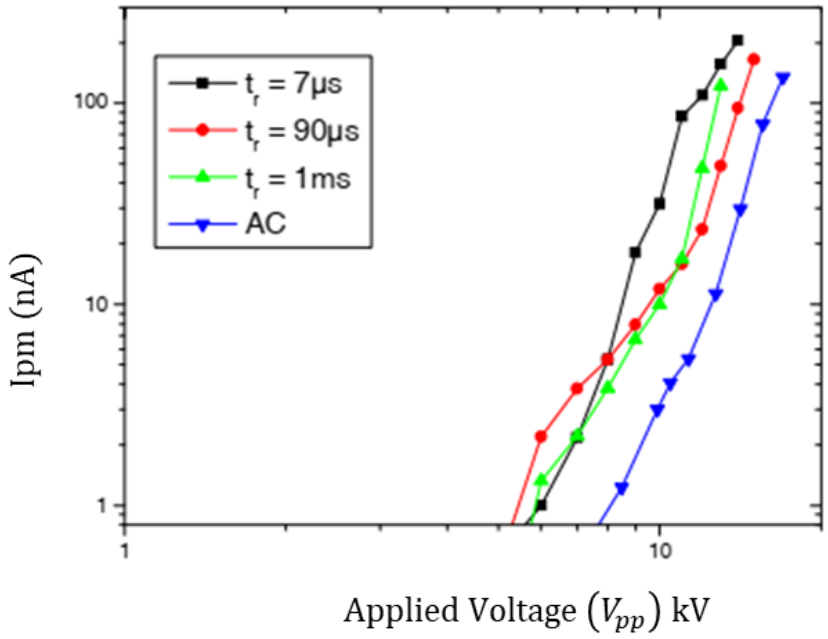

Fig 1.21. Average light intensity (I_{pm}) at different voltage rise time (τ_r) *[31]*

PD detection under bipolar impulse voltage (symmetrical square wave) in Al_2O_3 substrate embedded in silicone oil [31] showed that most light emission occurs during rise and fall of the voltage. Almost no light was detected during the plateau of the square wave. This light emission during the rise and fall were tentatively related to the occurrence of PDs resulting from high electric field enhancement near the edges of the metallization. The electric field enhancement at this triple junction can be greatly influenced by the voltage rise time (τ_r) of the voltage. For long τ_r, injected charges usually reduce the actual high field around the metal edges, and lower PD activity should be expected.

If τ_r is reduced (down to ns), the charges do not have enough time to propagate away from the sharp metal edges, resulting in higher field enhancement. Such phenomenon was previously observed with point-plane geometry: discharge inception voltage in liquids decreases with shorter rise time, Fig 1.21 [31]. This is particularly interesting to study for practical application involving fast switching electronics with slew rate in the order of 100kV/µs.

A preliminary result for different τ_r was reported with Al_2O_3 substrates in [31, 33]. However, no significant decrease in PDIV was observed with decrease in τ_r though slight increase in light intensity was observed. Compared to PDs recorded under AC, the PDIV under impulse was reduced by almost 2kV. This result is of great practical interest, since it suggests that fast impulses could induce larger material degradation by PDs compared to ac. Degradation would also increase with frequency of impulses, by increasing the PD number. These effects should be confirmed and developed in future studies, since fast impulses are relevant of actual power modules.

A detailed study of influence of space charge (with different τ_r) is reported in [36] . The authors used a PCB substrate (no mention of the name of the substrate) embedded in Nytro 10XN mineral oil. Both materials are reported to be non-electroluminescent. A very large influence of space charge was observed when τ_r was reduced from 400µs to 100ns (Fig 1.*22*). Compared to AC, the PDIV deduced from optical measurements was reported to be reduced by

$8kV_{pp}$. PDIV and light intensity did not change when the polarity of the square voltage was reversed.

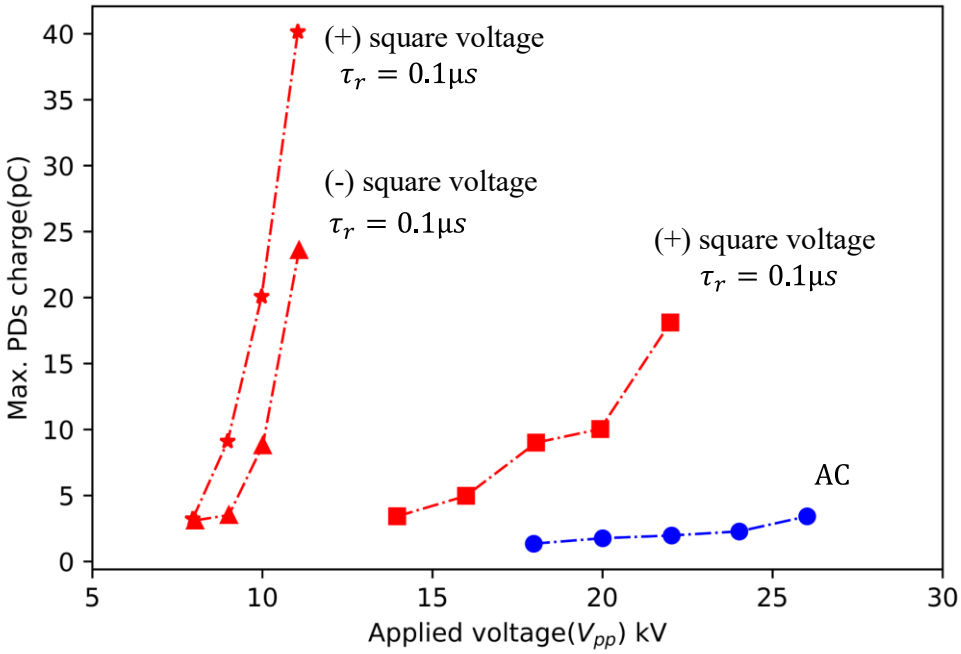

Fig 1.22. Average light intensity (Ipm) at different voltage rise time (τ_r) with PCB embedded in ester liquid *[36]*

1.6. Remaining questions and Thesis objectives

In the context of finding a new encapsulating material for high temperature and high voltage power modules, several previous studies dealing with the idea of using liquids have been summarized in the previous sections. Several points were addressed, but as noted above many aspects remain either insufficiently understood or characterized, or even not yet considered. A short list of remaining questions, both dealing with the practical application of liquids, and with understanding of some basic phenomena, is provided below.

Some remaining questions:

- Partial discharge detection under steep impulses using optical method has provided first qualitative interesting results in the case of one liquid (silicone oil) and one substrate (Alumina). Could it be extended to other materials, and is it possible to obtain a more quantitative evaluation of PD intensity with this method ?

- Previous studies were mostly focused on DBT and Midel. Are there any other potential liquids of interest ? Can we evaluate the thermal stability of these liquids on the long term when subjected to high temperatures?

- Dielectric properties at high temperature were only characterized at moderate field (some kV/mm), whereas in a real substrate geometry the field would be much higher (possibly above 100 kV/mm), and the impulses are steeper. It would be very interesting to characterize the non-linearity of properties (especially conductivity) at such field, and evaluate its impact on the actual field distribution in a realistic substrate geometry, also taking into account the quite specific conditions present: very high local divergent field, high temperature, presence of thermal gradients, transient applied voltage.

- Could a liquid also contribute significantly to the cooling of power semiconductors in a practical module geometry, and what can we expect from electrohydrodynamic (EHD) movement that should set up and enhance heat transfer in the presence of high electric fields ?

Thesis Objectives:

The present work constitutes a continuation of prospective studies already carried out at G2Elab in this field. We will address the following objectives:

- Development of liquid characterization relevant to power modules conditions: electrical conductivity measurements at high transient field and high temperature in different potential liquids, and evaluation of their thermal stability;

- Transient electric field simulation taking into account the non-linear material properties (versus temperature and field) in a realistic triple junction geometry;

- Development of the partial discharge measurements with various ceramic substrates embedded in dielectric liquids, using optical method under ac and impulses, and influence of space charge on PDs activity;

- Evaluation of heat transfer enhancement with EHD in conditions relevant to modules (no forced circulation, high electric field, large temperature gradients present), and of practical cooling enhancement obtained in a real module geometry.

This manuscript will be organised as follows:

Main Chapters:

Chapter 1: Review on potential encapsulation and substrates for wide band gap power modules

Chapter 2: Dielectric properties of liquids, non-linear conductivity and electric field simulation

Chapter 3: Optical partial discharge measurement for fast rise impulse voltage

Chapter 4: EHD heat transfer enhancement studies and possible application

Chapter 5 : Conclusion and Perspectives

Annexes

Annex A : Accelerated thermal aging studies in dielectric liquids

Annex B : Conductivity and dielectric spectroscopy measurements in Al_2O_3 substrate at high voltage and high temperature

Annex C: Surface breakdown studies with Si_3N_4 substrate embedded in dielectric liquids

2| Dielectric properties of liquids, non-linear conductivity and electric field simulation

This chapter presents characterization of different dielectric liquids to evaluate their feasibility to be used as encapsulation in power modules. Dielectric properties (low field conductivity, permittivity and dielectric loss factor) of four commercial liquids, i.e., DBT, BT06, Silicone Oil (S.Oil) and Mobil Jet^{TM} Oil (MJO) were compared using dielectric spectroscopy at temperature upto 150°C. In continuation, conductivity measurements were made at high temperature and high electric field for DBT (upto 300°C and 30kV/mm) and Silicone Oil (upto 200°C and 10kV/mm). The measurement of conductivity in DBT for wide range of temperature and electric field are used to develop an empirical equation representing electrical conductivity as functions of both temperature and electric field. This equation is then used to for transient electric field simulation with alumina substrate embedded in DBT.

2.1. Characterization of different insulating liquids by Dielectric Spectroscopy

2.1.1. Broadband dielectric spectroscopy (BDS): principle

Dielectric spectroscopy experiments involve application of low sinusoidal voltage U(t) of frequency ranging from µHz to GHz [37] across the sample under test with capacitance C. The capacitance of two parallel plates of area A filled with a dielectric medium of permittivity ϵ is given by the equation 2.1.1(a).

$$C = \epsilon \frac{A}{d} \qquad 2.1.1\ (a)$$

The capacitive nature of dielectric material results in a phase shift (φ) of the current I(t) relative to the applied voltage (Fig 2.1). The voltage and current are expressed as:

$$U(t) = U_o \cos(\omega t) \qquad 2.1.1(b)$$

$$I(t) = I_o \cos(\omega t + \varphi) \qquad 2.1.1\ (c)$$

The values of U_o and I_o are measured by a high precision phase sensitive current and voltage analyser. Transforming the time domain representation into frequency domain using Fourier transformation over N periods of current measurement, the complex current I^* is given by:

$$I^*(\omega) = I'(\omega) + i\, I''(\omega) = \frac{2}{NT}\int_0^{NT} I(t)\, e^{i\omega t} dt \qquad 2.1.1(d)$$

This allows the determination of impedance $Z^*(\omega)$:

$$Z^*(\omega) = Z'(\omega) + i\,Z''(\omega) = \frac{U_o}{I^*(\omega)} \qquad 2.1.1(e)$$

The software program dedicated for Dielectric Spectroscopy experiments allows calculating several parameters from the measured impedance $Z^*(\omega)$.

Dielectric spectroscopy analysis often uses the complex forms of conductivity (σ^*) and permittivity (ε^*) derived from the measured impedance Z^* as in following equations:

$$\sigma^*(\omega) = \sigma'(\omega) - i\sigma''(\omega) = \frac{1}{Z^*(\omega)}\frac{d}{A}\ [S/cm] \qquad 2.1.1\ (f)$$

$$\varepsilon^*(\omega) = \varepsilon'(\omega) - i\varepsilon''(\omega) = \frac{-i}{\omega\, Z^*(\omega) C_o} \qquad 2.1.1(g)$$

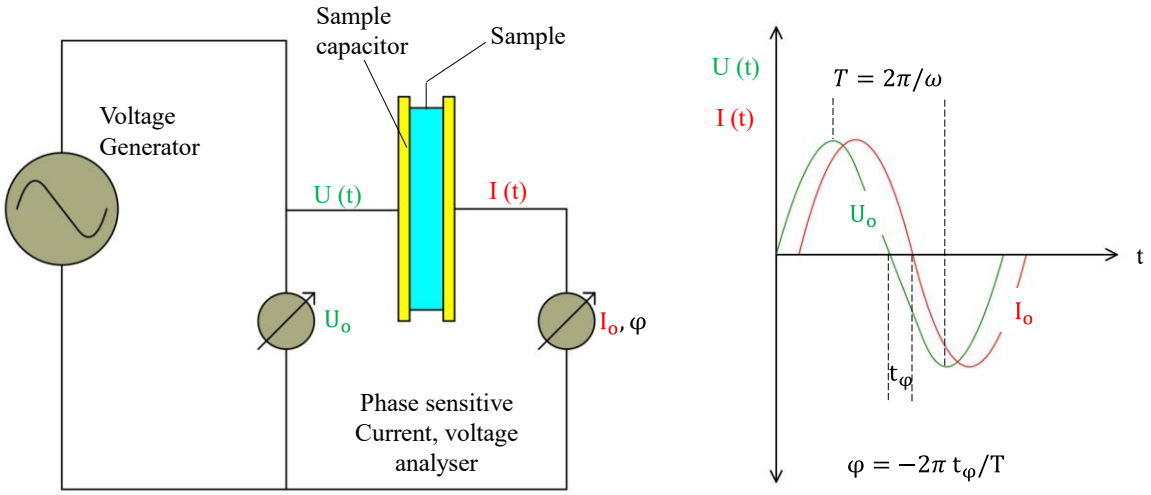

Fig 2.1. Principle of impedance measurement used in broadband dielectric spectroscopy experiments *[37]*

The real component of conductivity (σ') results from two contributions, i.e., bulk conduction current due to charge carriers (σ_{DC}) and displacement or charging current related to change of electric field and ε'. For comparison of different liquids, the determination of σ_{DC} gives an insight into initial insulating properties of the liquid, and also possibly on variations due to the presence of impurities, or to ageing. The real component of permittivity (ε') is often refered as the dielectric constant. It represents how dipoles align under electric field, and is related to the storage of energy by the material stressed by an electric field. In typical applications, a high value of ε' is desired for dielectrics used for capacitors to maximize energy storage, but conversely a low ε' is preferred for electrical insulation. A low ε' (non-polar liquids) is associated to a lower content of polar groups, and consequently to a low ability to dissolve impurities (i.e. water), providing a lower conductivity and better stability. The imaginary component (ε'') is often referred as loss index of the dielectric liquid. The ratio of ε'' to ε' gives the dissipation factor.

$$\tan(\delta) = \frac{\varepsilon''}{\varepsilon'} \qquad 2.1.1\ (h)$$

2.1.2. Measurement setup and procedure

A BDS dielectric spectrometer, Novocontrol Alpha-A was used for the measurement of dielectric properties of different liquids. It uses an applied voltage of 1V (rms) with frequency range from 10mHz to 1MHz. The Alpha A-main frame (Fig 2.2) [38] is the master unit of the measurement system that contains frequency response analyser, power supply, analog/digital control units, etc. A general-purpose test interface (ZG2) converts the sample current and voltage into two voltage signals, providing access to the sample impedance. All system functions of the mainframe and test interface are controlled by the mainframe IEEE488 GPIB interface port by high level GPIB commands via an external CPU equipped with WinDATA software application. The WinDATA contains routines to control temperature, initiate measurement and visualize/export data.

The test cell used for measurements in liquids, designed and built by G2Elab, is a stainless-steel container with volume of 200ml, equipped with a coaxial electrode system (cylinder diameters of 44.7 mm and 37.2 mm, and length of 62 mm). The gap distance between the two electrodes is 3.75 mm providing a capacitance in air C0=23.7 pF. The test cell and electrode systems are thoroughly rinsed with acetone and dried with pressured air before filling with a new liquid.

The test cell filled with liquid is placed under vacuum (2 hours) to remove trapped air bubbles introduced primarily during the filling process. It is then placed in a climatic chamber. The temperature of climatic chamber was controlled at 25°C, 50°C, 100°C and 150°C. Temperatures higher than 150°C were avoided in order to prevent oxidative thermal aging during measurements (since the free surface of the liquid is partially exposed to ambient air in this test cell). The temperature controller was set to wait for 1 hour after reaching temperature stabilization, ensuring uniform temperature within the test cell before initiating the measurement.

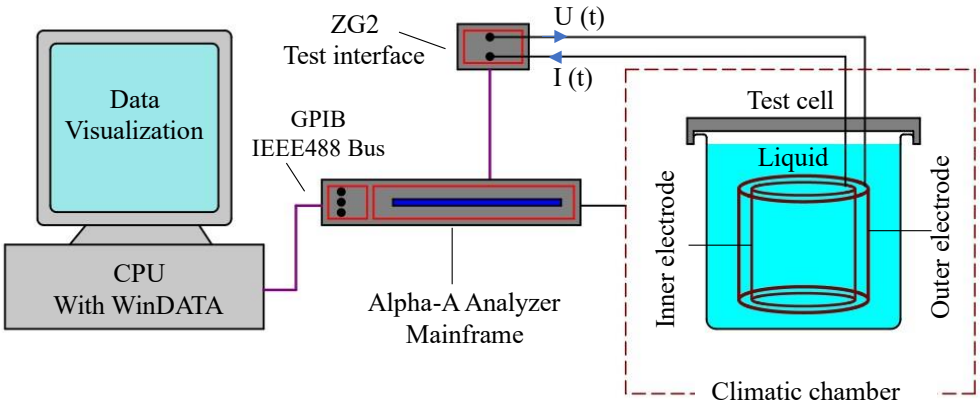

Fig 2.2. Test setup for dielectric spectroscopy measurements with liquids *[38]*

2.1.3. Low field conductivity measurements, and comparison between different liquids

Conductivity measurements as a function of frequency at different temperatures in the four different liquids investigated can be seen in Fig 2.3. In liquids, a clear distinction between the frequency independent DC conductivity (σ_{DC}) and frequency dependent AC conductivity (σ_{AC}) is usually observed. The low field σ_{DC} results from conduction current component ($\sigma_{DC}\bar{E}$) while the σ_{AC} results from displacement current density ($\varepsilon'\epsilon_o \frac{\delta\bar{E}}{\delta t}$) as in equation 2.1.3 (a).

$$\bar{J} = \sigma_{DC}\bar{E} + \varepsilon'\epsilon_o \frac{\delta\bar{E}}{\delta t} \qquad 2.1.3(a)$$

The measured σ_{DC} mainly results from impurities (weakly bonded ions, free ions, charged particles etc,) already present in the liquid at very low electric field (0.37 V/mm in BDS measurements, calculated from peak voltage of 1.4V across electrode gap of 3.75mm). This implies that the influence on conductivity enhancement by electric field is negligible in such measurements.

The lowest DC conductivity at 25 °C was measured in silicone oil (S.Oil, 5.3 x 10^{-16} [S/cm]) while Mobil Jet™ Oil (MJO) showed the highest conductivity of 5.3 x 10^{-12} [S/cm]. This result is qualitatively linked to the larger permittivity of MJO ($\varepsilon' = 3.5$, see next section), compared to the other liquids investigated ($\varepsilon' < 2.8$).

The high conductivity of Mobil MJO also probably results from the presence of additives (not known in detail) added to the base ester liquid to improve lubricating, oxidation, corrosion, pour point, and other properties, since MJO is primarily used as lubricating oil in aeronautic applications.

In measurements at high frequency on Fig 2.*3*, the conductivity departs from the stable σ_{DC} value above some critical frequency, for two main reasons:

- In liquids showing the lowest conductivity (S.Oil, DBT), measurements are limited by the theoretical maximum resolution of the Novocontrol spectrometer (indicated in broken line), that depends on frequency and sample capacitance. Measurements quoted below this limit only result from noise and measurement errors, and have no practical significance

- In liquids with higher conductivity (BT06, MJO), measurements are above the experimental limit and hold meaningful significance. The few available data in this region indicate that AC conductivity now decreases with temperature, aligning with similar variation reported in other liquids. Previous analyses have attributed these variations to dipolar relaxation, which is mostly responsible for liquid losses in this region [39]. Unfortunately, the limited and somewhat scattered data obtained in this study hinders further in-depth analysis.

The synthetic hydrocarbon liquids, Jarytherm®DBT and Jarytherm®BT06 have similar chemical composition (benzyltoluene isomers). However, a significant difference in DC conductivity is observed, $\sim 10^{-14}$[S/cm] in DBT and $\sim 10^{-12}$ [S/cm] in BT06 measured at 25°C, Fig 2.*3*. This essentially results from their marked difference in viscosity (Table 1.2), and hence of charge mobility in these two liquids. Conductivity in DBT is more than 1 order of magnitude larger compared to silicon Oil, even though they have similar viscosity and permittivity. This discrepancy may be attributed to the higher presence of impurities in DBT. This industrial liquid is primarily intended to heat transfer, and during manufacturing no special treatment (i.e., removal of polar impurities) was applied to reduce its electrical conductivity. Other commercial liquids of similar composition (e.g., Jarylec C101™, built by Arkema) dedicated to electrical insulation within capacitors or transformers also exist, and undergo such special dielectric treatment to reduce conductivity. Unfortunately, the maximum temperature allowed (about 120 °C, due to the presence of epoxide additives) is much reduced compared to DBT and BT06, and such liquids were not considered in our study.

The expression for total ionic conductivity in dielectric liquid is generally written as,

$$\sigma_{DC} = q\ \mu \qquad 2.1.3(b)$$

Where, q is the total electric charge density resulting from different charge carriers, and μ is the average charge mobility of charge carrier species within the liquid. Temperature influence both q and μ thereby resulting in a significant change in conductivity.

The conductivity in all the four liquids significantly increased versus temperature. For example, the conductivity in S.Oil and DBT increases by 4 orders of magnitude when temperature increases from 25°C to 150°C. Similarly, around 2 orders of magnitude increase in conductivity is recorded in BT06 and M.Oil. This marked increase in conductivity with temperature is essentially due to increase of charge mobility, as a result of decreased viscosity. If the ion dissociation rate is not affected by the temperature ($i.e.\,\mathrm{q} = \mathrm{constant}$), the product of conductivity by viscosity (ν) should remain constant (Walden's Rule),

$$\sigma_{DC}\,\nu = \mathrm{Constant} \qquad 2.1.3(b)$$

This does not hold true for many non-polar dielectric liquids containing weakly bonded ionic impurities, which dissociates with increasing temperature ($\mathrm{q} \neq \mathrm{constant}$) [40]. For example, the product of viscosity and conductivity of BT06 and DBT has been observed to increase slightly with temperature. However, it helps to explain why there is much more increase in conductivity of DBT compared to BT06 when temperature is increased.

Fig 2.*4* shows the influence of the decrease in viscosity with temperature in comparison to the variations in conductivity. The viscosity of DBT drops much faster compared to BT06 with increasing temperature, in line with the increase of DC conductivity. Such comparison could not be made for M.Oil and S.Oil due to their very low conductivity, which approaches the measurement limit.

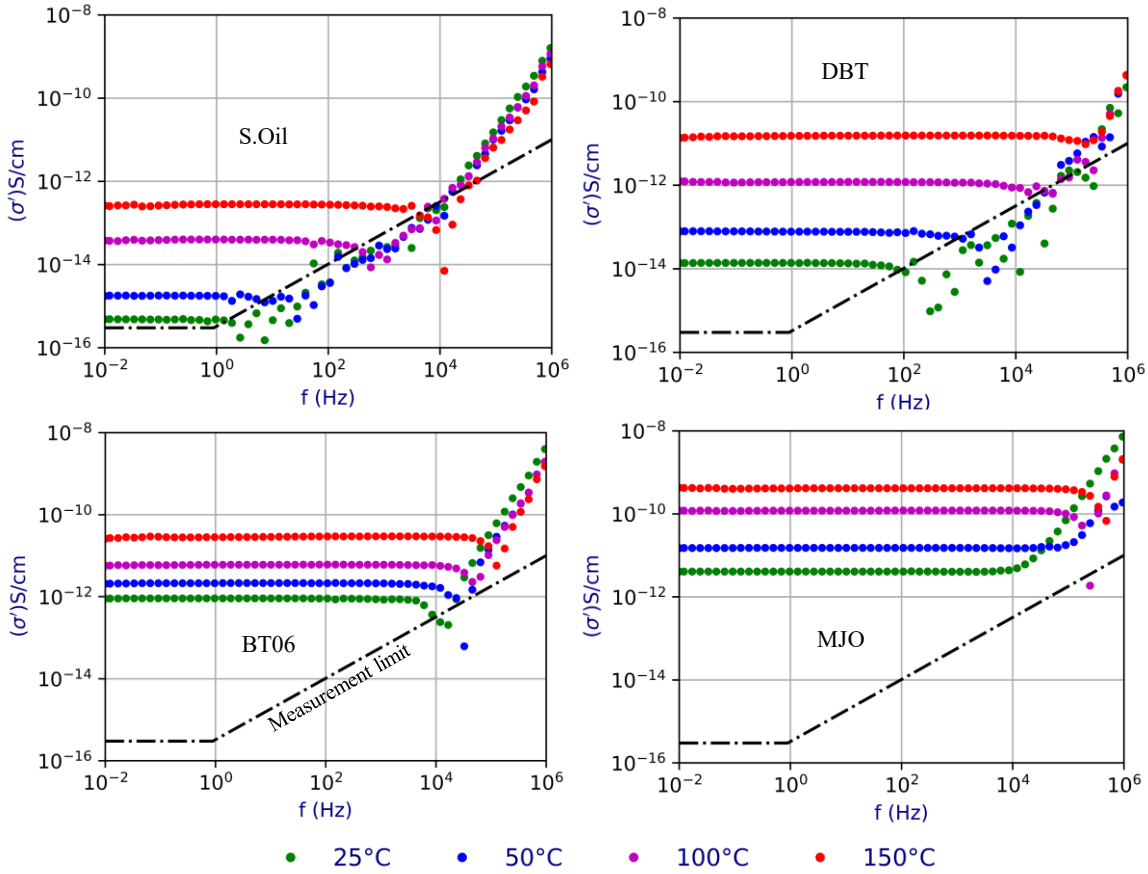

Fig 2.3. Conductivity comparison of different insulating liquids

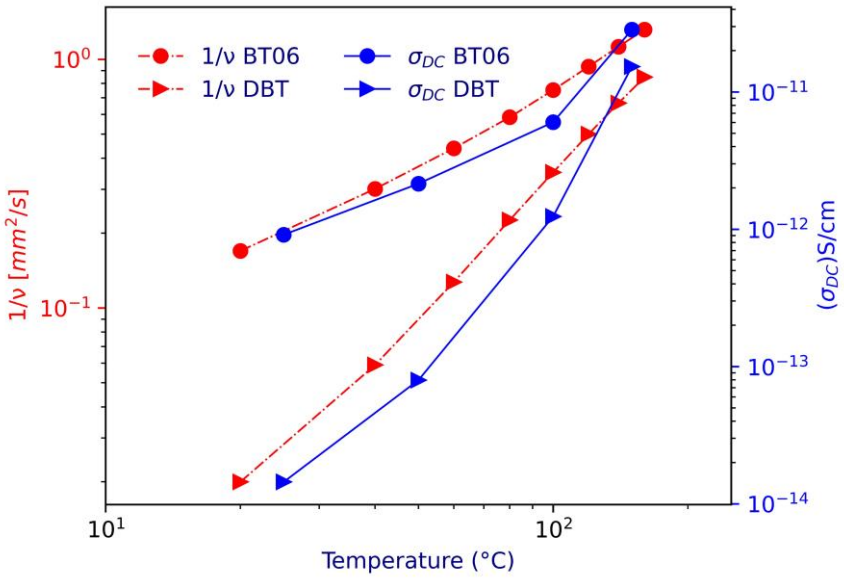

Fig 2.4. Relation between kinematic viscosity and conductivity of DBT and BT06 at different temperatures

2.1.4. Estimation of ionic activation energy

The temperature dependence of ionic conductivity usually follows an Arrhenius-type dependence which is expressed as:

$$\sigma_{DC}(T) = \sigma_0 \exp\left(-\frac{E_a}{kT}\right) \qquad 2.1.4\ (a)$$

Where σ_0 is the pre-exponential conductivity factor [4], k the Boltzmann's constant, T the temperature (in Kelvin) and E_a the minimum energy required for ionic conduction to start. Equation 2.1.4 (a) can be linearised using natural log as,

$$\ln(\sigma_{DC}(T)) = -\frac{E_a}{kT} + \ln(\sigma_0) \qquad 2.1.4\ (b)$$

This equation now takes the form (y = mx+b) where $y = \ln(\sigma_{DC}(T))$, $x = \frac{1}{T}$, $m = \frac{E_a}{k}$ and $b = \ln(\sigma_0)$. The Arrhenius plot for ionic DC conductivity σ_{DC} of the four liquids measured at temperatures ranging from 25°C to 150°C is shown in Fig 2.5 . The activation energy is deduced from the slope, $E_a = -mk$. It is found that activation energy in DBT (0.6eV) is double that of BT06 (0.29eV). S.Oil and DBT show similar activation energies while M.Oil showed an intermediate activation energy.

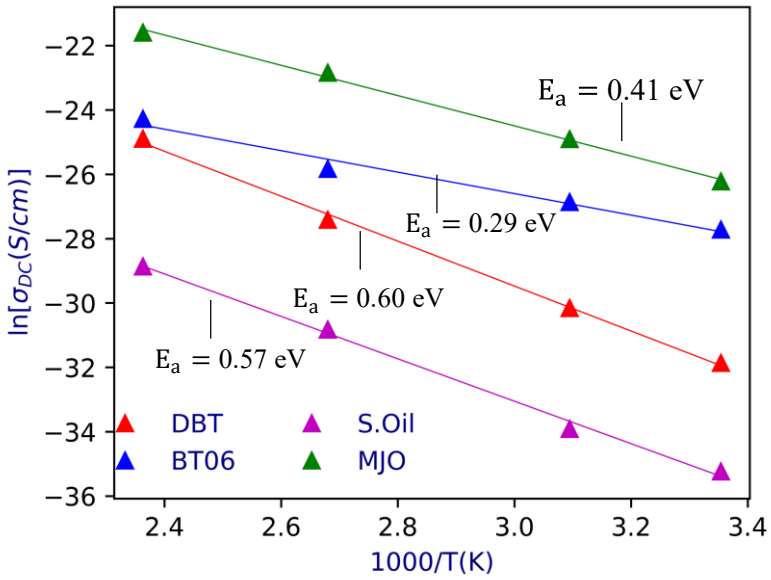

Fig 2.5. Activation energy of ionic conduction in different investigated insulating liquids

2.1.5. Permittivity measurements

In the case of non-polar dielectric liquids, the permittivity (ε′) is mainly determined by its electronic/atomic polarizability. Measurements of ε′ as function of frequency at different temperatures in different liquids are shown in Fig 2.6. At high frequencies, ε′ is constant, resulting from electronic/atomic polarization which happens on a much shorter time scale [41]. At very low frequency, other phenomena such as electrode polarization, not studied in detail here, may explain the increase of permittivity recorded. For practical purposes, the constant ε′ at high frequency is normally considered as the true permittivity or simply dielectric constant.

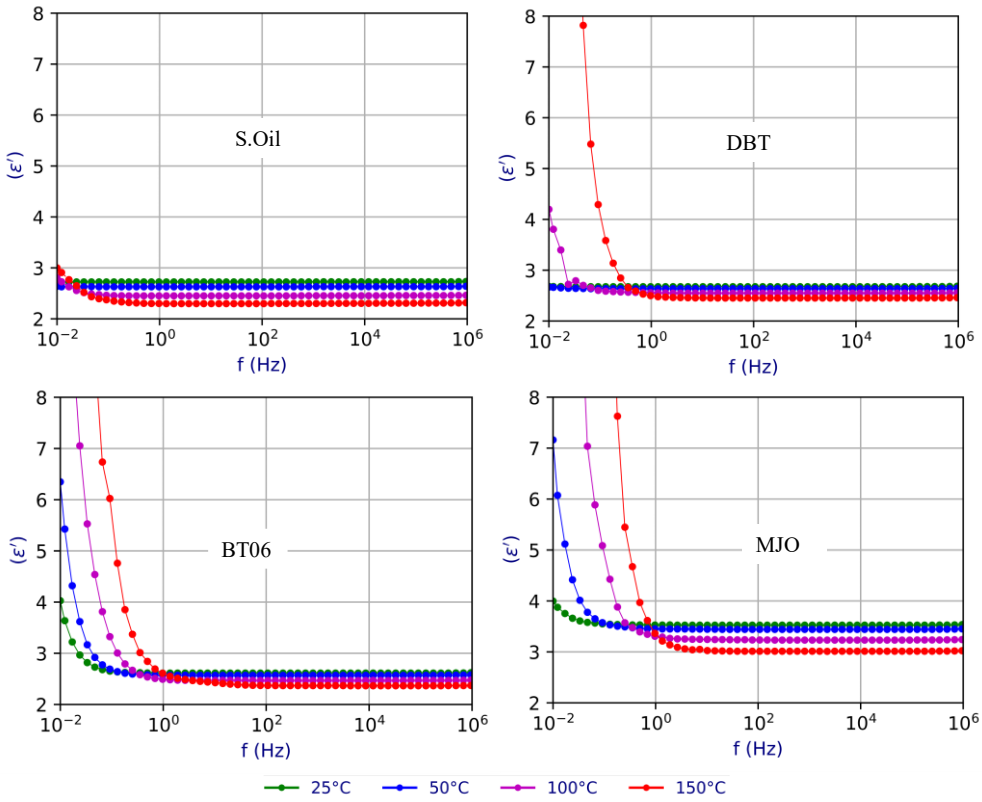

Fig 2.6. Permittivity variation versus frequency and temperature in different insulating liquid

In all liquids a slight decrease of permittivity ε′ versus temperature is recorded. This can primarily be attributable to the decrease in density, which in turn leads to a reduction in dipole density, resulting in a decrease in the dielectric constant. For constant pressure (atmospheric pressure), a linear decrease of dielectric constant versus temperature is observed in all the four liquids (Fig 2.7). The change of permittivity ε′ with temperature can be expressed as,

$$\epsilon'(T) = \epsilon_{ref} + \alpha\, T \qquad 2.1.5\ (a)$$

Also, the change in density of liquid with respect to temperature at constant pressure can be represented as,

$$\rho(T) = \rho_{ref} + \beta\, T \qquad 2.1.5\ (b)$$

Where ϵ_{ref} and ρ_{ref} are the permittivity and density extrapolated to T= 0°C respectively. The linear coefficient α and β represents the slope of graphs in Fig 2.7. These calculated parameters are presented in Table 2.1

Table 2.1. Calculated parameters of permittivity depending on density change due to temperature

Liquids	ϵ_{ref}	ρ_{ref}	α	β	$\frac{\beta}{\alpha} * \frac{\epsilon_{ref}}{\rho_{ref}}$
DBT	2.72	1059	-0.00179	-0.724	1.03
BT06	2.66	1023	-0.00192	-0.742	1.01
S.Oil	2.80	-	-0.00338	-	-
MJ.Oil	3.64	-	-0.00415	-	-

Variation of permittivity with change in density caused by increasing temperature is evaluated by resolving them into per unit system in ratio of its reference values (ϵ_{ref} and ρ_{ref}). For strong correlation between $\epsilon'(T)$ and $\rho(T)$, the ratio of the slopes (β/ρ_{ref}) to (α/ε_{ref}) should be close to unity. The compariosn was possible with DBT and BT06 thanks to the density data provided by Arkema. For both BT06 and DBT, the ratio of the slopes were close to 1 indicating that permittivity in these liquids are mostly dependent on variation of density.

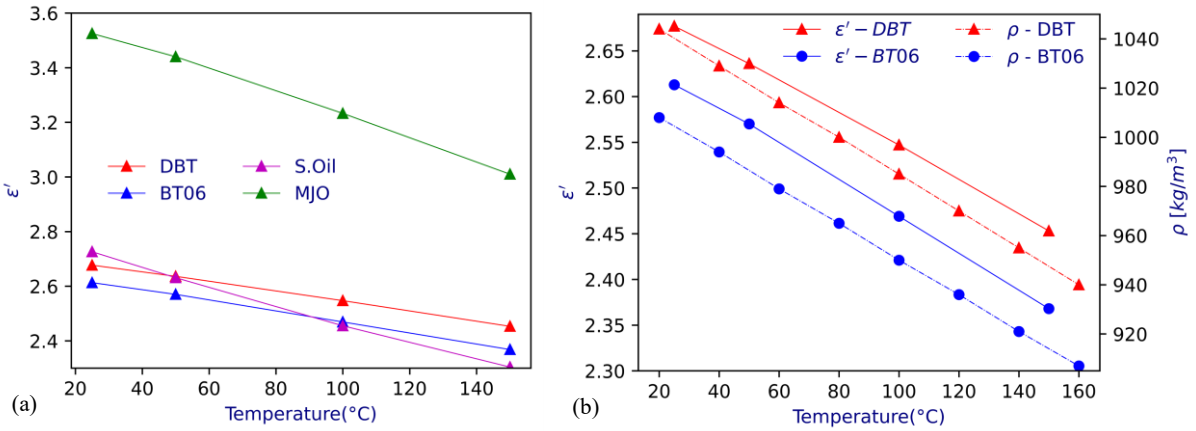

Fig 2.7. (a) Permittivity (0.5MHz) variation with temperature (b) Variation of permittivity and density of DBT and BT06 with increasing temperature

2.1.6. Dielectric losses in different liquids

Dissipation of energy in dielectric liquid, manifesting as heat, is influenced by several factors. These losses are produced by the movement of ions or charged particles, rotation of permanent and induced dipoles, interfacial relaxation, space charge relaxation, etc. In non-polar dielectric liquids, the losses due to leakage conduction current are dominant especially for low frequencies. The dissipation can be alternatively represented as,

$$\tan(\delta) = \frac{\sigma_{dc}}{2\pi\varepsilon'\varepsilon_o} \times \frac{1}{f} \qquad 2.1.6\ (a)$$

This implies that for dielectric losses resulting from pure ionic conduction current, the slope of log [tan(δ)] plotted against log [f] should be equal to -1. This can be observed in almost all the four liquids at frequencies below 10kHz, Fig 2.8.

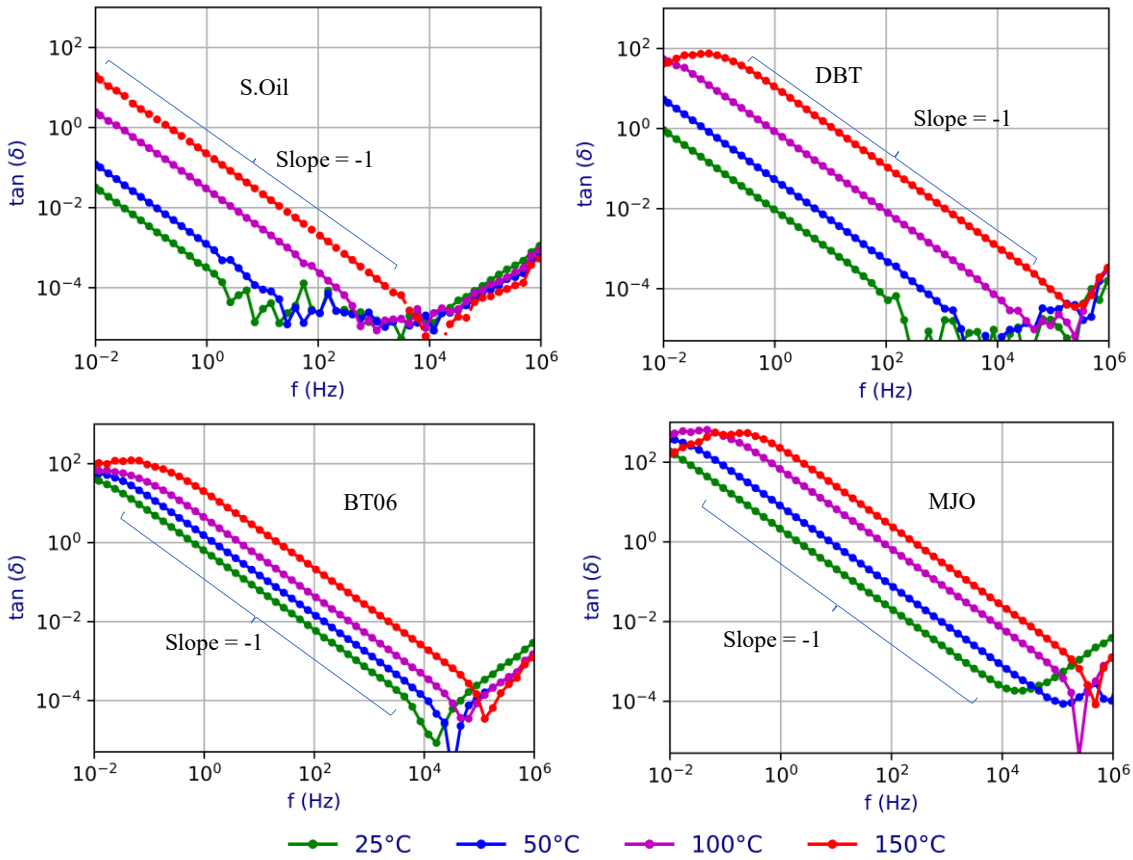

Fig 2.8. Dissipation factor in different dielectric liquids

S.Oil logically shows the lowest losses while maximum losses were recorded in MJO, very similar to conduction characteristics described in previous sections. At power frequency of 50Hz, the dissipation factor is purely ionic.

The recording of tan (δ) at 50Hz in S.Oil drops below the 10^{-4} measurement limit of the Novocontrol for temperatures below 50°C. Below this limit, tan (δ) measurements become erratic and without significance, Fig 2.9. In a similar way, measurements above 10^4 Hz, showing an increase of losses in S.Oil and DBT, are purely instrumental, while in BT06 and MJO, they are slightly above the instrument limit, and show the influence of dipolar relaxation, although poorly resolved.

The dissipation factor in BT06 at 50Hz is observed to be 2 orders of magnitude larger than in DBT at 25°. However, it increases faster in DBT versus temperature, linked to the faster decrease in kinematic viscosity (Fig 2.4) compared to BT06.

At the maximum temperature investigated (150 °C), S.Oil still shows the properties of a fairly good insulating liquid (tan (δ) < 10^{-2}) whereas MJO is quite weak (tan (δ) ≈ 8), and DBT and BT06 intermediate.

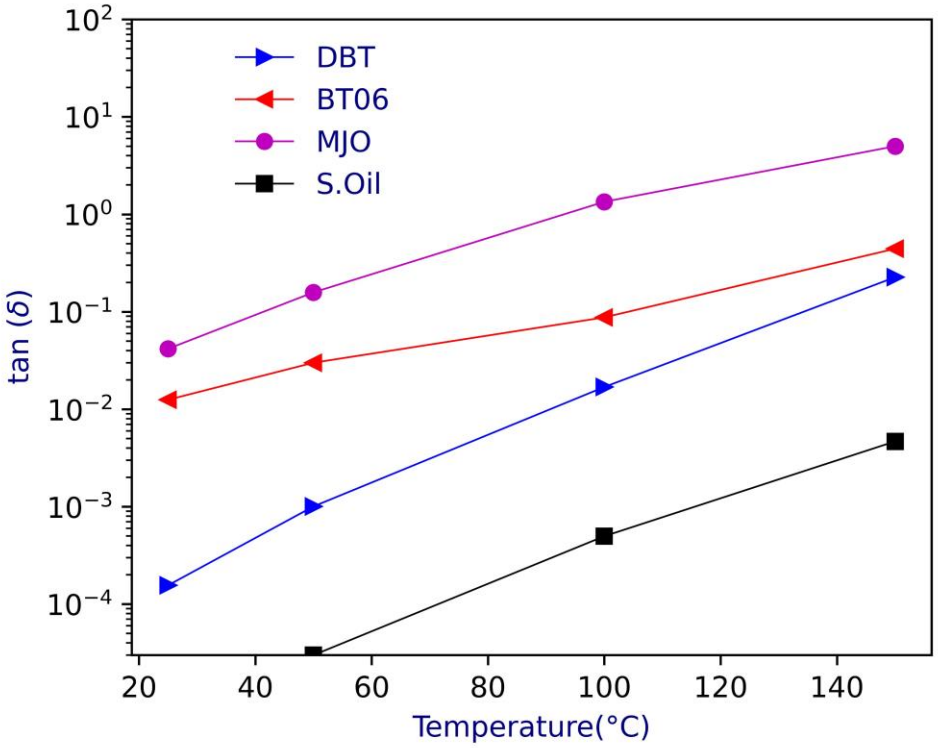

Fig 2.9. Comparison of loss factor at power frequency (50Hz) for different liquids

2.2. Conductivity measurement in dielectric liquid at high temperature and high voltage

In this part, conductivity measurements will be developed along with the two main specific conditions existing in a power module: high temperatures and high local electric field. The data obtained will allow calculating field distributions taking into account both the influence of temperature, and the non-linearity of conductivity with electric field.

2.2.1. Conduction mechanism in dielectric liquid

In pure state, non-polar liquids are known to be excellent insulators with very low conductivity less than 10^{-14} S/cm. At room temperature, the generation of electron / hole is negligible since such liquids are known to have ionization energy in the range of 6.8eV to 10eV [42]. Therefore, at low electric field and low temperature, conduction in liquid is mostly caused by impurities such as weakly bonded ions, free ions or additive particles. With increased applied electric field, dielectric liquids are known to exhibit non-linear conduction phenomenon as illustrated in Fig 2.10. It can be generally divided into three regions:

Ohmic region - Low field region where the current density is proportional to applied field. It is characterised by a constant conductivity which in most case is due to free ions present in the liquid. These charge carriers are mainly free ions resulting from dissociation - recombination equilibrium [43].

$$[A^+B^-] \underset{k_r}{\overset{k_d}{\rightleftharpoons}} [A^+] + [B^-] \qquad 2.2.1(a)$$

Where $[A^+B^-]$ is the concentration of weakly bonded ionic electrolyte, $[A^+]$, $[B^-]$ are the dissociated ions which contributes to current conduction, k_d and k_r are the dissociation and recombination rate constant. At very low field and without convective motion of the liquid, the dissociation and recombination rates are at equilibrium, resulting in a linear relationship between current density and applied electric field. The conductivity measured in this region is considered as the "true" conductivity of the liquid, as in the case of conductivity obtained from dielectric spectroscopy measurement at low voltage in the previous section. The conductivity (σ) can be generally expressed in terms of free charge concentration (n), electronic charge (e), and net charge mobility (μ_i) as in equation 2.2.1 (b).

$$\sigma = ne\mu_i \qquad 2.2.1(b)$$

The ionic dissociation energy is < 1eV in most non-polar dielectric liquids. Therefore, charge carrier generation from ionic dissociation is significantly enhanced at high temperatures. In addition, decrease in viscosity of liquid with temperature also increase the charge mobility, thereby increasing the conduction current density of the liquid as observed in the previous section. The mobility of the low field charge carriers is usually determined experimentally from the time-of-flight (*ToF*) method [44, 45]:

$$\mu_i = \frac{d^2}{V \times ToF} \qquad 2.2.1(c)$$

Where *V* is the applied voltage and *d* the gap distance between electrodes.

Saturation region – An increase in electric field leads to destruction of the dissociation-recombination equilibrium. The current density tends to saturate due to complete dissociation of all available easily dissociable electrolytes [46, 47]. This results in an apparent decrease of conductivity versus electric field.

Field enhanced region – Under intense electric field (>10^6 Vm^{-1}), several phenomena happen simultaneously contributing to an exponential increase of current density. In addition to ionic charge carriers originating from the liquid bulk, charge carrier injection takes place at the liquid-electrode interfaces. This contributes to further increase of current density through the liquid. The apparent mobility of the charges at high field is also significantly enhanced by the convective flow caused by electrohydrodynamic (EHD) motion (see more explanations in Chapter.4). The induced liquid motion strongly promotes ion transport, resulting in an apparent mobility much higher than the ion mobility occurring in a static liquid. This apparent charge mobility enhanced by EHD (μ_{EHD}) is theoretically calculated as in equation 2.2.1(d).

$$\mu_{EHD} = \sqrt{\frac{\epsilon_r \epsilon_o}{\rho}} \qquad 2.2.1(d)$$

Where ρ is the liquid density, ϵ_r is the relative permittivity and ϵ_o is the permittivity of free space. Since temperature effects on ρ and ϵ_r are weak and roughly proportional, the μ_{EHD} is generally almost independent of temperature.

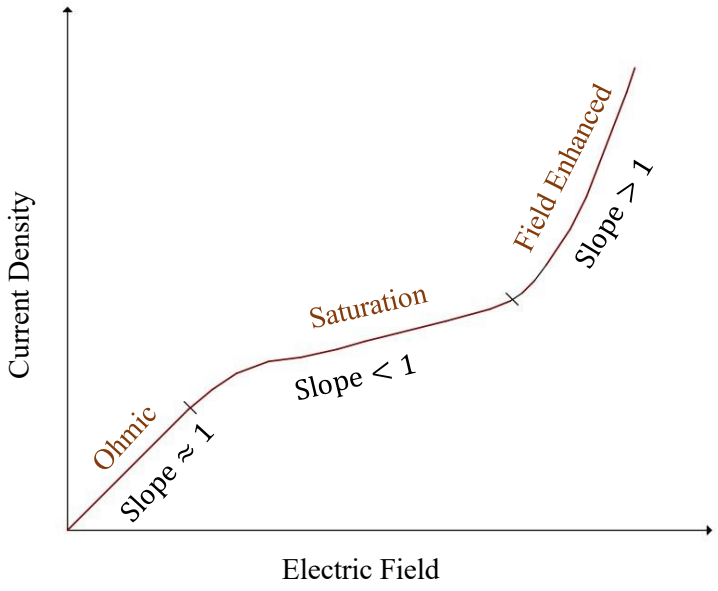

Fig 2.10. Idealized schematic representation of different conduction mechanism in dielectric liquid

In the following experiments, the evolution of conductivity will be investigated in DBT and S.Oil over a wide range of temperatures (25°C – 300°C) and electric field (10^{-3} kV/mm – 30kV/mm), thanks to the use of a special test cell previously developed at the G2Elab.

2.2.2. High temperature and high voltage conductivity measurement test cell

A schematic diagram of the test cell previously developed in the laboratory [17] to measure conductivity in liquids at high temperature (up to 350°C) and high voltage (up to 30kV) is shown in Fig 2.11. An air tight sealing is achieved by a high temperature "Helicoflex™" metallic gasket ring, which can be used at temperatures up to 500°C.

The test cell consists of a stainless-steel container with a volume of 300 ml which houses the parallel plate electrodes assembly as shown in Fig 2.*12*. The measurement electrode has a diameter of 12 mm and the gap distance to the high voltage electrode is 1 mm. A guard ring is provided to have uniform electric field between the measuring electrode and high voltage electrode. The electrodes and guard ring are held together by using three spacers and two MACOR™ ceramic holders. Insulating materials used to build the test cell (HV feedthrough, low voltage connections, holders, etc.) are made of ceramic.

A 500W heating mantle connected to a digital temperature regulator is used to control temperature. The temperature stabilization takes at least 1 hour for temperatures below 200°C. Fluctuations about ± 2°C @ 250°C are observed after stabilization.

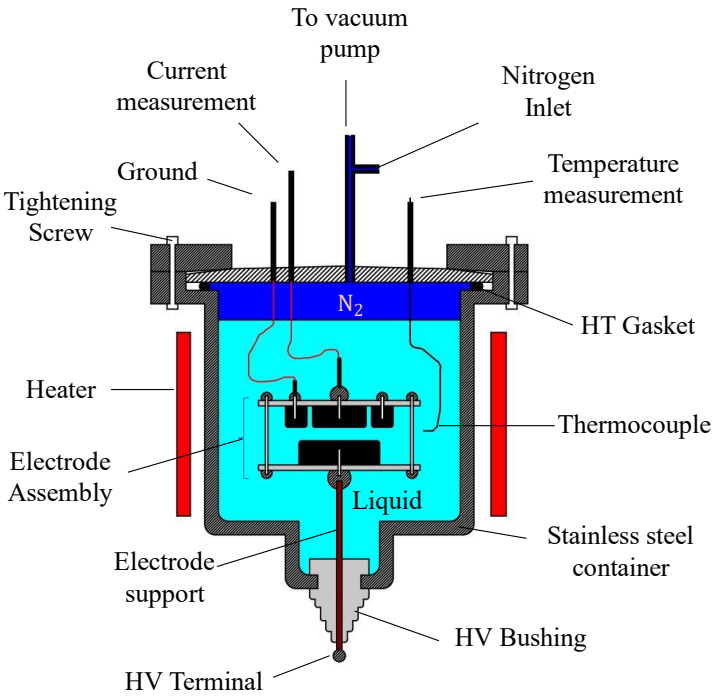

Fig 2.11. Schematic diagram of high temperature high voltage conductivity measurement test cell

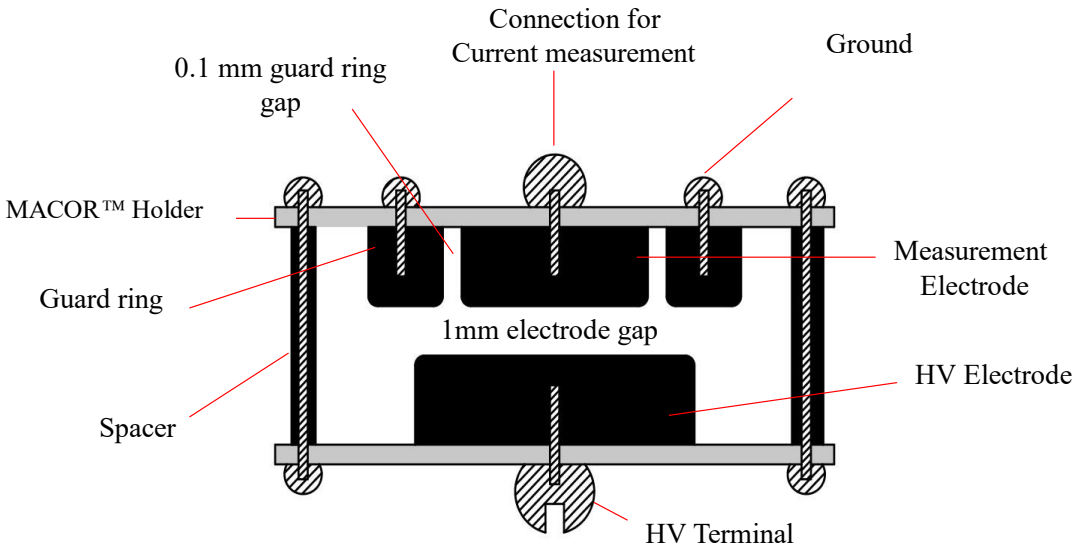

Fig 2.12. Schematic diagram electrode assembly for conductivity measurement

2.2.3. Experimental setup and measurement procedures

The test cell and electrode assembly are thoroughly cleaned with acetone and dried with high pressure air. It is then filled with fresh DBT or S.Oil, closed, and sealed via a high temperature Helicoflex® metallic gasket. The cell is then placed under vacuum and heated to 60°C for about 3 hours to remove trapped moisture and gases. Dry nitrogen is then introduced above the liquid surface, and its pressure is maintained at 0.1 MPa during measurements.

DC voltage (V_{DC}) was used for measurement up to 10kV. A Keithley™ 6517 electrometer was used to record the current and supply voltage up to 1kV. At higher voltage (up to 10kV) a Spellman™ HV supply was used, equipped with a high voltage RC filter at the output (10MΩ, 4nF) to reduce noise. Each voltage level was applied for about 15 minutes to obtain a stable conduction current measurement i_c. Typical recording under V_{DC} can be seen in Fig 2.14.

Rectangular voltage impulses with adjustable duration were used for higher voltages V_a up to 30kV in DBT. As compared to DC, the shorter impulse duration contributes to reducing the risk of breakdown at high field. Measurements were made up to 30kV/mm, i.e., half of the typical breakdown field measured in sphere/sphere gap. Transient current measurements were made with an oscilloscope, using a shunt resistor R equipped with free-wheeling diodes and spark gap to protect the oscilloscope in case of breakdown. For example, at 100 °C, the pulse duration was typically decreased from 230 ms @ 10kV, down to 10ms @ 30kV, Fig 2.15. Depending on the current i_c to be measured, the minimum measurement resistor R allowing accurate measurement with the oscilloscope was chosen (typically between R = 100Ω @30kV and 1MΩ @10kV). This contributed to maximize the measurement bandwidth (which depends on R and on stray capacitances) to properly record transient currents.

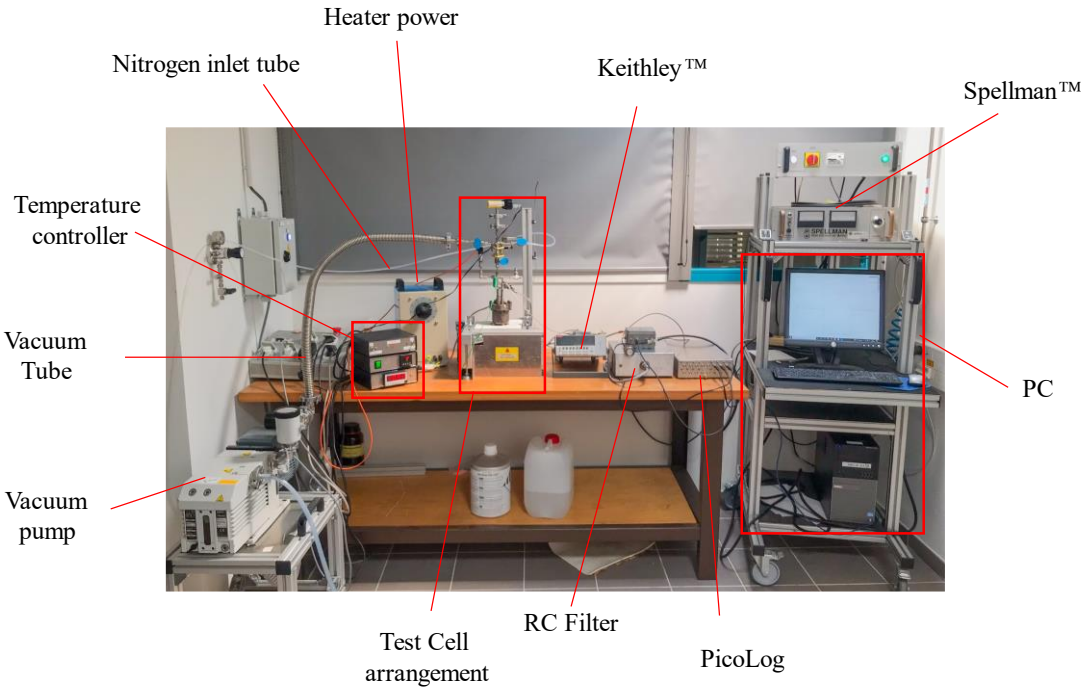

Fig 2.13. Conductivity measurement test setup under DC voltage suitable for temperature up to 300°C and maximum voltage of 30kV

The current density (J) and electrical conductivity (σ) are then calculated from the measured current (i_c) using the following equations:

$$J = \frac{4\, i_c}{\pi D^2}\ [A/cm^2] \qquad 2.2.3(a)$$

$$\sigma = \frac{J}{E}\ [S/cm] \qquad 2.2.3(b)$$

Where D is the diameter of the measurement electrode (12mm) and E is the uniform electric field between the measuring electrode and the high voltage electrode.

2.2.4. Conductivity measurements in DBT

2.2.4.1. Typical current measurements

The current recordings were made for logarithmic voltage steps V_{DC} from Keithley™ (1,2,5…1000) V and from Spellmann™ (1, 2,5,10) kV. These measurements are made for temperatures ranging from 22°C (room temperature), 50°C, 100°C…300°C. An initial current peak at t = ToF following voltage application occurred for each voltage level, with time ToF strongly decreasing with increasing voltage. At low field, this peak corresponds to the transient current caused by ionic charge carriers. The ionic charge carrier mobilities for low voltages in DBT were investigated in [17], therefore it was not carried out in this study. The stable current i_c (reached after 5 to 15 minutes) provides the conduction current, enabling the calculation of conductivity using the equation 2.2.3(b). A typical current recording for V_{DC} at 22°C can be seen in Fig 2.14.

The current recording under rectangular impulse voltage (10, 15, 20, 25, 30kV) were made for impulse duration of (230, 50, 35, 20,10) ms respectively. The impulse had a fast risetime (< 1 µs). A typical recording of current under V_{IMP} can be seen in Fig 2.15. Strong space charge injection from electrodes should be observed at such high electric field (10 x 10^6 to 30 x 10^6 V/m). Therefore, the initial current 'bump' observed at $t = ToF$ is primarily due to the transit of injected ions toward the opposite electrode. The current stabilises after about $t \sim 5ms$ enabling the measurement of i_c. Thanks to the high recording time resolution (µs) of the oscilloscope, the ToF could be recorded even for higher voltage. The calculated charge injection mobilities using ToF method from equation 2.2.1(c) is shown in Fig 2.15. The injection mobility (μ_i) varies significantly with temperature below 150°C and saturates at higher temperature. However, no apparent variation with voltage was observed, Fig 2.12.

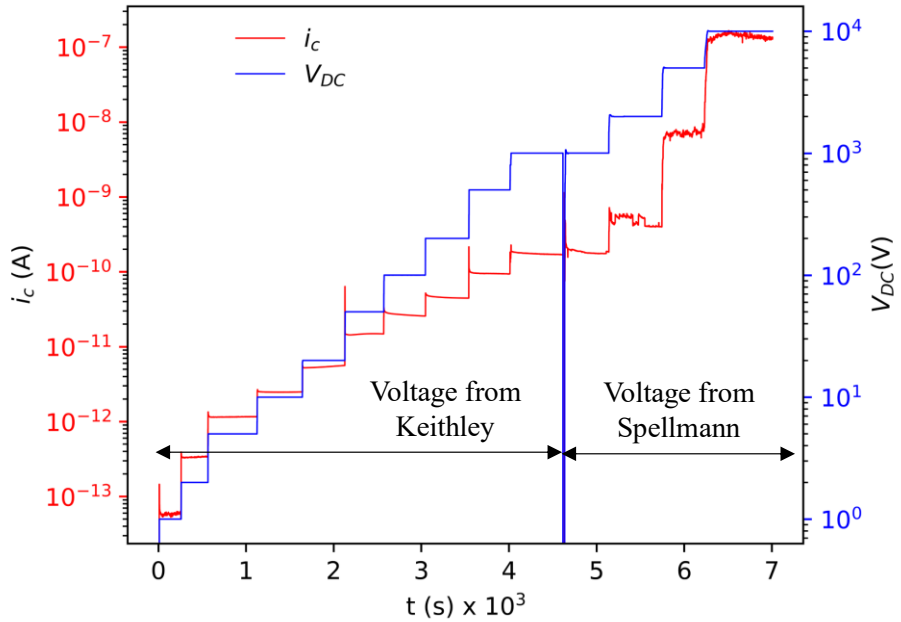

Fig 2.14. Typical current recording under dc voltage V_{DC} using KeithleyTM for voltage range 1V to 1kV and SpellmannTM voltage range of 1kV to 10kV at room temperature (22°C).

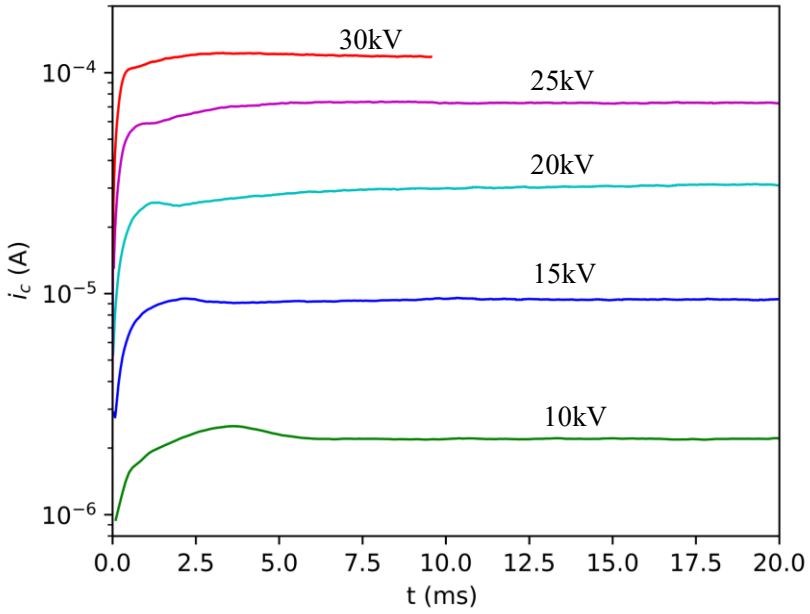

Fig 2.15. Typical transient current recording under rectangular impulse voltage from 10kV (R=1MΩ) to 30kV at 100°C (R=100Ω)

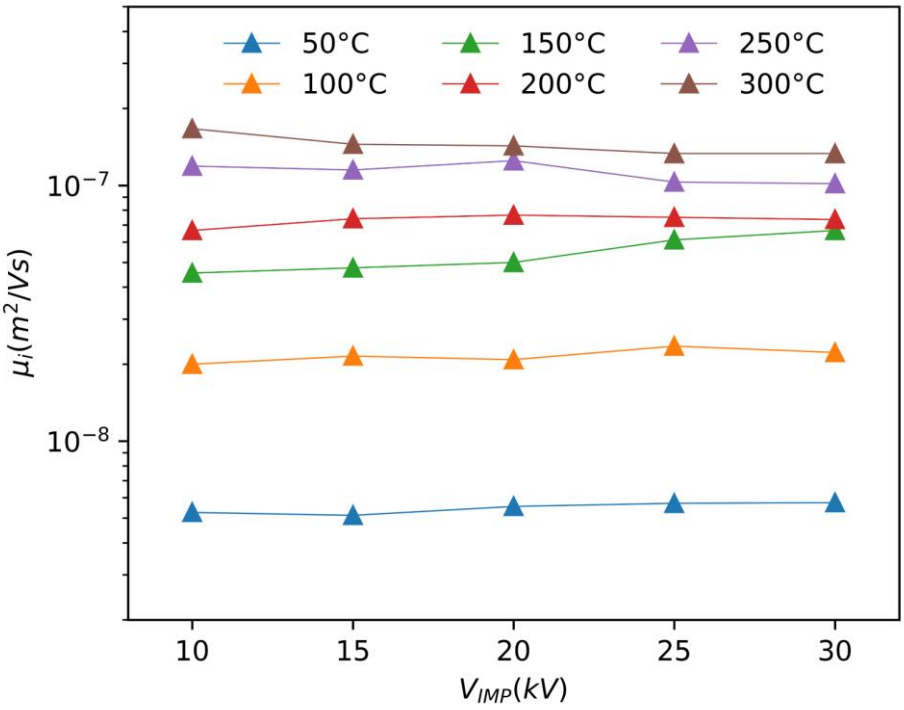

Fig 2.16. Charge mobility at high filed calculated from time of flight (ToF) in DBT under rectangular impulse voltage.

2.2.4.2. Evolution of conductivity with temperature and electric field in DBT

Measurements done with DC and impulses are in fairly good continuity as shown in Fig 2.17. At T = 22 °C, an Ohmic current (i.e., constant conductivity σ) is observed up to electric field of 0.5kV/cm, and slightly increases (saturation region) up to electric field of 1kV/cm, Fig

2.18 . The further increase in electric field results in an exponential increase of conductivity (field enhanced region).

The low field Ohmic conductivity increases a lot with temperature: from 2×10^{-14}(S/cm) at T = 22 °C, to 3×10^{-10}(S/cm) at T = 300°C. At low temperatures (≤ 100 °C), an exponential increase of σ is clearly seen above some threshold field: the higher T, the higher threshold field. Various mechanisms (field enhanced dissociation or injection at electrodes) may explain this behaviour, but it remains difficult to clearly identify the process involved. At high temperatures (≥ 150 °C), the increase of conductivity is mostly due to temperature, and only a marginal increase is observed when the maximum field is increased to 30 kV/mm. To summarize these results, the influence of field dominates at high field and low temperature, whereas the influence of temperature becomes dominant above ≈ 150 °C.

The activation energy (E_a) for temperature range 22°C to 300°C shows two distinct regions (Fig 2.19). At electric field E<100kV/cm and lower temperature T< 150°C, the calculated E_a (0.62 eV) is similar to the one obtained in section 2.14. The E_a decreases by factor of 2 for higher temperature range 150°C to 300°C indicating an enhanced ionic dissociation with increase in temperature. At high electric field E~300kV/cm, the activation energy decreases to 0.34 eV compared to 0.62 eV at lower field.

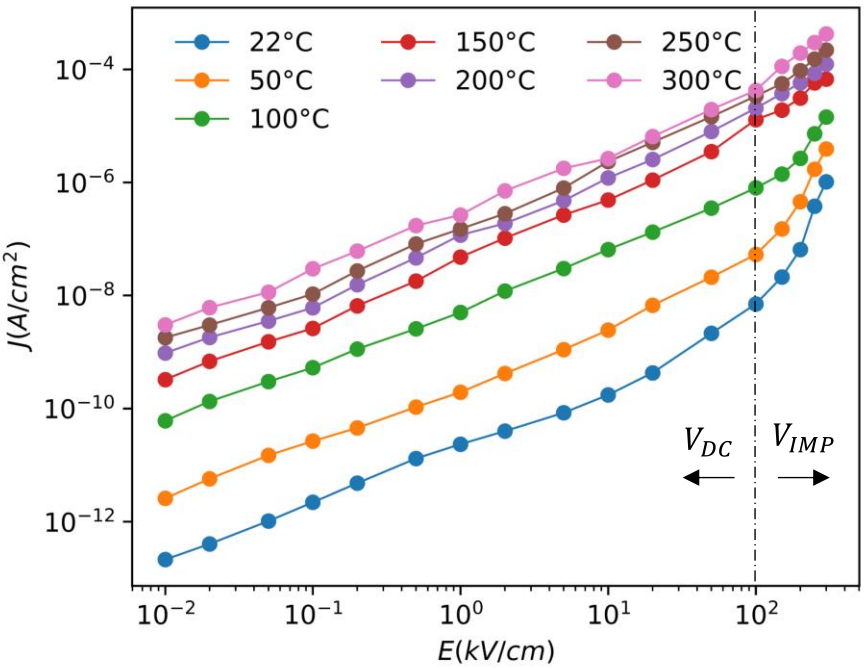

Fig 2.17. Current density (J) variation with electric field (E) and temperature (T) of DBT in uniform field with electrode separation of 1mm.

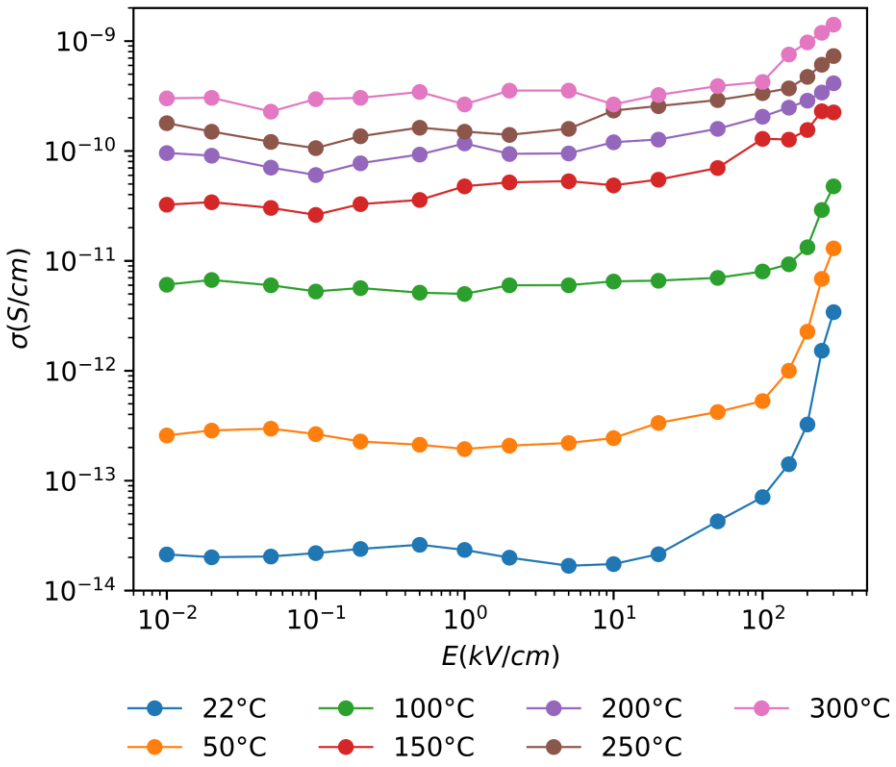

Fig 2.18. Electrical conductivity (σ) of DBT as function of uniform temperature and uniform electric field.

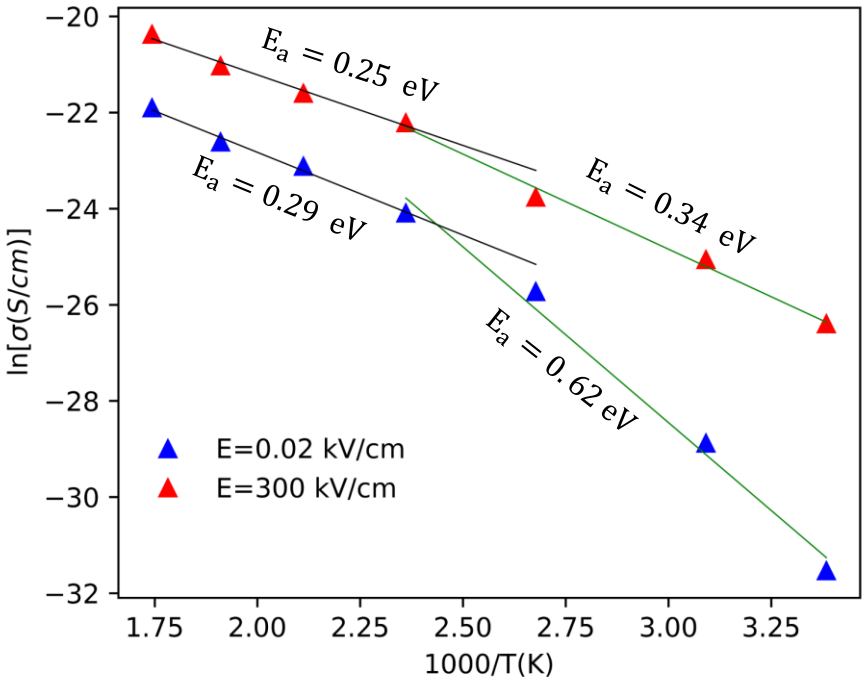

Fig 2.19. Activation energies calculated using Arrhenius plot for electric fields 0.02kV/cm and 300kV/mm with temperature varying from 22°C to 300°C

The non-linear behaviour of conductivity as a function of temperature and electric field $\sigma(E,T)$ can be expressed in terms of an empirical formula deduced from the measured

conductivity as in equation 2.2.4.(a). This empirical equation will be useful for electric field simulation presented in the latest part of this chapter.

$$\sigma(E,T)_{dbt} = \sigma_0 (\frac{T}{T_{ref}})^{\vartheta_1} exp\left(\beta_d E (\frac{T}{T_{ref}})^{\vartheta_2}\right) \qquad 2.2.4.(a)$$

Where ϑ_1 and ϑ_2 are the temperature exponents 3.7645 and -0.457 respectively, β_d = 0.6501 $[\mathrm{kV/mm}]^{-1}$ and conductivity σ_0 of $2 * 10^{-19}[\mathrm{S/cm}]$ at reference temperature T_{ref} (1°C).

2.2.4.3. Estimation of charge mobility from Space Charge Limited Current under uniform field

When a "pure" space-charge limited current (SCLC) exists, the charge mobility μ_i can be calculated using Motts's Relation [48] as in 2.2.4.(b). This calculation is based on the assumption that the liquid has a very low intrinsic conductivity, and the electric field is ideally uniform.

$$\mu_i = m^2 \frac{8d}{9\epsilon} \qquad 2.2.4.(a)$$

Where m is the slope calculated from $J^{0.5}$ plotted against E, d is the electrode gap and ϵ is the absolute permittivity. The measurements (Fig 2.*17*) show that SCLC mobility can be calculated only for $T \leq 100$ °C since the Ohmic conduction current is dominant at $T \geq 100$ °C (the non-linear current at high field is not any more clearly observed at high temperatures). The corresponding SCLC plot is shown in Fig 2.20. The linear variation of $i_c^{0.5}$ versus *E* is observed at high field, typically from 20 to 30 kV/mm. At lower field, this variation is masked by the large Ohmic current. A comparison between injected charge mobility (from SCLC and ToF), low field ion mobility from [17] and theoretical EHD mobility is shown in Table 2.2. Mobilities measured at high field either from SCLC current or from *TOF* are in correct agreement, and about 10 times larger than those measured at low field, where the contribution of EHD is totally absent. The maximum theoretical mobility μ_{EHD} is about 100 times larger than mobility calculated from space-charge plots and *ToF* methods, showing that EHD has a limited impact on charge transport.

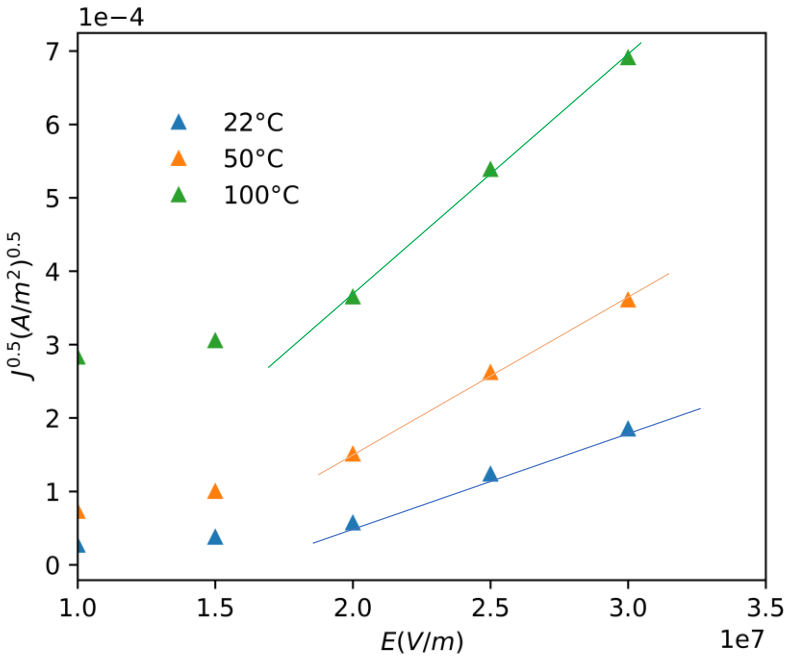

Fig 2.20. Calculation of mobility of injected charges from the plot of $J^{0.5}$ vs. E at high field

Table 2.2. SCLC mobility (μ_i) and EHD mobility (μ_{EHD}) and low filed ion mobility (μ_0) comparison in DBT

Charge mobility ($m^2/V.s$)	22°C	50°C	100°C
μ_i	2×10^{-9}	5×10^{-9}	2×10^{-9}
	1.7×10^{-9}	4.0×10^{-9}	1.8×10^{-8}
μ_0	2×10^{-10}	7×10^{-10}	1.5×10^{-9}
μ_{EHD}	1.5×10^{-7}	1.5×10^{-7}	1.5×10^{-7}

2.2.5. Conductivity measurements in Silicone Oil

2.2.5.1. Current measurement under uniform field

Conduction current in S.Oil was measured only under DC voltage up to 10kV with the same voltage levels as in figure 2.13. The measurements were recorded for temperature ranging from 22°C (room temperature) to 200°C (maximum operating temperature of S.Oil). Since currents are very low in S.Oil, and thus quite noisy, the quoted current values I_m are the averaged current over 5s, with 10^3 samples per second.

The current measurement was not possible at low voltage and low temperature, since it was below the measurement limit of the Keithley™ electrometer (about 0.1 pA). At room temperature, the measured current was lower than 10^{-13} A at voltages below 500V, Fig 2.21. At 100°C, current measurements were possible at voltages above 50V.

The current measurement range could be improved by increasing the surface of measurement electrode, but it was limited by the size of the high temperature test cell. Some instability in the measured current was observed at voltages above 5kV, similar to the measurements in DBT. This could have probably resulted from strong charge injection at the

electrodes combined with the convective motion of the liquid by EHD. The maximum voltage was limited to 10 kV to avoid breakdown (the quoted values for breakdown field is 18 kV/mm, significantly lower compared to DBT).

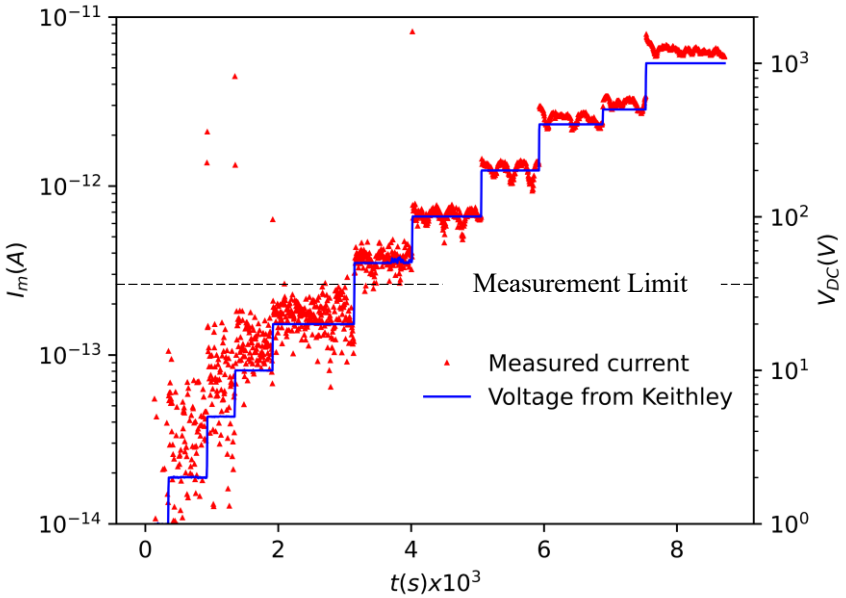

Fig 2.21. Current measurement in S.Oil at 100°C, showing measurement limitations at low voltages.

2.2.5.2. Current density and conductivity in S.Oil

The current density J and conductivity σ are calculated from equations 2.2.3.(a) and 2.2.3.(b) respectively. A clear ohmic regime could not be observed in S.Oil. owing to measurement limitations. Calculation of slope from J vs. E (Fig 2.22) show that for E = 0.01 kV/cm to 20 kV/cm, the slope is less than 1. This is typical in very pure dielectric liquids with very low ionic impurities. The dissociation and association equilibrium are strongly affected by application of electric field, whereby, the limited weakly bonded ionic impurities are fully dissociated. It is the case of current saturation with increase in electric field, resulting in an apparent decrease of conductivity as seen in Fig 2.*23*. At electric fields E > 20 kV/cm, an exponential increase of current density is recorded, typical of field enhanced conduction resulting from several factors such as electrode injection and EHD.

The conductivity of S.Oil is highly dependent on temperature as in the case of other dielectric liquids. For S.Oil, the increase of conductivity (5 orders of magnitude when temperature is increased from 22°C to 200°C) cannot be solely attributed to the thermal dissociation of ionic impurities.

As in DBT, the increase of conductivity is mostly due to the decrease of viscosity (from 50 mm^2/s at 25°C down to 8 mm^2/s at 180°C [49]). The decrease of viscosity results in an increase of charge mobility, and hence of conductivity. For better understanding of influence of temperature on charge mobility, an experiment on charge mobility based on ToF method will be discussed in the following section.

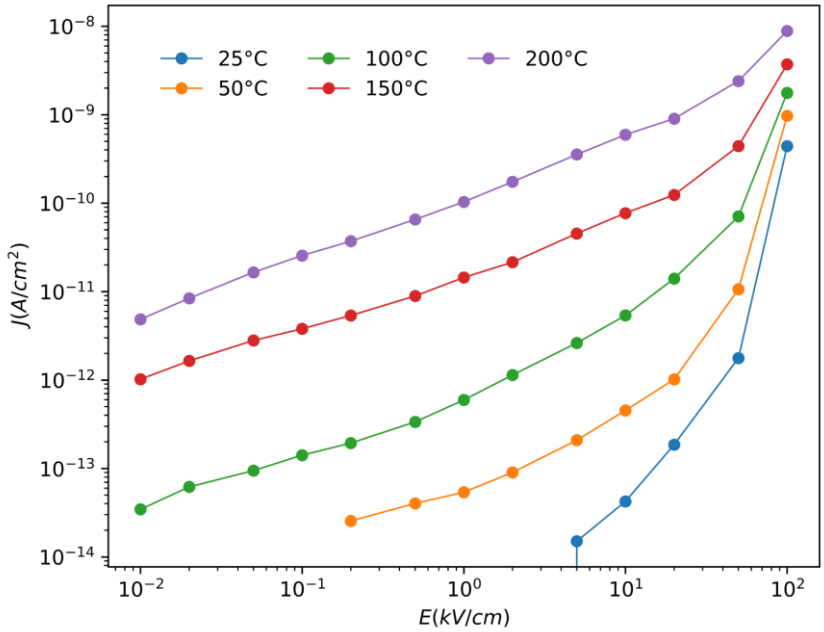

Fig 2.22. Current density measurement in S.Oil under uniform electric field. Electrode separation = 1mm.

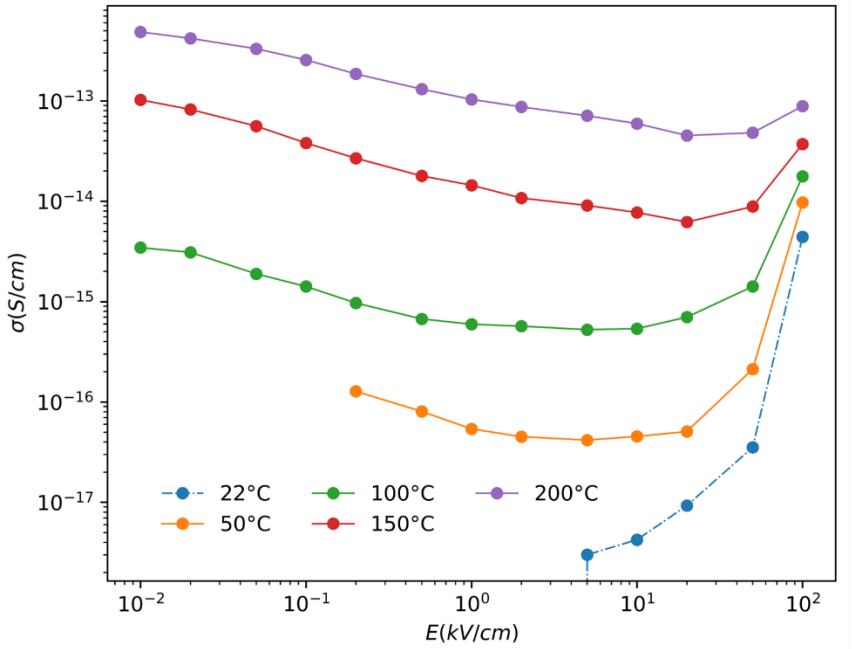

Fig 2.23. Variation of conductivity versus temperature and electric field in S.Oil

2.2.5.3. Low voltage charge mobility estimation in S.Oil

The coaxial concentric test cell (Fig 2.2) was used for low voltage charge mobility measurements, rather than the parallel plate electrode system (Fig 2.12). This increased the electrode surface, and thus the current at low voltage which could be measured with the Keithley™ electrometer. The larger gap distance of 3.75 mm allows measurement of ToF at voltages up to 1kV (ToF α d^2/V) in S.Oil, which was not possible for gap distance of 1mm (Fig 2.12).

Charge mobility estimation from time-of-flight method (ToF) involves measurement of time at which the current attains its peak value after applying a voltage step. A unipolar

rectangular voltage was used for such measurements. The variation of ToF on several factors was first investigated at room temperature (22°C):

- number of voltage cycles
- pulse period (T/2) of applied voltage
- variation with increasing voltage

A rectangular pulse voltage of $\pm 400V$ with pulse period of 300s was applied for 3600s (total cycle = 6) to test the variation of ToF with number of voltage cycles. In most cases, the first positive current peak could not be clearly observed (Fig 2.*24*). The ToF for the first two cycles varies slightly, therefore calculating the charge mobility from these first two cycles can lead to probable errors. Afterwards, from 3rd to 6th cycles no more variations were observed in current peaks as well as ToF, and these values were used to estimate charge mobility. For negative and positive peaks, the ToF at 400V were 40s and 46s respectively. This results in a slightly higher charge mobility during negative than during positive voltage, i.e., $\mu_- = 9.1 \times 10^{-10}$ m^2/Vs and $\mu_+ = 7.6 \times 10^{-10}$ m^2/Vs.

The variation of ToF with pulse period was evaluated from 200s to 600s at 200V. A slight variation of peak currents was recorded, but no variation of ToF (Fig 2.25). This indicates that the pulse period can be reduced to shorten the total time needed for each measurement, as long as ToF < T/2, where T is the pulse period. The ToF should not vary for voltage levels at which there is no field enhanced conduction. Indeed, the mobility measured from 200V to 1000V at room temperature shows that there is no significant variation of charge mobility within this voltage range. The difference between mobilities during positive voltage (μ_+) and negative voltage (μ_-) was negligible, therefore only the variation of $\mu_+$with voltage is shown in Table 2.*3*.

Finally, a 200V rectangular voltage signal of duration T/2 = 200s with total duration of 1200s (3 cycles) was chosen to measure charge mobility at different temperatures (22°C to 150°C). The main goal was to evaluate the variation of charge mobility (μ) with temperature and check its correlation with kinematic viscosity (ϑ). Electrical conductivity σ should be related to charge mobility and kinematic viscosity as:

$$\sigma \; \alpha \; \mu \qquad 2.2.5.\,(a)$$

$$\sigma \; \alpha \; \frac{1}{\vartheta} \qquad 2.2.5.\,(a)$$

The viscosity of S.Oil is highly susceptible to variation of temperature, when temperature increases from 25°C to 150°C, the viscosity decreases from 50 m^2/s to 9 m^2/s [13], in a similar way as in DBT. A fair correlation is observed between measured charge mobility and viscosity versus temperature, as shown in Fig 2.*26*.

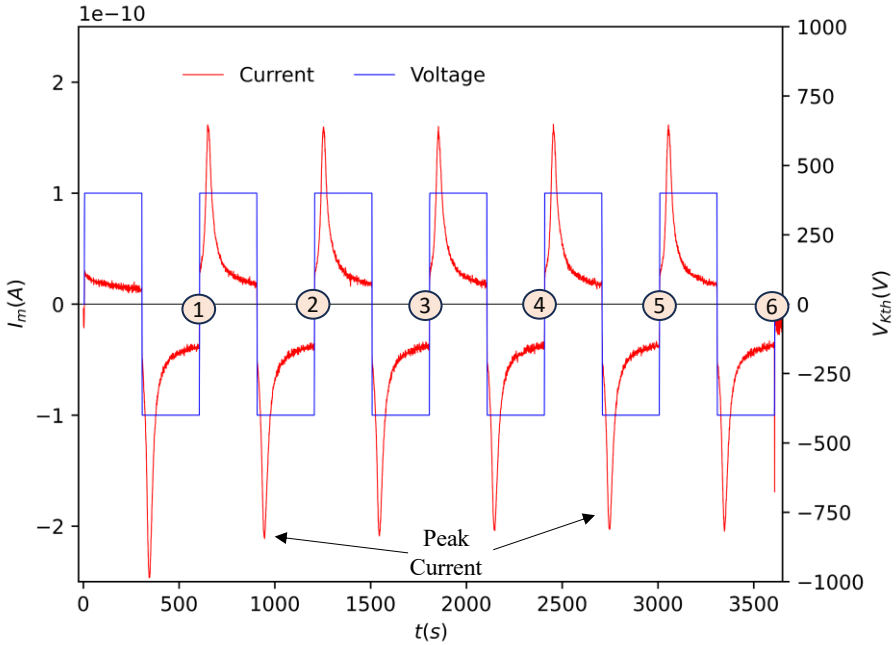

Fig 2.24. Current recording in S.Oil showing peak currents for both positive and negative plateau of rectangular voltage signal (400V) at 22°C for 6 cycles

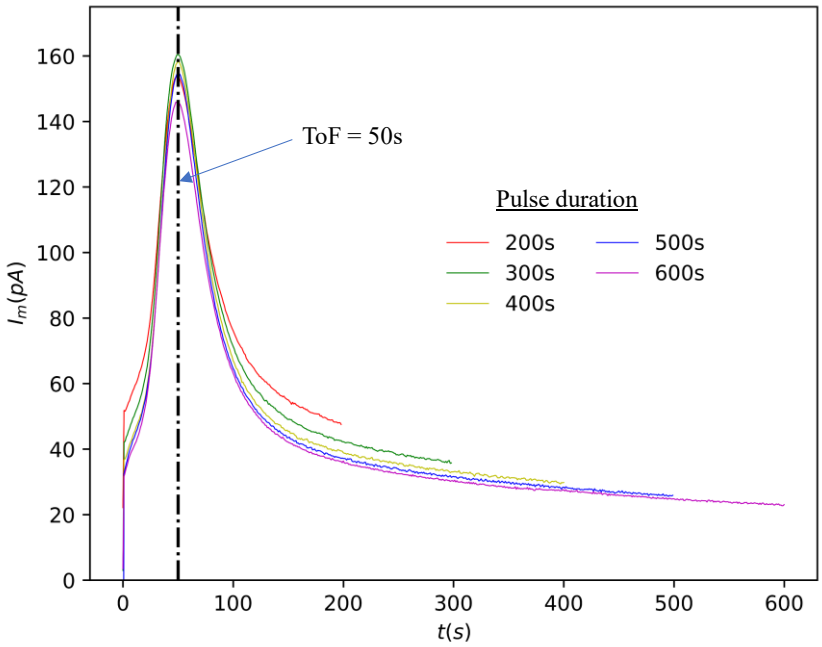

Fig 2.25. Current recording in S.Oil showing peak currents during positive plateau of rectangular voltage signal (200V) at 22°C at 3rd cycle with different pulse period

Table 2.3. Variation of charge mobility with voltage at 22°C in S.Oil

Voltage (V)	200	400	600	800	1000
$\mu_+(m^2/V.s)$ x10^{-10}	5	4.88	4.9	4.88	4.86

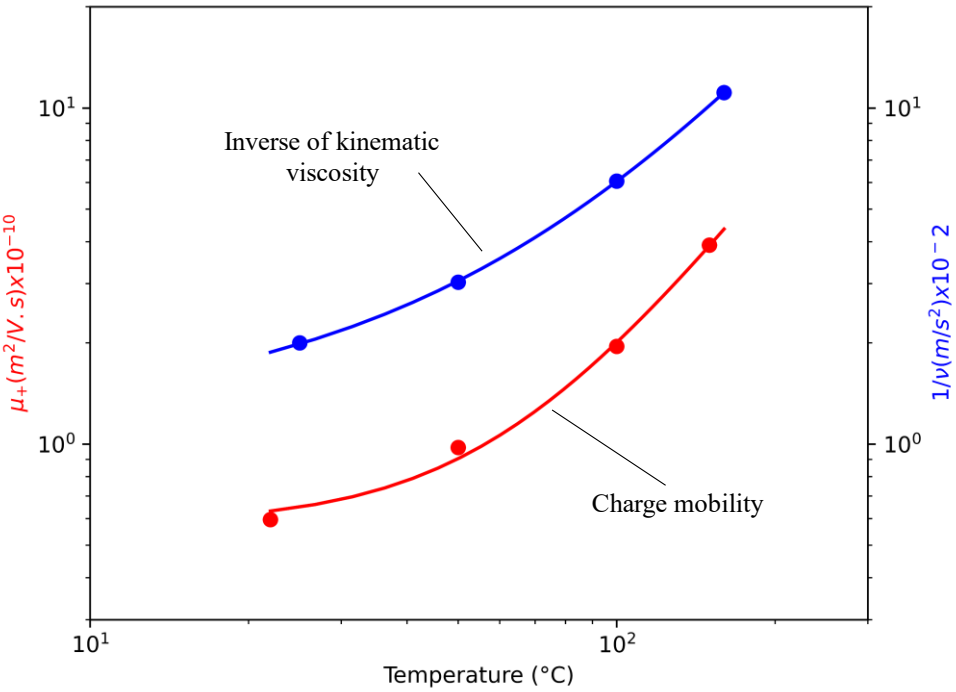

Fig 2.26. Variation of charge mobility and kinematic viscosity [49] of S.Oil with temperature

2.2.6. Current measurements with point-plane electrode geometry in DBT

2.2.6.1. General properties of point-plane configuration

Point plane electrode systems are widely used for studying pre-breakdown characteristics (partial discharge, streamers…) in insulating materials. A reasonably low applied voltage V can lead to large electric field at the tip, E_{tip}. For example, V= 1kV, the E_{tip} is approximately 2* 10^6 V/cm for a tip radius of 1µm [50]. Such geometry is more representative of practical applications where sharp metal protrusion exists, such as at the triple point within power modules. Electrostatic properties and space-charge limited current behaviours under point-plane electrode have been studied by Coelho and Debeau [50]. They used hyperboloid geometry approximation to deduce the electrostatic field along the tip-plane axis (0X), Fig 2.*27*. Assuming no space charge distortion of electric field, the maximum field at the tip is,

$$E_{tip} = \frac{V}{\mathrm{r}\ln\{2\,(\frac{a}{r})^{1/2}\}} \qquad 2.2.6.(a)$$

Where 'a' is the distance between plane and the centre of electrode tip, r is the tip radius. The electric field (E_p) at the plane along the centre line is also approximated as,

$$E_p = \frac{V}{\mathrm{a}\ln\{2\,(\frac{a}{r})^{1/2}\}} \qquad 2.2.6.(b)$$

The injection of charge from sharp electrode often leads to formation of a space charge cloud around the tip, thereby reducing the actual field. The space-charge-limited current (I_s) is approximated as:

$$I_s = \frac{\pi}{0.78} \epsilon \mu \frac{{V_{DC}}^2}{\mathrm{a}} \qquad 2.2.6.(c)$$

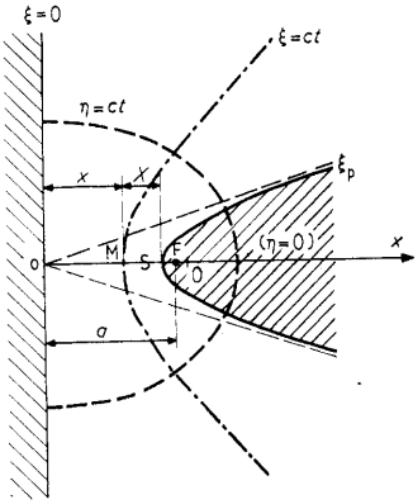

Fig 2.27. Representation of a point-plane configuration [50]

2.2.6.2. Point-plane current measurement in DBT

The measurement set up used for measurements at high voltage and high temperature (Fig.2.12) was adapted for current measurements in point-plane configuration. To reduce the risk of breakdown at high voltage, the needle was placed at 5 mm from the plane electrode of diameter 30 mm, Fig 2.28. This electrode assembly was placed inside the test cell (Fig 2.11) filled with DBT. The measurement procedure was the same as described in previous section (2.2.3). ± DC voltage from Keithley™ (5 V to 1 kV) and from Spellmann™ (1 kV to 12 kV) were used to record the current I_m, Fig 2.29. The measured current is numerically averaged for 15 s with one sample per second. It was more stable compared to the current recorded with plane-plane electrode system.

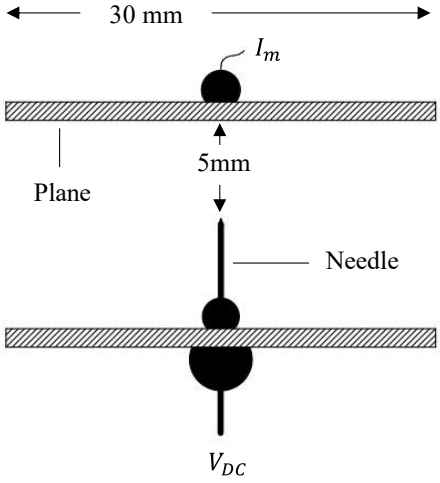

Fig 2.28. Electrode assembly for current measurement under point-plane configuration in DBT

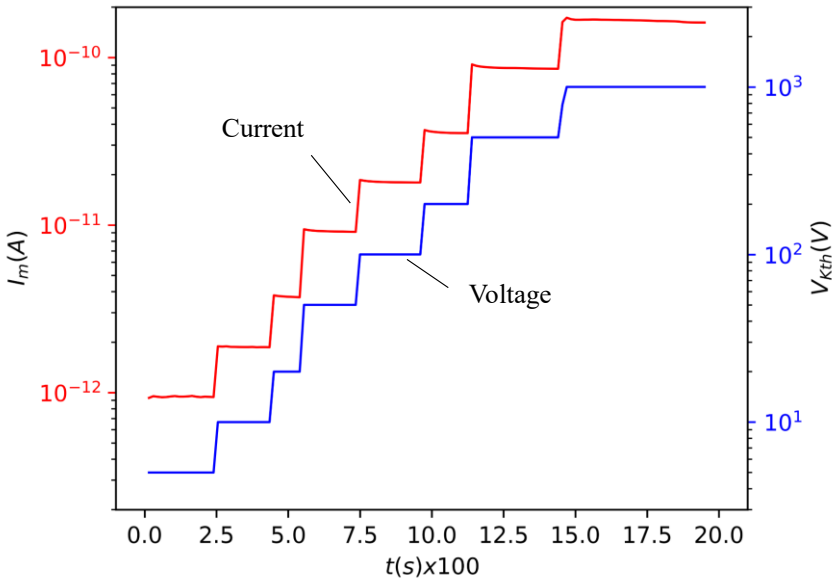

Fig 2.29. Typical current recording with point-plane electrode system in DBT under DC voltage for tip radius r = 3µm.

2.2.6.3. Influence of voltage and temperature with point-plane electrode system in DBT

Current measurements were carried out for temperature range from 22°C to 300°C with maximum DC voltage of 12 kV, Fig 2.30. A slightly higher current during negative voltage compared to positive voltage has been observed for all temperatures. Two main current components are clearly observed at temperatures below 100°C, i.e., conduction at low voltage, and space-charge limited current (SCLC) above some threshold voltage. At temperatures above 100°C, the SCLC is totally masked by the increase of conduction current. Therefore, measurements above 100°C cannot be used for estimation of injection charge mobility.

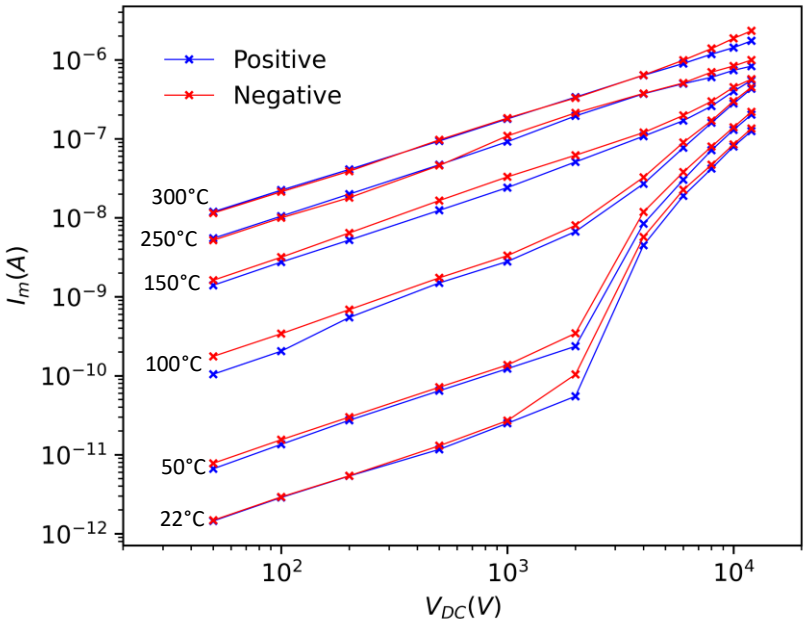

Fig 2.30. Average stable current measurement under point-plane electrode configuration (r = 3µm) in DBT as function of temperature and voltage

2.2.6.4. Charge mobility estimation from SCLC plots at lower temperatures

A simple first-order analysis can be done considering that the total measured current is the sum of a background conduction current originating from the entire point electrode (including cylindrical body, conical end, support, …), and injection current occurring from the high field tip extremity. The conduction and injection components of the measured current can be numerically separated thanks to a clear distinction between them. An obvious linear variation is observed from 50V to 2kV (conduction current), which can be extrapolated up to 12kV, Fig 2.31. The difference between the extrapolated conduction component and the total measured current provides an estimate of the injection current (I_s). The injection current component is useful to estimate the SCLC charge mobility by taking the square root of equation 2.2.6.(c) yields:

$$\sqrt{I_s} = m\, V_{DC} \qquad 2.2.6.(d)$$

Where 'm' is the slope calculated from the plot of $\sqrt{I_s}$ vs. V_{DC}. For tip radius of few µm, the gap between tip of the needle and plane electrode (d) is equivalent to 'a'. Therefore, $a \approx d = 5$ mm. Hence, the charge mobility can be calculated from the slope 'm' from the following equation,

$$\mu_{SCLC}(T) = \frac{0.78\, d}{\pi} \times \frac{[m(T)]^2}{\epsilon(T)} \qquad 2.2.6.(e)$$

Where $\epsilon(T)$ is the permittivity of DBT at temperature T obtained from the experiments in section (2.1.5). The extrapolation of the plot $\sqrt{I_s}$ vs. V_{DC} at $\sqrt{I_s} \approx O$ gives an estimation of the "threshold" injection voltage V_o. The threshold electric field (E_o) at the tip at which the SCLC initiates can be then estimated using equation 2.2.6.(a). It is commonly accepted that when the DC voltage is raised above V_o the maximum field at the tip remains close to E_o due to space-charge limitation. On the other hand, when impulse voltage with fast risetime is used, the tip field instantaneously rises to the maximum electrostatic value calculated without space-charge, and decreases afterwards down to E_o when space charges propagate far enough from the tip (i.e., when the space-charge limited current establishes).

The mobility estimation in DBT for three different temperatures at a fixed tip radius is calculated from the slope of $\sqrt{I_s}$ vs. V_{DC} as shown in Fig 2.*32*. No significant variation in mobilities during negative and positive voltage are observed (Table 2.4). The mobility is close to the theoretical EHD mobility ($1.5\ 10^{-7}$ m^2/Vs), indicating the dominant influence of EHD on charge transport. The initial injection voltage V_o is around 2kV. At this voltage, the maximum tip field E_o is around 150 kV/mm, strong enough to inject charges from the point electrode into the liquid.

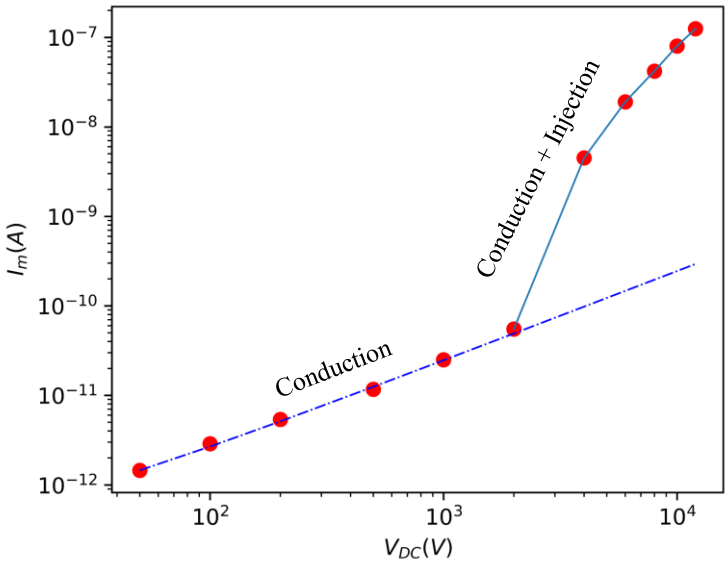

Fig 2.31. Measured current showing conduction and injection components in DBT

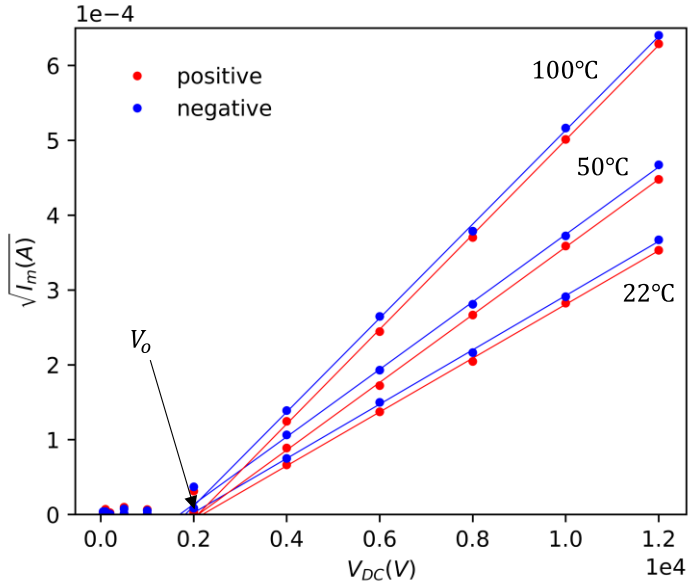

Fig 2.32. Plot of space charge limited injection current $\sqrt{I_m}$ vs. V_{DC} for tip radius of 3μm at different temperatures

Table 2.4. Space charge limited current (SCLC) mobility at different temperatures in DBT for a tip radius of 3μm placed at a distance of 5mm from the plane electrode

μ_{SCLC} (m^2/Vs)	22°C	50°C	100°C
μ (+) x 10^{-8}	6.75	10.8	20.3
μ (-) x 10^{-8}	6.88	10.7	20.1

2.2.6.5. Influence of tip-radius

The electric field should decrease with increase in the tip radius. Therefore, the initial injection voltage must be higher for needles with larger tip radius. Three needles with tip radii of 3μm, 10μm and 20μm of same materials were used to investigate variations of injection threshold voltage V_o , threshold field E_o , and charge mobility in DBT. The distance between

the tip and the plane electrode was maintained at 5mm. For constant temperature of 50°C during measurements, a slight decrease of μ_{SCLC} can be seen in Table 2.*4* with increase in tip radius. This could be linked to stronger EHD convective flow at higher electric field for smaller tip radius [51]. Extrapolating the linear fit of $\sqrt{I_s}$ vs. V_{DC} at $\sqrt{I_s} \approx 0$ gives larger value of V_o when r is increased. However, this does not correspond to a constant threshold field E_o when r is changed: E_o decreases when r is raised.

To obtain more insight and quantitative analysis of these phenomena, it would be necessary to carry out modelling of EHD processes taking into account the coupling between fluid motion, injection law at the tip, charge and field repartition. Such very complicated analysis was out of the scope of this PhD. However, we may expect that quite similar phenomena would occur in the very divergent field region existing in the liquid at the triple junction over metallized substrates, i.e., field limitation due to space charges at long times (under DC), and maximum field occurring with fast impulses before space-charge limitation occurs. In such complicated geometry, the EHD flow (and hence charge and field distribution) should also be strongly influenced by the presence of the liquid/substrate interface.

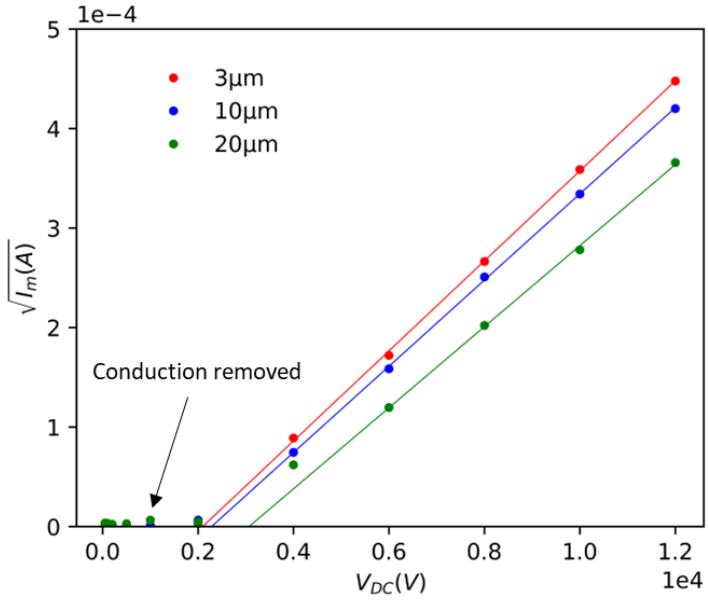

Fig 2.33. Plot of space charge limited current $\sqrt{I_m}$ vs. V_{DC} for different tip radius at 50°C

Table.2.5. Space charge current limited (SCLC) mobility at different tip radius in DBT at 50°C

Tip radius (x 10^{-6} m)	V_o (kV)	E_o (kV/mm)	μ_{SCLC} (x 10^{-8} m^2/Vs)
3	2.09	158	10.9
10	2.25	59	9.97
20	3.07	44	8.81

2.3. Transient electric field simulation with liquid embedded ceramic substrates

As previously discussed, a critical region in embedded ceramic substrates used in power electronics modules is the "triple point", located at the junction between the encapsulant, electrode and the substrate as illustrated in Fig 1.7. High blocking voltages in WBG power modules increase the electric field at the triple point, which may accelerate the degradation of insulators if partial discharges do occur. In this section, this issue will be addressed by simulating the electric field near the triple point region using Jarytherm®DBT. This simulation will consider the non-linear influences of temperature and electric field on the conductivity and permittivity of materials. The values measured in DBT under uniform electric field will be used for such simulation. A complete modelling should also include injection laws and EHD liquid motion, but such very complex objective was out of the scope of this work. The calculation will be based on a simpler finite element method (FEM) model, considering the time-resolved electrical simulation based on local Ohm's law and electrostatic field.

2.3.1. Typical geometry along the edges of metallization

A 2-D geometry based on an industrial grade power module [52], is implemented in the finite element software Comsol®Multiphysics version 5.6. The dielectric properties of materials which significantly influence the field at the triple point are considered (Alumina substrate, DBT encapsulant), as well as the shape of electrodes. Materials are considered to be linear, isotropic and free of space charge.

Depending on the etching process, thickness and material of metallization, the actual geometry along the edges of metallization varies extensively. In this study, the typical shape near the triple point regions of a direct bonded copper (DBC) substrate is as presented in Fig 2.*34*. These dimensions are used to represent the geometry along the edges of metallization of a DBC substrate, separated by electrode gap of 1 mm (see Fig 2.*35*). This DBC sample is embedded in an encapsulating material (DBT/ silicone gel) of dimensions 7.5 x 4.2 mm^2.

The upper electrodes, i.e., grounded g1 (1.4 x 0.292 mm^2) and high voltage (3.6 x 0.292 mm^2) are separated by a lateral gap distance of 1 mm Fig 2.35, typical gaps in trenches of power module. The g1 is used as ground electrode during surface breakdown experiments and kept at floating voltage during partial discharge measurements. The metallization on the other side of substrate g2 (6 x 0.292 mm^2) also serves as a ground. In practical applications, g2 is at floating voltage and grounded during partial discharge measurements. The various configurations of g1 and g2 will be in subsequent sections.

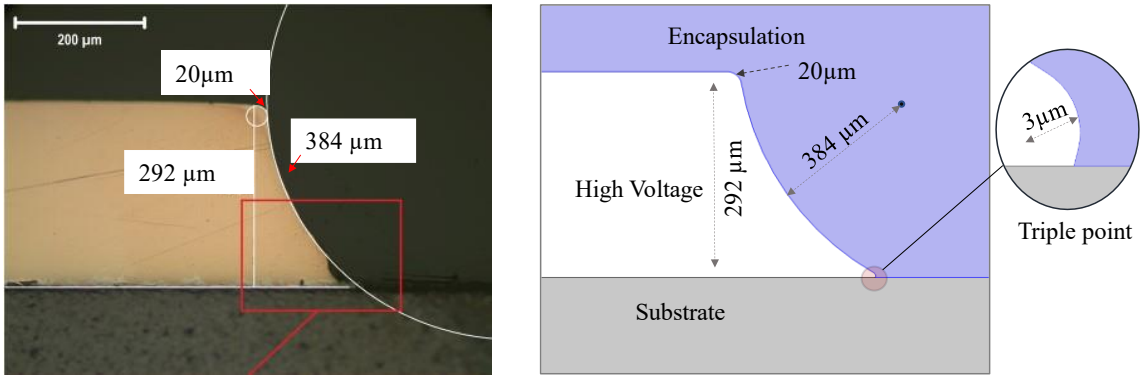

(a) (b)

Fig 2.34. Typical geometry along the edges of metallization and triple point of power module, (a) industrial DBC substrate *[52]* (b) Triple point geometry reproduced in Comsol®Multiphysics 5.6

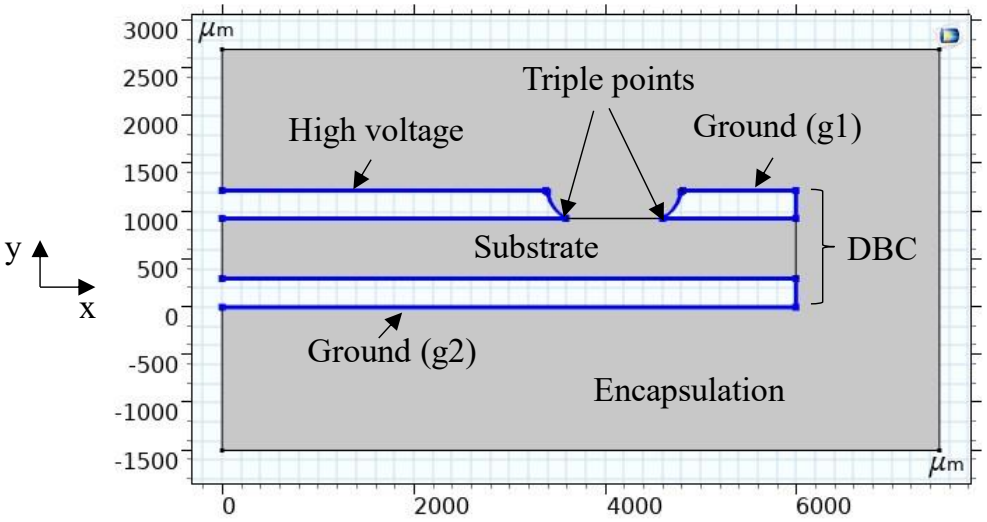

Fig 2.35. 2D geometry of a direct bonded copper substrate (DBC) with gap distance of trench 1 mm embedded in encapsulation material (DBT/silicone gel)

2.3.2. Mesh quality and convergence

The accuracy of the FEM simulation is highly dependent on the mesh resolution. The higher the mesh density, the more accurate the simulation results. However, a high-resolution meshing for the whole geometry needs a lot of memory resources and time. To address this issue, different mesh sizes (triangular element) were defined at different regions as shown in Fig 2. *36*. The convergence of the mesh was checked by varying the mesh size in different regions. The quality of mesh is defined in terms of skewness s:

$$s = 1 - \max\left(\frac{\theta_{max} - \theta_e}{180 - \theta_e}, \frac{\theta_e - \theta_{min}}{\theta_e}\right) \qquad 2.3.2.(a)$$

Where $\theta_{max}(\geq 60)$ and $\theta_{min}(\leq 60)$ are the largest and smallest angles of the cell, respectively. $\theta_e(= 60)$ is the angle of equilateral triangle. Skewness determines how close to ideal (i.e., equilateral) a cell is. A regular mesh element (equilateral triangle) has mesh quality 1 while a degenerated element has zero. The skewness of mesh in this simulation was maintained between 0.6 and 1. This avoids presence of any degenerated mesh elements.

Sharp edges near triple point regions are susceptible to have degenerated mesh elements. Therefore, the mesh elements in the region surrounding sharp edges have to be very small (µm) to have skewness close to 1. The mesh size along these sharp edges (curvatures of radius r) can be varied by defining segments (e.g., S1…S6, see Fig 2.*37*) and allocating fixed number of mesh elements (n) for each segment. The mesh convergence can be evaluated by varying the mesh 'n' and observing the stability electric field 'E' by using electrostatics simulation module in Comsol®Multiphysics [53]. Four observation points (pt.1…pt.4, see Fig 2.*37*) are designated to observe the variation of the electric field 'E' with the number of mesh elements. Fig 2.*38* shows that 'E' stabilizes when the n > 60. For all simulations in these sections, the number of mesh element along the defined segments (Fig 2.37) are maintained at 60. For n = 60, the mesh size at the triple points is around 0.05 µm (i.e., mesh size = 3µm/60).

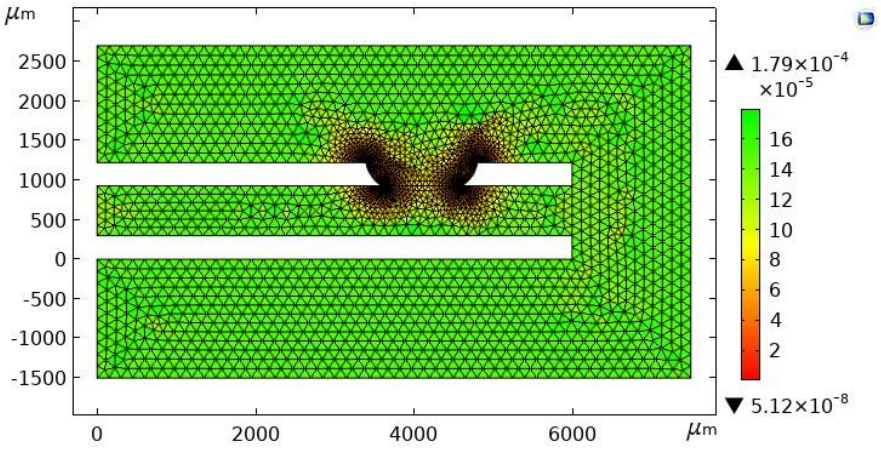

Fig 2. 36. 2D Geometry of power electronic substrate embedded in liquid showing triangular mesh and size

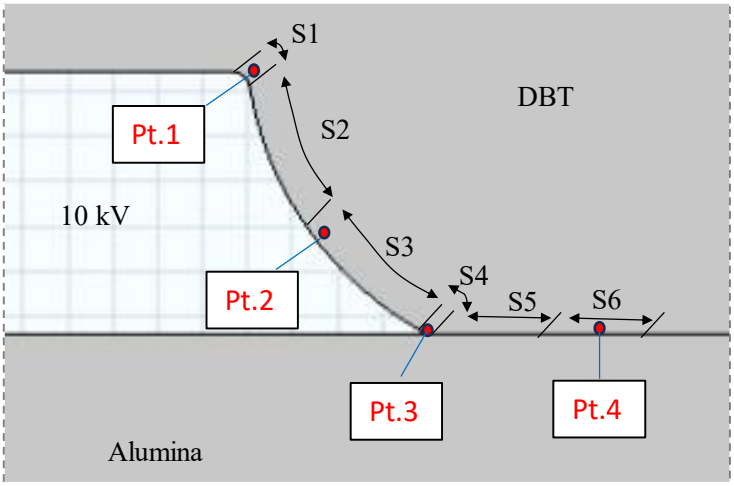

Fig 2.37. Mesh refinement using segmentation

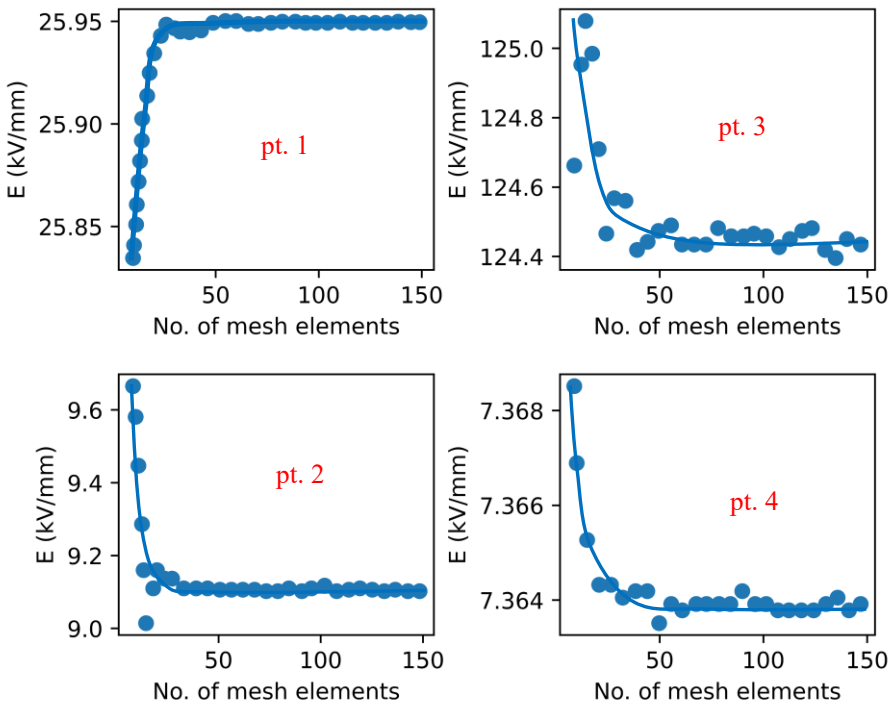

Fig 2.38. Mesh convergence

2.3.3. Transient AC-DC physics and boundary conditions

The AC-DC transient physics (i.e., with time t dependent solver) has been used to simulate electric field evolution in the geometry described in Fig 2.35. It solves the following current conservation equations:

$$\nabla . \mathrm{J} = Q_{j,v} \qquad 2.3.3.(a)$$

$$\mathrm{J} = \sigma \mathrm{E} + \frac{\partial \varepsilon \mathrm{E}}{\partial \mathrm{t}} \qquad 2.3.3.(b)$$

$$\mathrm{E} = -\nabla \mathrm{V} \qquad 2.3.3.(c)$$

Where J is the current density (A/m^2), $Q_{j,v}$ is the current sources ($Q_{j,v}$ = 0), E the electric field (V/m), σ the electrical conductivity (S/m) and ϵ the absolute permittivity (F/m). It should be noted that σ in solid and liquid dielectrics are highly dependent on temperature and electric field, whereas permittivity ε shows only slight variations.

From equations 2.3.2 (a - c), a partial differential equation (PDE) is derived, describing the voltage distribution in the domain Ω_1(encapsulation) and Ω_2(substrate):

$$-\left[\sigma \nabla^2 V(t) + \epsilon \frac{\delta}{\delta t}\left(\nabla^2 V(t)\right)\right] = Q_{j,v} \qquad 2.3.3.(d)$$

The default Neumann boundary condition, i.e., $\hat{n}.J = 0$ is defined along Γ_n. It is equivalent to an insulation where the normal surface current density is zero, no current can flow through the interior boundary and that the electric potential is discontinuous across the boundary.

The Dirichlet boundary conditions are: V (t) = 10 kV with rise time 1ns (typical of blocking voltage of recent WBG power devices), defined along Γ_{d2} and $V_0 = 0V$ as ground

potential defined along Γ_{d1}. The initial condition V(0,x,y) is set to zero in all domains Ω_1 and Ω_2.

This simulation does not include the influence of the electrohydrodynamic (EHD) fluid motion that would considerably complicate calculations, as well as that of temperature gradients present in real power modules.

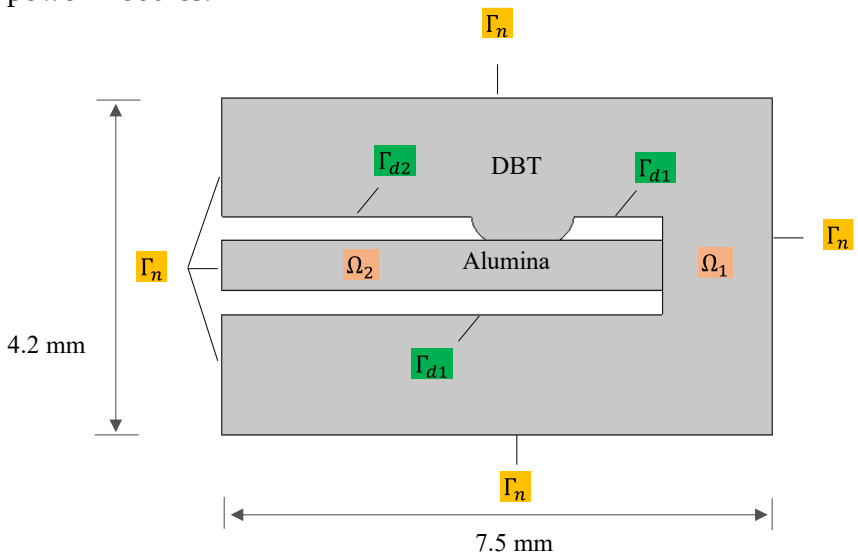

Fig 2.39. Boundary conditions and simulation domains

2.3.4. Non-linear material properties

It's obvious that experimental results are required to obtain the material parameters for both encapsulant and substrate, since the available literature is limited to low values of electric field and temperature. This section details such a study for the identification of the relative permittivity ε' and σ up to 300°C, with an electric field up to 15.7kV/mm in alumina Al_2O_3 and 30kV/mm in DBT. The values in DBT are extracted from the dielectric spectroscopy and conduction studies under uniform field, as discussed in previous sections. The detail of measurement of conductivity and permittivity of Alumina as function of temperature and electric field can be seen in Annex B. It is worth noting that measurements in alumina were done for temperatures starting from 50°C. A very low current ($i_c \ll 10^{-12}$A) at voltage below 2kV at room temperature (~22°C) was beyond the measurement sensitivity of Keithley™ 6517.

Empirical equations expressing permittivity as function of temperature and local conductivity as function of both temperature and electric field are derived from the experimental results. These equations are required to implement the non-uniform and non-linear material properties while simulating electric field distribution within the geometry described in Fig 2.*35*.

Permittivity empirical equations:

$$\epsilon'_{al}(T) = 10.5 + \alpha_a T \qquad 2.3.4.(a)$$

$$\epsilon'_{dbt}(T) = 2.5 + \alpha_d T \qquad 2.3.4.(b)$$

Where $\epsilon'_{al}(T)$ is the permittivity of Alumina, $\epsilon'_{dbt}(T)$ is the permittivity of DBT, α_a(2.4*10^{-3} °C^{-1}) and α_d(- 1.9*10^{-3} °C^{-1}) are temperature coefficients of $\epsilon'_{al}(T)$ and $\epsilon'_{dbt}(T)$ respectively.

Conductivity empirical equations:

$$\sigma(E,T)_{al} = \sigma_{a0}\ \exp(\alpha_1 T + \beta_a E \exp(\alpha_2 T)) \qquad 2.3.4.(c)$$

$$\sigma(E,T)_{dbt} = \sigma_{d0}\left(\frac{T}{Tref}\right)^{\vartheta_1} \exp\left(\beta_d E\left(\frac{T}{Tref}\right)^{\vartheta_2}\right) \qquad 2.3.4.(d)$$

Where $\sigma(E,T)_{al}$ and $\sigma(E,T)_{dbt}$ describes the variation of conductivity with temperature and electric field in alumina and DBT respectively. The temperature constants in alumina, $\alpha_1 = 0.052\ (°C^{-1})$ and $\alpha_2 = -0.0068\ (°C^{-1})$. Electric field constant in alumina is $\beta_a = -0.0068\ [kV/mm]^{-1}$ conductivity σ_{a0} at reference temperature (1°C) $2 * 10^{-18}[S/cm]$. The temperature exponents in DBT are $\vartheta_1 = 3.7645$ and $\vartheta_2 = -0.457$. Electric field constant in DBT is $\beta_d = 0.6501\ [kV/mm]^{-1}$ and conductivity σ_{d0} of $2 * 10^{-19}[S/cm]$ at reference temperature T_{ref} (1°C).

2.3.5. Simulation results at temperature T = 20°C in Al_2O_3 substrate and DBT encapsulation

Fig 2.*40* shows voltage profile at V(t) = 10kV with both g1 and g2 grounded, g1 floating with g2 grounded, and g1 grounded while g2 floating in alumina substrate embed in DBT. The simulation is carried out at 20°C (by substituting T = 20°C in equations described in section 2.3.4).

The evolution of electric field in dielectrics highly depend on duration of the applied voltage (t) as well as on the charge relaxation time constant (τ). This relaxation time is related to conductivity (σ) and permittivity (ϵ) as:

$$\tau = \frac{\epsilon}{\sigma} \qquad 2.3.5.(a)$$

For a very short duration ($t \ll \tau$) in dielectrics, the electric field is purely due to static charges and called "electrostatic" condition. The electric field distribution for ($t \gg \tau$) results from the flow of conduction currents, and hence it is often referred to as "conduction" condition. Typical τ in non-polar liquid is in the order of 10^1s while in ceramic substrates, the τ is in the order of 10^3 s, considering low field and room temperature.

It is possible to simulate electric field transition from purely electrostatic to pure conduction. A typical transient evolution of electric field at points M1 and M2 (each 1µm from triple point in DBT and Alumina respectively) are shown in Fig 2.*41*.

At T = 20°C and for g1 and g2 grounded, the high electric field (220kV/mm in DBT, 160kV/mm in Alumina) resulting from electrostatic condition lasts for a few ms. This high electrostatic field is concentrated in a very small area (radius ~ few µm). This corresponds to the initial instants of impulses induced by semiconductor switching, where the electric field is mostly dependent on the permittivity of DBT and Alumina. Hence, the field is higher in DBT than in Alumina. At t > 10s, the electric field at M1 and M2 reduces to 20 kV/mm and 40kV/mm respectively. The electric field in the conduction regime is higher in Alumina than in DBT, this is because Alumina has a higher resistivity compared to DBT.

The electric field in DBT at M1 in the conduction regime is well below its breakdown strength ($> 60\text{kV/mm}$). Therefore, breakdown or partial discharges are unlikely to occur for a dc blocking voltage of 10kV. These results are in qualitative agreement with partial discharge measurements [17] where it was deduced that PDs under 50 Hz ac (i.e., in a region intermediate between pure electrostatic and conduction regimes at 20°C) mainly originate from the porous ceramic substrate and not from the encapsulant.

When g2 (rear electrode) is grounded and g1 (upper electrode) is at floating voltage (typical configuration for breakdown measurements), the electric field variation at M1 and M2 is very similar to when both g1 and g2 are grounded (see Fig 2.*42* and Fig 2. *43*). The interface electric field along the trench was also observed to be similar to when g2 and g1 are grounded, Fig 2.44. A large reduction of electrostatic field at M1 and M2 was observed when g1 was grounded and g2 was kept at a floating voltage (typical configuration for surface breakdown measurements, see Fig 2. *43*). However, an increase in electric field at short times (µs) at the grounded electrode (g1) was observed when g2 was floating. This suggests that surface breakdown under impulse could initiate from the grounded electrode.

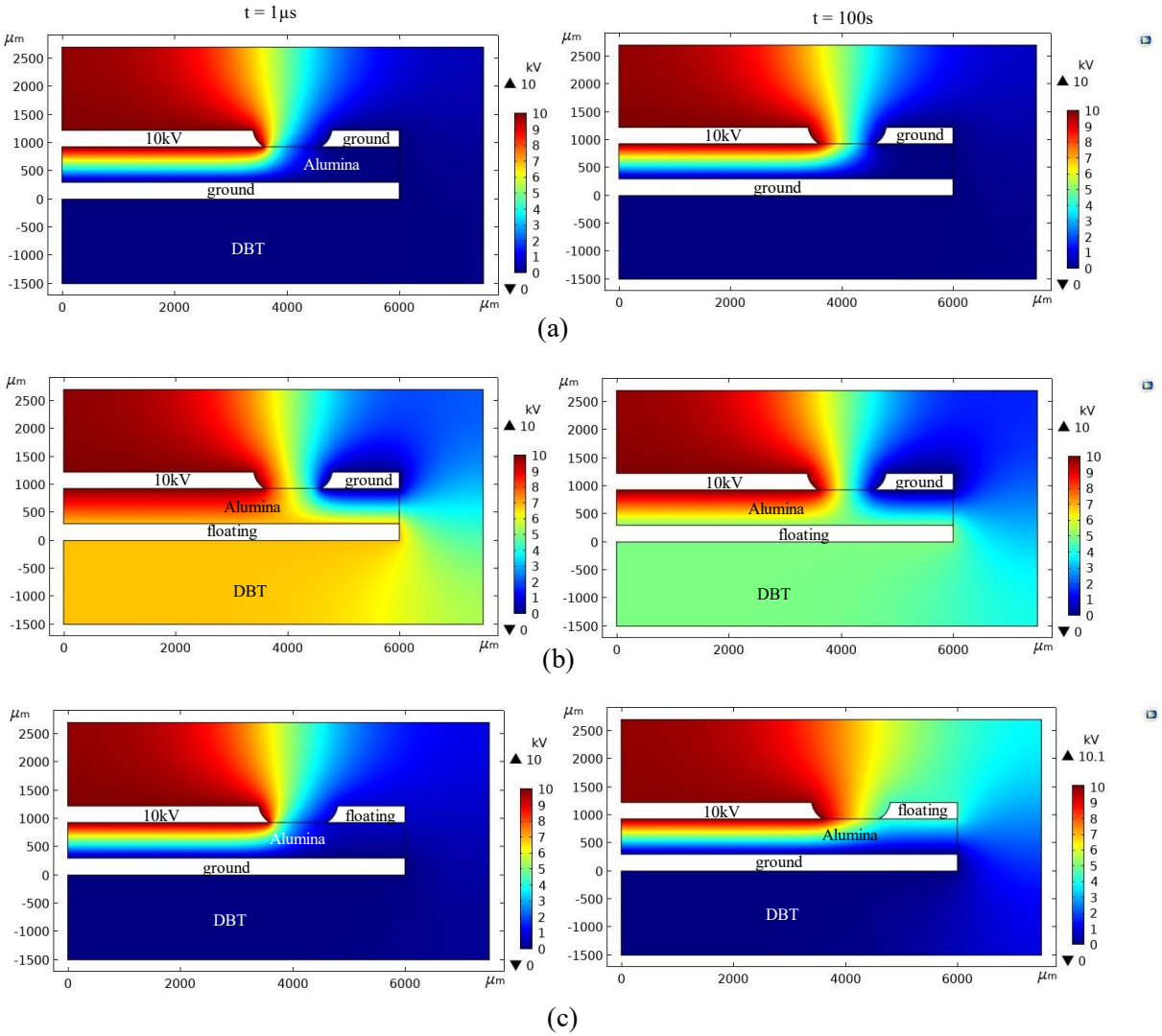

Fig 2.40. Typical voltage profile at T = 20°C with Alumina substrate embedded in DBT at V(t) = 10kV (a) g1 and g2 grounded, (b) g1 grounded and g2 floating (c) g1 floating and g2 grounded

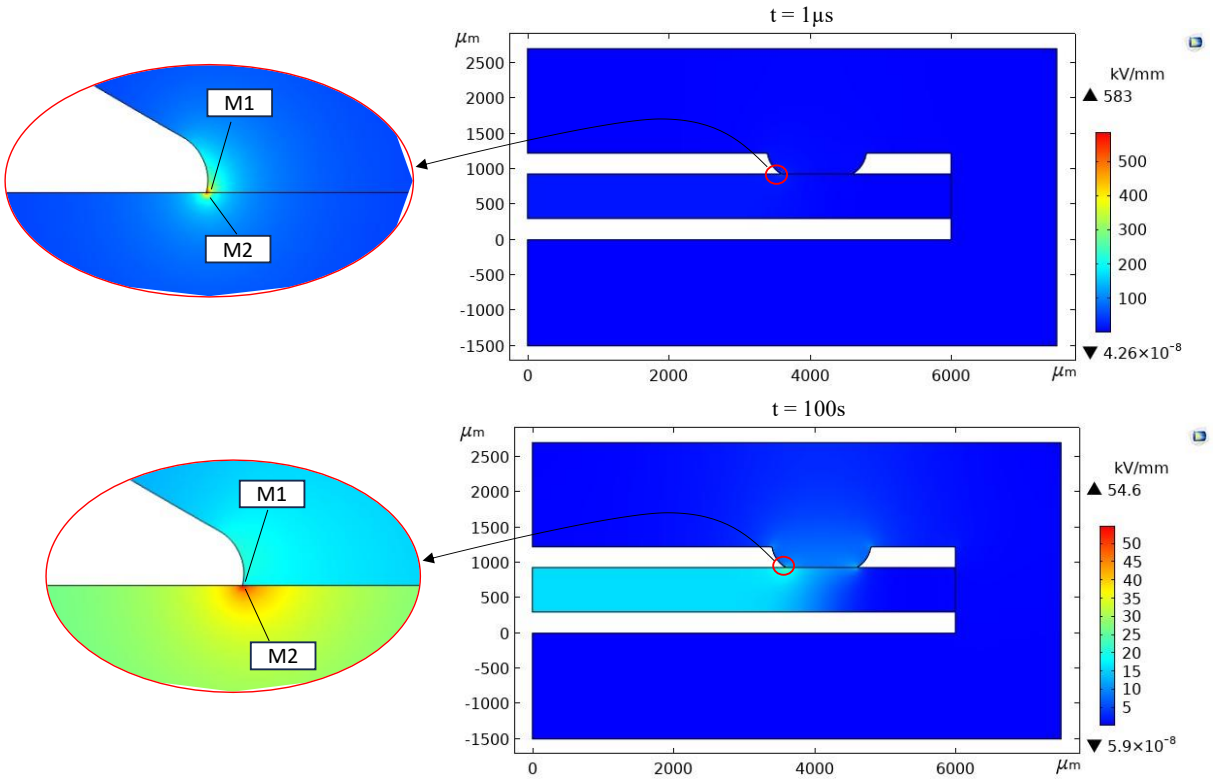

Fig 2.41. Typical electric field distribution in alumina substrate embedded in DBT at T = 20°C, V(t) = 10kV, g1 and g2 grounded

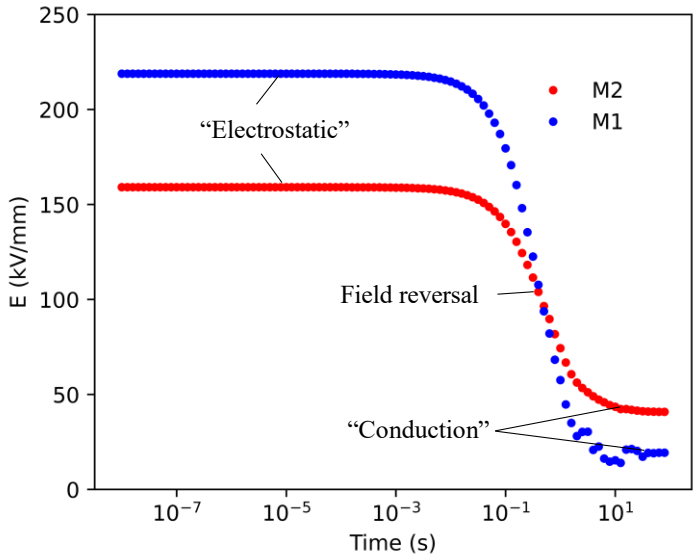

Fig 2.42. Typical transient field evolution near triple point region of alumina substrate embedded in DBT at T = 20°C, V(t) = 10kV, g1 and g2 grounded

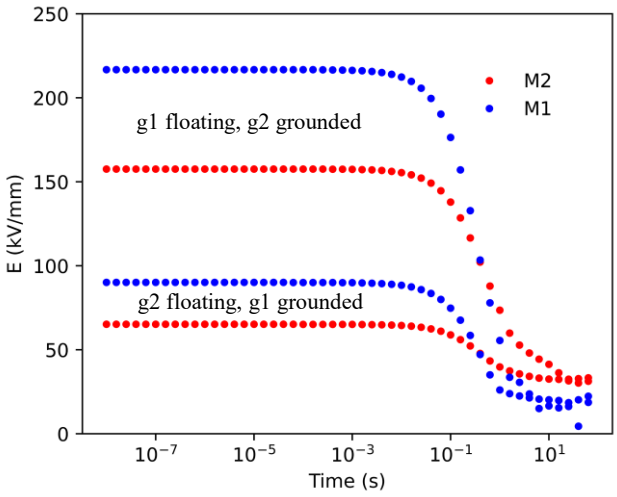

Fig 2. 43. Transient electric field with g1 and g2 grounded or floating

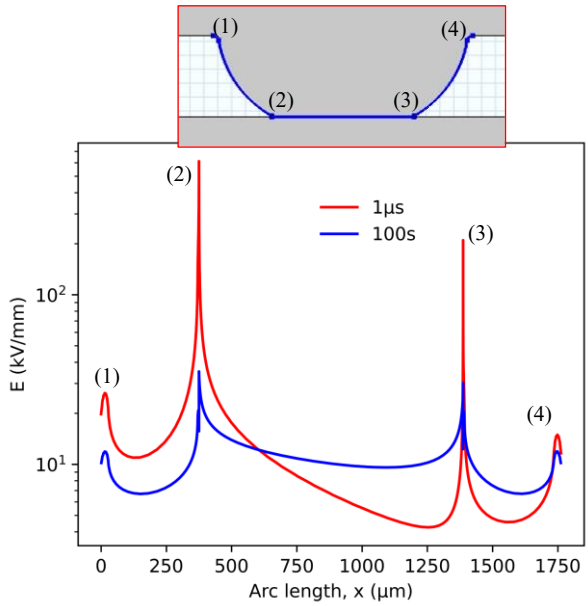

Fig 2.44. Electric field at interface of alumina and DBT along the trench with g1 and g2 grounded

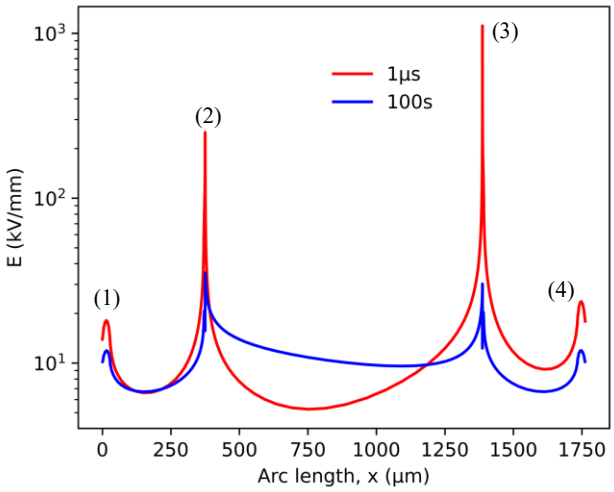

Fig 2. 45. Electric field at interface of alumina and DBT along trench with g1 grounded and g2 floating

In all the following simulations, g1 and g2 remain grounded.

2.3.6. Transient electric field evolution at different electrode gap distances

The gap distances (d) between high voltage electrode and grounded upper electrode g1 were varied from 0.5 mm to 2 mm. This was achieved by keeping the high voltage electrode fixed while shifting the ground electrode in x-direction. The applied voltage V(t) = 10kV while temperature T =20°C. Fig 2.46 shows typical electric field for gap distance of 0.5mm and 1.5 mm. The maximum electric field decreases with an increasing gap distance for both regimes, i.e., from 625 kV/mm (d = 0.5 mm) to 576 kV/mm (d=1.5mm) during 'electrostatic' and from 76 kV/mm (d = 0.5 mm) to 46 kV/mm (d=1.5mm) during 'conduction'. It was observed that the electrostatic field at M1 (DBT) and M2(Alumina) becomes nearly independent of electrode gap distances at d > 1.5 mm, see Fig 2.47. However, the electric field at M1 and M2 decreases with an increase in electrode gap.

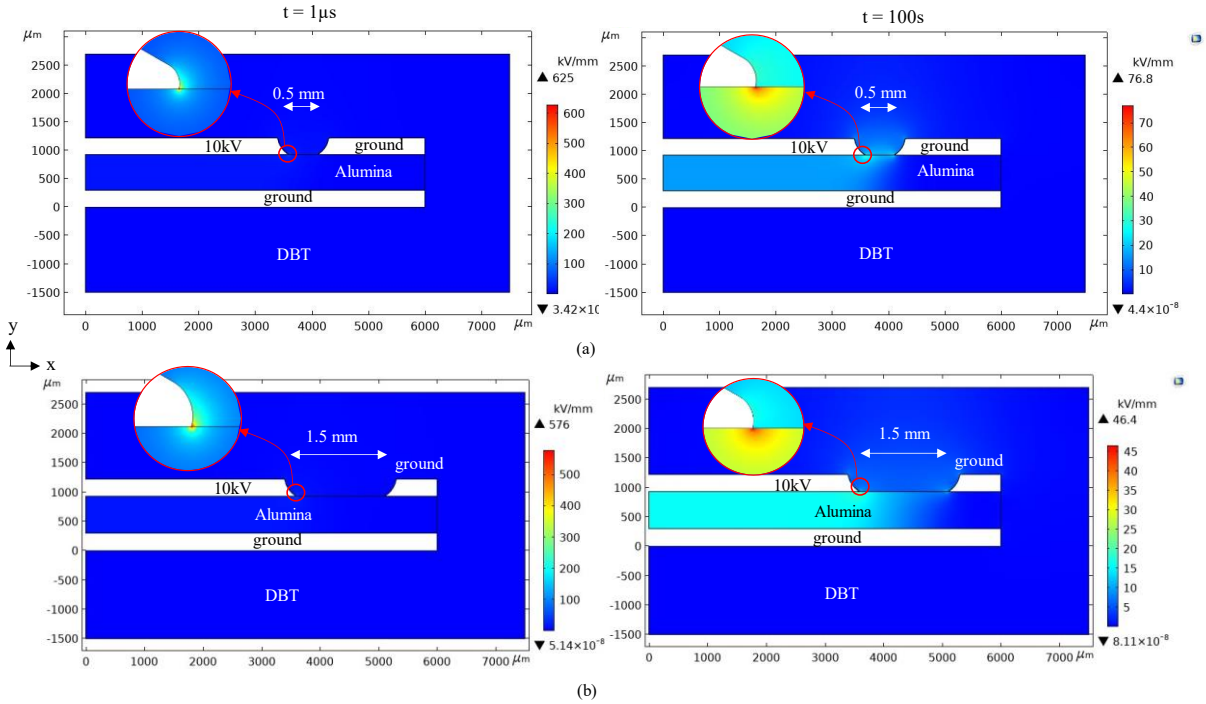

Fig 2.46. Electric field distribution in alumina substrate embedded in DBT at 20°C (a) 0.5 mm electrode gap, (b) 1.5 mm electrode gap

Fig 2.*48* shows variation of electric field at the interface of DBT encapsulation and alumina substrate at different electrode gap. The high electrostatic field (t=1µs) at triple point near high voltage side was observed to be independent of variation of gap distances. Also, high electric field exists during both electrostatic and conduction (t=100s) regimes along the interface for short gap (d = 0.5 mm), as well as at the triple points. Here, point (2) corresponds to the triple point of the high voltage electrode and point (3) corresponds to the triple point of the ground electrode (g1). Logically, breakdown should occur at the interface or very close to the interface (either in DBT or alumina) for short gaps. However, the high electric field along the interface decreases with increasing gap distances. Also, electric field was observed to be higher in alumina during conduction regime (see Fig 2.46).

The combined effect of the field reduction along the interface with increasing gap distance and the electric field reinforcement in alumina poses a potential risk of breakdown in the alumina substrate. Such phenomena were previously observed in surface breakdown

measurement under DC in alumina substrate embedded in DBT [17], where most breakdowns occurred in the liquid or at the interface for d < 0.6 mm, while breakdowns mostly occurred in alumina at longer electrode gaps. Similar observations were made during surface breakdown measurements with Silicone Nitride substrate embedded in different liquids, refer Annex C. Interestingly, liquids recovered quickly after surface breakdowns for short gaps unlike in silicone gel (Annex C). This characteristic could have potential applications in compact wide band gap power modules where trench gaps are typically reduced.

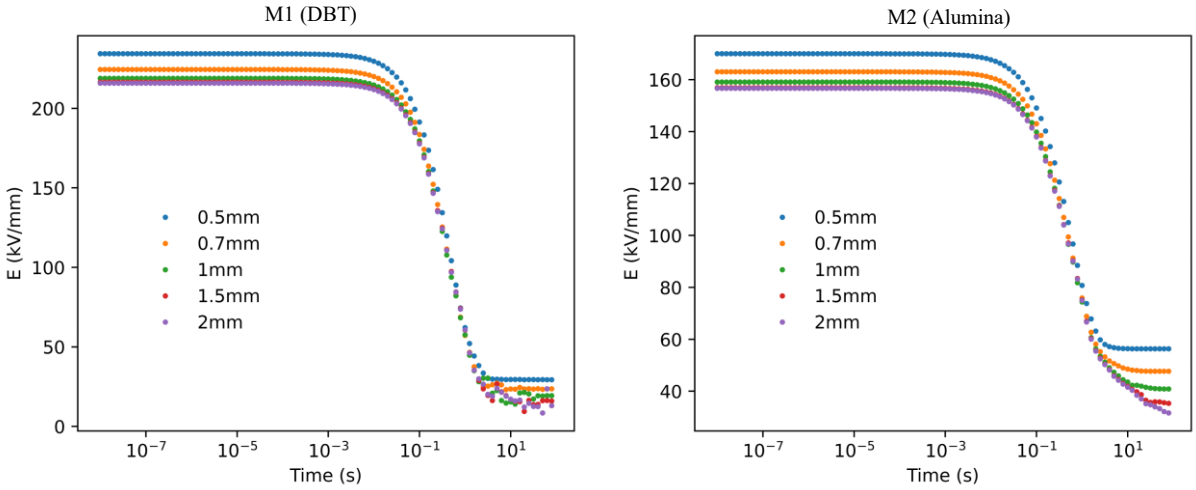

Fig 2.47. Transient electric field evolution near triple point at M1 (DBT) and M2 (Alumina) for different electrode gap distances

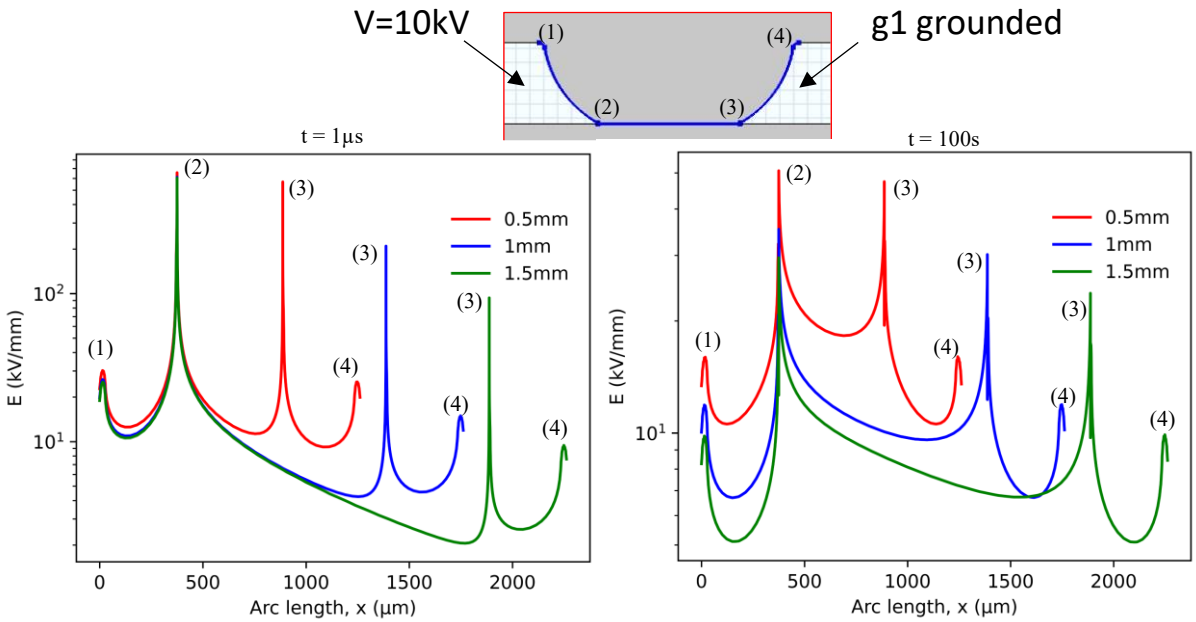

Fig 2.48. Electric field variation along the surface interface of DBT and alumina for different electrode gaps

2.3.7. Influence of temperature on electric field near triple point

Electric field versus time has been simulated for temperatures 20°C–300°C. A uniform temperature distribution is considered. Increasing the temperature reduces the duration and

magnitude of the maximum electrostatic field, as can be seen in Fig 2.49. This is due to the large increase in conductivity in both alumina and DBT. At 300°C, the maximum fields occur for a duration not longer than 100 µs. In turn, the PD activity under 50 Hz AC should decrease with temperature, a fact observed with AlN substrates in DBT up to 300°C and Alumina up to 100 °C [17]. Further experiments would be however necessary to fully ascertain this tendency observed on a very limited number of substrates. The field reversal occurs at 100kV/mm, and appears to be independent of temperature.

It is worth noting that this simulation at different temperature is not fully representative of practical power electronic substrates. For more realistic simulation, coupled heat transfer and electric current multi-physics simulation would be necessary, in which the actual thermal gradient existing near the semiconductor chip could be implemented (instead of a uniform temperature in our simulation).

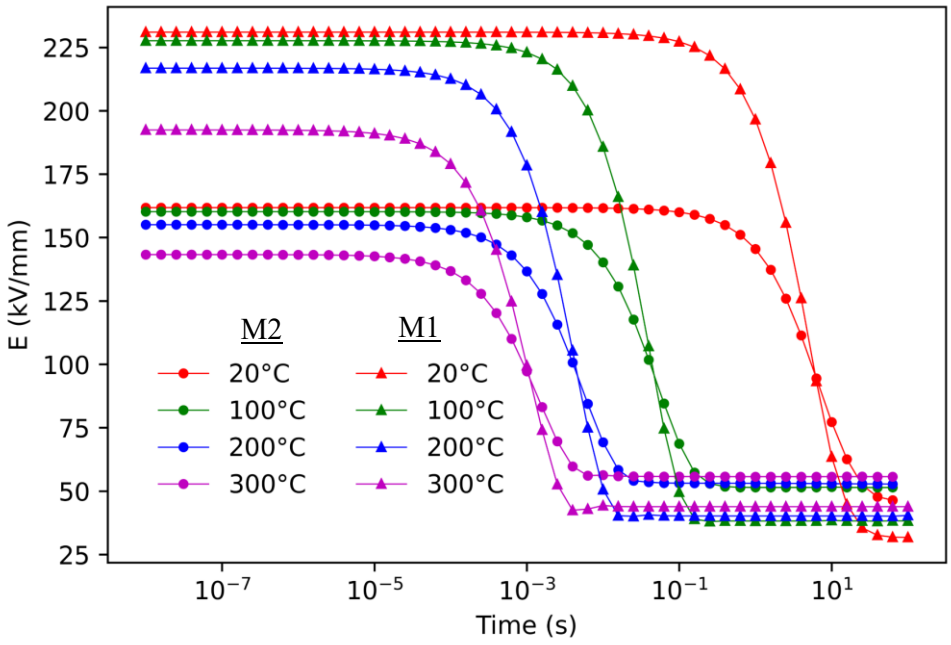

Fig 2.49. Typical electric field evolution versus time at different temperatures with alumina substrate embedded in DBT for electrode gap d = 1mm.

2.3.8. Simulation results at temperature T = 20°C in Al_2O_3 substrate and Silicone gel encapsulation

Conductivity and permittivity of silicone gel at 20°C from [54] have been used to perform similar simulations by replacing DBT. Permittivity of Silicone gel at 20°C is approximately 2.7 [54]. The empirical equation describing electrical conductivity of silicone gel $\sigma_{gel}(S/cm)$ as function of electric field E (kV/mm) is as :

$$\sigma_{gel}(\mathrm{E}) = 2 \times 10^{-16} \exp\left(\frac{E}{30}\right) \qquad 2.3.8.(a)$$

The electric field during electrostatic regime using silicone gel is very similar to the results obtained using DBT as encapsulation (see Fig 2.*42* and Fig 2.*50*). This is due to similar permittivity of DBT (ε_r~2.5) and silicone gel (ε_r~2.7).

However, the duration of the highest electrostatic field is much longer with silicone gel compared to DBT. This is due to the high resistivity of both alumina and silicone gel, that results in a long charge relaxation time (τ), see section 2.3.5. Silicone gel and alumina show conductivity in the order of 10^{-16} S/cm, corresponding to τ in order of 10^{3} s, see Fig 2.*50*. This may have practical implication on the risk of breakdown in silicone gel or alumina, due to longer exposure to high electrostatic field.

In a similar way, the electric field during conduction regime with silicone gel is around 72 kV/mm at M1 and M2, significantly higher than with DBT (field at M2 = 40kV/mm, M1 = 20kV/mm), Fig 2.*50*. Also, the electric field at the interface of silicone gel and alumina is much higher than with DBT (see Fig 2.44 and Fig 2.51). This may explain why partial discharge inception voltage (PDIV) was much higher with DBT compared to silicone gel [17].

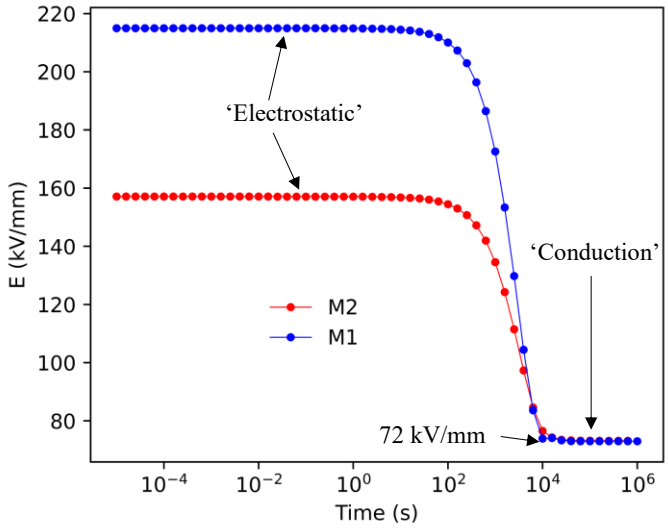

Fig 2.50. Transient field evolution near triple point region of alumina substrate embedded in silicone gel at 20°C

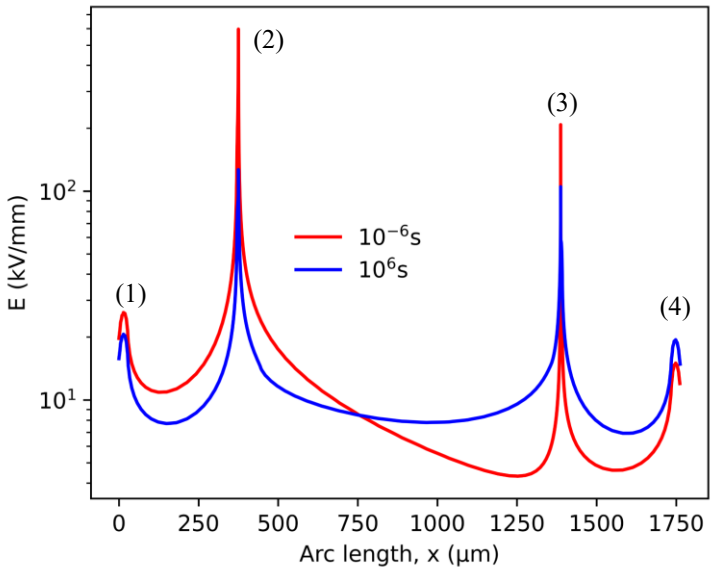

Fig 2.51. Electric field at interface of alumina and silicone gel along the trench

2.3.9. Conclusion on transient electric field simulation

FEM simulations carried out by considering the non-linear conduction properties of materials show that electric field distribution within ceramic substrate embedded in DBT liquid is highly dependent on time and temperature. Following a voltage step with fast risetime, a reorganization of the field distribution rapidly occurs due to conduction properties. Since high field conduction shows a large non-linearity (conductivity of DBT at the maximum calculated field of 20 kV/mm is about 4 decades larger compared to low field conductivity at 20°C), the typical transition time from electrostatic regime to conduction regime is shorter than that estimated from "standard" low field conductivities usually quoted for materials. At high temperature, the maximum electrostatic field in the liquid lasts only for several 10µs, within a very small region of radius < 1µm near the triple point. At longer times, the maximum field in materials considerably drops, and become larger in the Alumina substrate, regardless of the encapsulant nature (liquid or gel). Some qualitative correlation with previous PD measurements carried out at 50 Hz versus temperature can be found: increasing the temperature induces some increase of the PDIV with DBT. The calculations carried out indicate that voltage impulses with fast risetime may constitute critical conditions, by inducing a maximum field in the triple point region. In the next chapter, the detection of PD under fast impulses will be tentatively carried out by optical measurements, in order to further investigate this important question, since fast impulses constitute the actual conditions found in a power module.

Only qualitative correlation between calculations and PD (or breakdown) measurements can be established. To obtain a more realistic field calculation, additional phenomena such as space charge injection in the liquid, charge transport enhanced by EHD motion, should be also considered. Calculations were also obtained for a fixed geometry of the triple point and a uniform temperature.

3 Electrical and optical partial discharge measurements with liquid embedded substrates

Partial discharges (PD) lead to degradation and failure of insulation system exposed to high electric field. As discussed in previous chapters, high electric field exists in power electronic modules especially at the triple points (intersection of encapsulation, metallic electrodes and ceramic substrate) due to sharp edges and permittivity differences at the interface. These triple point regions are hotspots for PD activities or initiation of insulation breakdown. This chapter is dedicated to PDs detection techniques to study PD activity along the triple point regions of ceramic substrate embedded in dielectric liquids. One of the main objectives is to study PD under fast rise impulse (where electric field distribution is mostly of 'electrostatic' nature), typical of fast impulses in power modules.

3.1. Partial discharge detection techniques in power electronics

The occurrence of partial discharges (PD) in an insulation material is accompanied by fast electrical pulses, light pulses, electromagnetic waves, ultrasonic waves. Depending on type of applications, several methods exist to detect PDs. Standard electrical methods are widely used to detect and measure electrical discharges, via detection of current pulses produced by PDs in the external circuit. Such measurements are easily carried out under high voltage AC, and another advantage is the possibility to calibrate measurements in terms of apparent charge associated to a PD. However, in the case of pulsed high voltage waves, relevant of power electronics systems, such methods become very difficult or even impossible, because current pulses induced by the power supply can be hardly distinguished from PD pulses. Other methods such as optical detection does not suffer from such drawback, but can be used only with transparent materials, and can be also difficult to interpret since various mechanisms of light emission under high electric field may exist. Calibration of such measurements is also another question.

In the followings, we will use both electrical and optical methods to detect PDs occurring on substrate embedded in liquids, in order to discuss the validity of such measurements, and obtain data relevant to power electronics modules with fast rise impulses.

3.1.1. Partial discharge sources in power electronics modules

High electric field occurs at the triple point due to sharp electrodes edges and mismatch of material properties such as conductivity and permittivity, see Fig 3.1. Various defects occurring in embedded substrates may exists and explain the occurrence of PDs in the triple point region under high voltage: cavities within substrate material, trapped bubbles in gel or liquid encapsulation, delamination at the substrate / metal interface, sharp metallic protrusions

at the metallization edges. In the case of air-filled voids, their breakdown strength (about 3kV/mm under standard conditions) is considerably lower than the breakdown strength of either ceramic substrates or encapsulation materials (gel/liquid), which have a breakdown strength far exceeding 15kV/mm. Previous PD measurements with AlN substrate in air [17] showed a typical PD inception voltage below 1.4 kV and very large PDs (> 500 pC), whereas encapsulation with silicone gel or DBT lead to discharge inception voltage above 5 kV, and PD amplitudes reduced to about 1 pC.

Once air is replaced by gel or liquid, the presence of voids either in the encapsulation or in the substrate can promote appearance of PDs, and this phenomenon is even more pronounced when the permittivity mismatch between gaseous cavity and surrounding material is larger. In the absence of pre-existing voids, PDs can also occur within the materials themselves (gel, liquid, possibly substrate) due to a very high local field, and this effect can be enhanced by the existence of metallic asperities reinforcing the local field. With AlN and Al_2O_3 ceramics, made by sintering powders and containing µm size pores, previous measurements under AC concluded that PDs recorded at low voltage occur in these pores, and then in the surrounding encapsulation material at higher voltage [33].

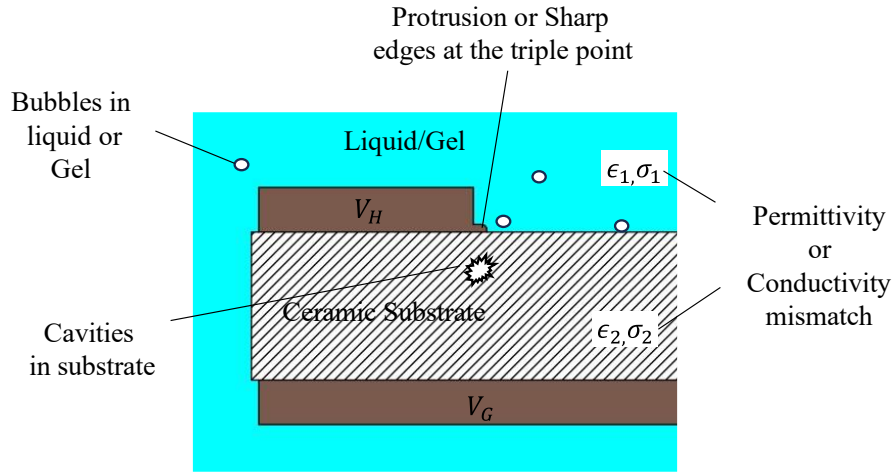

Fig 3.1. A schematic of metalized ceramic substrate embedded in gel/liquid showing critical locations and sources of partial discharge

The PD activity is expected to increase in WBG power modules operating at higher voltage, increased switching frequency and high slew rate (fast rise impulses). As shown in the previous chapter, the local maximum field with long duration voltage (DC, AC) can be significantly reduced due to space-charge injection (such as in point-plane gap), and also to conductivity mismatch between substrate and encapsulant in a more realistic substrate geometry. Therefore, it is crucial to characterize and understand partial discharge activity under AC as well as impulses of different frequency and slew rates. Two PD detection techniques are used in the following experiments:

- *Electrical recording of PD pulses* : well established and standardized method to detect PDs under AC voltages. It allows quantitative measurements via calibration in terms of apparent recorded charge of PD pulses. However, it is not suitable to detect PDs under fast rise impulse voltages.

- *Optical method* : this method appears suitable for PD detection with substrates for any voltage types, taking advantage of the transparency of the encapsulant (i.e.: liquids and

silicone gels). However, the interpretation of measurements can be doubtful if light emission due to electroluminescence of materials takes place (spontaneous light emission under high electric field, not involving electrical discharges).

A description of both these methods are presented in the following section.

3.1.2. Electrical PD detection – Equivalent 3-capacitances model

In an energized insulation system containing cavities, the voltage appearing across the cavity (V_c) will follow the waveform of the applied voltage (V), Fig 3.2. If C_B is the capacitance of the healthy insulation in series with the capacitance C_c of the gas cavity, the voltage across the cavity can be expressed as,

$$V_c = V\ x\ \frac{C_B}{C_B + C_C} \qquad 3.1.2.(a)$$

The breakdown voltage of the cavity is represented by V_g. If the electric field within the cavity is greater than the breakdown field of the gas within the cavity, i.e., $V_c > V_g$, and if an initial "seed" electron is present, a gas discharge of "streamer" or "electron avalanche" type will develop within the cavity. The charge deposited on the cavity walls by the streamer will cause the electric field across the cavity to collapse, and the streamer will stop growing once the field is below that required to sustain its growth. In turn, an increase in capacitance between electrodes will result from the collapse of the electric field. This sequence can be portrayed using an equivalent circuit diagram, as shown in Fig 3.3. The PD induces a fast electrical current pulse i(t) (typical duration ≈ ns) in the external circuit. The integration of such pulse over time (t_2-t_1 = duration of current pulse) provides a charge 'q' that characterizes the amplitude of the PD:

$$q = \int_{t1}^{t2} i(t)\, dt \qquad 3.1.2.(b)$$

The recorded PD charge 'q' in the external circuit, called "apparent charge", is proportional to the real charge amount flowing through the gas (called "real charge"), with a ratio that depends on capacitances C_A, C_B, C_C. Only the apparent charge q can be recorded in practice (C_A, C_B, C_C are usually not known), and it can be used to characterize the PD intensity, provided the measurement circuit was previously calibrated. The calibration of measurements (in terms of apparent charge) must take into account all stray capacitances occurring in the measurement circuit. Calibration is achieved by injecting a charge pulse from a reference source connected to the tested sample.

PD measurements under AC are usually represented by superimposing on a single figure all measured PD pulses versus their occurrence phase, producing the so-called "Phase Resolved Partial Discharge" (PRPD) recording (see examples in the followings). The PRPD figure shows typical characteristic shapes that may be tentatively used to determine the type of defect present in the insulation system being tested [55]. The sum of all recorded PD charges divided by the recording time (typically 60s in our experiments) provides an "average equivalent PD current" I_{pd} that can be used to characterize the average PD activity, in addition to other parameters such as PD number, charge, statistical distributions and parameters derived from PD recordings.

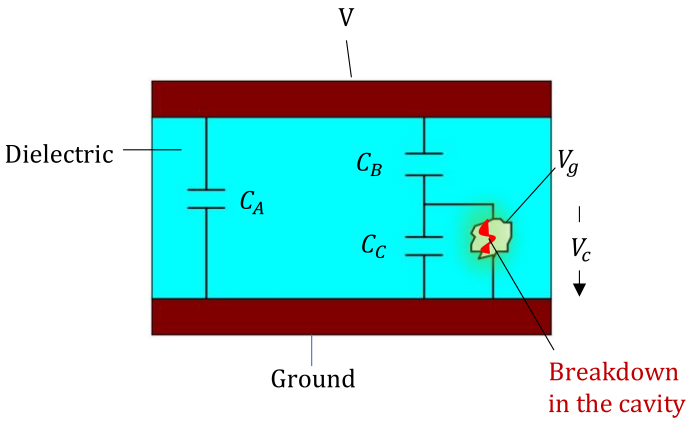

Fig 3.2. Voltage occurring across a cavity in insulating material under AC

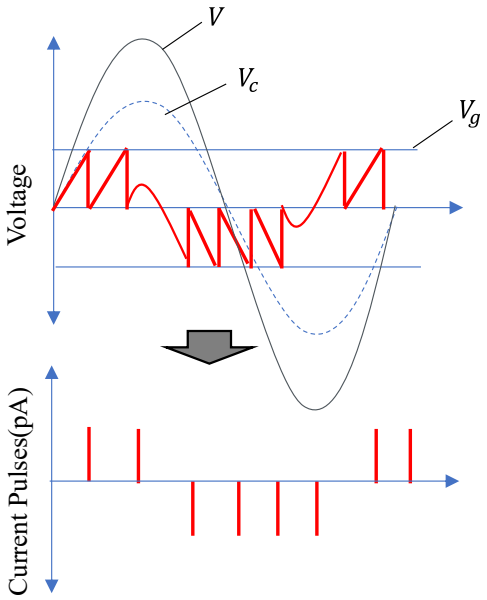

Fig 3.3. Graphical representation of the voltage occurring across a gaseous cavity in a dielectric medium under AC conditions *[56]*

3.1.3. Optical PD detection method

The optical partial discharge detection is based on the detection of light produced as a result of various ionization, excitation and recombination processes occurring during partial discharges. The wavelength of PD light emission depends on the material nature, but usually includes emission in the visible range between 400nm to 700nm as reported in [56]. This allows the use of photomultipliers (PM) with typical responsivity range of 200nm to 700nm, very high sensitivity (down to single photon), and fast response (ns risetime), to properly detect the light produced from PDs. The incident light (photons) is converted by the PM into current pulses (about 3 ns in duration for 1 photon), which is then recorded with oscilloscope as illustrated in Fig 3.4 .

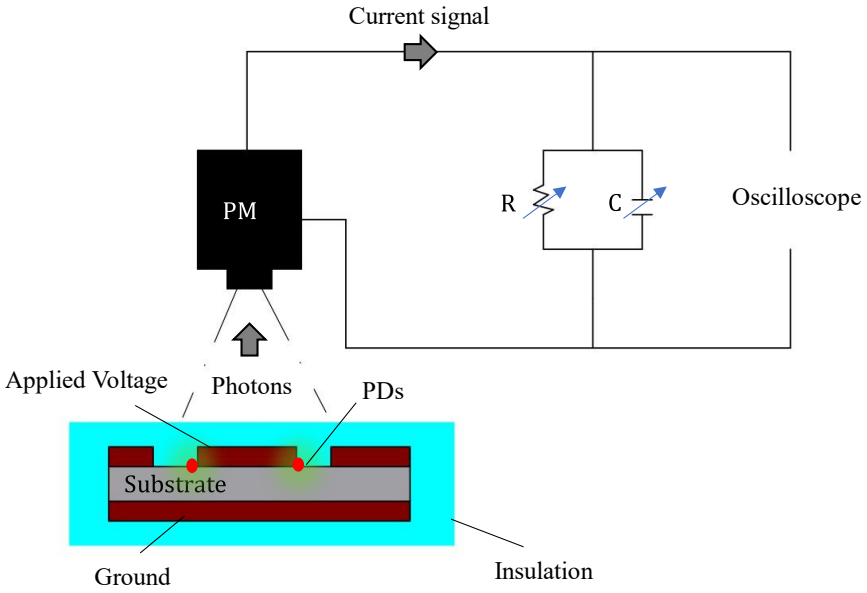

Fig 3.4. Representation of optical PD detection with a power electronic substrate embedded in insulating liquid/gel using photomultiplier

The light measurement sensitivity and bandwidth with the oscilloscope can be varied by changing the time constant $\tau = RC$, where R and C are the measurement resistance and capacitance (see next sections).

Recordings with short measurement time constant ($\sim$ns up to ms) provides time resolved light measurements (TRLM) which may be correlated with PRPD obtained from electrical PD detection. In a previous study [57] optical PD measurements in Air and SF6 gases could be calibrated by comparison with electrical measurements, provided measurement time constant τ was properly adjusted to be consistent with electrical measurements.

The current signal from the PM can be also integrated by increasing the measurement time constant ($\tau \sim 0.1\ s$). Such integrated signal provides the average PM current I_{pm}, showing a high sensitivity, and providing a measurement of the average PD activity. It may be tentatively compared to the average PD current I_{pd} calculated from standard electrical measurements.

3.2. Materials and Experimental system

3.2.1. Substrates and encapsulation materials

Optical PD detection is not possible for substrate and encapsulation materials which are electroluminescent. The light from electroluminescence can be hardly distinguished from the PD light, and interpretation of signals is not obvious. A summary of the known electroluminescence behaviour of several ceramic substrates and encapsulation candidates can be seen in Table 3.1.

Previous works [31, 33] showed that AlN substrates are electroluminescent, due to their chemical nature and to the presence of numerous additives for their elaboration. In addition, they also show thermo- and photo-luminescence properties. Therefore, AlN substrates, widely used to build power modules, cannot be used for optical PD detection. PD measurements under AC using optical and electrical methods in Al_2O_3 substrate embedded in silicone oil/gel were

reported in [34]. Silicone oil, silicone gel, and Al_2O_3 materials were reported to be non-electroluminescent.

Table 3.1. Different power electronic substrates and encapsulation materials for PD studies

Materials		Electroluminescence	Previously tested at G2elab	
			Optical method	Electrical method
Substrates	Aluminium Nitride (AlN)	Yes	Yes	Yes
	Alumina (Al_2O_3)	No	Yes	Yes
	Silicone Nitride (Si_3N_4)	Unknown	No	No
Encapsulation	Silicone gel (Sylgard 527)	No	Yes	Yes
	Silicone Oil (47V50)	No	Yes	Yes
	Dibenzyltoluene (DBT)	Unknown	No	Yes

Thanks to the non-electroluminescent nature of silicone oil and Al_2O_3, it is possible to investigate whether Si_3N_4 substrates, Mobil jet oil and dibenzyltoluene materials (not yet investigated) are electroluminescent or not. In our study, the following combination of substrates and encapsulation materials was used for PD detection using both optical and electrical methods.

- *Substrates*: Alumina and Silicon nitride
- *Encapsulation liquids*: Silicone oil, di–benzyltoluene and Mobil jet oil (refer to Table 1.2)

Silicon nitride is a ceramic substrate material used for high temperature and high voltage applications in power electronics. It has superior mechanical strength, essential for high temperature application to withstand thermo-mechanical stress resulting from CTE mismatch and thermal gradients. It also has high thermal conductivity allowing better thermal management, and high dielectric strength to withstand high voltage (refer to Table 3.2). Aluminium nitride AlN is best suited for thermal management due to its higher thermal conductivity, however, it has inferior mechanical and electrical properties. At present, alumina substrates are widely used due to low cost, and suitable properties for applications in Si-based power modules.

Table 3.2. General properties of ceramic substrates used in power electronics

Properties	Al_2O_3	Si_3N_4	AlN
Conductivity (S/cm) at 20°C	4.5	8	3.5
Relative Permittivity at 1 MHz	9.7	-	8.8
Dielectric strength (kV/mm)	11-16	>14	14-17
CTE (ppm/°C)	8.1	3.3	4.2
Thermal conductivity (W/mK)	20-30	30-32	260
Tensile strength (MPa)	200	450	310

3.2.2. Experimental system

Conventional AC electrical partial discharge measurements are based on the use of high pass RLC parallel filter, that attenuates the low frequency harmonics produced by the AC power supply, enabling the detection of fast impulses produced by PDs. The present Power Diagnostix™ system used has a measurement bandwidth from 40 kHz to 800 KHz.

In practical situations, the substrates and encapsulation materials in power modules are subjected to impulse voltages with fast rise time. In this case, the presence of high harmonics on the supply voltage makes the detection of discharges problematic: it becomes very difficult to separate the pulsed supply current from the pulses due to PDs. Conversely, the optical detection can be used whatever the shape of high voltage wave.

The experimental system in Fig 3.5 was designed to detect PDs in power electronic substrates embedded in dielectric liquids or gels, using both electrical and optical methods. It is composed of several basic parts:

- Measurement test cell
- Sinusoidal or pulsed high voltage power source
- Electrical PDs detection system under AC voltage
- Optical PD recording system under both AC and impulse voltages
- Light visualization system to detect and locate light produced by PDs or electroluminescence

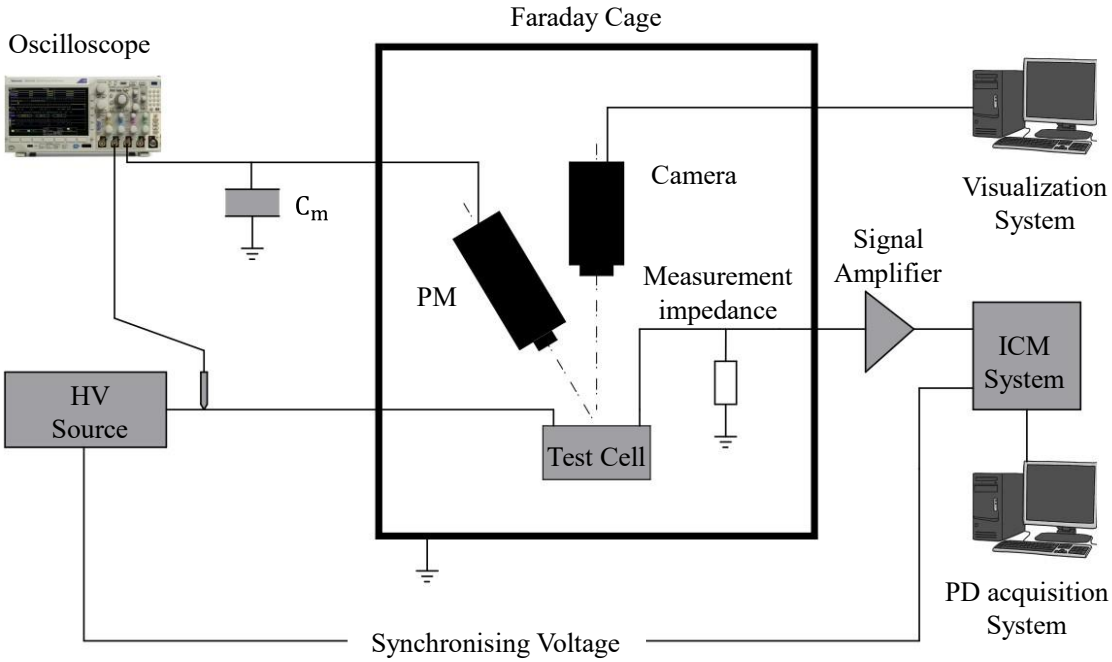

Fig 3.5. Measurement system for electrical and optical PD detection

3.2.2.1. **Test cell for PD measurements with ceramic substrates embedded in liquids/gel**

The structure of the measurement test cell is shown in Fig 3.6. It consists of a Teflon container of diameter 10 cm and height 5 cm. The substrate sample and the test cell are thoroughly cleaned with acetone and dried with high pressure air to remove any dust particles

or contaminants before filling it with fresh liquid. A ground wire is soldered directly on the lower metallization for all measurements. The test cell filled with liquid is kept under vacuum for 2 hours to remove trapped air bubbles introduced mostly during filling process.

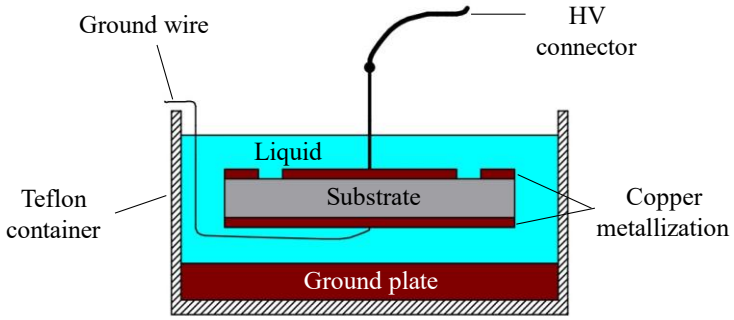

Fig 3.6. Measurement test cell for PD detection and visualisation

3.2.2.2. **Low noise High voltage AC power source**

The low noise and low distortion sinusoidal supply voltage is provided by a low frequency (LF) generator associated with a 100 W amplifier, feeding a PD free transformer (20 V/20 kV). The maximum value of the voltage at secondary was limited to 15 kV in order to avoid PDs from occurring within the transformer. The frequency can be adjusted from 10 Hz to 1 kHz. This arrangement, together with careful shielding in a Faraday cage, and careful connections to avoid discharges, leads to a very low noise level on PD measurements (about 0.2 pC), corresponding to the intrinsic limit of the PD measurement system. No additional noise occurs due to the AC high voltage source, PDs in connections, or external perturbations.

The synchronisation for PRPD recordings using the ICM™ system is provided by the LF generator (see Fig 3.7). Some phase shift exists between this signal and the high voltage output of the transformer, due to the amplifier and transformer as shown in Fig 3.8. Therefore, phase corrections were made for all PRPD recordings, depending on frequency (see Table 3.3).

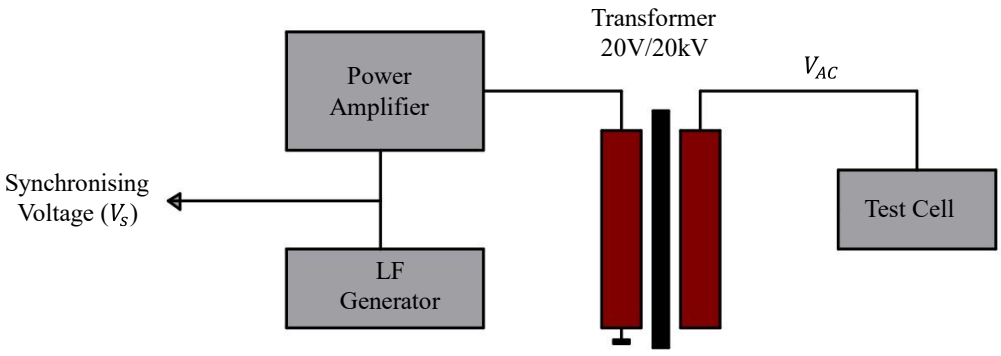

Fig 3.7. AC Voltage source

Table 3.3. Phase deviation corrections of PRPD recording using ICM system

Frequency (Hz)	20	50	100	150	200
Phase corrections (°)	5.2	-18.9	- 43.8	-57.3	- 65.8

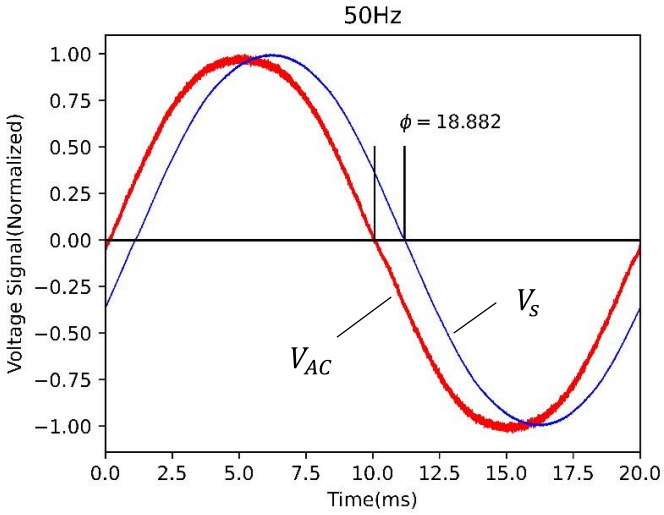

Fig 3.8. Phase deviation existing between the synchronisation voltage (Vs) and actual voltage applied on the sample (VAC) at 50Hz

3.2.2.3. **High voltage impulse voltage source**

A high voltage DC power supply is connected to a fast high voltage push-pull switch, to obtain a unipolar rectangular pulse voltage U (Fig 3.9). It is based on a MOSFET solid-state switch (Behlke HTS301-03 GSM, 30 kV, 30 A). An adjustable resistor R is placed in series with the sample, so as to modify the rise time of the voltage across the sample. A high DC offset *V* can also be superimposed to the pulses. A decoupling capacity of 20 nF placed in series with the push-pull switch prevents direct paralleling of voltage sources. The 100 MΩ resistor protects the DC power supply from voltages impulses and possible short circuit by breakdowns. The main characteristics of this impulse supply system are:

- Minimum impulse rise and fall times of 200 ns
- Repetition frequency of 0 to 10 kHz
- Adjustable pulse width from 0.1 µs minimum
- ± DC offset 1kV to 10kV

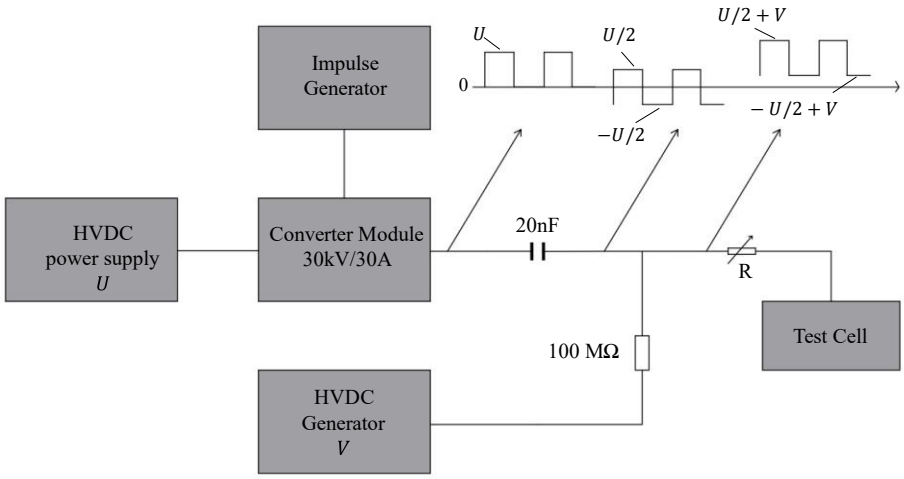

Fig 3.9. High voltage rectangular impulse voltage source, with or without DC offset

3.2.2.4. **Electrical PD acquisition using the Power Diagnostix ICMsystem™**

The acquisition of PD pulses under AC is carried out using the ICMsystem™, Fig 3.10 . It performs the electrical PD detection, acquisition, and processing explained in section 3.1.2. The test cell is connected in series with a quadrupole RLC high pass filter, CILM4/V1µ0. The signal is then fed to the input of pre-amplifier RPA1 of low signal distortion, variable gain, low noise and bandwidth 40 kHz - 800kHz. Calibration is made by injecting a 5-pC charge using PD calibrator CAL1A connected to the test cell.

The Power Diagnostix ICMSystem™ software was used to record PD patterns, Fig 3.11. The background noise of PD charge during measurements was around 0.2 pC, corresponding to the noise level of the PRPD system itself. The adjustable PD rejection threshold during recordings was set to 0.3 pC in order to avoid recording noise. Therefore, PD's smaller than this threshold were ignored during measurements. PDs recording duration was 1 minute, and this procedure was repeated 6 times for each condition. From PRPD recordings, an equivalent average PD current *Ipd* could be calculated, by adding all positive and negative PD charges, and dividing by recording time.

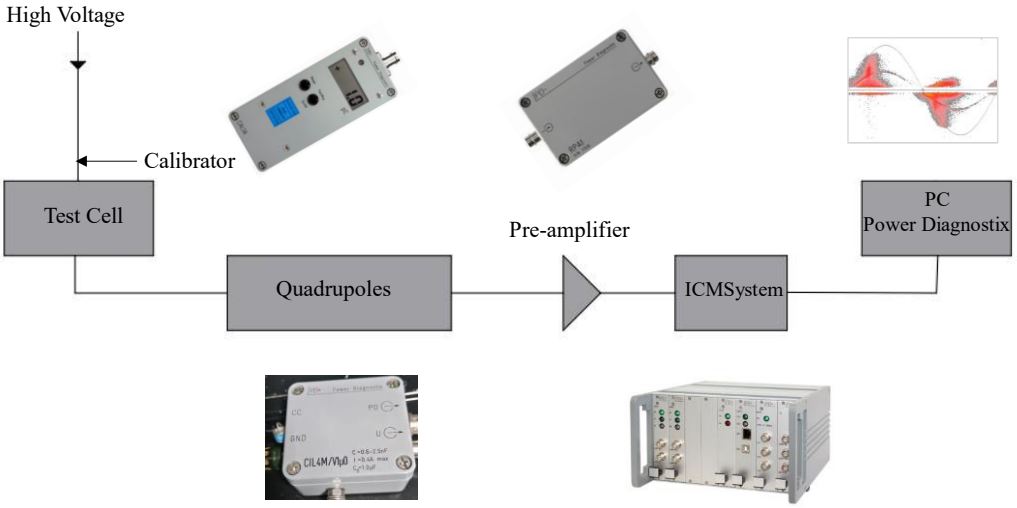

Fig 3.10. Electrical PD recording devices

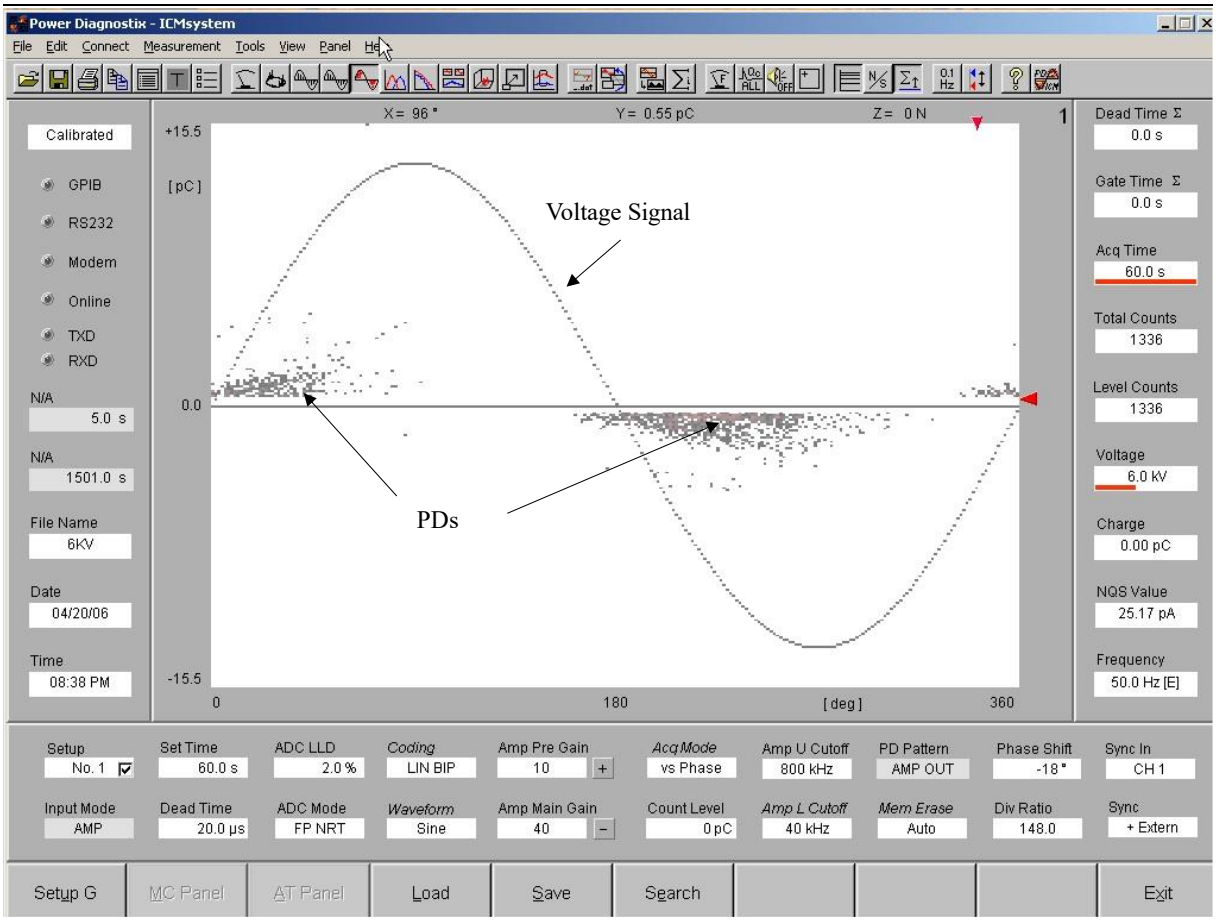

Fig 3.11. Power Diagnostix – ICMsystem™ software showing typical phase resolved partial discharge recording (PRPD), and typical parameters derived from recording. Each data point corresponds to a recorded PD, and the color of this point is related to the total number of PDs recorded with the same amplitude and phase. The NQS value corresponds to the average PD current, and the 'ADC LLD' corresponds to adjustable rejection threshold (2% of the full scale in this example)

3.2.2.5. **Optical PD visualization system**

The use of a very sensitive intensified camera makes it possible to visualize and locate areas of light emission due to partial discharges. The system is placed in a dark Faraday cage, Fig 3.*12*. The ultimate sensitivity of the camera is limited by its intrinsic noise, which results in the presence of random bright spots on the recorded images, Fig 3.*13*(a). Each point corresponds to at least one photon.

The camera used consists of a CCD camera in series with a gated double stage intensifier (Hamamatsu™ C4274). The image intensifier has a spectral response ranging from ultraviolet to near infrared. The PD light emission is often of very low intensity, and the camera was adjusted so as to capture maximum light with a large aperture (f = 1.2) objective with 50 mm focal length.

Image acquisition and processing was carried out via a DT3120 acquisition card (Twin 8-bit A/Ds) and GLOBAL LAB Image/2®3.7. software. This software allows averaging of images, and therefore considerably reduce the impact of background noise. An average of 50

consecutive images was enough to obtain a noise free camera image, Fig 3.13.(b). providing an equivalent total exposure time of 2 s. This helped obtaining better images of stable light sources (e.g., repetitive PD's occurring at a fixed location). However, unstable intermittent PDs could not be captured in this way.

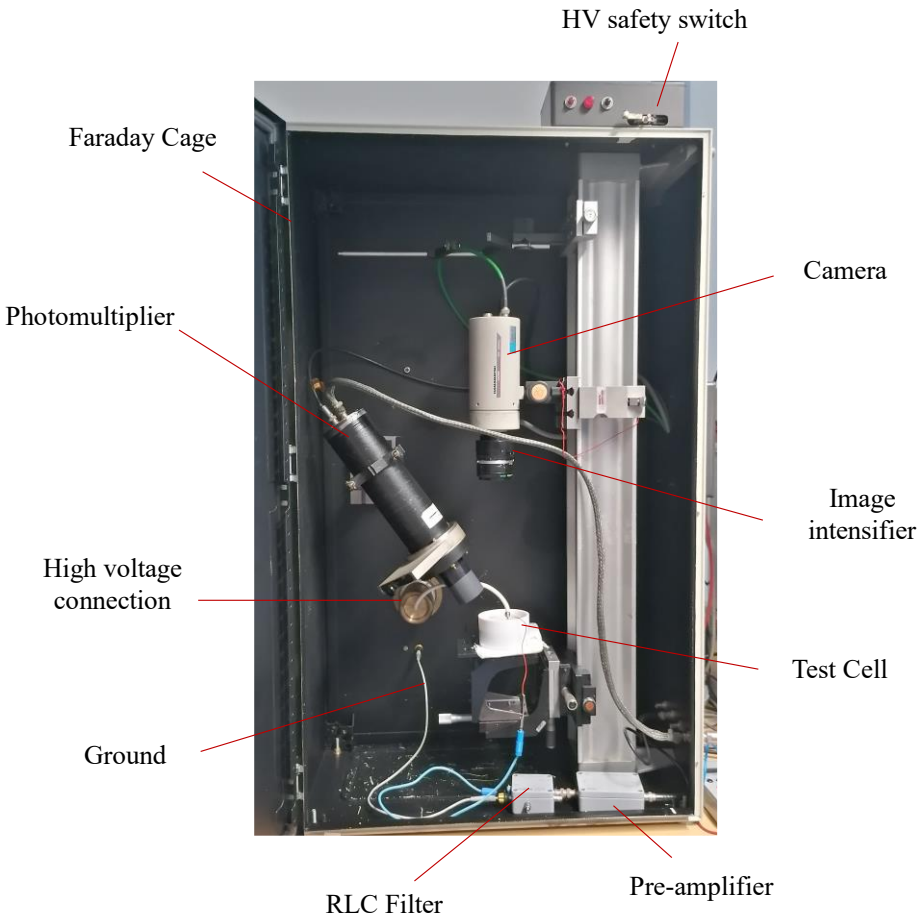

Fig 3.12. PD recording system

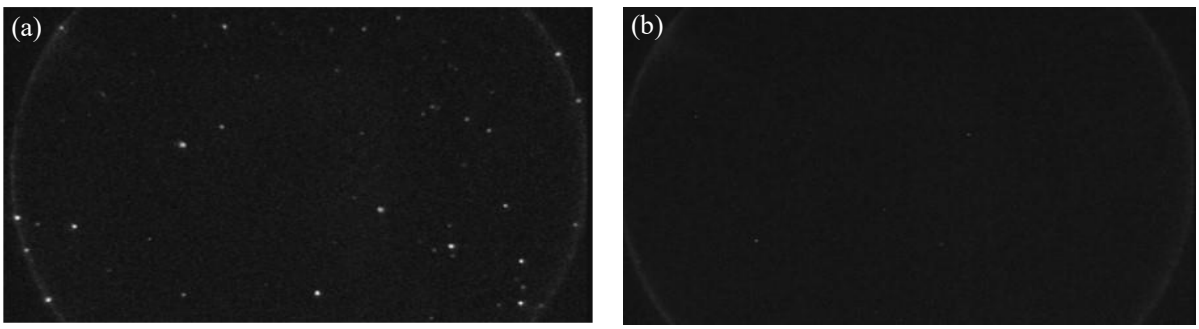

Fig 3.13. Background noise from CCD camera (a) Single image with random bright spots corresponding to noise (b) Average of 50 images eliminating the random background noise

3.2.2.6. **Optical PD intensity recording with photomultiplier (PM)**

Optical PD recording was made with a BURLE^{TM} 8575 photomultiplier. It consists of 51 mm diameter, 12-stage photomultiplier having a bialkali (K-Cs-Sb) photocathode, and pyrex faceplate [57]. Some key features of this PM are:

- Maximum average anode current : 200 µA
- Electron transit time : 37ns
- Anode pulse rise time : 2.8 ns
- Current amplification (gain) : 2.7 x 10^7
- Light responsivity wavelength : 200 nm to 700 nm
- Dark current (PM background noise) : 0.5 nA to 1.5 nA

A temporary increase in anode dark current (noise) by as much as 3 orders of magnitude may occur if the tube is exposed momentarily to high-intensity light from sources such as fluorescent room lighting even though voltage is not applied to the tube. Therefore, to keep a low noise current (typically below 1 nA), the PM was never exposed to direct light during all measurements, thanks to an optical shutter.

The light emitted by PDs or electroluminescence was measured in terms of photomultiplier signal U_{pm}. The PM constitutes a current source proportionnal to light intensity, and was connected to different impedances (*RC* parallel circuit), providing various trade-off between bandwidth and sensitivity. The measuring resistor, R = 0.5 MΩ comes from PM and oscilloscope internal resistors. With C = 400 nF, a long measurement time constant $\tau = R \times C$ = 0.2 s was obtained. This allowed integrating the PM current for a duration much longer than the voltage period (at 50 Hz), and obtaining the average current $I_{pm} = U_{pm}/R$ that provided the highest measurement sensitivity.

With no light entering the Faraday cage, I_{pm} shows a low-level background signal (about 1 nA) corresponding to the "dark current" (i.e., noise) of the PM, Fig 3.*14*. This background noise was measured when the Faraday cage was closed and when the PM is open and energized. This stable noise was subtracted from all I_{pm} measurements presented in this chapter. With C reduced to 0.6 nF (due to stray capacitances of PM, cables, and oscilloscope), the time constant reduces to τ = 300 µs, allowing to observe and compare the light emission occurring during positive and negative half waves of ac, as well as following rise and fall of impulses.

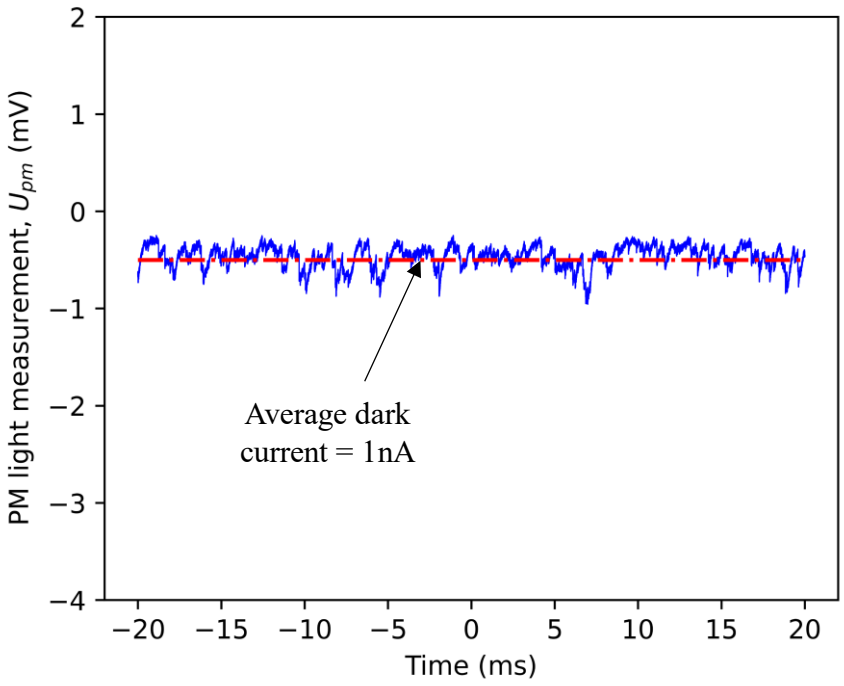

Fig 3.14.Background noise of PM BURLETM 8575 measured with oscilloscope for R = 0.5 MΩ and τ = 300 µs.

3.3. Measurements with Alumina substrates

The alumina substrate sample (54mm x 38mm) was etched to obtain two high voltage electrodes of 20 mm x 20 mm, Fig 3.15. Direct bonded copper (DBC) alumina substrate. Copper metallization, 300µm in thickness, was etched using perchloride. The thickness of the alumina substrate is 600µm. Only one electrode is used at a time while the other remains as a spare electrode in case of breakdown. A ground wire is soldered directly to the metallization on the backside of the sample.

From samples to samples, slightly different PD characteristics (inception voltage, PD amplitudes) may occur. Therefore, it was important to keep a single sample to check the relative influence of parameters such as voltage, frequency, encapsulant nature, etc. Thus, high voltage was limited to crest-to-crest value V_{cc} = 22.6 kV to ensure breakdown and destruction of a sample does not occur. Therefore, in the followings, all comparative results correspond to a single sample used for all sets of measurements.

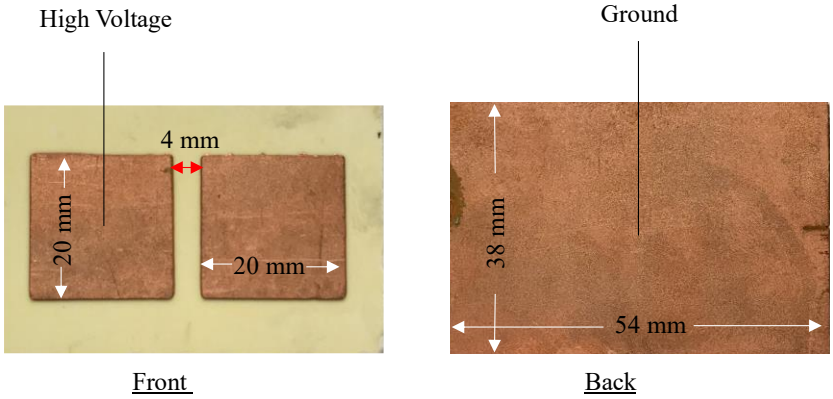

Fig 3.15. Direct bonded copper (DBC) alumina substrate

3.3.1. PD detection under AC

PD detection using both electrical and optical methods were made under AC with alumina substrate embedded in either DBT or silicone oil. The non-electroluminescent nature of alumina substrate is useful to evaluate the optical properties of DBT by making electrical PD measurement, optical light recording and camera observation simultaneously.

3.3.1.1. Measurements with silicone oil encapsulation

Sinusoidal AC voltage V_{AC} was varied from 0.5 kV to 8kV (rms) at 50Hz. Breakdown in substrate occurred at V_{AC} = 10kV (rms). The average PD current (I_{pd}) and number of PDs were recorded for duration of 60s. Six recordings were made for each voltage level. The variation of Ipd and number of PDs (mean of 6 recordings) can be seen in Fig 3.*16*. No PD activity was observed at voltages below 5 kV(rms). The partial discharge inception voltage (PDIV) was defined as the voltage producing 10 PDs during 1 minute. Although this definition is arbitrary, it allowed comparing different experiments on a reproducible statistical basis, considering the usually large scatter of PD measurements. In turn, this required doing a rather large number of experiments to obtain the plot of average PD number versus voltage (see Fig 3.*16*), with six recordings at each voltage level. Both I_{pd} and number of PDs increased exponentially with increasing voltage. In Fig 3.*16*, a PDIV of 5 kV was derived.

A typical PRPD recording can be seen in Fig 3.17. More PDs are seen during negative phase, and less PDs with larger magnitudes are observed during positive phase. Such asymmetry is typical for discharges occurring in liquids [25], due to different discharge process occurring in both polarities.

Optical light detection was made simultaneously with the electrical recoding. A typical time resolved light measurement is shown in Fig 3.*18*. On all recordings, light intensity indicated by the PM current appears as a negative signal, due to the PM wiring. Since both silicone oil and alumina are known to be non-electroluminescent, the light recorded by the PM originates from the PD activity. Light intensity is slightly higher during negative cycle than during positive cycle, showing a qualitative correlation with PRPD recordings. The phase position of PRPD and time resolved light measurements are also similar. Since PM current is recorded with a RC time constant τ = 300 µs, a single PD produces a pulse with fast rise followed by exponential decay with τ = 300 µs time constant. When numerous PDs occur, the recorded signal results from the overlapping of all pulses, and shows a large noise typical of the random character of PDs. The average PM signal is maximum around 90° and 270° phases, i.e. when the repetition frequency of PDs is maximum. Similar results were reported in [15].

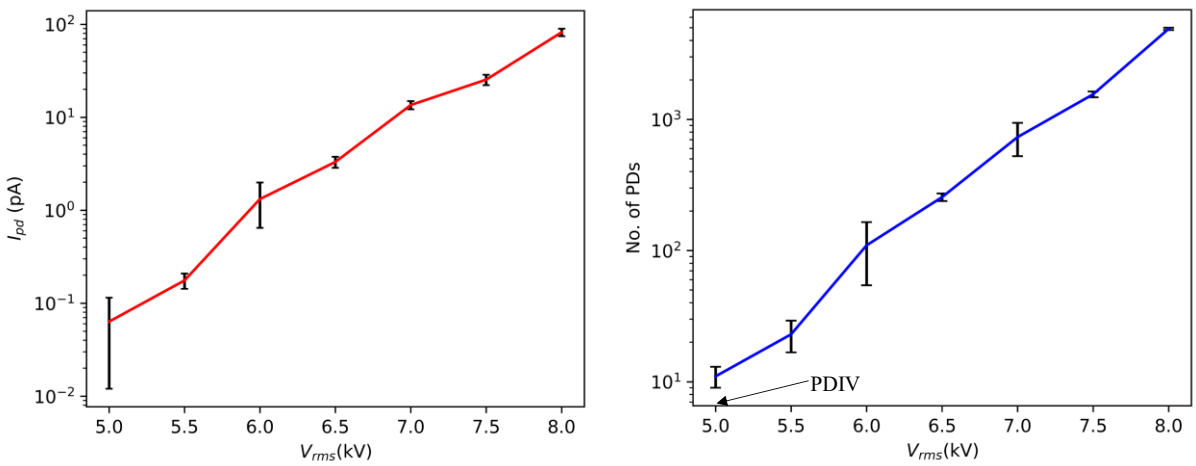

Fig 3.16. Average PD current and number of PDs in alumina substrate embedded in silicone oil at room temperature with recording duration of 60s.

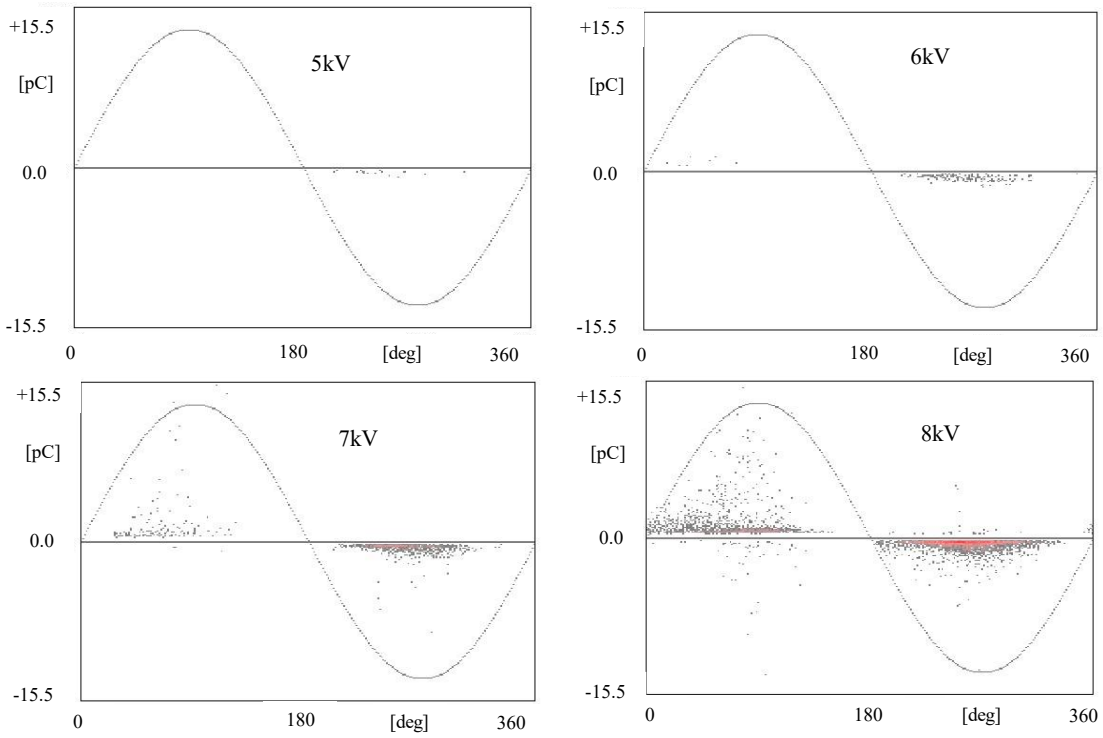

Fig 3.17. Phase resolved PD (PRPD) in alumina substrate embedded in silicone oil at 50Hz (voltage in rms) with recording duration of 60s.

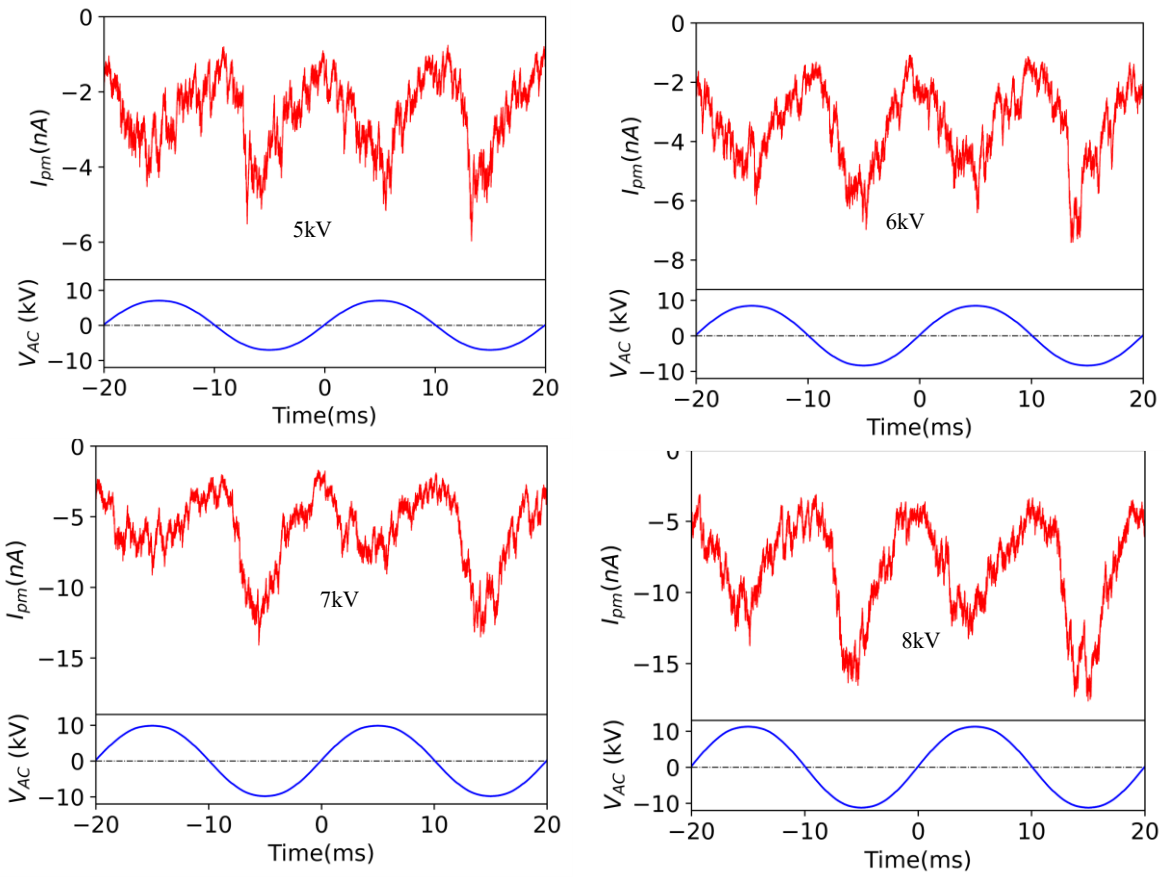

Fig 3.18. Typical time resolved light measurement (TRLM) in alumina substrate embedded in silicone oil at various voltage V_{AC} (rms), 50Hz, τ = 300 µs

3.3.1.2. Measurements with DBT encapsulation

Measurements with alumina substrate embedded in DBT showed rather different results. In marked contrast with silicone oil, PDIV with DBT was 7.5 kV (rms), with almost no PD activity detected at lower voltage. This shows that DBT provides much better PD suppression properties at 50 Hz than silicone oil. This observation agrees with the fact that liquids of similar chemical nature (such as Jarylec ™) were designed and used for the impregnation of power capacitors, in which a low PD level is essential for long-term reliability.

At 8 kV (rms), the PD pattern is constituted by PDs of very small amplitudes (maximum 1 pC) with a nearly symmetrical distribution, Fig 3.*20*. The large influence of liquid nature shows that PDs recorded with silicone oil mainly originated from the liquid. With DBT, the symmetrical distribution obtained at high voltage can be tentatively attributed to PDs occurring in the substrate pores (such as in previous measurements with AlN substrates), and not in the liquid. Indeed, such PD distribution is very different from those obtained in DBT alone with point-plane gap [17]: in this case, distributions showed high dissymmetry, with numerous small negative PDs, and very few large positives. We may therefore suppose that with DBT, PDs at 8 kV mainly originated from cavities existing within the substrate bulk (pores), due to the sintered nature of Alumina. Such PDs may also exist at high voltage with silicone oil, and contribute to PD recordings, in addition to PDs occurring in the liquid.

Measurements above 8 kV were avoided to limit the risk of substrate destruction by breakdown, and it was therefore not possible to obtain some evidence of PDs occurring in DBT.

With DBT, light emission also totally differs from silicone oil, see Fig 3.*19*. Strong light signal was detected for voltages as low as 2.5 kV, i.e. well below the PDIV with DBT. Strong light was detected during negative polarity, and almost no light during positive, while no PDs can be detected. Light recordings are much smoother compared to silicone oil, and do not show the noisy feature of PDs. This behaviour is typical for electroluminescence. PM current reached up to 4 µA @ 8 kV, whereas in silicone oil it remained lower than 20 nA, i.e. a 200x stronger light intensity due to electroluminescence compared to PDs. Unfortunately, it appears that DBT, that shows the best PD suppression properties (as suggested from 50 Hz measurements) cannot be used for optical PD detection, due to too high electroluminescence.

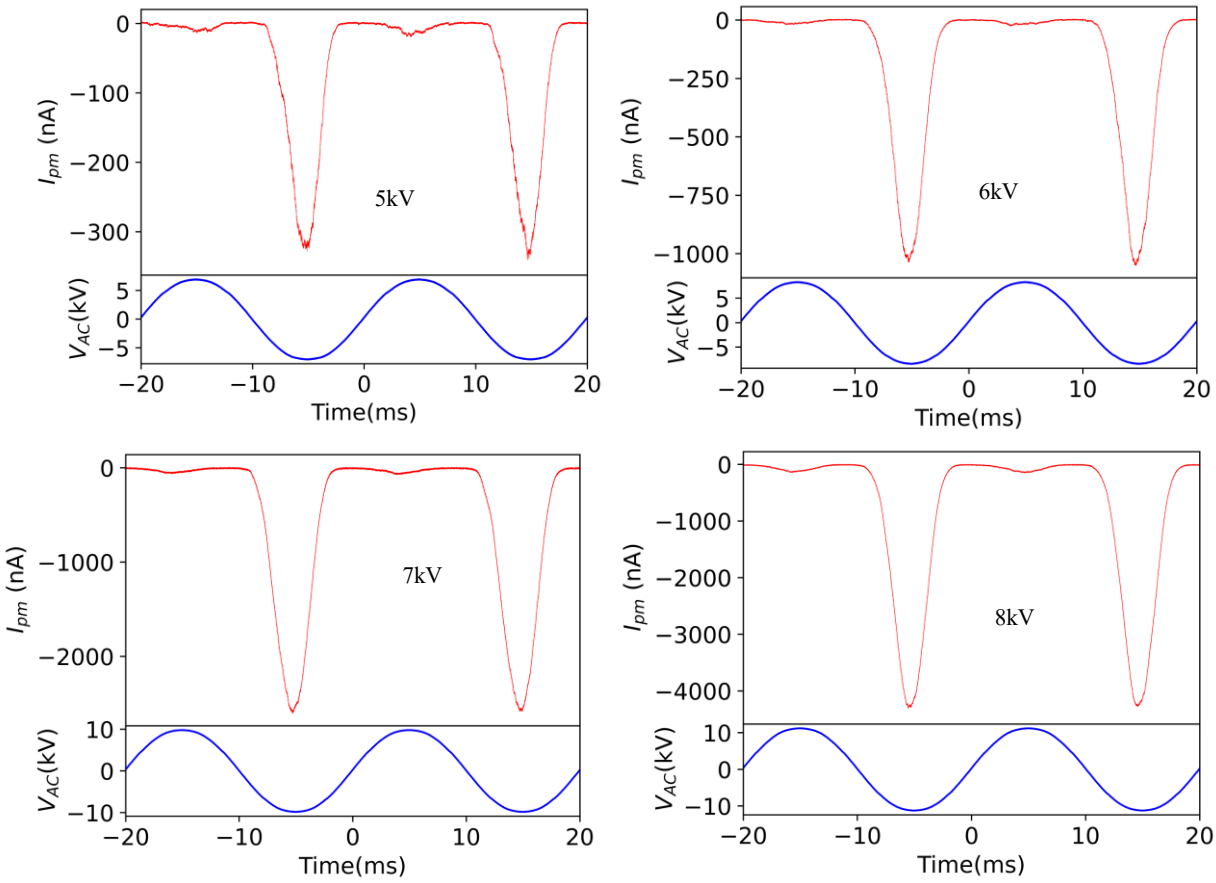

Fig 3.19. Time resolved light measurement (TRLM) in alumina substrate embedded in DBT at various voltage V_{AC} (rms), 50Hz, τ = 300 µs

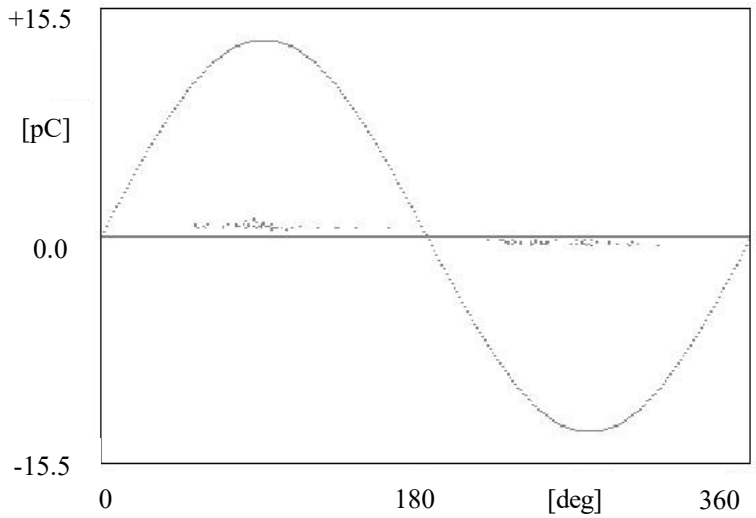

Fig 3.20. Phase resolved PD (PRPD) in alumina substrate embedded in DBT V_{AC} = 8kV (rms), 50Hz

3.3.1.3. Comparison of optical and electrical PD measurements with alumina substrate embedded in DBT and Silicone oil

If the light detected by the PM comes solely from PDs in the liquid, the average light intensity (I_{pm}) measured with a long time constant (τ= 0.2 s) can be compared to the average PD current (I_{pd}) recorded electrically. In the case of alumina embedded in silicone oil, the variation of I_{pd} and I_{pm} versus voltage show some qualitative correlation particularly at high voltages, Fig 3.*21*. At low voltages, and because of the difference in sensitivity between electrical and optical measurements, I_{pm} is detected at lower voltages than I_{pd}. In PD recordings, the minimum PD amplitudes correspond to the rejection threshold of measurements (0.3 pC), suggesting that many very small PDs with charge < 0.3 pC probably exist, but are not recorded and integrated in the calculated average I_{pd} current. This probably explains why the ratio between I_{pm} and I_{pd} changes at low voltage, with a relative larger light emission compared to PD recording. This also suggests that the calibration of light measurements in terms of PD amplitude (pC) would be hardly feasible, mainly due to experimental limitations induced by the very low amplitude of PDs, close to the limit of measurement capabilities (<< 1 pC).

On the other hand, in the case of alumina embedded in DBT, it is clear that under AC, the light detected by the PM comes from electroluminescence. Fig 3.21 shows the corresponding strong light emission, compared to the light due to PDs in silicone oil. When PD start occurring above 7.5 kV RMS with DBT (corresponding to 21 kVcc), no sudden increase of the light emission is observed, because light induced by PDs is negligible compared to that of electroluminescence. The images obtained with the sensitive intensified camera are shown in Fig 3.*22*. With silicone oil, weak discrete light spots are seen along the metallization edge, corresponding to several different PD locations. The number of spots increases with voltage. With DBT, much more luminous and numerous spots are seen, presumably corresponding to local metal defects (protrusions of µm size) where the field is further enhanced.

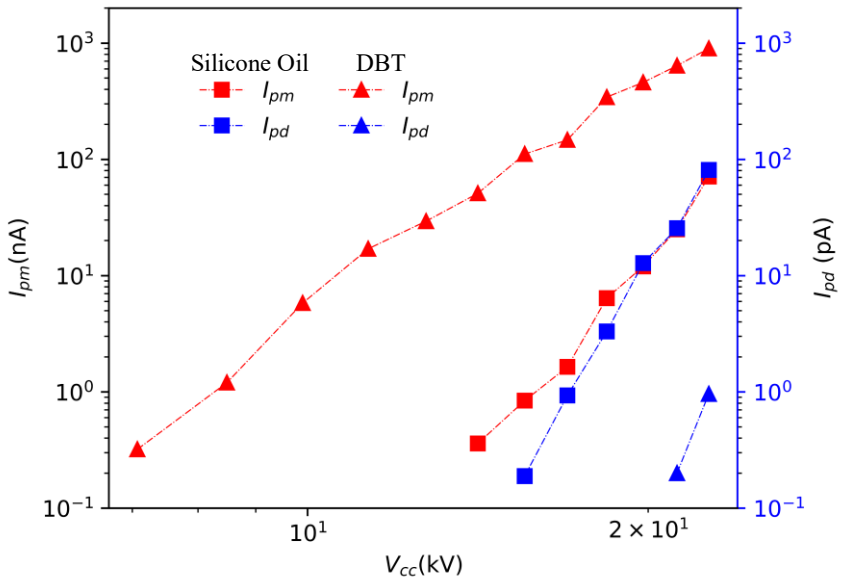

Fig 3.21. Comparison between average light measurement (Ipm at τ = 0.2s) and average PD current (Ipd)

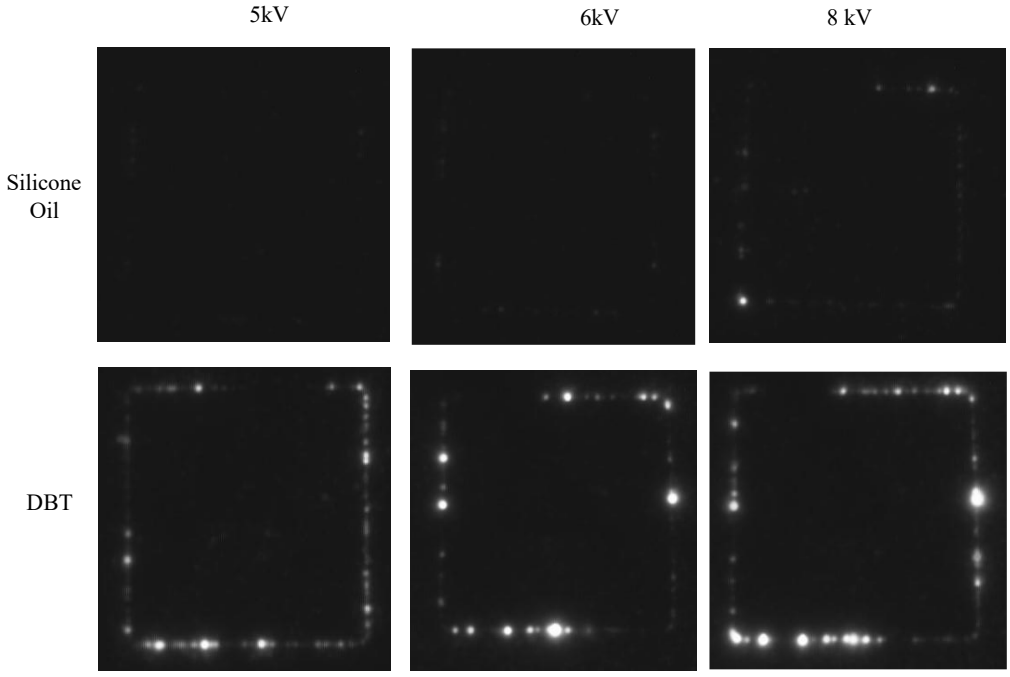

Fig 3.22. Light visualization using CCD camera at different voltage (rms) in alumina substrate embedded in DBT and Silicone oil

3.3.2. PD detection under impulse voltage with alumina substrate

Optical light detection and visualization were made under bipolar rectangular impulses with fast rise and fall time of 280 ns, and frequency of 50 Hz. Most of light was detected during a short time (<< ms) during rise or fall of the voltage, see Fig 3.23. This provides direct evidence that under impulse voltage, the high electric field inducing light emission (i.e. PD inception and/or electroluminescence) lasts only for a short time following voltage rise, and sharply drops afterwards, in qualitative agreement with calculations carried out in the previous chapter.

Time resolved optical light detection under bipolar impulse shows similar patterns in DBT and silicone oil, with larger instantaneous maximum intensity in DBT. In both liquids the maximum PM current recorded with the same circuit parameters (τ = 300 µs) is much larger under bipolar impulse compared to ac (Fig 3.18 and Fig 3.19). This increase is also larger in silicone oil compared to DBT:

- in silicone oil, the instantaneous PM current reaches 200 nA @ 10 kVcc, whereas it was close to the detection limit ($\approx$ 1 nA) under ac at the same crest to crest voltage. This indicates an intense PD activity immediately following the voltage rise (light is only due to PDs in this liquid). Peak PM currents are slightly higher in negative polarity such as under ac, and some scatter typical of PD phenomenon is also observed. In DBT, the maximum current reached was 800 nA @ 10 kVcc, compared to 100 nA under ac. In marked contrast with ac, light is now observed in positive polarity, although with lower maximum intensity compared to negative polarity.

When measured with a long time constant (τ = 0.2s), the average PM current Ipm in silicone oil (Fig 3.*24*) considerably increased as compared to ac: at 10 kVcc, Ipm raised to 40 nA with bipolar impulses, whereas it was not measurable (< 0.1 nA) under ac at the same voltage (Fig 3.*21*). In DBT, Ipm remained almost unchanged compared to ac, and average currents become now nearly comparable in both liquids, due to the marked increase in silicone oil. The light seen from CCD camera did not show significant difference in DBT and Silicone oil, Fig 3.25.

Under bipolar impulses, light due to PDs in silicon oil was detected at voltage as low as V_{cc} = 4kV (Fig.3.24), compared to PDIV = 14 kVcc (i.e. 5kVrms) under 50 Hz AC. This indicates that PDs occur at much lower voltage under impulse, due to the maximum electrostatic field occurring during fast rise and fall of the voltage. Consequently, experiments with bipolar impulses were limited to 10 kVcc to reduce sample degradation by numerous PDs.

The fact that light can be seen in DBT in positive polarity with bipolar impulses has no simple explanation. If this light is due to electroluminescence only, the fact that almost no light was observed under ac could be tentatively attributed to a larger reduction of maximum field under ac in this polarity. It is however not consistent with the general observation that electroluminescence previously reported in other liquids is always much lower in positive polarity. Another possible explanation could be that PDs now occur with DBT at reduced voltage compared to ac, in a similar way as in silicone oil. In that case, light under bipolar impulse in DBT may result from a combination of electroluminescence and PDs, that may explain the occurrence of light in positive polarity. However, since PDs with Alumina substrates can also originate from the substrate itself due to porous structure (producing the symmetrical PRPD pattern under ac, Fig 3.*20*), it is difficult to obtain a clear conclusion. However, it is obvious that PD inception in DBT should be reduced under impulse, such as in silicone oil.

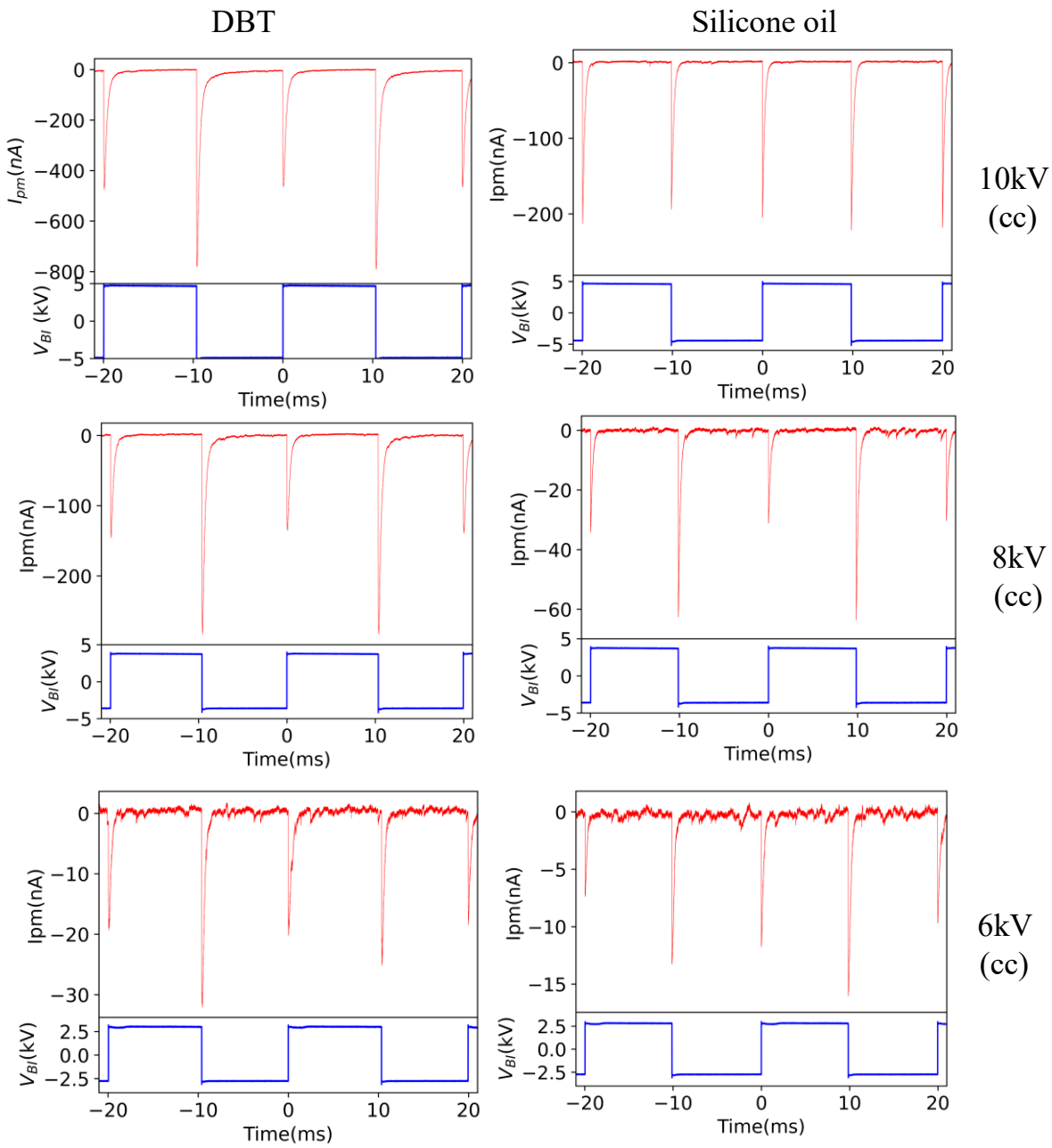

Fig 3.23. PM time resolved light measurement (TRLM) under various bipolar impulse voltage V_{BI} (cc) rise time t_r = 280 ns and integration time constant τ = 300μs with alumina substrate embedded in DBT and silicone oil.

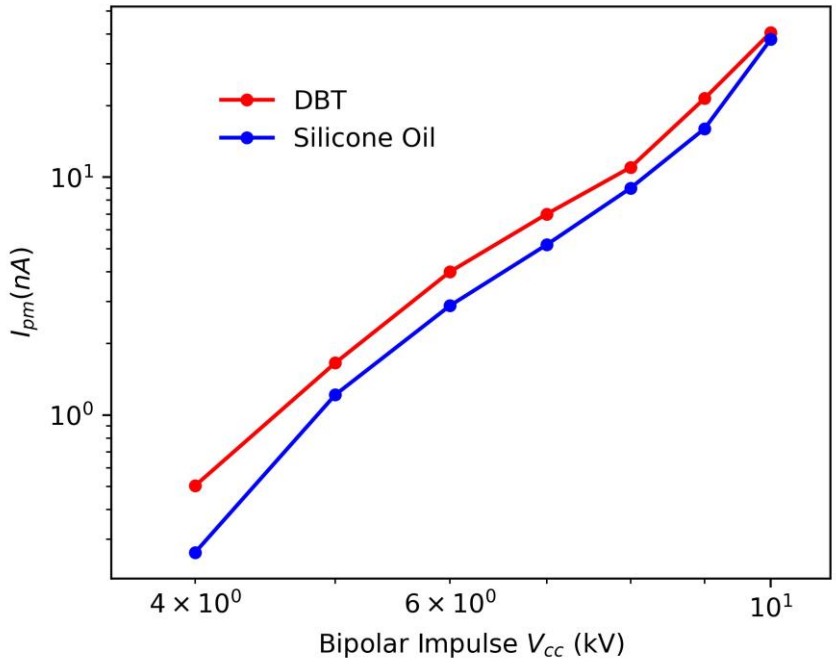

Fig 3.24. Average PM light measurement (Ipm) under bipolar impulse voltage with alumina substrate embedded in DBT or silicone oil ($\tau = 0.2s$)

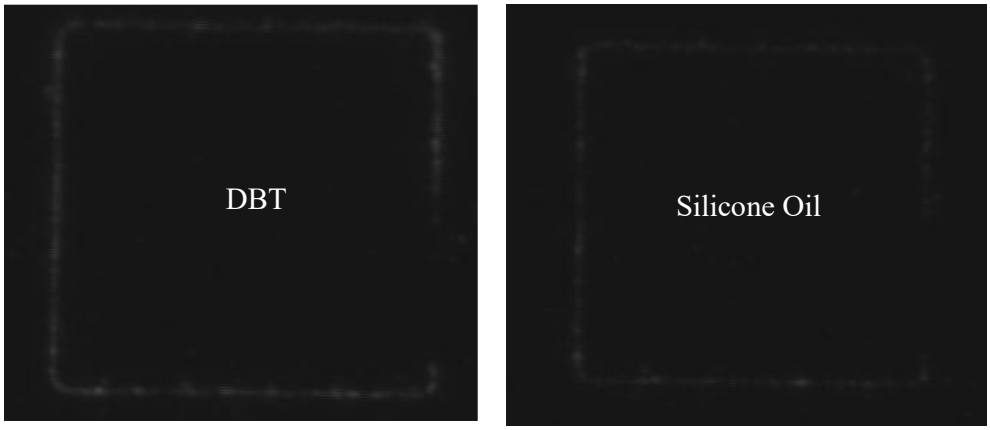

Fig 3.25. Light visualization using camera in alumina substrate embedded in DBT and Silicone oil under bipolar impulse voltage

3.4. **Measurement with Silicon nitride substrates**

Single-layer and double-layer Si_3N_4 ceramic substrates were used for PD studies. These industrial substrate samples manufactured by Kyocera for power module packaging were obtained from Safran Company, which is greatly acknowledged. These substrates are particularly interesting for high temperature and high voltage power module applications, because of their high mechanical strength, thermal conductivity and breakdown strength (see table 3.2). However, information about optical or electrical PD detection with these substrates embedded in liquid were not available prior to this study.

The single-layer Si_3N_4 ceramic substrate, 300µm in thickness, has a rectangular copper top metallization (20 x 44 mm^2, 0.3 mm thick) with a thin layer of silver connected to the high voltage, see Fig 3.*26*. The lower copper metallization (60 x 68 mm^2, 0.3 mm thick) was used as ground electrode as shown in Fig.3.25. The double layer Si_3N_4 substrate has two square copper

top metallization (18 x 18 mm^2, 0.3 mm thick), see Fig 3.*26*. Only one top electrode connected to high voltage was used for all measurements presented here, in order to be able to properly compare results obtained in different conditions without changing the substrate. The lower copper metallization (26 x 54 mm^2, 0.3 mm thick) is grounded as shown in Fig 3.*26*. The substrate includes two Si_3N_4 layers of equal thickness (0.32 mm) in series, with an intermediate copper electrode (thickness 0.6 mm). During measurements, this intermediate electrode, as well as other electrodes, were floating. Considering the capacitances between lower, intermediate, and upper electrode, the intermediate electrode potential was 24 % of applied voltage.

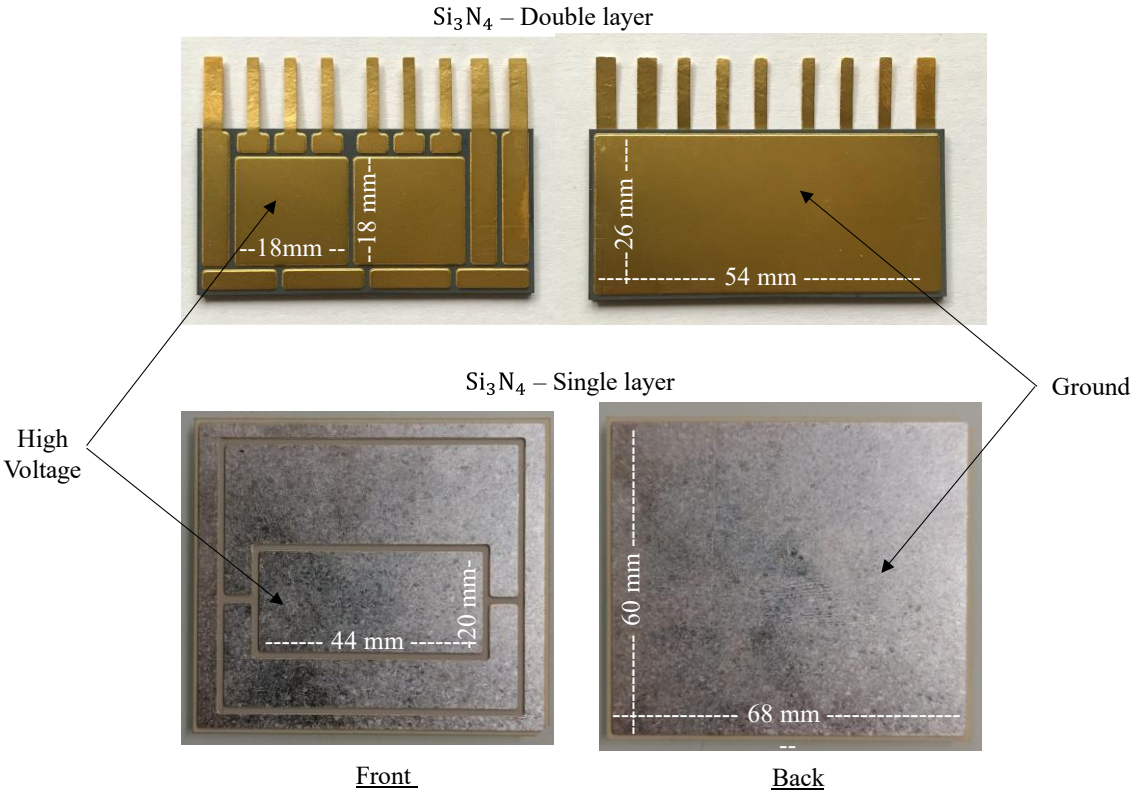

Fig 3.26. Silicon nitride substrate samples

3.4.1. Measurements under AC in Si_3N_4 substrate embedded in silicone oil or in DBT

3.4.1.1. Electrical PD detection

PD measurements were made with both Silicone oil and DBT using double and single layer Si_3N_4 substrates. With Silicone oil, the PDIV, defined by the occurrence of more than 10 PD's during 1 minute, was around 3 kV_{rms} when double layer sample was used, see Fig 3.*27*. The PDIV with single layer was reduced to 2kVrms. This variation is consistent with the different structures of samples: at PDIV, the average mean field in the upper ceramic of double layer substrate is 7.1 kV/mm, and nearly identical (6.7 kV/mm) in the single layer. These values are slightly lower than those calculated at PDIV with Alumina and silicone oil: 7.9 kV/mm. At 5 kVrms, breakdown of the Si_3N_4 ceramic occurred in the single layer substrate (corresponding to an average breakdown field of 16.7 kV/mm for Si_3N_4), therefore measurements were limited to 4 kVrms with this single layer substrate. Both PDs number and average PD current were logically higher in the single layer silicone nitride substrate compared to the double layer substrate, see Fig 3.27 and Fig 3.28.

With DBT, no PDs were detected when voltage was increased up to twice the PDIV recorded with silicon oil (i.e. 6 kV_{rms} with double layer sample, and 4.5kVrms with the single layer substrate sample). With a further increase in voltage, the substrate was permanently damaged due to breakdown of the ceramic. Therefore, no PD measurements under AC could be made with DBT. This confirms that DBT provides much better PD suppression than silicone oil with Si_3N_4 substrate under 50 Hz AC, such as previously observed with Alumina.

The large influence of the liquid nature indicates that partial discharges actually originate from the liquid, and not from the substrate itself, contrary to previous similar measurements carried out with other ceramics (AlN) [31]. Typical PRPD recordings in silicone oil with both samples are shown in Fig 3.*29*. More PDs occur in negative polarity, in agreement with typical PD recording carried out in silicone oil with point-plane electrode system [32]. In contrast, quasi symetrical PRPDs were obtained with AlN ceramic substrate [33]. This further confirms the hypothesis that PDs originate from the silicone oil when Si_3N_4 substrate is used. Contrary to Alumina, no PDs could be recorded with DBT, even when the voltage was raised up to breakdown of the ceramics. This indicates that no PD occurred within the Si_3N_4 ceramic material, contrary to Alumina and AlN.

To summarize, it appears from these measurements that the PD behaviour under 50 Hz AC of different substrate material embedded in liquids widely differs according to the materials used:

- AlN: PDs first occur within the ceramic bulk [31] (symmetrical PRPD, insensitive to liquid or gel nature), and possibly in the liquid at about twice higher voltage;
- Alumina: PDs first occur in the liquid (asymmetric PRPD in silicone oil, highly sensitive to liquid nature), and possibly in the ceramic bulk at high voltage (measurements with DBT);
- Si_3N_4: PDs first occur in the liquid (asymmetric PRPD in silicone oil, highly sensitive to liquid nature), no evidence of PDs in the ceramics up to breakdown.

In both cases where PDs first occur in the liquid (Alumina and Si_3N_4 with silicone oil), DBT shows very good PD suppression properties, by nearly eliminating PDs.

The combination of Si_3N_4 and silicone oil is interesting for better understanding PD processes, since PD measurements reflect the properties of the encapsulant only. Fig 3.*30* shows the average PM current (I_{pm}) and the average PD current (I_{pd}) measured with silicone oil. Although I_{pm} and I_{pd} show some correlation at high voltage, some very low-level light ($\sim 0.1\ nA$) is still recorded at voltages below PDIV. Assuming that both silicone oil and Si_3N_4 substrate show no electroluminescence, the light recorded below PDIV probably comes from low amplitude PD's (< 0.3 pC), not detected with electrical measurements. A similar result was observed with Al_2O_3 embedded in silicone oil in previous section (Fig 3.21). Since the maximum PD charge shows no marked increase with voltage, the increase of both I_{pm} and I_{pd} versus voltage is mainly attributable to the increase in PD number.

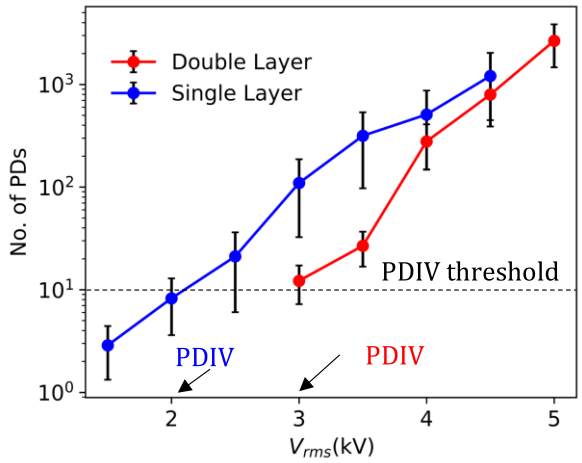

Fig 3.27. PD number (during 60s) vs applied AC voltage (50Hz) in Si_3N_4 substrates embedded in silicone oil

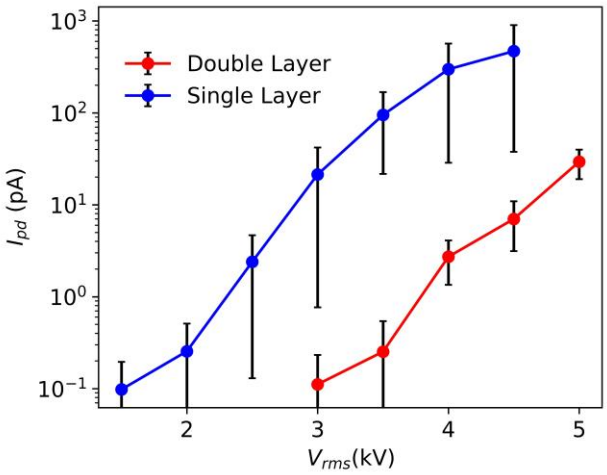

Fig 3.28. Variation of average PD current vs applied AC (50Hz) voltage in Si_3N_4 substrate embedded in silicone oil

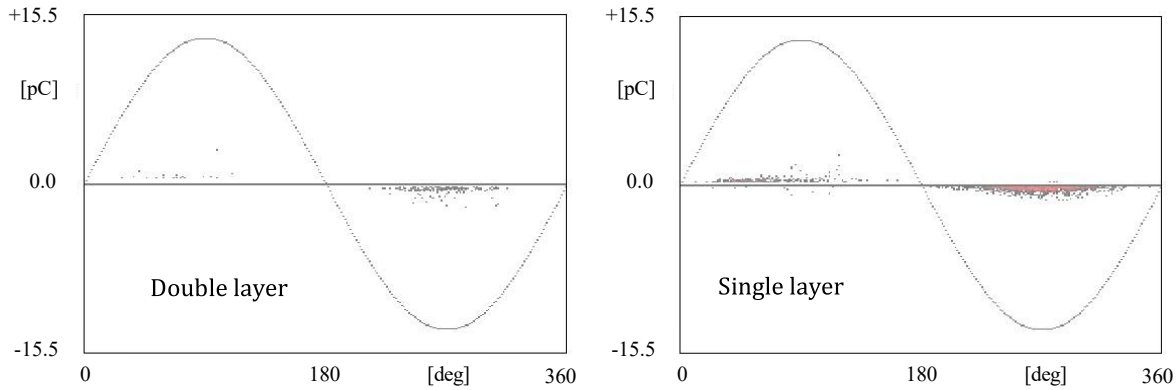

Fig 3.29. Typical PRPD recording with Si_3N_4 substrate (5kVrms with double layer and 4.5kVrms with single layer, 50Hz) embedded in silicone during 60s.

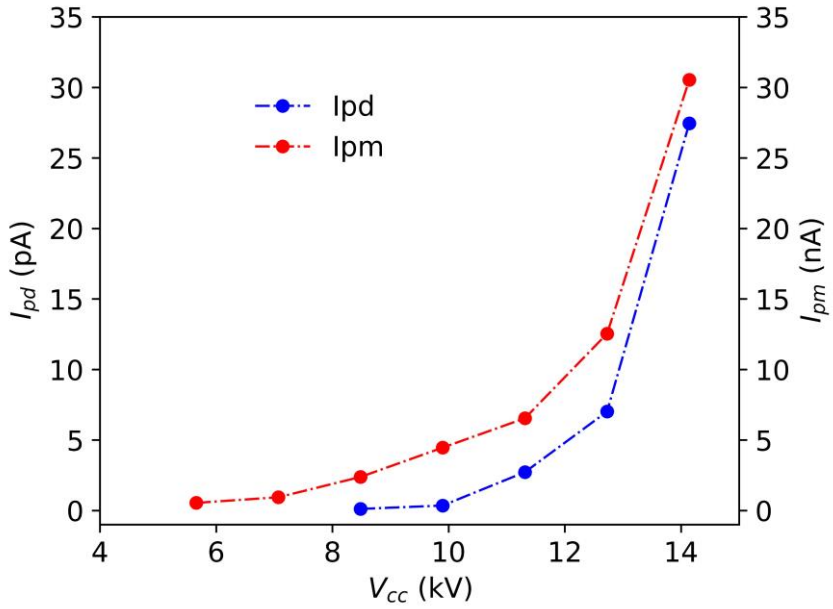

Fig 3.30. Ipm (τ = 2s) and Ipd measured at 50 Hz AC in Si_3N_4 substrate (double layer) embedded in silicone oil

3.4.1.2. Time resolved light measurement and camera visualization with Si_3N_4 substrate embedded either in DBT or silicone oil

The time resolved light measurement (τ = 300 µs) in Silicone oil (Fig 3.*31*) shows higher light intensity in negative polarity, in agreement with PD recordings (Fig 3.*29*). Recordings also show 'spikes' around the maximum intensity, related to PDs. In DBT, light due to electroluminescence mainly occurs in negative polarity, and is considerably larger (about 20 times at 5 kV_{rms}) than in silicone oil. The trace is smoother than in Silicone oil, in agreement with the absence of PD activity.

Very low light level, evenly distributed along the electrode edge is recorded with the camera in silicone oil (Fig 3.32). The even light distribution indicates that PDs equally occur at different locations. In DBT, images show bright light intensity concentrated at several spots, probably indicating the presence of "defects" where the field is enhanced, inducing electroluminescence.

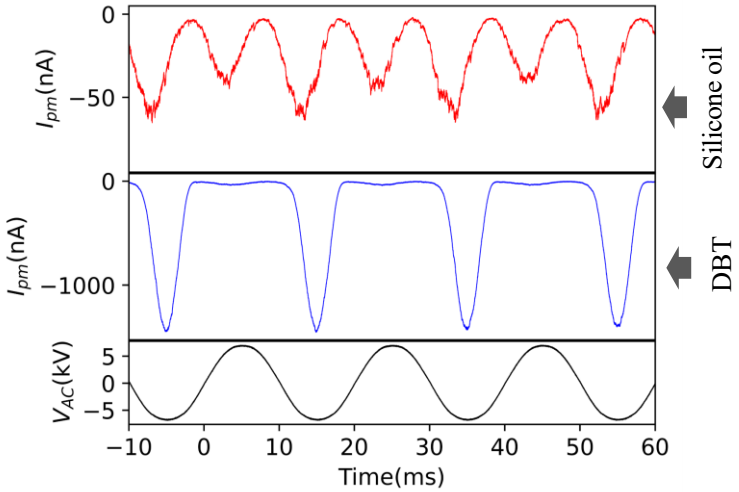

Fig 3.31. Time resolved light measurement of Ipm with Si3N4 (double layer) at 50Hz AC in silicone oil and DBT at 5kVrms ($\tau = 300\mu s$)

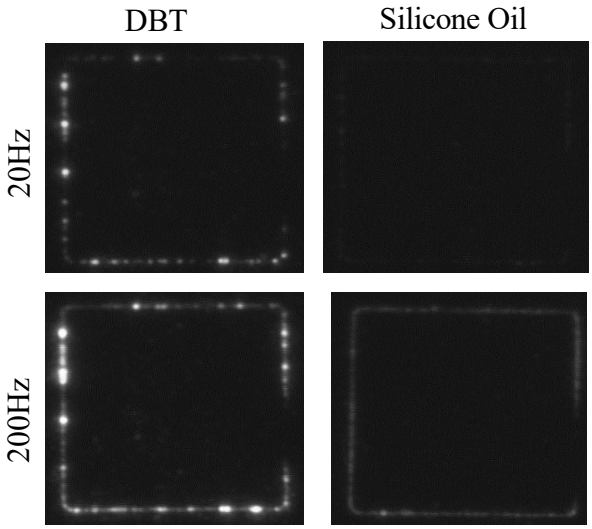

Fig 3.32. Light visualization in Silicone Oil and DBT with Si3N4 Substrate (double layer) at 5kVrms, 50Hz

3.4.1.3. PD detection under AC at different frequencies

Influence of ac voltage frequency f (20Hz, 50Hz, 100Hz, 200Hz) on PD activity in silicone oil was evaluated at fixed voltage (5kVrms) with double layer Si_3N_4 substrate. The PD count (number of recorded PD's/minute) at fixed voltage shows that more PDs are recorded in negative polarity. The PD number rapidly increases versus frequency as shown in Table 3. *4*. No variation of PDIV and typical maximum PD charge were observed at various frequencies. However, an important drawback on such measurement must be pointed: from the recorded PD distributions (Fig 3. *33*), it is clear that many PD's with amplitudes lower than the detection threshold (0.3 pC) do exist, but are ignored in recordings. Therefore, the total PD number is probably underestimated.

With silicone oil, an increase of I_{pm} versus frequency f and voltage can be observed (Fig 3.*36*). I_{pm} shows an exponential increase versus voltage V, and is roughly proportional to frequency f at fixed voltage. Such variation is consistent with an increase of PD number proportional to frequency, i.e. a feature frequently observed in PD measurements (e.g., in cavities). In DBT, where no PDs are recorded, I_{pm} due to liquid electroluminescence increases

much more rapidly with AC voltage, and is not any more proportional to frequency (at high voltage Ipm is nearly doubled when frequency increases from 20 to 200 Hz). These different variations versus voltage and frequency evidence that different physical processes are involved in light emission.

At low voltage (3 kVcc) the light intensity due to electroluminescence in DBT is nearly identical to that due to PDs in silicone oil, and more than 10 times larger at 7 kVcc.

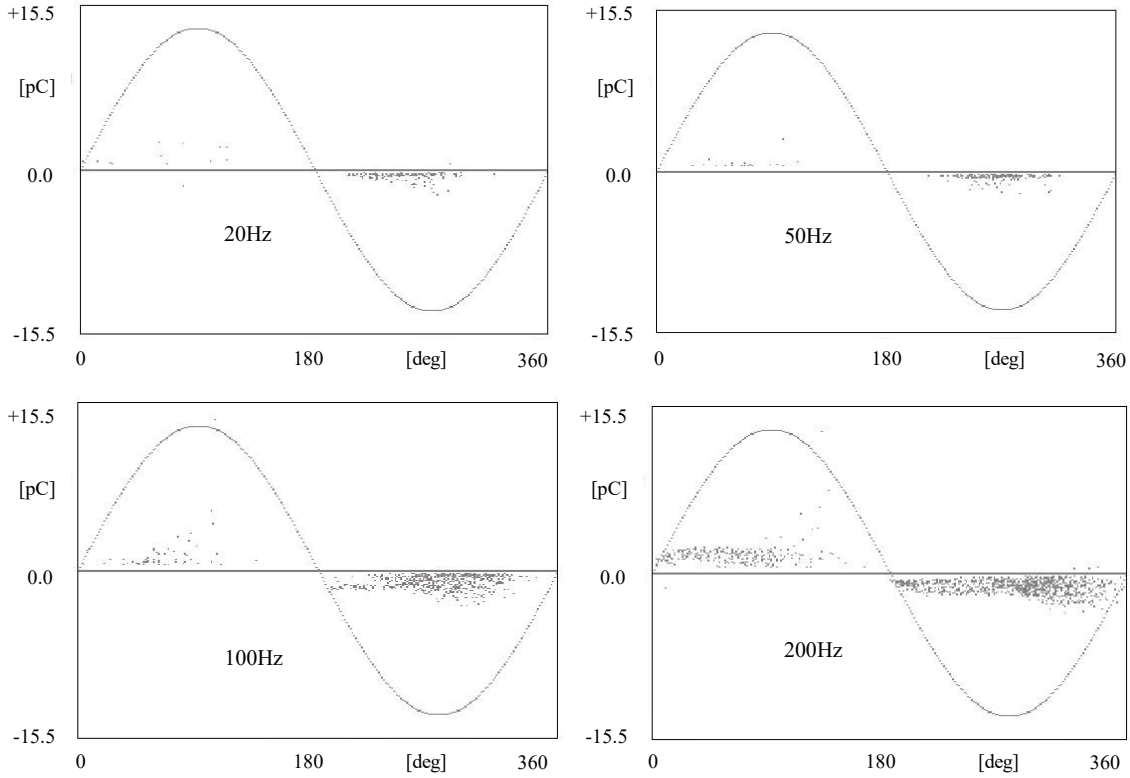

Fig 3. 33. Typical PRPD recording with silicon nitride (double layer) substrate embedded in silicone oil at V_{AC} = 5kVrms at different frequencies.

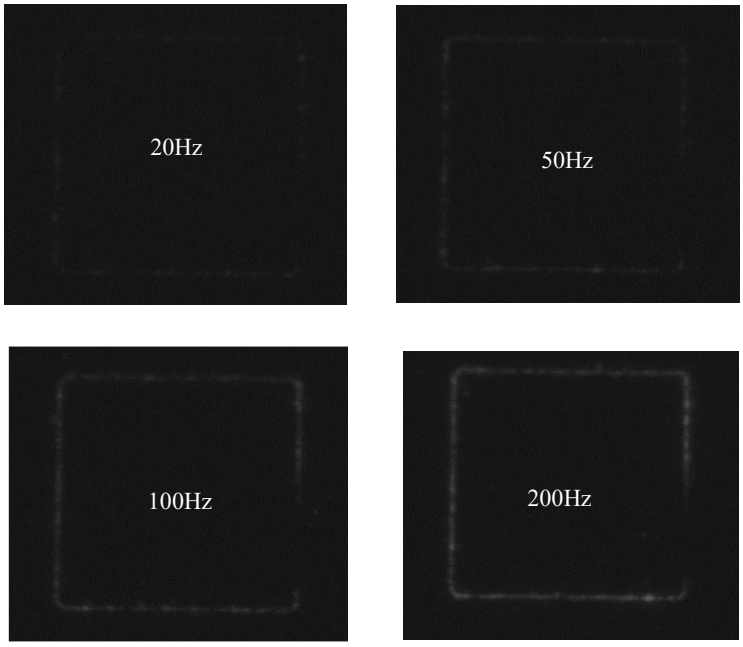

Fig 3.34. Light visualization using CCD camera under V_{AC} of 5kVrms with Si3N4(double layer) substrate embedded in silicone oil

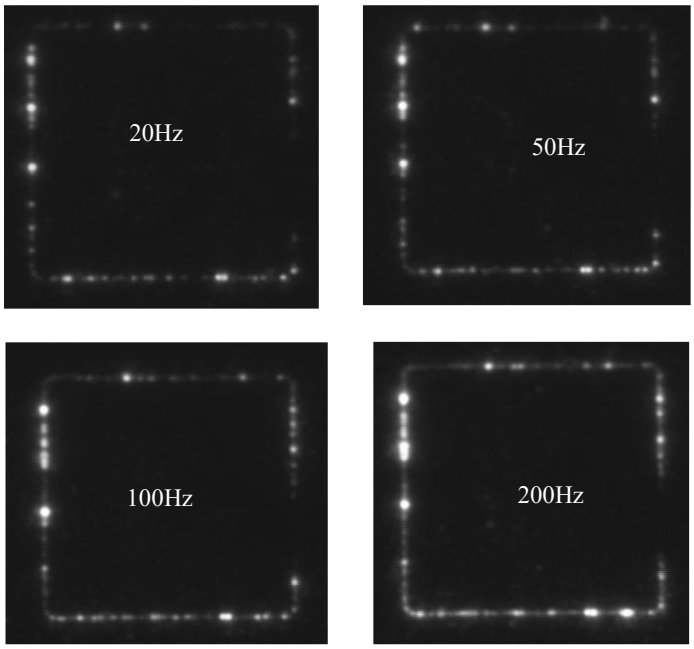

Fig 3. 35. Light visualization using CCD camera under V_{AC} of 5kVrms with Si3N4 (double layer) substrate embedded in DBT

Table 3. 4. Variation of PD number and PD current vs frequency at 5kVrms using double layer Si_3N_4 sample embedded in silicone oil

Frequency (Hz)	No. of PDs		Ipd (pA)
	Negative	Positive	
20	148	13	1.982
50	189	18	2.235
100	596	51	12.4
200	944	267	28.74

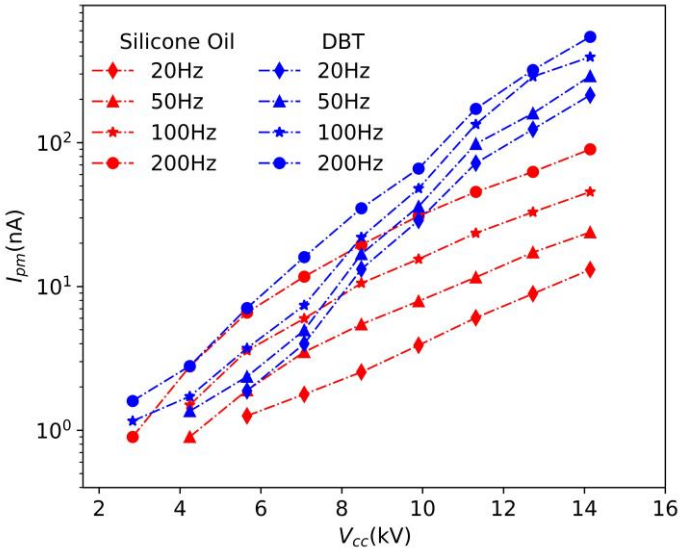

Fig 3.36. Ipm (τ = 0.2 s) measured at different AC frequencies in Si3N4 substrate (double layer) embedded in silicone oil and DBT

3.4.2. PD detection under bipolar impulse voltages

3.4.2.1. Typical light detection in double layer Si_3N_4 substrate embedded in silicone oil and DBT

Optical light detection under fast rising bipolar impulse voltage (risetime: 280 ns) shows a similar TRLM pattern with both DBT and silicone *oil* (Fig 3. 37), characterized by a high amplitude light peak during voltage rise and fall. This is in agreement with measurements obtained with Alumina, showing a similar contrast to what was observed under AC (Fig 3.31), where most of light was detected during negative voltage only with DBT, and lower light emission in silicone oil (at 7 kVcc 50Hz, Ipm under bipolar impulse was about 20 nA, compared to 3 nA under ac). As with Alumina, no large difference is observed between DBT and silicone oil on average PM light detection (Fig 3. 37) and light visualization using CCD camera (Fig 3.38).

As with Alumina, the occurrence of light emission in positive polarity in DBT with fast rise impulse voltage, suggests that the light detected in this liquid may correspond to PDs superimposed to electroluminescence.

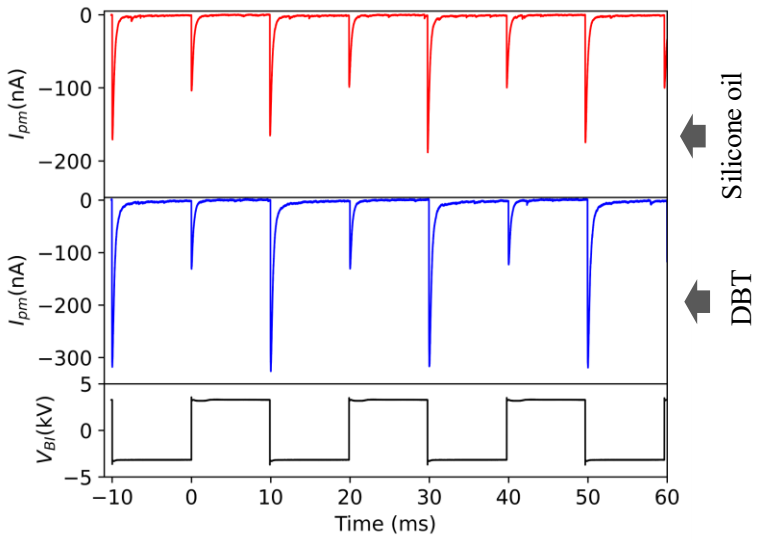

Fig 3. 37. TRLM with Si3N4 (double layer) under 50Hz bipolar impulse voltage V_{BI} = 6 kV (cc) in silicone oil and DBT at R = 0.5 MΩ , τ = 300 µs and t_r = 280 ns

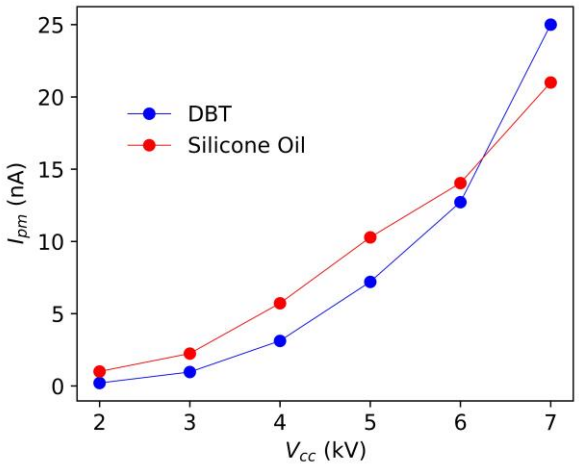

Fig 3.38. Average Ipm with Si3N4 (double layer) under 50Hz bipolar impulse voltage R = 0.5 MΩ , τ = 0.2s and t_r = 280 ns

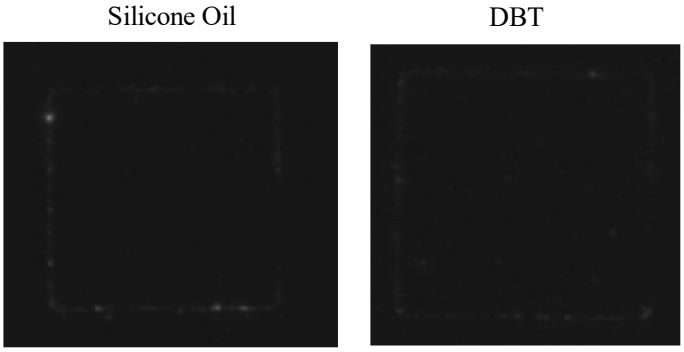

Fig 3.39. Light visualization in Silicone Oil and DBT with Si3N4 Substrate (double layer) under bipolar impulse voltage VBI = 6 kV (cc), average of 50 images, total exposure time 2s

3.4.2.2. Influence of frequency on light intensities under bipolar impulse and AC voltages

Light detection was made at frequencies ranging from 20Hz to 200Hz under bipolar impulse and AC voltages, for double layer Si_3N_4 embedded in silicone oil and in DBT. The variation of integrated light under AC or Impulse voltage with frequency at 7kV (cc) can be seen in Fig 3.*40*. Since silicone oil and Si_3N_4 are non-electroluminescent materials, the light detected corresponds to PD activity.

Fig 3.*41* (a) show average light intensities at different frequencies measured with silicone oil. Light intensity is much higher under impulse voltage than AC, indicating higher PD activity due to high field enhancement resulting from high slew rate 'dV/dt'. On average, light emission under ac is proportional to frequency (Ipm increases by a factor of 10 between 20 and 200 Hz), but lower under impulse (factor ≈ 3 between 20 and 200 Hz).

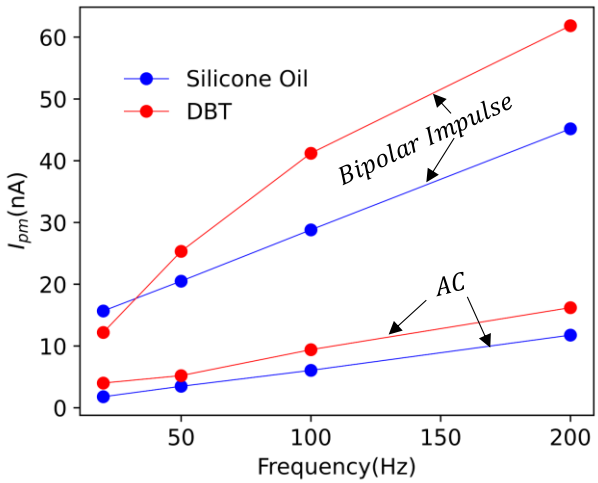

Fig 3.40. Variation of total integrated light Ipm vs frequency under at $V_{BI} = V_{AC} = 7kVcc$, with Si3N4 (double layer) embedded in DBT or silicone oil

Light detection at different frequencies with DBT can be seen in Fig 3.*41* (b). The I_{pm} measured under impulse voltage is comparable to the case of silicone oil. However, it is unclear if the light in this liquid comes from PDs, electroluminescence, or both. Therefore, further measurements described in the following sections were made only using silicone oil with Si_3N_4 substrate, with the view to better evaluate the influence of space charge on PD activity.

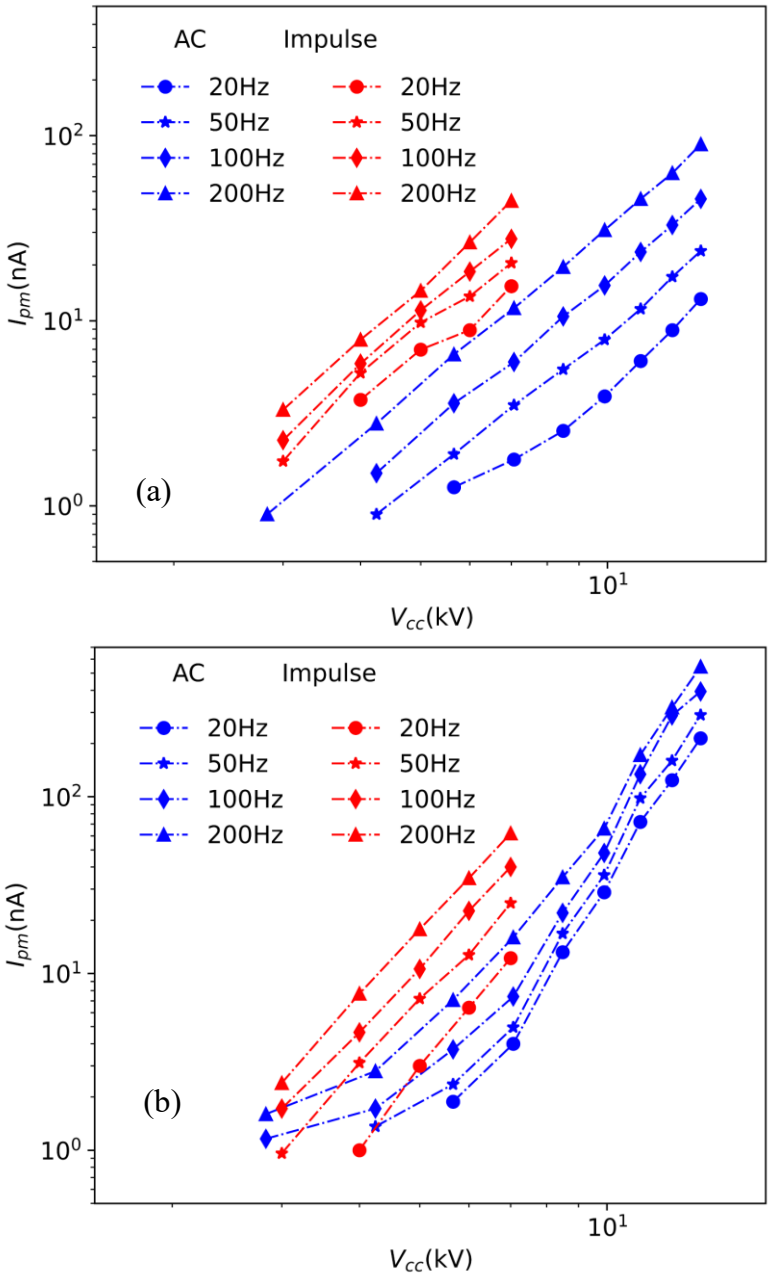

Fig 3.41. Comparison of average PM light Ipm (τ = 0.2 s) measured under AC and bipolar impulse at different frequencies in Si3N4 substrate (double layer) embedded in (a) silicone oil and (b) DBT

3.4.3. Influence of impulse voltage rise time on PD activity

In order to better understand the differences between PD inception in the encapsulant material under ac and impulses with fast rise, a study was carried out using optical detection under impulse voltage with single layer Si_3N_4 substrate, and silicone oil. The rise and fall times t_r of symmetrical bipolar impulse voltage (Fig 3.42) was increased by adding resistors in series with the test cell (refer Fig 3.9 for location of the resistor). The rise time obtained increased from 280 ns to 2.85 ms according to the resistor used:

- No resistor added → risetime: 280 ns
- 40 kΩ → risetime: 7.5 µs
- 1.5 MΩ → risetime: 135 µs
- 10 MΩ → risetime: 2.85 ms

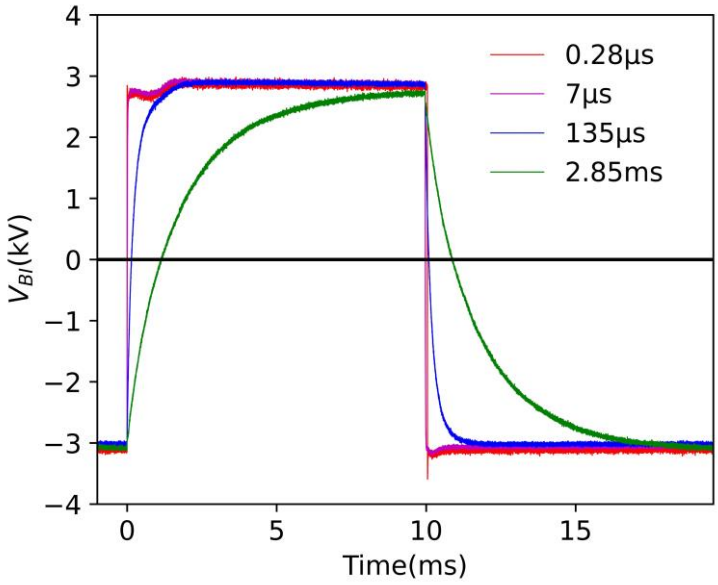

Fig 3.42. Bipolar impulse (V_{BI}) voltage signal with different rise times

Direct observation using CCD camera (Fig 3.*43*) and time resolved light measurement with PM (Fig 3.*44*) were done at different impulse voltage rise times. It was observed that the maximum light intensity recorded significantly decreased with increased rise time. At tr = 2.85ms, the time-resolved light peaks intensity reduced by 3 orders of magnitude compared to t_r = 0.28µs, while their duration increased. Typically, PD light emission was observed during rise of voltage, and nearly stopped during the voltage plateau.

With fixed impulse frequency (f = 50 Hz) and voltage, a large increase in average PM current I_{pm} (measured with τ = 0.2 s) was observed for shorter rise time (i.e., higher dV/dt), see Fig 3.*45*. With t_r = 2.85 ms, light emission was quite close to that recoded with sinusoidal AC, see Fig 3.*45*. Compared to sinusoidal AC, the voltage required to induce a similar average light emission (and hence PD activity) with fast risetime impulses is nearly divided by two, i.e. a very large impact. Low-level light measurements were limited by the PM noise to about $I_{pm} \approx 1$ nA. With short rise time impulses, light could be detected above about 1.5 kV_{cc}, instead of 4.2 kV_{cc} under 50 Hz AC.

The large impact of rise time on PD activity can be attributed to the influence of space charge injection into the liquid, from the high field area along the metallization edge. With fast dV/dt, time is too short for injected ions to propagate and attenuate the maximum field at the electrode edge. Considering a typical ion mobility µ of 10^{-7} m^2/Vs in DBT (deduced from Space Charge Limited Currents in point-plane gaps), and a maximum electrostatic field E of 2.10^7 V/m (calculated with 1 kV applied voltage), a maximum ion velocity $\mu.E \approx 2$ m/s can be estimated. After a short risetime (280 ns) the ion propagation length should be lower than 0.5 µm, i.e. a quite low distance compared to typical electrode dimensions. With longer risetimes, the space-charge zone will increase accordingly, and the limitation of the maximum field will occur and reduce PD activity. Similar effects of pulse risetime were previously observed in various liquids with point-plane gap [32]. This influence of space charge accumulation in front of the electrode will be further documented in next sections, by checking the influence of a DC prestress added to impulses, and by checking the influence of pulse repetition frequency.

An important practical conclusion is that PD activity considerably increases when large dV/dt impulses are involved, which corresponds to practical situations existing in power modules during switching. It appears that classical PD measurements carried out under 50 Hz AC tend to overestimate the PDIV, and underestimate the PD activity as compared to fast impulses.

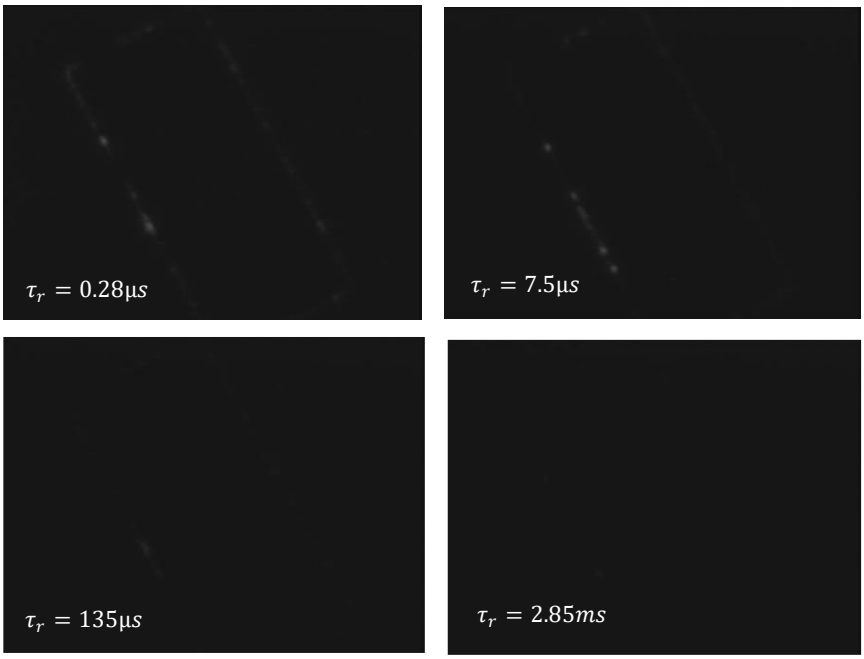

Fig 3.43. CCD camera observation of light under V_{BI} at 6kV(cc) with Si_3N_4 substrate (single layer) embedded in silicone oil at different rise time (t_r)

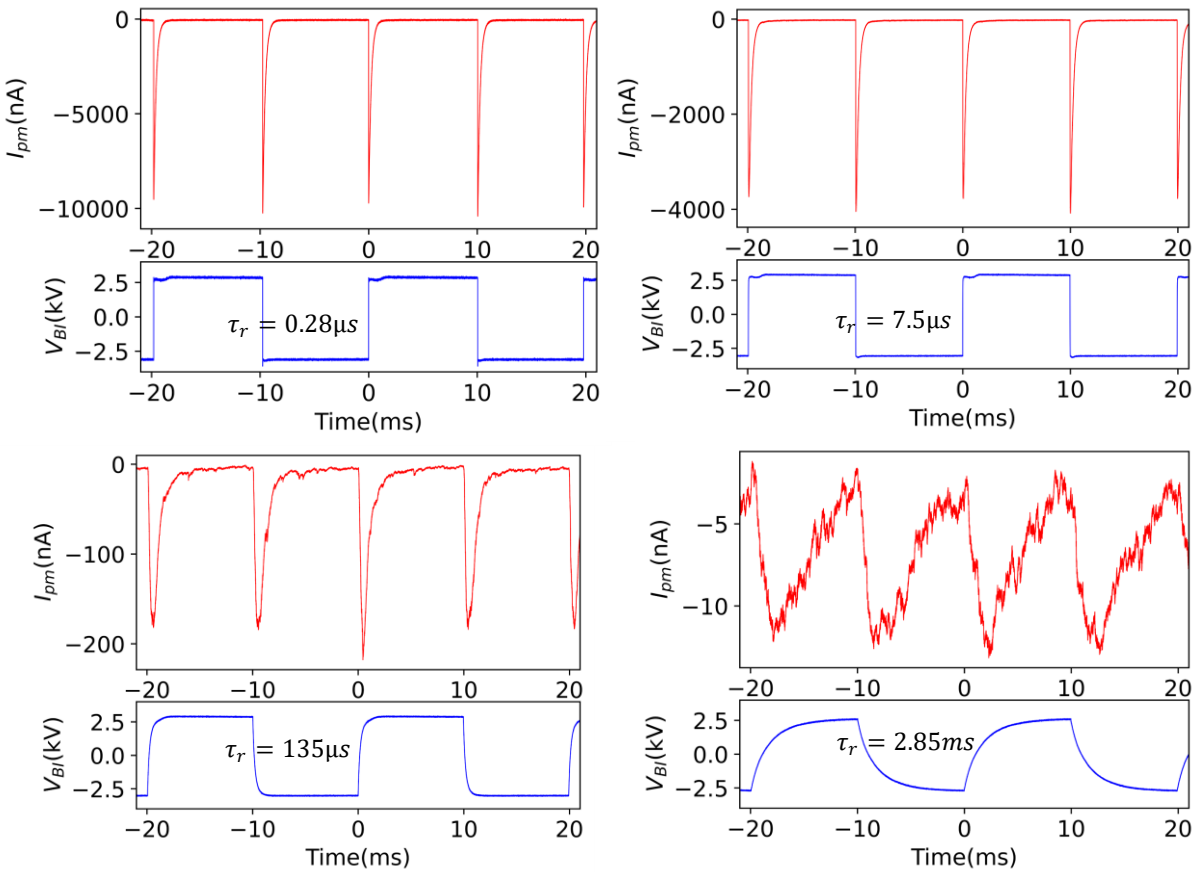

Fig 3.44. TRLM of PM light for different impulse rise time (t_r) at V_{BI} = 6kV(cc) with Si_3N_4 substrate(single layer) embedded in silicone oil with τ = 0.2 s.

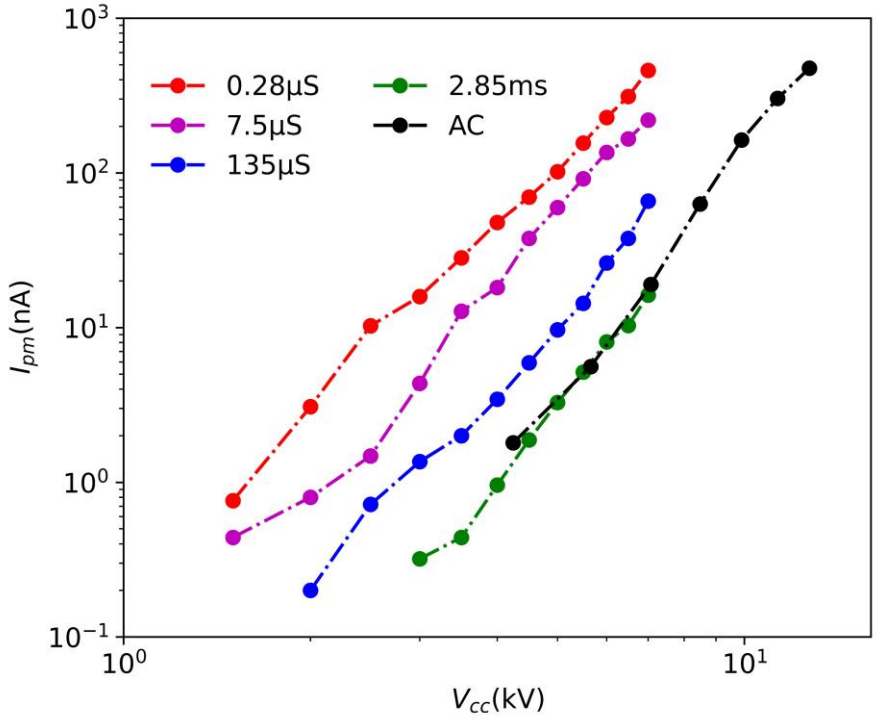

Fig 3.45. Variation of average PM current Ipm (τ = 0.2 s) with different voltage rise and fall times of bipolar impulse, and comparison with AC (50 Hz). Measurements are done with a single layer Si3N4 embedded in Silicone oil

3.4.4. Influence of pulse frequency with unipolar impulses

Influence of space charges on PD activity has been further investigated by varying the pulse period T of a unipolar impulse (V_{UI}), while maintaining a fixed pulse duration T_d, see illustration in Fig 3.*46*. For this experiment, a unipolar impulse V_{UI} = 6kV with fixed duration T_d = 200µs was used. The pulse period T was varied from 300µs (f = 3.3 kHz) to 10s (f = 0.1Hz). The objective was to estimate a typical relaxation time of space charges injected during a pulse, by measuring the total light produced during each pulse, representative of the total PD activity during this pulse. This was done by measuring the charge Q (Coulombs) corresponding to the integration of the PM current during each pulse. Q was calculated from the average PM current and the pulse period, Q = I_{pm} x T.

Fig 3.*47* shows the variation of PM charge Q per pulse, as a function of pulse repetition frequency. The measured charge Q corresponding to the PD activity during the pulse is maximum and independent of the repetition frequency for low frequencies f < 10Hz. This means that all pulses are independent from each other, provided a minimum "waiting time" about 0.1 s exists between each pulse. At higher frequencies, a decrease in Q is observed (Fig 3.*47*), indicating a decrease of PD activity during each pulse.

This effect can be interpreted by considering the influence of accumulated space charges in front of the electrode on the maximum electric field. At low frequency, pulses are independent from each other, meaning that space charges injected during the previous pulses can relax, and have no influence. Between subsequent pulses, the injected space charge has enough time to relax, the field (and then PD activity) is then maximum at each pulse. When the time between pulses decreases, space charge has no time to fully relax. Space charges accumulate in front of the electrode, reduce the field and hence PD activity per pulse. At high frequency (3.3 kHz, corresponding to 100 µs between 200 µs duration pulses), the system approaches the DC condition where space charge accumulation is maximum. Field and PD activity are then minimum (Q is divided by nearly 10 compared to the space-charge free case). This measurement provides a typical time required for space charge relaxation between consecutive unipolar pulses, close to 100 ms.

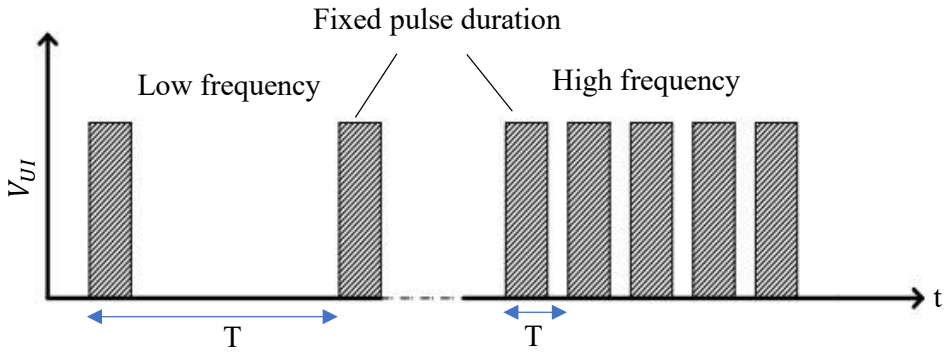

Fig 3.46. Illustration of frequency variation of unipolar impulse voltage

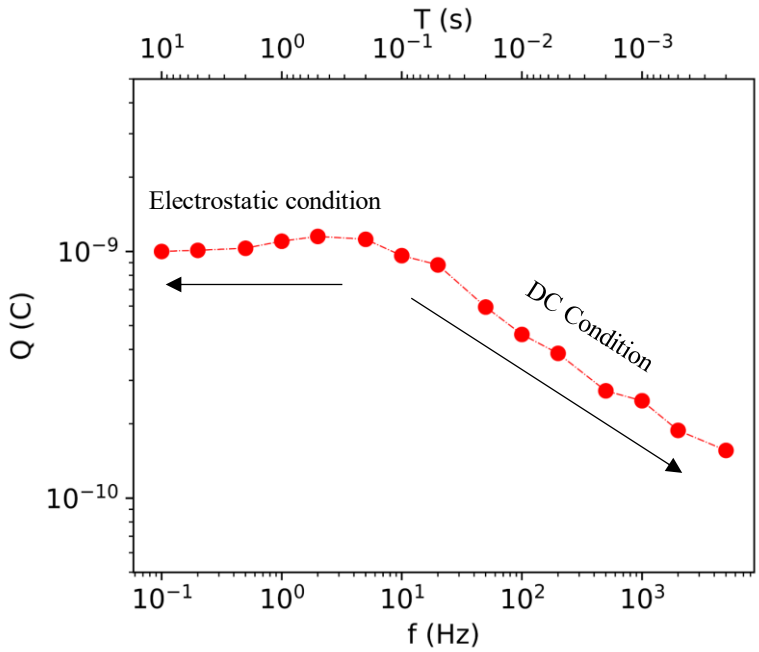

Fig 3.47. Influence of pulse frequency on PM charge per pulse Q. Fixed pulse duration Td =100µs, pulse rise and fall time: 280 ns, V_{UI} =6kV, substrate: Si3N4 (Single layer), encapsulation : Silicone oil

3.4.5. Influence of DC offset on PD activity

To further evidence the major influence of injected space charges on PD activity, experiments with a DC prestress V_{DC} added to impulses were carried out (refer Fig 3.*9* for experimental arrangement). Positive or negative V_{DC} from -4 kV to 4 kV was added to symmetrical bipolar impulses of fixed amplitude (6 kV_{cc}), see Fig 3.*49*. In extreme cases, the applied voltage switched between +1 and +7 kV (with V_{DC} = +4 kV), -3 to +3 kV (with V_{DC} = 0 kV), and -7 to -1 kV (with V_{DC} = -4 kV).

In measurements, no significant variation of time resolved PM currents occurred, see Fig 3.*48*. The statistical fluctuations in average current I_{pm} (Fig 3.*49*) recorded with various prestress V_{DC} compare with those measured without prestress, and no influence of the prestress on the total PD activity could be observed. PDs under repetitive impulse voltage are independent of the maximum applied voltage, depend only on the peak-peak amplitude variation, and do not change with imposed dc offset. Under dc alone, no PD activity was recorded up to V_{DC} = +/- 5 kV. This confirms that under dc, the actual field at the electrode edge is strongly reduced by injected space charges accumulating in front of the electrode. A similar conclusion was obtained by modelling, by considering only the non-linear conductivity of materials.

Under 50 Hz ac, PD's do occur. One may conclude that under 50 Hz ac, the attenuation of field is not as large as under DC. However, some attenuation of field obviously occurs, as evidenced by the lower PD activity under ac compared to fast rise impulses (Fig 3.*49*), and also by the influence of pulse risetime. 50Hz ac therefore constitutes an intermediate case between fast rise impulse and dc. It is however not representative of actual conditions found in a power module, and PD measurements carried out with such applied voltage do not provide data directly relevant of such systems.

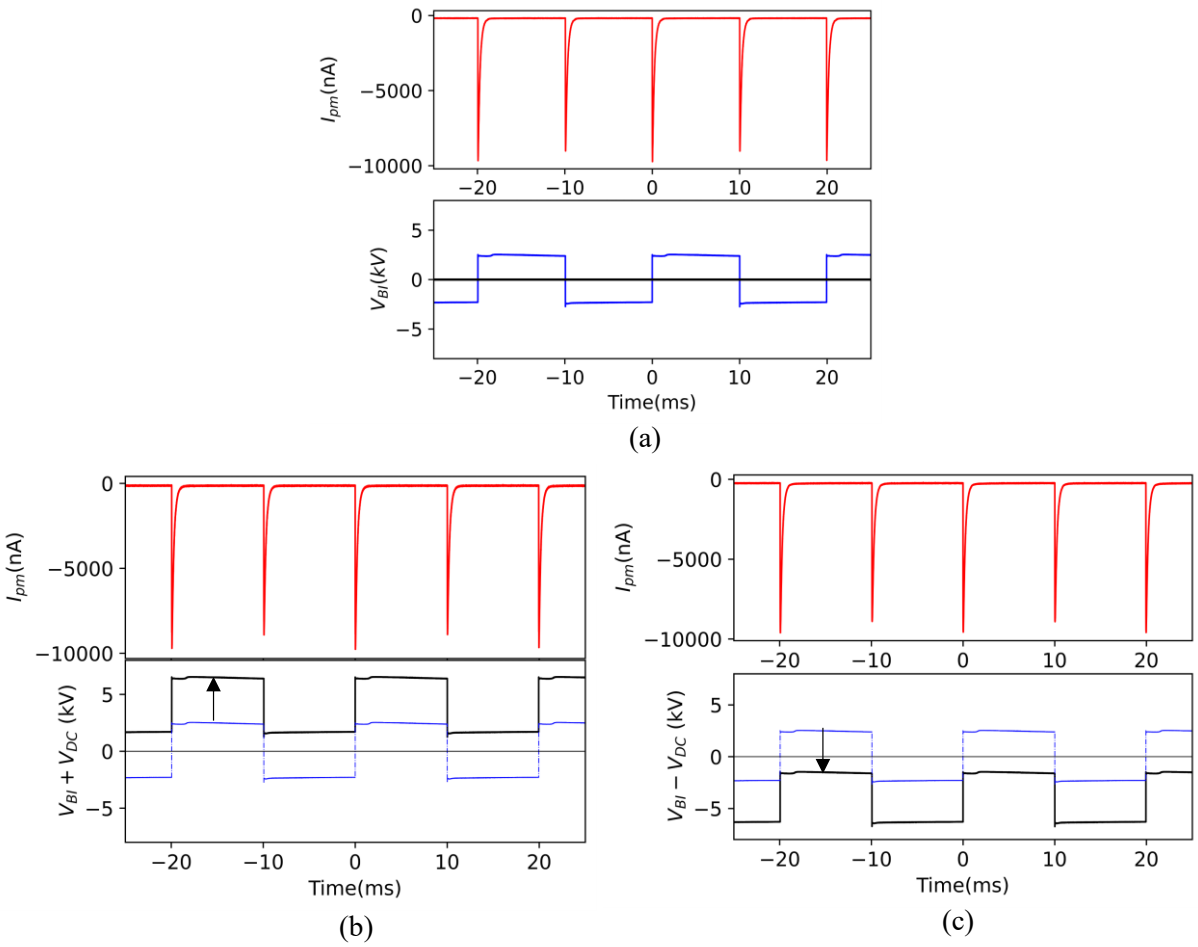

Fig 3.48. Time resolved PM current with Si_3N_4 substrate (single layer) embedded in silicone oil (a) With V_{DC} = 0kV, V_{BI}=6kV(cc), (b) with V_{DC} =+4kV, V_{BI}=6kV(cc) and (c) with VDC = - 4kV, VBI=6kV(cc)

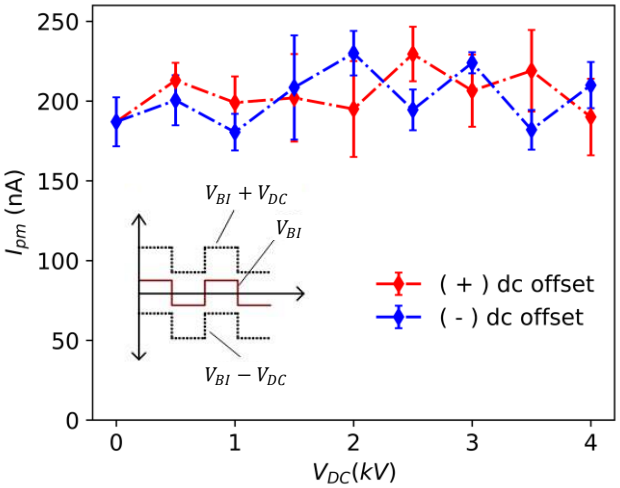

Fig 3.49. Average PM current Ipm (τ = 0.2 s) measured with DC prestress Vdc superposed to 6kVpp bipolar impulses (tr = 0.28 µs, f = 50 Hz). Measurements are done in a single layer Si3N4 embedded in Silicone oil

3.5. Summary of partial discharge measurement with ceramic substrate embedded in dielectric liquids

A test bench including both electrical and optical methods to study partial discharge activity in power electronic substrate embedded in liquids/gel encapsulation has been used. The electrical method consisted of classical method to measure PDs using Power Diagnostix™ system. This PD acquisition system served as a standard means to determine occurrence of PD under AC. Simultaneously, an optical PD detection system constituted with a photomultiplier and CCD camera were used to detect any light emitted, especially along the electrode edges (triple point). Studying the correlation between the light detected/observed with PD activity measured with electrical method allowed to determine if the materials are electroluminescent. It was found that DBT is highly electroluminescent and therefore cannot be used for PD detection using optical method. Silicone oil, Alumina and Silicone nitride substrates are found to be non-electroluminescent. Therefore, the PD detection under impulse voltage was made mostly with Alumina and Silicone nitride substrates.

Light measurements corresponding to PD activity in silicone oil under impulse with fast rise time showed large increase compared to light measured under AC at the same voltage level. Also, most light is produced during the rise or the fall time of the impulse voltage, i.e. PDs under impulse are mostly related to slew rate dV/dt. This indicated that PDs mostly occur due to the highest electrostatic field occurring when injected space charges do not have enough time to propagate away from the triple point region. Further investigations were made by varying the impulse rise time from 280ns (typical of impulse in power electronics) to 2.85ms (equivalent to AC at 50Hz). It was observed that the very strong light (and hence PD activity) recorded for fast rise impulse drastically reduces as the rise time is slowed down to 2.85ms. At long rise time, space charges are injected and propagate in front of the triple point, thereby reducing the electric field and PD activity. When DC pre-stress was applied to the impulse voltage, no significant changes in PD activity was recorded. This further confirmed the strong influence of dV/dt and space charge accumulation on PD activity under impulse voltage.

Altogether, the measurements evidence the fact that conventional PD measurements under 50Hz ac are not relevant for the actual conditions existing within power modules encapsulated with dielectric liquids. Such ac measurements tend to overestimate the PD inception voltages, and then minimize the risk associated to PD occurrence. In a realistic situation, the actual PD behaviour depends in a complex way on several factors such as pulse amplitude, risetime, and repetition frequency. Investigations involving several other factors, such as pulse duration and temperature, remain necessary to fully assess the PD phenomenon and associated risk in such situations.

Experiments under ac also show the very good PD suppression capabilities of DBT, but its behaviour under impulse voltage remains to be fully documented. Unfortunately, the interpretation of optical measurements in this liquid remains complex due to its marked electroluminescent properties.

4| EHD heat transfer enhancement in liquid and direct cooling of power electronics

The heating of power module is mainly due to conduction and switching losses during the operation. The conduction losses occur during the on-sate, and depend on the voltage drop across the semiconductor chips and on the conducted current. The switching power losses depend on the current, duty cycle, switching voltage and frequency. With increased current capacity, switching frequency, and junction temperature, the typical heat flux in SiC power modules reaches 500W/cm^2, compared to maximum heat flux of 200 W/cm^2 in Si power modules [59]. The high heat flux leads to increase of temperature in power modules, resulting in long term failure due to solder cracks, encapsulation gel ageing, delamination of bonded surfaces, heel cracks of wire bonding, etc. Therefore, thermal management and cooling solutions constitute a major concern for the development of Wide Band Gap power modules. The low thermal conductivity (0.2 W.m^{-1}.K^{-1}) of silicone gel used for encapsulation does not contribute significantly to cooling, by heat conduction from the semiconductor chip toward the surrounding encapsulant. Therefore, in practical power module packaging, the heat is first carried via substrates of high thermal conductivity (e.g: 20, 30 and 260 W.m^{-1}.K^{-1} at room temperature for Al_2O_3, Si_3N_4 and AlN, respectively), and dissipated through heat sinks by means of passive (natural convection and conduction) or active cooling (forced convection) solutions. Passive cooling involves heat exchange between the heat sink and surrounding air or liquid. Active cooling uses forced air/liquid with the help of a fan or pump. The active cooling solutions are very efficient compared to passive cooling solutions. However, it involves use of external bulky equipment that increases the system cost and weight.

Using a liquid as an alternative encapsulant for high temperature power module may add some advantage for cooling, by producing some additional heat transfer from the chip toward the environment. Presumably, due to the presence of high electric field surrounding chips, an Electro-Hydro-Dynamic (EHD) motion in the encapsulating liquid should occur, which in turn may enhance the high transfer, as evidenced in several previous studies done with simple laboratory geometries. To evaluate the possible practical benefit of liquid encapsulation for cooling power electronics chips within modules, a preliminary experimental study of heat transfer enhancement in DBT and BT06 will be first carried out, using a coaxial electrode system, without forced circulation of the liquid such as in modules. This system will allow imposing large temperature gradients, such as those occurring in a module where the chip constitutes an intense source of heat of small size. The simple geometry will allow obtaining a quantitative evaluation of heat transfer coefficients, and also the identification of optimum parameters (applied voltage and time variation) for maximum EHD heat transfer enhancement.

In a second series of experiments with a real module geometry (dissipating power diode soldered on a substrate over a heat sink, and embedded in liquid), the practical benefit of liquid encapsulation for cooling will be evaluated.

4.1. Experimental study of EHD heat transfer enhancement.

A first experiment was designed to evaluate the effectiveness of heat transfer enhancement by EHD in DBT and BT 06 liquids, in the presence of large thermal gradients, high electric field, and without forced circulation.

4.1.1. Principle of heat transfer enhancement

An insulating liquid subjected to electric field experiences electric forces that drags the fluid along the direction of the electric field lines [60]. The different types of electric forces (F_{EHD}) acting on the dielectric liquid are generally expressed by the equation 4.1.1 (a) [60, 61].

$$F_{EHD} = qE - \frac{1}{2}E^2\nabla\epsilon + \frac{1}{2}\nabla\left[\rho E^2\left(\frac{\partial\epsilon}{\partial\rho}\right)_T\right] \qquad 4.1.1(a)$$

The forces inducing liquid motion have different origins:

- Coulomb force (qE): it is the strongest force that results from the interaction of ions with charge (q) moving due to electric field (E), with the surrounding liquid.

- Dielectric force ($\frac{1}{2}E^2\nabla\epsilon$): this result from permittivity gradients $\nabla\epsilon$ introduced mainly by temperature gradients in the liquid.

- Electro-constrictive force ($\frac{1}{2}\nabla\left[\rho E^2\left(\frac{\partial\epsilon}{\partial\rho}\right)_T\right]$): Charge species move to opposite electrodes under electric field. This causes a gradient of liquid density ρ and results in constrictive pressure force.

Several previous studies of heat transfer enhancement due to EHD were carried out [60, 62, 63], mainly using forced circulation, i.e. in quite different conditions compared to a power module were the liquid would remain in a closed enclosure, with a very localised heat source, and without forced circulation.

A concentric electrode system was used to evaluate heat transfer enhancement thanks to its geometrical simplicity (Fig 4.*1*). In such coaxial geometry, the electrostatic field E(r) at radius r is written as:

$$E(r) = \frac{(V_o - V_i)}{r\ln(\frac{r_o}{r_i})}$$

Where V_i and V_o are the voltages across the inner and outer electrodes, respectively. With the dimensions used (inner radius r_i = 8 mm, outer radius r_o = 10 mm), the ratio of maximum field E_i to minimum field E_o is :

$$\frac{E_i}{E_o} = \frac{r_o}{r_i} = 1.25$$

The field enhancement is weak, and the field can be considered as “quasi uniform”.

The inner electrode can be heated with the help of a heater dissipating a power P, and the temperature of the outer electrode T_o remains at room temperature thanks to forced cooling. The large thermal gradient resulting from the temperature difference ($\Delta T = Ti - To$) across the dielectric liquid causes a thermal convective flow that carries the power P toward the outer electrode. Thermal calculations show that the heat flux through the inner electrode holder (at its extremities) is negligible, and therefore all the dissipated power P goes across the liquid. After some time, the inner electrode reaches some equilibrium temperature T_{io} that depends on P and on the equivalent thermal resistance of the liquid.

If high voltage is applied across electrodes, an EHD motion sets in, that modifies the convective heat transport by the liquid, and hence the equilibrium temperature T_i.

The heat transfer with forced convection is usually expressed in terms of heat transfer coefficient h (W/m^{2}K). The heat transfer coefficient h_o, resulting from only thermal convection (without applied voltage) is calculated as:

$$h_o = \frac{P}{A\,(T_{io} - T_o)} \qquad 4.1.1\ (b)$$

Where A is the area of the heated inner electrode. Upon application of high voltage V_o on the outer electrode and keeping the inner electrode grounded, the EHD-enhanced liquid motion should increase heat transfer, and hence reduce the equilibrium temperature T_i. The new heat transfer coefficient as a result of EHD can be calculated from the temperature difference between the electrodes as,

$$h_{ehd} = \frac{P}{A\,(T_i - T_o)} \qquad 4.1.1\ (c)$$

Therefore, the efficiency of the heat transfer enhancement due to EHD can be expressed as,

$$E_{ff} = \frac{h_{ehd}}{h_o} \qquad 4.1.1\ (d)$$

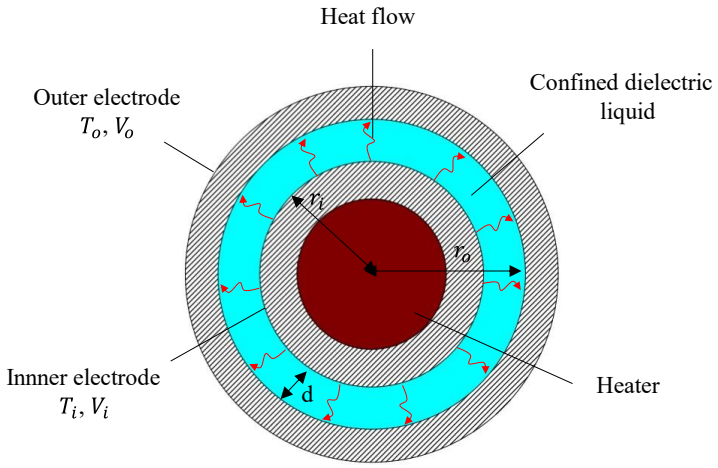

Fig 4.1. Cross section of concentric cylindrical electrodes filled with dielectric liquid for heat transfer enhancement studies under the influence of EHD

4.1.2. Heat transfer measurement test cell and experimental procedure

The test cell consists of vertical coaxial copper electrodes separated by gap d = 2 mm as shown in Fig 4.*2* and Fig 4.*3*. The external radius of inner electrode is r_i = 8 mm and the internal radius of the outer electrode is r_o = 10 mm. The length of the inner electrode is 63 mm. The inner electrode is grounded and contains a heating resistance with a maximum power P = 230 W. A DC power source HQpower™ PS1306 is used to set the power dissipated within the inner electrode. The temperature T_i is measured with a thermocouple placed close to the electrode surface. High voltage V_o is applied on the outer electrode. Its temperature (T_o) is maintained close to room temperature using forced air cooling. The measurement of temperature of the outer electrode is not possible with a thermocouple when high voltage is applied, and T_o was monitored with an infrared thermometer. An overview of the test arrangement can be seen in Fig 4.*4*.

Two dielectric liquids of similar chemical composition were used, i.e., mono-benzyltoluene (BT06) and di-benzyltoluene (refer Table 4. *1*.). The large difference in viscosity between these two liquids allows evaluating the effect of viscosity on EHD heat transfer enhancement. The test cell was thoroughly cleaned with acetone before filling with fresh DBT or BT06. It was then placed under vacuum with inner electrode heated to 60°C for about 2 hours to remove trapped moisture and gases. Dry nitrogen was then introduced above the liquid surface. The natural convective heat transfer coefficient h_o was recorded once T_i reaches stability, from equation 4.1.1 (b). The influence of thermal gradient has been recorded by varying the heater power. With applied high voltage V_o , EHD heat transfer coefficients was calculated using equation 4.1.1 (b). Different high voltage wave shapes produced by a high voltage amplifier TREK 10/10B were used: DC voltage (V_{DC}), sinusoidal AC voltage (V_{AC}), unipolar rectangular impulses (V_{UI}), bipolar rectangular impulses (V_{BI}), visible on illustration in Fig 4.*5*.

Fig 4.2. Inner and outer concentric copper electrodes used for EHD heat transfer enhancement studies in dielectric liquid

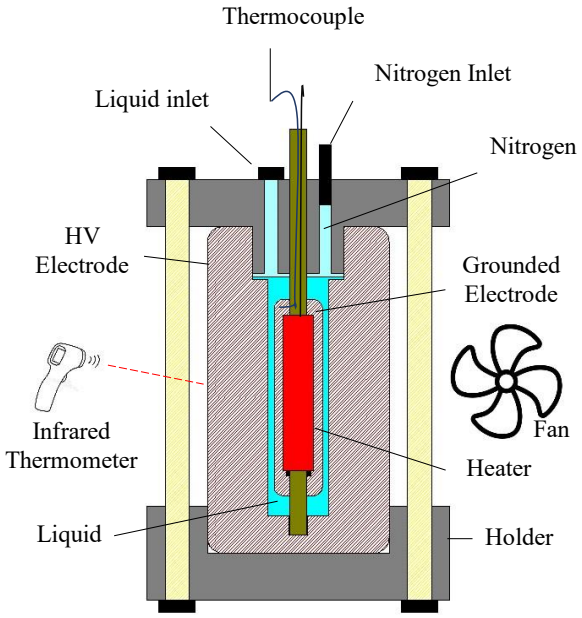

Fig 4.3. Schematic diagram of heat transfer measurement test cell

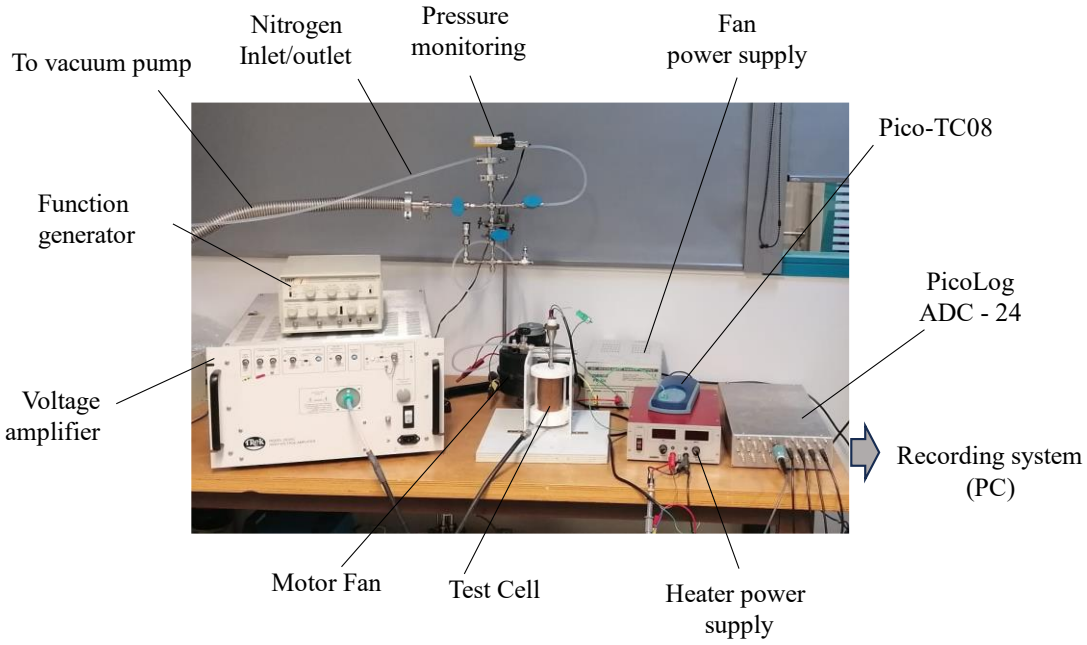

Fig 4.4. Overview of test arrangement for EHD transfer in liquids

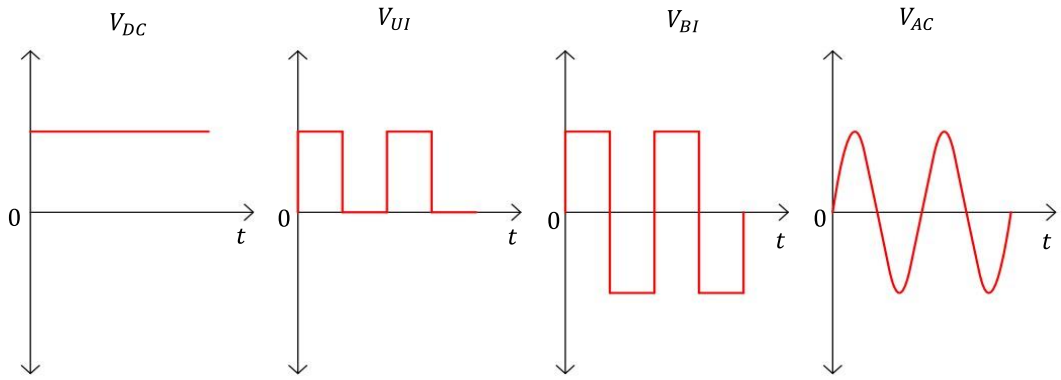

Fig 4.5. Schematic representation of different voltage shapes used for heat transfer enhancement studies

Table 4. 1. Dielectrics liquids used for heat transfer enhancement studies

Properties	BT06	DBT
Viscosity ($mm.s^{-1}$)	5.90	50.09
Thermal conductivity ($W.m^{-1}.K^{-1}$)	0.130	0.128
Density ($kg.m^{-3}$)	1008	1044

4.1.3. Heat transfer without EHD at different temperature gradients

Heater power P was varied from 3W to 122W which resulted in temperature difference ΔT between the electrodes from 7°C to 200°C respectively. The temperature difference is used for calculating the thermal gradient ($\Delta T/d$) and heat transfer coefficient h_o, Fig 4.6. The convective heat transfer coefficient logically increases with temperature gradient. With thermal gradient of 100°C/mm, the heat transfer coefficient is 3 times larger compared to the theoretical heat transfer coefficient calculated from the quoted thermal conductivity k (i.e., not involving convection). The conduction thermal coefficient h_k is calculated using the following relation,

$$h_k = \frac{k}{d} \qquad 4.1.3\ (a)$$

Such convective heat transfer is mostly determined by the complex liquid flow induced by the thermal gradient, but unfortunately such liquid flow could not be observed with the closed test cell used. The increase in heat transfer due to convection is interesting for spreading heat from the chip surfaces in power electronics where high thermal gradient exists. The effectiveness of natural convective cooling of chips will be discussed in later part of this chapter.

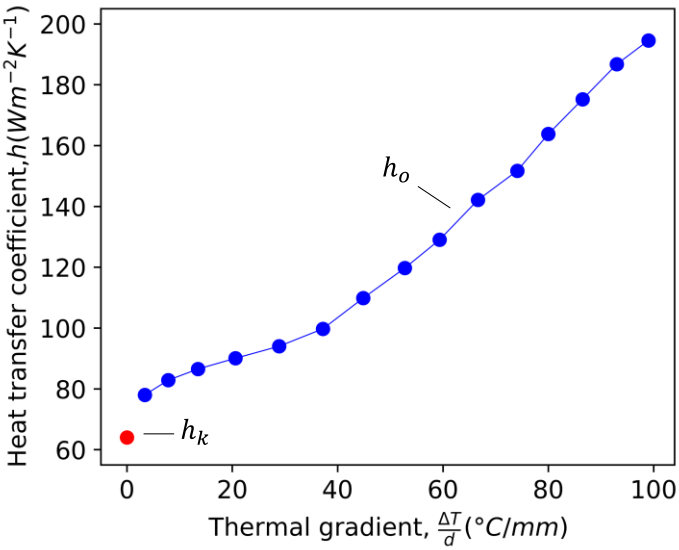

Fig 4.6. Convective heat transfer in coaxial test cell filled with DBT, and comparison with value h_k involving conduction only

4.1.4. EHD heat transfer enhancement under DC voltage

Heat transfer enhancement under DC voltage (V_{DC}) was evaluated for heater power P = 12 W, 45W and 110 W. A typical recording of EHD heat transfer enhancement in DBT with P = 45W is shown in Fig 4.*7*. Without applied voltage, it took around 40 minutes to reach temperature stability of T_i = 160°C and T_o= 44°C. In all experiments, a slight increase of outer temperature T_o was recorded above the ambient air temperature (25 °C). This increase was due to the limited efficiency of the forced air-cooling system, and also depended on the power P to be extracted.

The temperature difference between electrodes was ΔT = 116°C corresponding to h_o = 123 W/m^{2}K. As soon as V_{DC} was applied, the temperature of the inner electrode T_i dropped down to 114°C @ 2kV and 98°C @ 10kV. This evidences the strong influence of EHD on convective heat transfer. The heat transfer increases by 2.6 times under V_{DC} @ 10kV, compared with h_o. The heat transfer coefficient under DC at different heater power is shown in Fig 4.*8*.

Unfortunately, due to the noise induced by both the high voltage amplifier and the presence of the heater, it was not possible to measure the current flowing across the liquid gap, which would provide more insight into conduction and motion involved in the liquid. A more complex test cell allowing both visualisation and current measurements would be of great interest to better analyse EHD phenomena, but such development was outside the main objectives of this work.

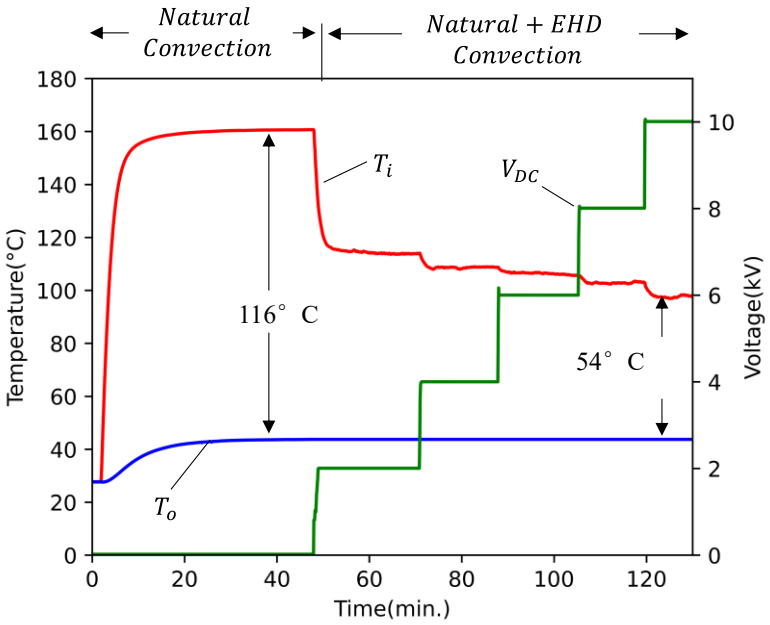

Fig 4.7. Typical temperature recording in DBT with DC voltage (P = 45 W)

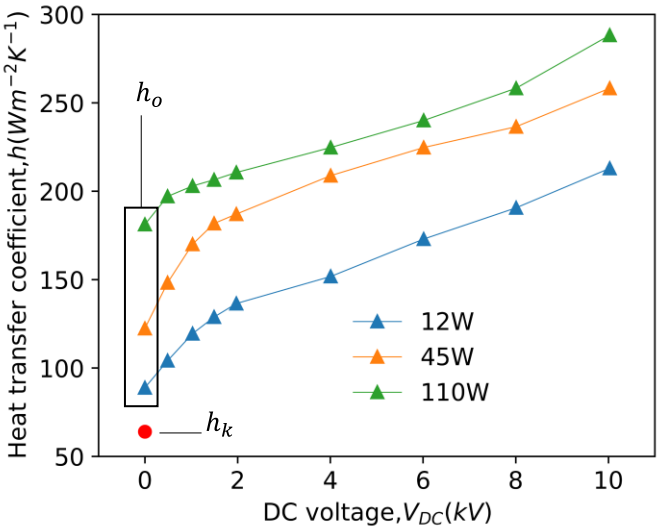

Fig 4.8. EHD enhanced heat transfer coefficient under DC voltage in DBT at different heater power

4.1.5. EHD heat transfer enhancement under AC, Unipolar and Bipolar impulses

A fixed heater power of P = 25W was used to evaluate the influence of different voltage shapes on heat transfer. Without voltage applied, this resulted in stable inner temperature T_i = 107°C and stable outer electrode temperature T_o = 35°C. With 1 kV unipolar rectangular impulses (duty cycle = 50%), Fig 4.9 shows that the heat transfer efficiency is maximum for a frequency $F \approx$ 0.5 Hz, and decreases at higher frequency. Fig 4.*10* shows a comparison of heat transfer coefficient h under V_{DC} , V_{UI}, V_{BI} and V_{AC} of different frequencies for a fixed voltage of V = 1 kV. In all cases, an increase of heat transfer versus frequency F is first measured, until it reaches a maximum value at frequency (F_m), and decreases afterwards. The best efficiency is observed with bipolar impulse voltage at 0.5 Hz resulting in 2.6 times increase compared to h_o without voltage.

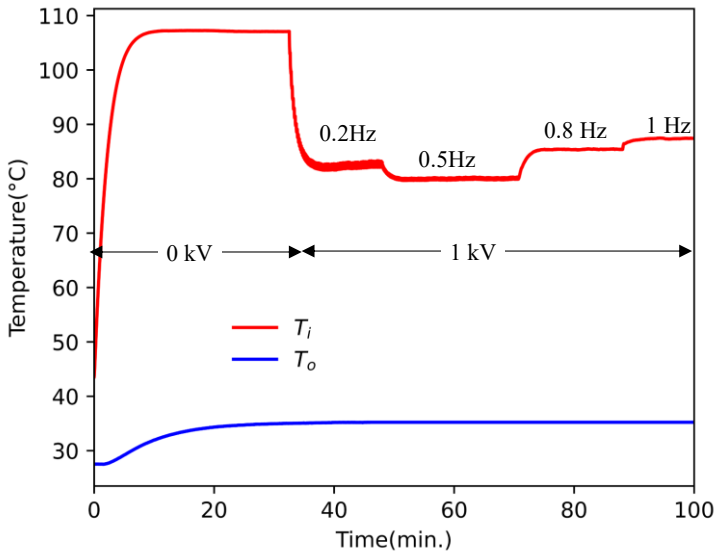

Fig 4.9. Typical temperature recording in DBT with unipolar impulses at different frequencies (P = 25W, V_{UI}= 1kV)

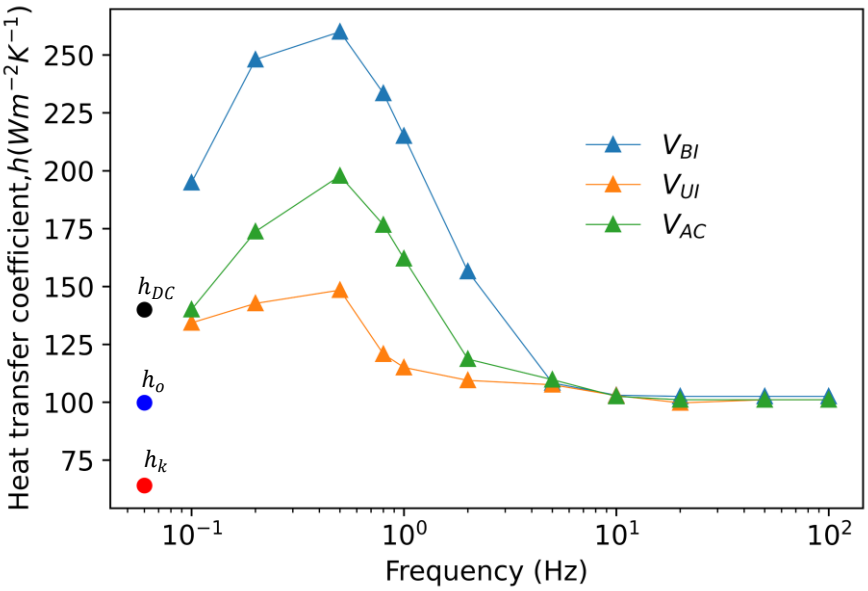

Fig 4.10. Heat transfer enhancement in DBT with various voltage shapes and frequencies (P = 25 W): V_{UI} (0 / 1kV impulses), V_{BI} (-1 kV / +1 kV impulses), V_{AC} (1kV rms voltage)

A first-step analysis shows that this frequency is probably related to the time-of-flight (*TOF*) of the liquid across the gap. *TOF* depends on the charge mobility μ:

$$\mu = \frac{d^2}{V\ TOF} \qquad 4.1.5\ (a)$$

The typical EHD charge mobility in DBT deduced from conduction measurements is close to $\sim 10^{-9}$ (m^2/V. s) as reported in [17], which corresponds to *TOF*~2s (i.e., 0.5 Hz frequency) at 1 kV and 2 mm electrode gap. It is also observed that at fixed voltage, changing the type of voltage (V_{UI},V_{BI},V_{AC}) does not change the frequency F_m at which the maximum heat transfer occurs. With further increase of frequency, hot liquid layers on the hot inner electrode cannot any more cross the gap toward the colder outer electrode acting as heat sink. Liquid

moves back and forth over a limited distance, and the heat transfer efficiency rapidly drops. Above 10 Hz, there is almost no more influence of EHD on the heat transfer at V = 1 kV: h becomes equal to h_0 (i.e., with no applied voltage). At very low frequency, h becomes logically close to that measured under DC.

Increasing the voltage produces effects in line with this analysis (Fig 4.*11*). With V increased to 5 kV, the optimum frequency F_m increases to 2.2 Hz, corresponding to a transit time of 0.45 s. This fairly agrees with equation 4.1.5, that indicates that the product V *x TOF* should remain constant.

Similar results on influence of frequency on heat transfer enhancement have been reported with EHD pump heat transfer apparatus [64]. Unfortunately, the direct observation of the liquid motion was not possible in the coaxial test cell, to better assess these assumptions.

4.1.6. EHD heat transfer enhancement for liquid with different viscosities

A significant increase in heat transfer enhancement is observed with BT06 compared to DBT (Fig 4.*11*). This is due to the 10 times lower viscosity of BT06 (see Table 4. *1*). Both liquids show almost the same thermal conductivity (k). At V = 0 V, h_0 increases from 100 W.m^{-2}. K^{-1} in DBT to 120 W.m^{-2}. K^{-1} in BT06, depicting the influence of viscosity on natural convective heat transfer. Ion mobility is inversely proportional to the viscosity of liquid and does not vary much with voltage as discussed in chapter 2. Logically, F_m should be higher for a liquid with lower viscosity, as observed in the comparison between BT06 and DBT at the same voltage (Fig 4.*11*). The maximum enhancement of heat transfer h / h_o with V = 5 kV is close to 8 with BT06 (f_m = 5 Hz), and 6 with DBT (f_m = 2 Hz).

One of the most important features of these results is that the new devices based on wide band gap semi-conductors have a switching frequency of several of kHz and thus EHD in insulating liquids for such frequencies appears to be negligible.

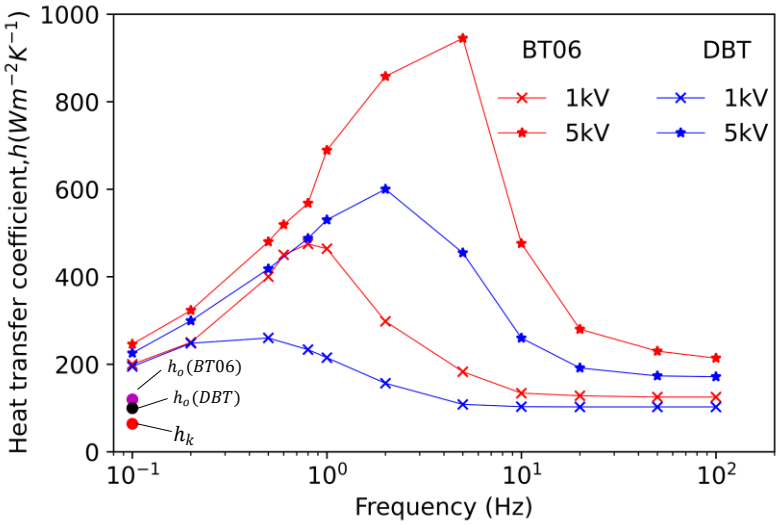

Fig 4.11. Comparison of heat transfer in DBT and BT06 under bipolar impulse voltage V_{BI}

4.2. Assessment of the contribution of liquid to cooling in a real module geometry.

A typical geometry of power converter module showing typical values of thermal conductivity of different materials can be seen in Fig 4.*12*. In order to prevent exceeding the semiconductor maximum temperature, the heat generated by semiconductor devices (diodes/IGBT) has to be extracted as much as possible toward the heat sink, through a metalized substrate with good thermal conductivity (usually a ceramic), also providing electrical insulation between semiconductors and heat sink. Almost no heat extraction occurs through the encapsulation material (typically silicone gel) due to its low thermal conductivity. If liquid is used instead of gel, convective heat transfer within the encapsulation could occur, and be enhanced by:

- either an external pump to circulate the liquid
- or EHD liquid motion within the module

The latter is desirable since it does not involve any external components. We may postulate that the EHD liquid motion could contribute to homogenize temperature above semiconductors, and to favour the heat transfer toward the ceramic substrate. Another possibility would be adding an electrode in the liquid above the chip, and polarize this electrode in order to maximize EHD motion of the liquid above the chip. Both solutions will be investigated here.

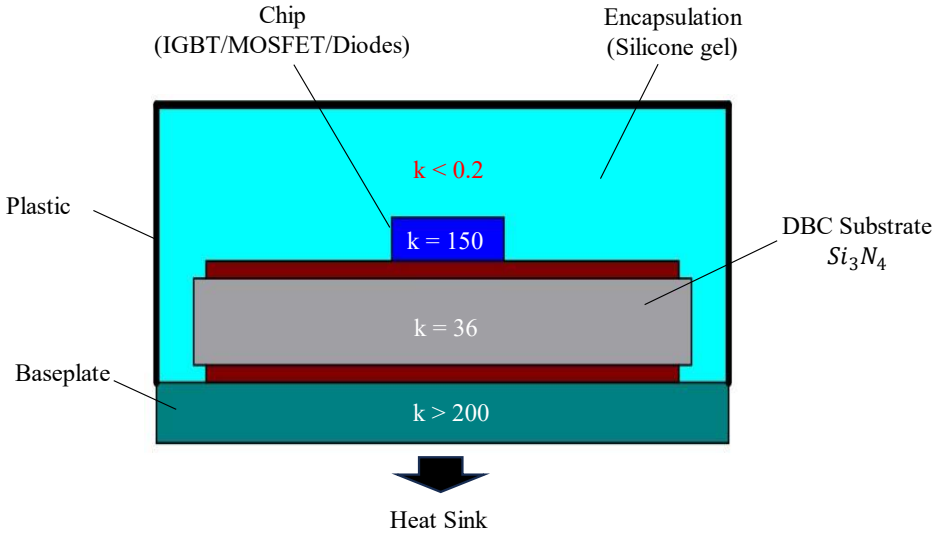

Fig 4.12. Thermal conductivity k (W/mK) of different components of a conventional power module

A test sample was prepared with two power diodes (ABB5SLY12E1200) soldered on a Silicon Nitride (Si_3N_4) ceramic substrate with silver coated copper metallization, as shown in Fig 4.*13*. The sample is placed in a metal box made of thin copper sheet, and is clamped on a cold plate, acting as a heat sink with regulated temperature. At interfaces between the substrate and the box, as well as between the box and the heat sink, a silicone pad thermal interface material is used. In order to estimate the diode junction temperature T_j, a semiconductor thermal analyser (AnalysisTech® Phase12) is used. The junction voltage drops V_j of the diode for a current of 10 mA was used as thermo-sensitive measurement parameter to obtain the diode temperature. After calibration up to 135°C, the $V_j = f(T_j)$ plot shows a linear dependence with a slope of -2.2 mV/°C.

During tests, the diode was heated by the application of a regulated DC current inducing a fixed power dissipation of 25 W, while the temperature of the heat sink was maintained to 26°C. Once the steady state was reached, the diode temperature was deduced from V_j @ 10 mA. The copper box could be either empty (diode exposed to open air), or filled with either BT06 or DBT.

With no liquid embedding the diode, the junction temperature (T_j) in open air was 80°C. When the box was filled with DBT or BT06, T_j only slightly decreased to 78.5°C, indicating a minor influence of convection in the liquid on the diode cooling.

To further check the influence of EHD, a copper plate was added 5 mm above the diode as shown in Fig. 10.(b), and tied to 1 kV voltage with different shapes (DC, bipolar impulses with frequency from 0.1 Hz to 100 Hz). Whatever the voltage shape used, the measured T_j remained around 78°C, indicating no large impact of EHD to enhance the cooling of the diode in this geometry, typical of a power module. In such geometry, the high thermal conductivity of the Si_3N_4 substrate (k = 36 $W.m^{-1}.K^{-1}$) and its low thickness (0.3 mm) both induce a low thermal resistance between the semiconductor chip and the heat sink. This explains why the liquid surrounding the diode provides only a minor contribution to the heat transfer: most of heat is carried toward the heat sink via the ceramic substrate. Even with the contribution of EHD, the thermal convection occurring in the liquid above the diode does not contribute significantly to further cooling it.

Of course, the module geometry is not optimized to enhance the contribution of the liquid to cooling, and other geometries probably may lead to better results. However, cooling was not the primary objective of using liquids, which are mainly considered as a potential solution for insulation and PD suppression at high temperatures. The data obtained here provide some basic knowledge about EHD heat transfer, which may be used in future designs of power modules involving liquids.

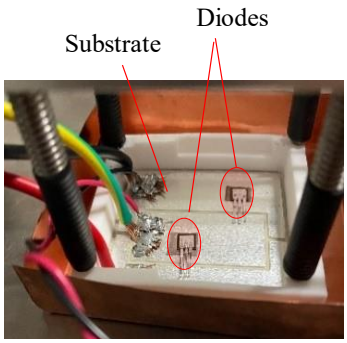

(a)

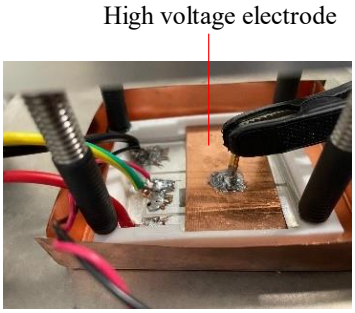

(b)

Fig 4.13. Test setup for studying EHD heat transfer contribution to cooling of diodes; (a). Natural convection in air, (b). In liquid with V = 1 kV

4.3. Conclusion on EHD heat transfer enhancement in liquid and possible cooling of power electronics

When a dielectric liquid is placed between a hot and a cold electrode inducing a quasi-uniform electric field, the convective heat transfer from the hot to cold electrode can be considerably enhanced by the EHD motion of the liquid, up to about x8 times with optimized conditions in this study. However, in a typical power electronic module geometry, replacing the standard gel encapsulation by a liquid in which EHD motion occurs does not lead to a significant increase in semiconductor cooling. Nevertheless, replacing gel by a circulating liquid may pave the way for a new class of high-performance power module.

Conclusions and Perspectives

Encapsulation materials play a very important role in power module packaging, by providing electrical, mechanical and chemical protection to active parts. At present, silicone gel provides all these basic features for silicone-based power modules (operating temperature < 175°C). Therefore, it is not suitable for higher temperature and higher voltages encapsulation of wide bandgap power semiconductors (operating temperature > 200°C and blocking voltage > 10kV). The need to find an alternative encapsulation material compatible with high temperature is crucial to harness the potential of wide band gap power modules. In this regard, an evaluation of the suitability of dielectric liquids as an alternative encapsulation to silicone gel has been addressed in this thesis, according to different topics relevant to this problem:

- *Comparison of different dielectric liquids properties at low electric field*: Dielectric properties (low field conductivity, permittivity and loss factor) of four different liquid, i.e., mono-benzyltoluene (BT06), mono-di-benzyltoluene (DBT), Silicone Oil and Mobile Jet Oil, at temperature up to 150°C using dielectric spectroscopy.
- *Characterization of conduction at high temperature and high electric field*: in DBT (maximum electric field: 30kV/mm, maximum temperature: 300°C) and Silicone Oil (maximum electric field: 10kV/mm, maximum temperature: 200°C). These measurements were done with the help of a specific high temperature test cell (voltage up to 30kV and temperature up to 350°C).
- *Transient electric field simulation*: Non-linear material properties versus temperature and electric field were used to calculate electric field evolution near triple point of ceramic substrate embedded in DBT. The simulations were made with COMSOL™ Multiphysics 5.6.
- *Partial discharge measurements under AC and fast rise impulses*: PD measurements were made with standard electrical method under AC and optical method for both AC and impulse voltages with ceramic substrates (Alumina and Silicone Nitride) embedded in dielectric liquids (DBT and Silicone Oil). The optical method involved a very photosensitive intensified CCD camera and photomultiplier (PM).
- *EHD heat transfer enhancement and cooling possibility of power devices*: voltage shapes for optimal EHD heat transfer were evaluated with the help of a specific concentric electrode system filled with either DBT or BT06. These parameters have been then used to evaluate the contribution of EHD to cooling in a real module geometry.

A. Main Observations and Conclusions Obtained

1. Dielectric spectroscopy and conductivity measurements in dielectric liquids

It was first observed that electrical conductivity in four different liquids (DBT, BT06, Silicone oil and Mobil Jet Oil) is highly dependent on temperature. An increase of temperature from 25°C to 150°C resulted in an increase of conductivity by 4 decades in DBT and Silicone oil, and 2 decades in BT06 and Mobil Jet Oil. This large increase is mainly attributable to the decrease of liquid viscosity with temperature, which in turn increases ion mobility. At room temperature, silicone oil showed the lowest conductivity ($\sigma \sim 10^{-15}$ S/cm) and Mobil Jet Oil the highest conductivity ($\sigma \sim 10^{-11}$ S/cm). Conductivity of BT06 ($\sigma \sim 10^{-12}$ S/cm) was found 2 decades higher than DBT ($\sigma \sim 10^{-14}$ S/cm) even though these liquids are chemically similar. This resulted from large differences in viscosities. The low field conductivity also enabled estimating the activation energy for ionic conduction, whereby DBT shows the highest activation energy of 0.6 eV, while Mobil Jet Oil had the lowest activation energy of 0.4eV.

Mobil jet oil was found to be slightly polar (permittivity > 3), with the largest conductivity and loss factor ($\tan(\delta) \sim 10^{-2}$) at room temperature compared to other liquids. Therefore, no further evaluations were made with this liquid.

It was also observed that conductivity in DBT and Silicone Oil at moderate temperatures exponentially increases at high electric field. However, this could not be clearly observed at temperatures above 150°C, due to the large increase in low field conductivity versus temperature, which then dominates over the influence of the field. A clear distinction between background conduction and injection occurring at high field was observed under highly divergent field (point-place electrode system) in DBT.

The observed non-linear variations of conductivity versus temperature and electric field provided basic data allowing to develop a calculation of electric field taking into account such large non-linearities, in a realistic module triple point geometry.

2. Transient electric field simulation with non-linear material properties

Electric field simulation model based on non-linear properties of materials showed that the electric field distribution with a ceramic substrate embedded in DBT is highly dependent of time, applied voltage, and temperature. A very high field (‘electrostatic regime’) exists only for several ms following a voltage step with fast risetime, within a small region of radius < 1µm. The maximum field occurs within the encapsulation. With increasing time duration, the maximum field strongly reduces, and enters a low field stable ‘conduction regime’. At high temperature, the maximum electrostatic field in the liquid lasts only for several µs. At longer times, the maximum field in materials considerably drops, and become larger in the Alumina substrate, regardless of the encapsulant nature (liquid or gel).

To obtain an even more realistic field calculation, additional phenomena such as space charge injection in the liquid and charge transport enhanced by EHD motion, should be also considered. Such very complex calculation was out of the scope of this study.

Some qualitative correlation with previous PD measurements carried out at 50 Hz versus temperature can be found: increasing the temperature induces some increase of the Partial Discharge Inception Voltage (PDIV) with DBT, due to the reduction of the maximum field at

50Hz versus temperature. AC 50 Hz appears to constitute an intermediate case between the 'electrostatic regime' producing the maximum field at short time, and the stable DC 'conduction regime' producing the minimum field. Such calculations indicate that voltage impulses with fast risetime may constitute critical conditions.

3. Partial discharge measurement in liquid embedded power electronic substrates

The PDIV under AC with Alumina and Silicone Nitride substrates in silicone oil were close to 5 kVrms and 3 kVrms respectively. With the same substrates embedded in DBT, no PDs occurred with Silicone Nitride up to 6kVrms, and PDIV raised to 8kVrms with Alumina, with PDs tentatively attributed to discharges occurring within the ceramic material. This confirmed that DBT shows excellent PD suppression capability under 50 Hz AC: contrary to Silicone oil, no PDs occurred in this liquid. This agrees with the fact that liquids of similar chemical nature are used in power capacitors to quench PDs occurring at electrode edges.

Light detection using a photomultiplier and observation using the sensitive camera showed light emission along the triple point with DBT encapsulation under AC voltage, while no PD activity could be detected. This showed that DBT is a highly electroluminescent liquid, that cannot be used for PD detection using the optical method. Thus, only silicone oil encapsulation was used for PD detection on substrates, using the optical method for impulse voltage.

The metallized Silicone Nitride ceramic substrate embedded in silicone oil provided an interesting opportunity to study partial discharges via optical measurements, since both materials are non-electroluminescent. The recorded light only comes from PD's occurring at the sharp edges of metallization. The comparison of light emission between ac voltage and impulses of variable risetimes showed that PD inception is greatly favoured in the case of impulses with fast risetime. Compared to sinusoidal AC, the voltage required to induce a similar average light emission (and hence PD activity) with fast (sub-µs) risetime impulses is nearly divided by two. This effect qualitatively agrees with field calculations taking into account non-linear conduction properties. Injected space charges, not considered in calculations, can also contribute to this effect. Adding a dc prestress to impulse voltage does not influences PD occurrence, and further evidences the major influence of injected space charges.

4. EHD heat transfer enhancement and cooling of power devices

The experimental study on EHD heat transfer enhancement using a concentric electrode system showed that the heat transfer through the dielectric liquid significantly depends on the type of voltage (dc, ac, impulses of different frequency), and on the nature of liquid. This agrees with similar previous studies. There exists an optimal frequency for each voltage shape and voltage level. If conditions are wrongly chosen (e.g. too high frequency) no effect of EHD on heat transfer occurs. The maximum EHD heat transfer enhancement (up to 8 times) was achieved with bipolar impulse voltage.

The evaluation of the influence of EHD on heat transfer carried out with a more realistic geometry (standard substrate encapsulated with liquid DBT or BT06) was found to be ineffective. This is because of the very high thermal conductivity of ceramic substrate used (ceramics), compared to the minor contribution added by the dielectric liquid. Even if the heat transfer through the encapsulation can be increased by 8 times by EHD, the effective thermal

conductivity remains lower than 1 W/m.K, when the thermal conductivity of ceramic substrates is much higher (80W/m.K in Silicone Nitride).

B. Perspectives

This thesis addressed several aspects of the possibility of using liquid insulation as encapsulation material in high temperature and high voltage power module applications. It is clear through this study and also from the work done by previous researchers that liquid dielectric has reasonable potential to be used as encapsulation for power electronics. Liquids such as DBT benefit from a proven efficiency and reliability in the industry as high temperature fluids (well above 200 °C) on the long term. Another notable property is a very good partial discharge suppression property evidenced by standard 50 Hz measurements, and self-healing capability typical of liquids when breakdown or partial discharge occurs. However, more research and validation studies are still required in continuation to this work, and work done by previous researchers. Some of the prospective topics to be continued are as follows:

- detailed assessment of accelerated thermal aging to complement the preliminary experiments already conducted as reported in Annex A. It is important to perform thermal aging under different voltage stress typical of power modules. Measurements of acidity, change of viscosity, possible chemical interactions with surrounding materials after long term aging would usefully complement the results already obtained;

- improved simulation model to study the electric field near triple point, by taking into consideration the effect on EHD, charge injection, charge transport models, thermal gradients that obviously exist in power modules;

- additional surface breakdown and partial discharge measurement have to be made, with a special focus on high temperature measurements and fast risetime impulses. Since it was not possible to carry out optical measurements under impulse voltage with DBT, it remains unclear today whether or not the good PD properties under AC of such liquid would remain under impulse voltage;

- thermal experiments to evaluate the efficiency of direct cooling of power modules by circulating liquids could be an interesting subject, such as the design of specific packaging geometries adapted to such cooling technique;

- many practical problems also remain to be solved before using liquids on an industrial scale (proper sealing design adapted to liquid encapsulation, material compatibility, resistance to internal pressure variations due to temperature, pollution of the liquid by solid particles, water, ageing, etc.).

Annex A – Preliminary results about accelerated thermal aging of several dielectric liquids

The results presented below are part of the internship work [65] carried out in 2023 by O. Diki, supervised by myself and R. Khazaka, in the context of a project involving the SAFRAN company.

A.1. Liquid samples and aging procedures

Three different dielectric liquids were used for thermal aging studies, i.e., Jarytherm®DBT (referred as 'DBT'), Silicone oil (47V50) and Mobil Jet™ Oil II (referred as 'MJO'). General characteristics of these liquids can be found in Table 2.1.

These liquids were aged in open air at temperature 150°C or 180°C using Heraeus VT6060P oven, fig-A.1. The glass beakers filled with liquids were partially closed with aluminium foil during heating to avoid mixing due to vaporization. Also, the ventilator suction pump connected to the oven evacuated any traces of vaporised liquid.

Several aging experiments were conducted for evaluating aging in these liquids:

- Fourier Transform Infrared Spectroscopy (FTIR): evaluation of any new functional groups different from the fresh liquid or change in the light absorbance after aging.

- Dielectric spectroscopy: This technique is often used in determining the quality of aged insulating materials based on conductivity, permittivity and loss factor measurements.

- Breakdown experiment: Useful in comparing insulation breakdown strength of different liquids

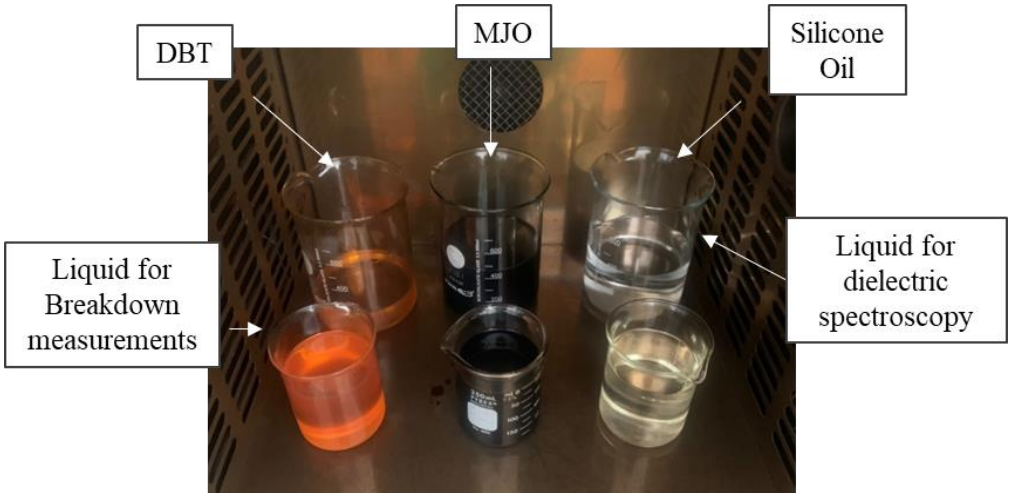

Fig - A. 1. Liquid samples aged in open air using Heraeus VT6060P oven (after 72 hr @ 150°C), 600 mL glass beaker for dielectric spectroscopy and 200 mL beakers for breakdown measurement

A.2. Preliminary aging evaluation of liquids in open air

Liquids were initially aged at 180°C in open air for 72 hours. A change of colour from clear to light yellow was seen in DBT, fig-A.3. No observable change in colour was seen with silicone oil. Colour changed from light brown to dark brown in MJO. It is difficult to established if the colour change is due to optical change in the molecular orientation of the liquids or due to aging caused by oxidation. However, colour change is an indicator of aging in liquids.

A Thermo-Scientific Nicolet^{TM} Summit FTIR Spectrometer (fig-A.3) was used to evaluate the difference in transmittance and functional FTIR pattern between fresh and aged liquids. No formation of new functional groups (peaks representing chemical bonds) was observed in all liquids, fig-A.4. However, a decrease in transmittance was observed with silicone oil and MJO. It is an indicator of thermal aging in liquids, but difficult to conclude since the decrease in transmittance is also related to changes in molecular/atomic orientations, not necessarily affecting the electrical properties of the liquid.

Fig - A. 2. Colour change in DBT, Silicone Oil and MJO liquids after thermal aging in open air for 72 hours at 180°C

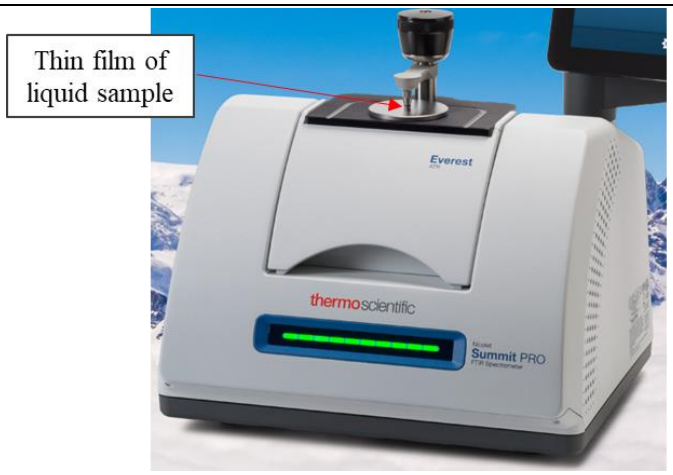

Fig - A. 3. Thermo-Scientific Nicolet FTIR spectrometer

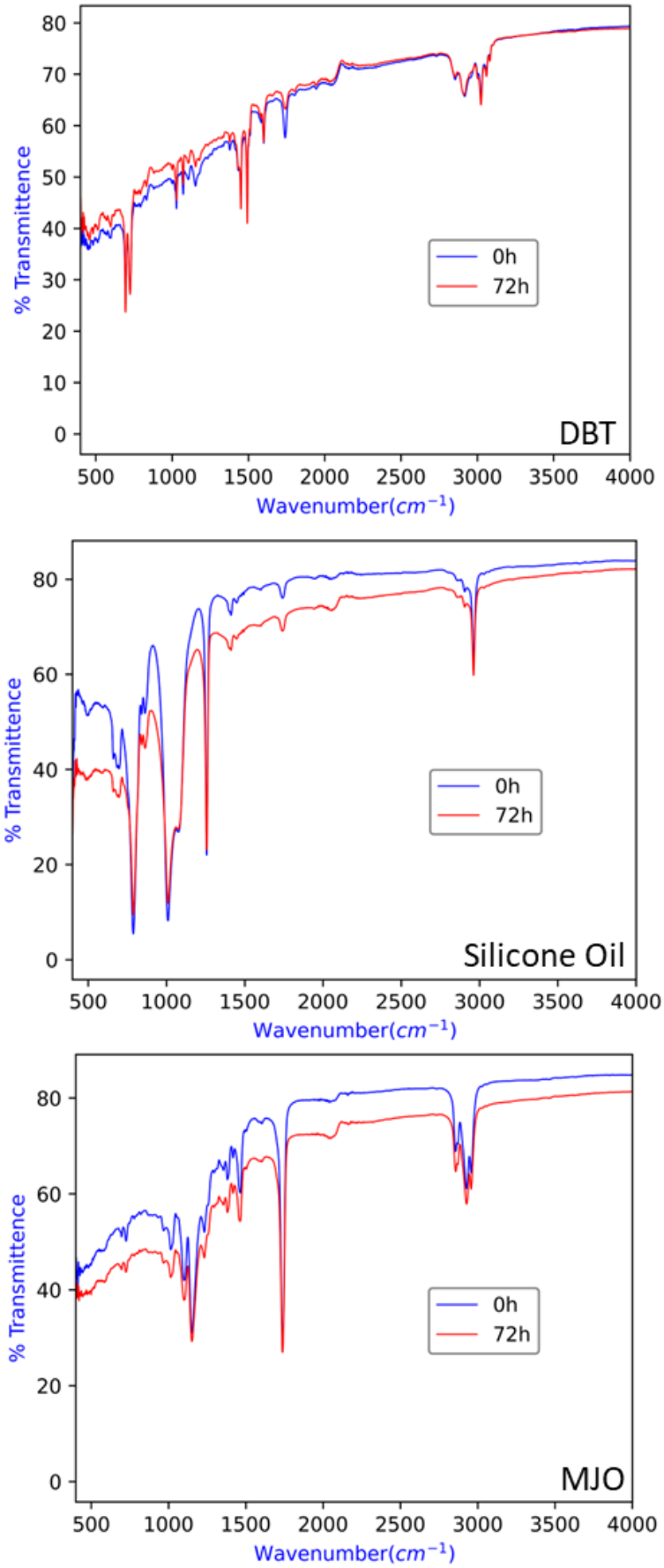

Fig - A. 4. FTIR spectrograph of fresh and aged liquids (72hrs at 180°C)

A.3. Dielectric spectroscopy of aged liquids in open air at 150°C

The experimental set up and test cells used for dielectric spectroscopy of aged liquid are the same as in chapter 2. Three identical test cells are used separately for each liquid to avoid traces of one liquid getting into another. The measurements are made at an interval of around 72hrs (3 days) for a total of 15 days, i.e., 6 sets of measurement for each liquid (including at day zero for fresh liquid). The temperature is maintained at 20°C for all liquids while doing the dielectric spectroscopy measurements. The change of colour from fresh liquid (D0) to 15th day (D15) can be seen in fig-A.5.

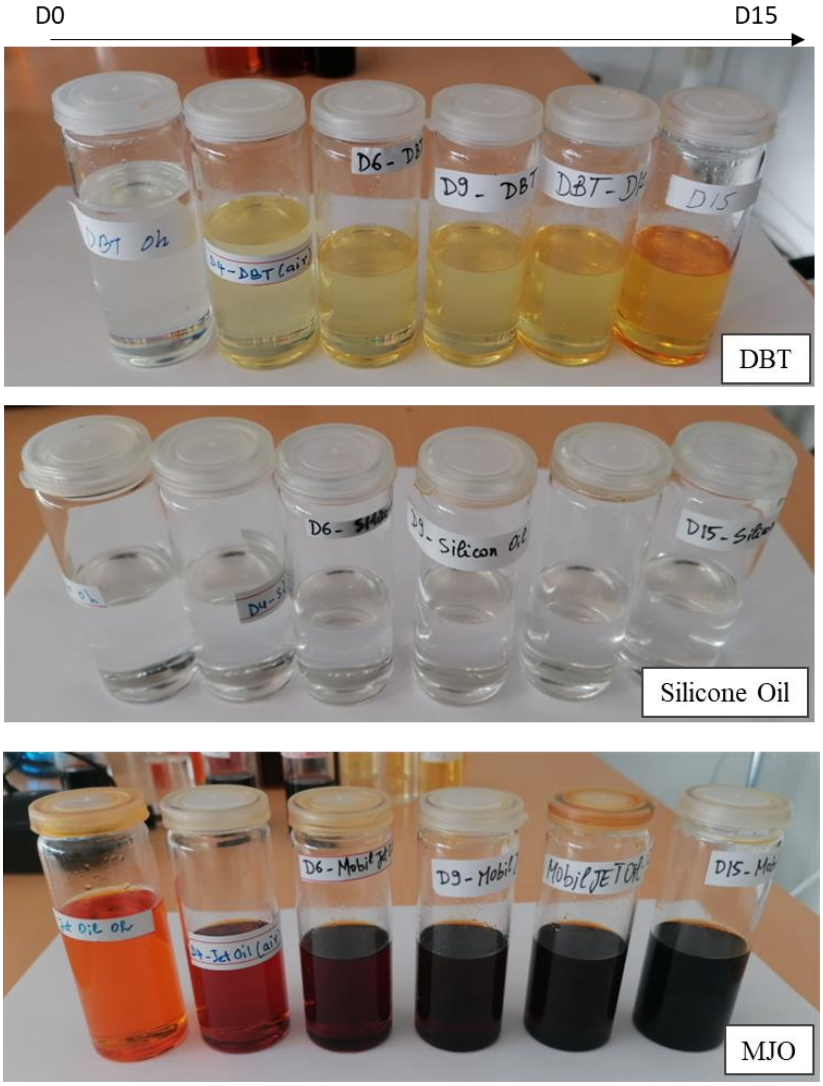

Fig - A. 5. Change of colour in liquids due to thermal aging in open air at 150°C

Frequency independent component of conductivity measured at 0.1mHz for the three liquids can be seen in fig-A.6. A faster increase in conductivity is observed in MJO compared to DBT. This indicates that MJO is more sensitive to thermal aging in open air. Similar effects are also observed with dielectric losses (fig-A.7).

The conductivity in Silicone oil rather decreased with increase in aging hours. This could be due to cross-link formation after prolonged exposure to temperature (typical in silicone oil). The cross-linking results in increasing the viscosity of silicone oil and hence reduce the conductivity. This hypothesis could be better explained by measuring the viscosity of silicone oil (not covered in this experiment).

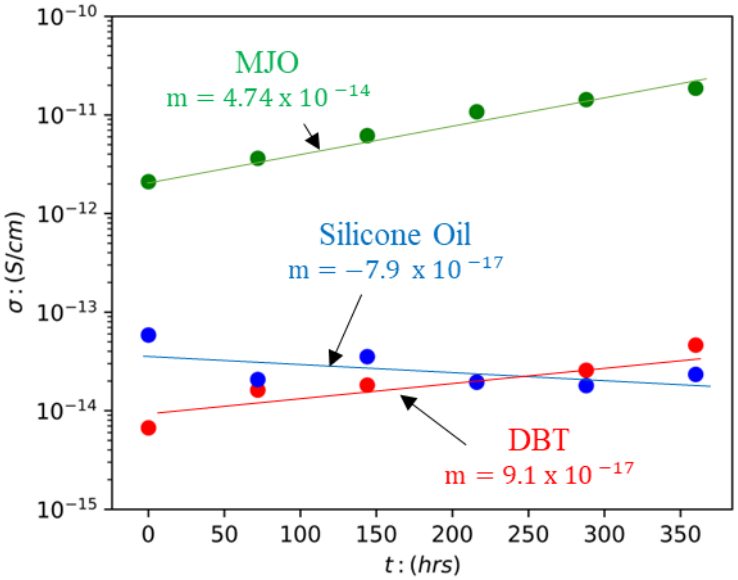

Fig - A. 6. Variation of conductivity (0.1mHz) vs aging time. Aging temperature at 150°C, measurement temperature at 20°C

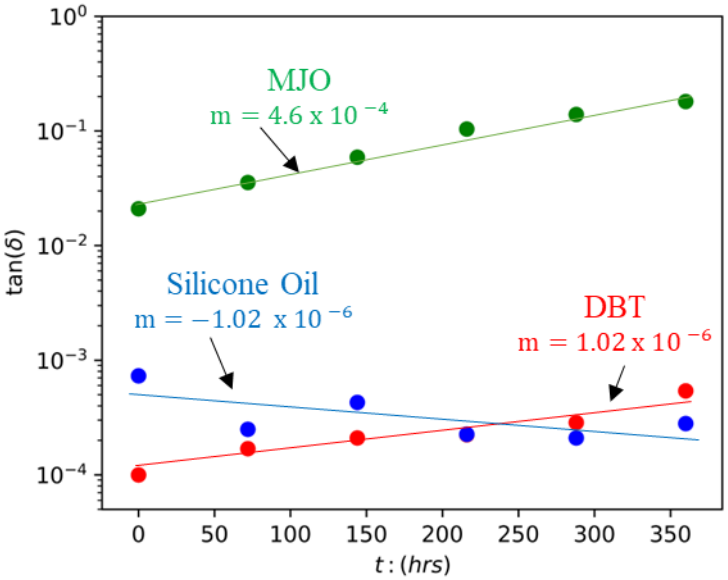

Fig - A. 7. Variation of loss factor (50Hz) vs aging time. Aging temperature at 150°C, measurement temperature at 20°C

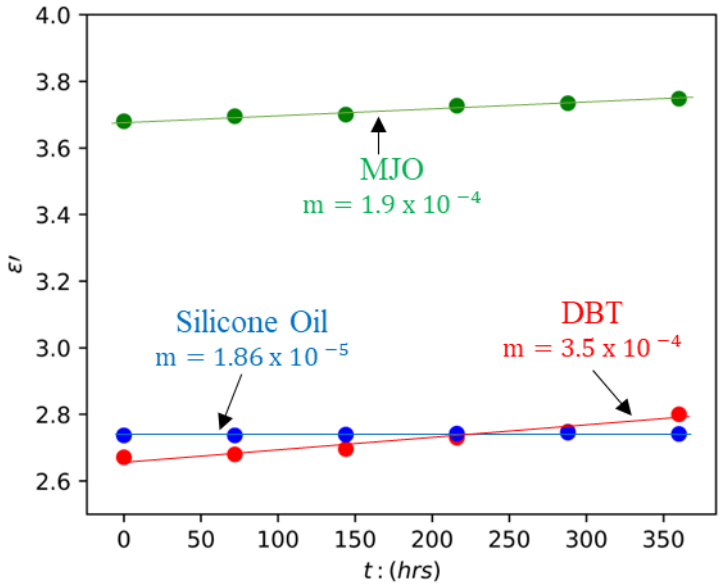

Fig - A. 8. Variation of permittivity (50Hz) vs aging time. Aging temperature at 150°C, measurement temperature at 20°C

A.4. Influence of thermal ageing on breakdown voltage

Breakdown measurements were made using the experimental set up used for DC breakdown studies in [16], fig-A.9. A standard test DC voltage ramp (1kV/s) was used for measurements in all liquids. The sphere-sphere electrode assembly has a gap distance of 0.4 mm. The test cell and the electrode assembly are cleaned with acetone and dried with pressured air before every experiment. The liquid samples are placed under vacuum at 60°C for 2 to 3 hours to remove any moisture or air bubbles introduced during the filling process. This reduces the influence of different moisture contents on breakdown strength.

A series of 16 breakdown measurements (waiting time of 5 minutes between each) were made for each liquid sample for every ageing time (D0…D3…to D15). This provided enough data to plot a statistical variation of breakdown voltage against thermal aging duration, fig-A.11 and fig.A-12. A slight decrease of breakdown voltage was observed in all the three liquids. Silicone oil and DBT show similar rate of degradation in terms of breakdown strength, about 7V/h for thermal aging at 150°C. Mush faster degradation rate of 14V/h was observed with MJO.

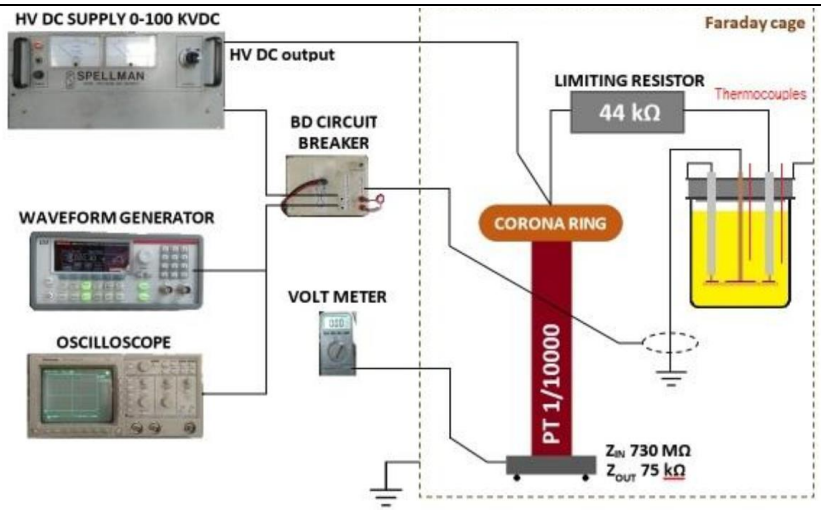

Fig - A. 9. DC breakdown experimental setup [16]

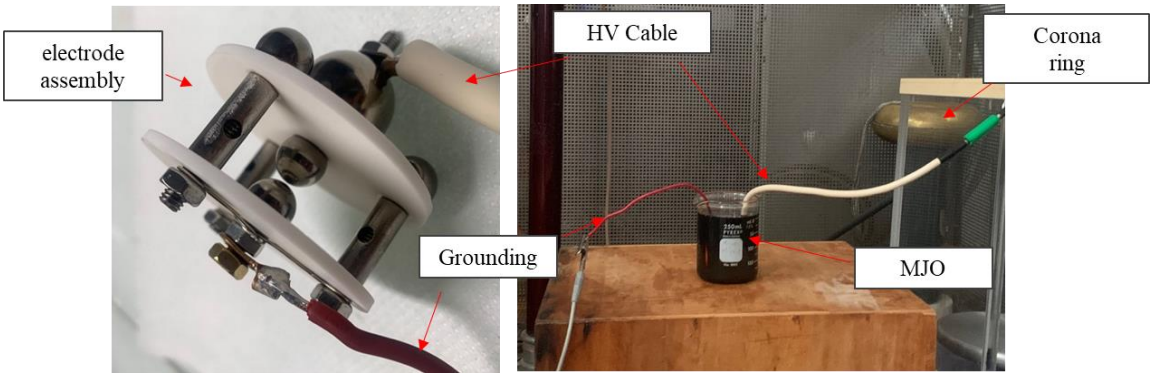

Fig - A. 10. Photograph of electrode assembly and beaker containing MJO for breakdown measurements

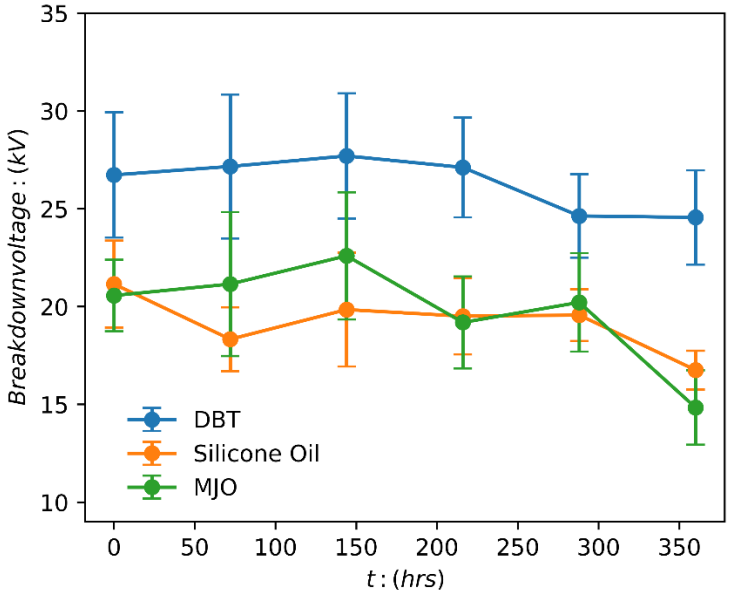

Fig - A. 11. Variation of breakdown voltage during ageing, sphere gap= 0.4 mm

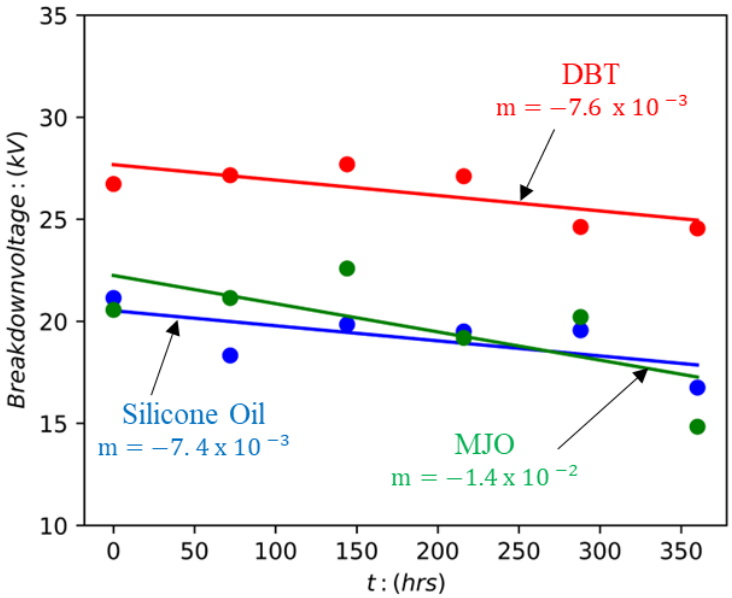

Fig - A. 12. Linear fit of mean breakdown voltage (16 series of breakdowns), sphere gap = 0.4 mm

Annex B – Conductivity and dielectric spectroscopy experiments with Al_2O_3 substrate

B.1. Alumina substrate sample

Alumina (Al_2O_3) substrate samples was prepared by etching the copper metallization (thickness = 0.3 mm) of a DBC substrate (fig - B.1). The high voltage (HV) side of the sample consist of a circular high voltage electrode of diameter D = 45 mm. The remaining metallization outside the HV electrode is removed to avoid surface breakdown at high voltages. The ground side of the sample consists of measurement electrode of D = 40 mm and a guard ring with 1 mm gap.

This sample substrate was used for both electrical conductivity and dielectric spectroscopy experiments using the same test cell (fig -2.1) and procedures used for liquids as in chapter 2.

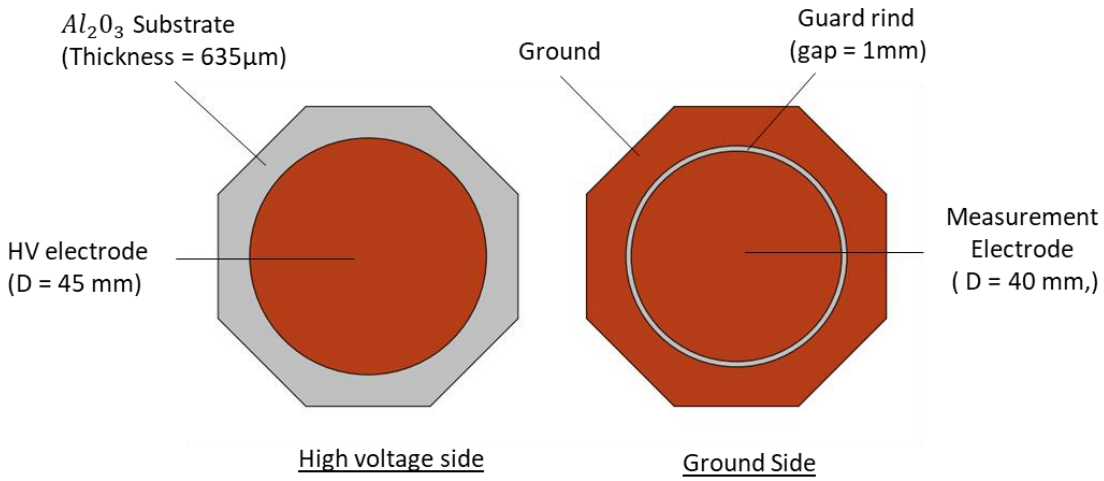

Fig - B. 1. Schematic of alumina substrate sample for conductivity and permittivity measurement

B.2. Conductivity measurement in Alumina substrate sample at high temperature and high voltage

Electrical conductivity measurement in alumina substrate has been carried out for dc-voltage (V_{DC}) ranging from 1kV to 10 kV at for temperatures 50°C to 300°C. The current measurement at room temperature and voltages below 1kV was beyond the measurement range of Keithley electrometer.

B.2.1. Typical current measurement

The polarization relaxation time in solid insulation can be very long (up to several days). Therefore, it is impractical to wait for several days to get a single value of conduction current (I_c), once the polarization current becomes lower than the conduction current. To reduce measurement time, the conduction current was obtained from the difference between total current measured ($I_T = Ip + I_c$) at a fixed V_{DC} and depolarization current (= I_p) when the V_{DC} = 0, where I_p is the polarization (also sometimes called "charging current"). A typical current recording during applied voltage V_{DC} , depolarization current during V_{DC} = 0 and resulting conduction current can be seen in fig – B.2.

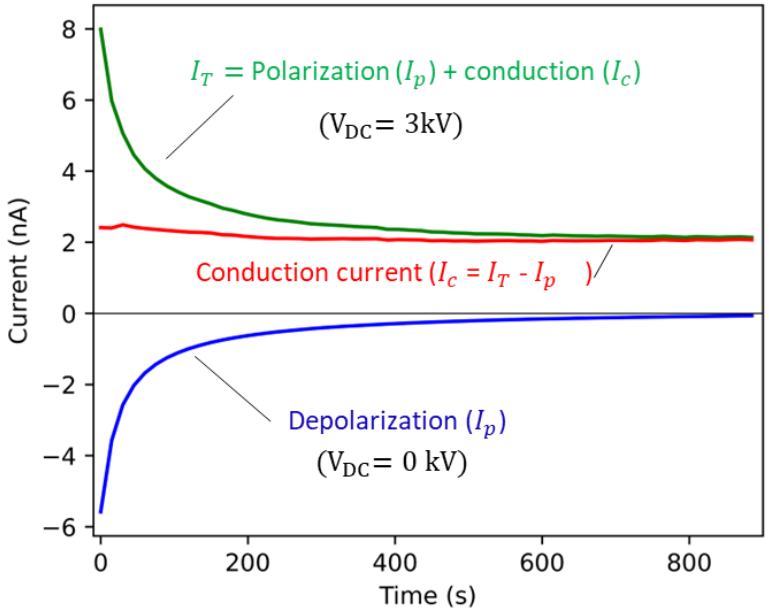

Fig - B. 2. Typical current recording and conduction current determination in alumina substrate at 3kV and 150°C

A.2.2. Current density variation with temperature and voltage

Fig-B.3. show the variation of current density with temperature and applied voltage V_{DC}. At lower temperatures (below 100°C), ohmic (slope m=1) and space charge limited (SCLC) conduction (V_{DC} > 4kV) can be distinctively seen. However, the SCLC component is dominated by the conduction component at temperatures above 100°C.

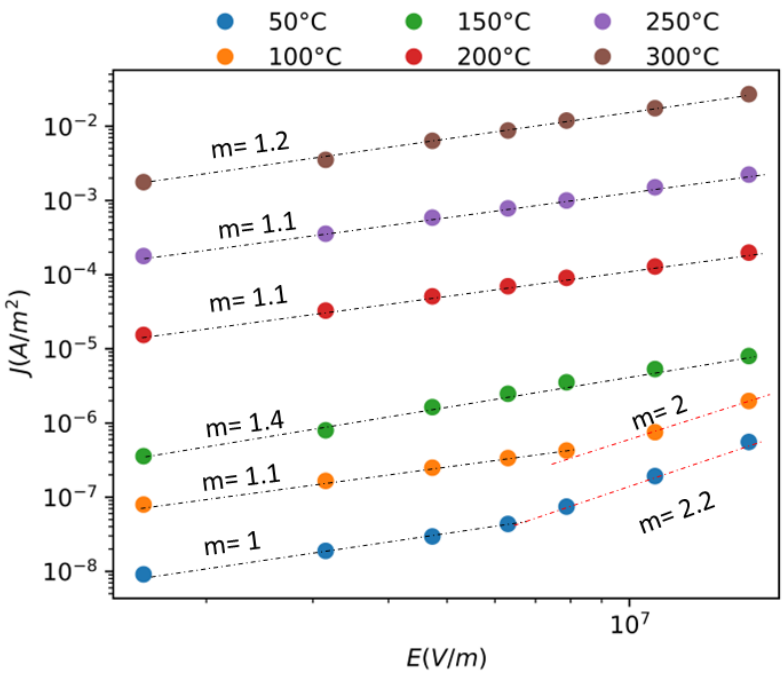

Fig - B. 3. Variation of current density in alumina substrate with temperature and voltage

B.2.3. Conductivity of alumina represented in the form of empirical formula

Fig-B.4. shows the measured conductivity of alumina substrate as function of temperature and electric field. The main goal of measuring conductivity of alumina substrate was to develop an empirical formula of conductivity as a function of temperature and electric field, $\sigma(E,T)$ (equation A.(a)). This equation was used for electric field simulation in chapter 2.

$$\sigma(E,T) = 2 * 10^{-18} \exp\left(\frac{0.052\mathrm{T}}{\mathrm{Tref}} + 0.0068\ \mathrm{E} \exp\left(-0.1967 \frac{\mathrm{T}}{\mathrm{Tref}}\right)\right) \qquad A.(a)$$

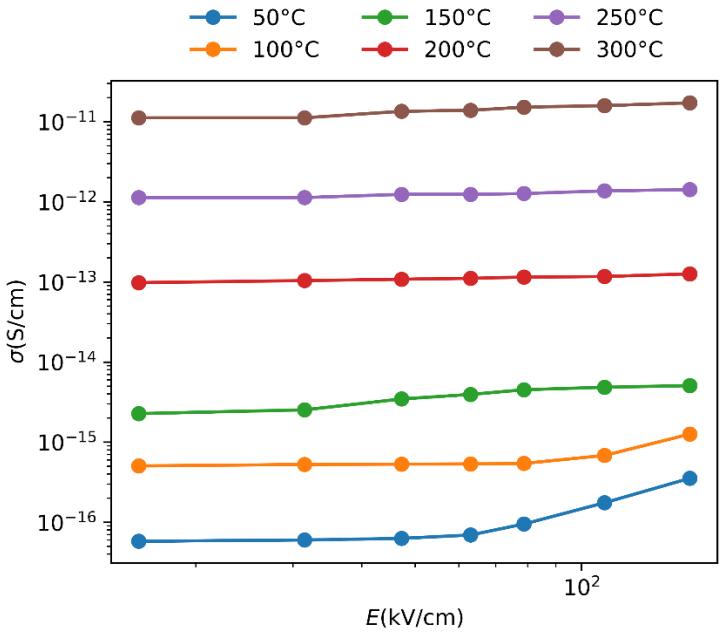

Fig - B. 4. Variation of conductivity of alumina substate with temperature and electric field

B.3. Dielectric spectroscopy measurements of alumina substrate

The permittivity increases with increase in temperature (typical in solid dielectrics) contrary to permittivity decrease of liquid dielectrics. The polarization component of the permittivity was also seen to increase by 2 decades when temperature is increased from 25°C to 300°C, see fig-B.5. The polarization free/frequency independent permittivity at high frequency (~ MHz) is usually considered as the actual permittivity of a dielectric material. Permittivity variation with temperature determined at 0.1MHz can be seen in fig -B.6. . The equivalent empirical formula representing the variation of permittivity with temperature $\epsilon'(T)$ is as in equation A. (b).

$$\epsilon'(T) = 10.5 + 0.024\mathrm{T} \qquad 2.3.3.(a)$$

Variation of loss factor in alumina substrate is shown in fig-B.7. The measurements at temperatures below 100°C were somewhat erratic, probably linked to too low sample capacitance.

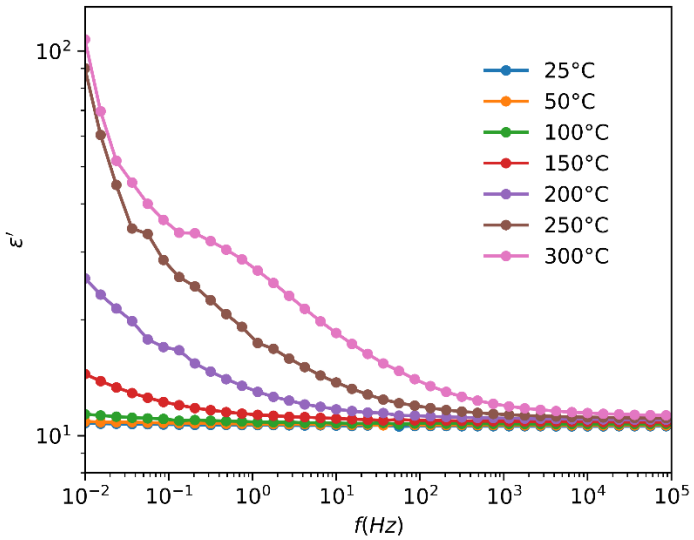

Fig - B. 5. Permittivity variation of alumina substrate against temperature at frequencies (0.1 Hz to 0.1MHz)

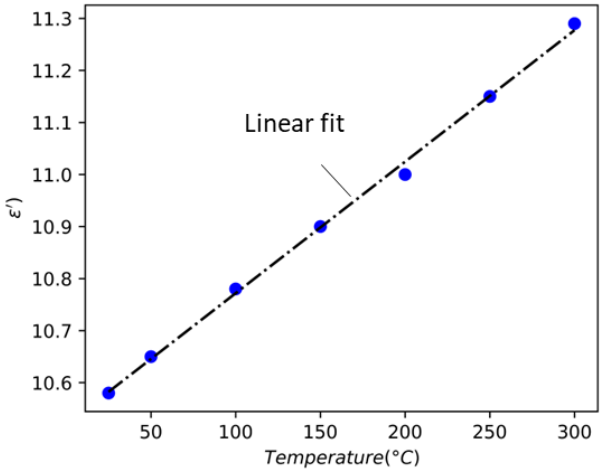

Fig - B. 6. Permittivity of alumina substrate at high frequency (0.1 Hz)

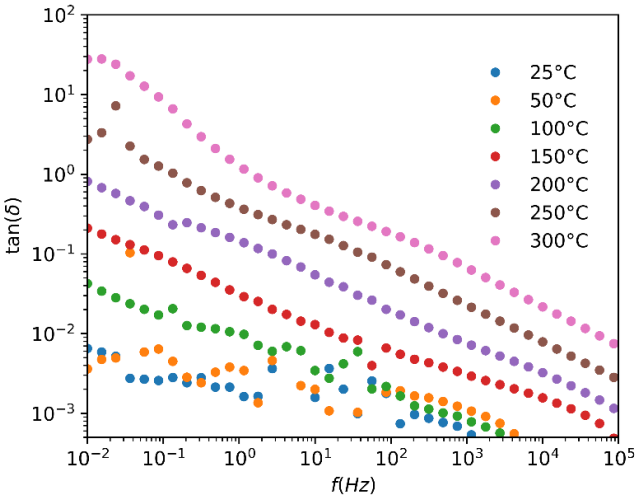

Fig - B. 7. Loss factor of alumina substrate

Annex C – Surface breakdown with Si_3N_4 substrate embedded in dielectric liquids and silicone gel: some preliminary results

C.1. Test sample

Double layer Si_3N_4 substrates (refer Chapter 3 for details) were embedded in four different liquids, i.e., DBT, BT06, Silicone oil (S.Oil) and MJO. A sample with silicone gel (S.Gel) was also prepared to do breakdown tests. Each Si_3N_4 substrate consists of six ground electrodes (numbered 1,2…6) and two high voltage electrodes, fig-C.1.

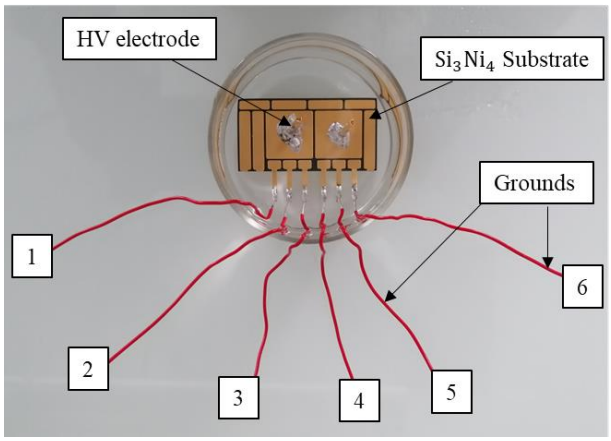

Fig - C. 1. Double layer silicone nitride substrate (Si_3N_4) embedded in DBT for surface breakdown test

C.2. Surface DC breakdown measurement results

The breakdown experiments was performed using the same DC breakdown test setup (fig-A.9). Fig-C.2 show typical images of substrate sample after repetitive DC breakdowns. It was observed that when the breakdown voltage does not exceed 18kV, a series of repetitive breakdown voltage around 10kV can be measured in all the liquids (showing a good self-healing response typical of liquids). No visible cracks on substrates were observed, however some traces of liquid by-products or damage on the surface of the substrate was noticed, fig-C.2 (a). Whenever the breakdown voltage exceeded 18kV, the next breakdown voltage immediately reduced down to 1 or 2 kV, leaving behind a complete crack in the substrate, fig-C.2(b). This implies that the breakdowns occurring at voltage below 18kV probably occurred in the liquid (with good self-healing property), whereas the breakdowns occurred in the substrate when the voltage exceeded 18kV (irreversible degradation). Similar results were already observed in [16] at short electrode gaps (the breakdown occurred in the liquid), and at large gaps (the breakdown at higher voltage mainly occurred within the substrate material).

Breakdown voltage with silicone gel was observed to be higher than in the liquids (fig-C.3). However, after 1st breakdown, a permanent carbonization of the gel bridges the electrode gaps, forming a permanent short circuit, fig-C.2 (c). This implies that the favourable self-healing property of liquid encapsulation can occur especially for short gaps and low breakdown voltage, compared to immediate irreversible degradation occurring in any circumstances with silicone gel encapsulation.

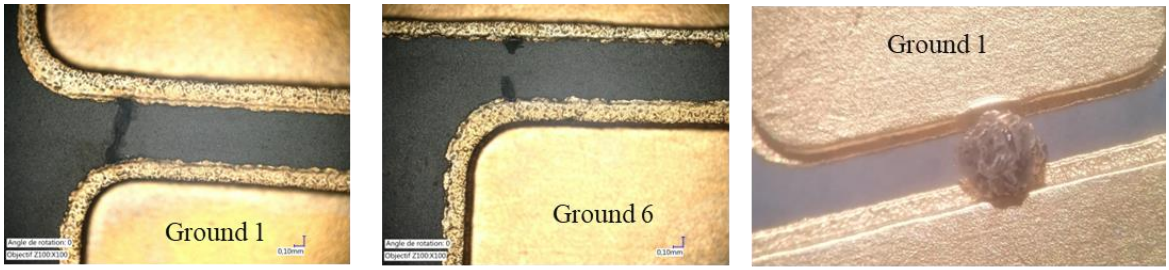

Fig - C. 2. Substrate after breakdown test at room temperature (a) embedded in DBT showing a crack in the substrate after 1st voltage shot at ground electrode no.1 (b) visible traces of damage at the surface of substrate at electrode no.6 (c) permanent breakdown in silicone gel after 1st voltage shot at electrode no.1

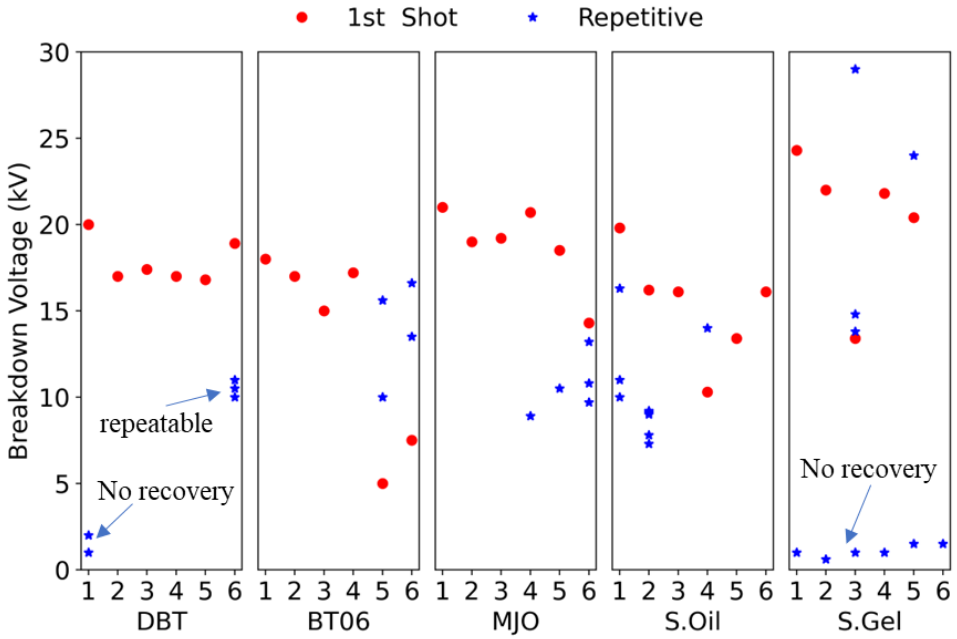

Fig - C. 3. Surface breakdown measurements with Si_3N_4 substrate embedded in liquids (DBT, BT06, MJO, Silicone oil) and silicone gel

References

[1] D. C. Prince, "Mercury arc rectifier phenomena," *Journal of the A.I.E.E.*, vol. 46, pp. 667-674, 1927.

[2] N. Kaminski, "State of the art and the future of wide band-gap devices," in *2009 13th European Conference on Power Electronics and Applications*, 2009.

[3] C. M. DiMarino, B. Mouawad, C. M. Johnson, D. Boroyevich and R. Burgos, "10-kV SiC MOSFET Power Module With Reduced Common-Mode Noise and Electric Field," *IEEE Transactions on Power Electronics*, vol. 35, pp. 6050-6060, 2020.

[4] G. Perez, A. Maréchal, G. Chicot, P. Lefranc, P.-O. Jeannin, D. Eon and N. Rouger, "Diamond semiconductor performances in power electronics applications," *Diamond and Related Materials*, vol. 110, p. 108154, 2020.

[5] X. She, A. Q. Huang, Ó. Lucía and B. Ozpineci, "Review of Silicon Carbide Power Devices and Their Applications," *IEEE Transactions on Industrial Electronics*, vol. 64, pp. 8193-8205, 2017.

[6] S. Ji, Z. Zhang and F. Wang, "Overview of high voltage sic power semiconductor devices: development and application," *CES Transactions on Electrical Machines and Systems*, vol. 1, pp. 254-264, 2017.

[7] J. Y. Tsao, S. Chowdhury and M. A. Hollis, "Ultrawide-Bandgap Semiconductors: Research Opportunities and Challenges," *Advanced Electronic Materials*, vol. 4, p. 1600501, 2018.

[8] S. Musumeci, "Gate charge control of high-voltage Silicon-Carbide (SiC) MOSFET in power converter applications," in *2015 International Conference on Clean Electrical Power (ICCEP)*, 2015.

[9] C. Raynaud, D. Tournier, H. Morel and D. Planson, "Comparison of high voltage and high temperature performances of wide bandgap semiconductors for vertical power devices," *Diamond and Related Materials*, vol. 19, pp. 1-6, 2010.

[10] M.-L. Locatelli, R. Khazaka, S. Diaham, C.-D. Pham, M. Bechara, S. Dinculescu and P. Bidan, "Evaluation of Encapsulation Materials for High-Temperature Power Device Packaging," *IEEE Transactions on Power Electronics*, vol. 29, pp. 2281-2288, 2014.

[11] H. Gao and P. Liu, "High-Temperature Encapsulation Materials for Power Modules: Technology and Future Development Trends," *IEEE Transactions on Components, Packaging and Manufacturing Technology*, vol. 12, pp. 1867-1881, 2022.

[12] L. Donzel and J. Schuderer, "Nonlinear resistive electric field control for power electronic modules," *IEEE Transactions on Dielectrics and Electrical Insulation*, vol. 19, pp. 955-959, 2012.

[13] L. Liu, D. Nam, B. Guo, J. Ewanchuk, R. Burgos and G.-Q. Lu, "Glass for Encapsulating High-Temperature Power Modules," *IEEE Journal of Emerging and Selected Topics in Power Electronics*, vol. 9, pp. 3725-3734, 2021.

[14] B. Boettge, F. Naumann, S. Behrendt, M. G. Scheibel, S. Kaessner, S. Klengel, M. Petzold, K. G. Nickel, G. Hejtmann, A. Z. Miric and R. Eisele, "Material Characterization of Advanced Cement-Based Encapsulation Systems for Efficient Power Electronics with Increased Power Density," in *2018 IEEE 68th Electronic Components and Technology Conference (ECTC)*, 2018.

[15] M. T. Do, Propriétés diélectriques des gels isolants : application aux composants d'électronique de puissance, Grenoble, 2008.

[16] T. A. T. Vu, "Etude de l'origine des décharges partielles sur les substrats céramiques enrobés," 2011.

[17] J. Muslim, "Study of dielectric liquids as alternative encapsulant for high temperature electronics power modules applications," Grenoble, 2019.

[18] Arkemagroup, "Jarytherm BT06 datasheet," Arkema, Paris, 2015.

[19] Arkemagroup, "Jarytherm DBT Datasheet," Arkema, Paris, 2016.

[20] Arkemagroup, "Jarylec Datasheet," Arkema, Paris, 2008.

[21] "Midel 7131 synthtic ester transformer fluid datasheet," Midel, Manchester, 2023.

[22] "Mobil Jet™ Oil II," ExxonMobil, Courbevoie, 2019.

[23] J. Muslim, R. Hanna, O. Lesaint, J. L. Reboud and N. I. Sinisuka, "Electrical characterization of synthetic ester liquid over wide temperature range (−60°C / 200°C)," in *2017 IEEE 19th International Conference on Dielectric Liquids (ICDL),* 2017.

[24] J. Muslim, O. Lesaint, R. Hanna and N. I. Sinisuka, "Discharges and Streamers Properties in Dielectric Liquids under Various Temperature," in *2020 International Conference on Technology and Policy in Energy and Electric Power (ICT-PEP),* 2020.

[25] O. Lesaint, "Prebreakdown phenomena in liquids: propagation 'modes' and basic physical properties," *Journal of Physics D: Applied Physics,* vol. 49, p. 144001, March 2016.

[26] J. Muslim, O. Lesaint, R. Hanna and N. I. Sinisuka, "Streamer Generation and Propagation in Dibenzyltoluene and Ester Liquids under High Temperature," in *2019 IEEE 20th International Conference on Dielectric Liquids (ICDL),* 2019.

[27] "Insulating Liquids − Determination of the breakdown voltage at power frequency – Test Method, IEC 60156, Ed. 3.0," 2018.

[28] J. Muslim, O. Lesaint, R. Hanna, J. L. Reboud and N. I. Sinisuka, "Electrical Characterization of Dibenzyltoluene Liquid at High Temperatures up to 350°C," in *2018 IEEE Conference on Electrical Insulation and Dielectric Phenomena (CEIDP),* 2018.

[29] J. Muslim, O. Lesaint, R. Hanna and N. I. Sinisuka, "Breakdown Properties of Epoxy and Ceramic Substrates Embedded in Liquids at High Temperature," in *2022 IEEE 4th International Conference on Dielectrics (ICD),* 2022.

[30] S. Anand, E. Vagnon, M. Guillet and C. Buttay, "Assessment of Partial Discharge Phenomenon in AC and Fast-rising Square Voltage Using Optical Detection Technique in Needle-Plane Configuration With Pressboard in Mineral Oil," in *2022 IEEE 21st International Conference on Dielectric Liquids (ICDL),* 2022.

[31] J. L. Augé, O. Lesaint and A. T. V. Thi, "Optical measurement of partial discharges under impulse voltage on ceramic substrates embedded in silicone oil," in *2013 Annual Report Conference on Electrical Insulation and Dielectric Phenomena*, 2013.

[32] M. T. Do, J.-L. Auge, T. A. T. Vu and S. Catellani, "Partial discharges in dielectric liquids," in *2008 International Symposium on Electrical Insulating Materials (ISEIM 2008),* 2008.

[33] J.-L. Auge, O. Lesaint and A. T. V. Thi, "Partial discharges in ceramic substrates embedded in liquids and gels," *IEEE Transactions on Dielectrics and Electrical Insulation,* vol. 20, pp. 262-274, 2013.

[34] T. M. Do, O. Lesaint and J.-L. Auge, “Streamers and partial discharge mechanisms in silicone gel under impulse and AC voltages,” *IEEE Transactions on Dielectrics and Electrical Insulation,* vol. 15, pp. 1526-1534, 2008.

[35] T. A. T. Vu, J.-L. Augé, O. Lesaint and M. T. Do, “Partial discharges in Aluminium nitrite ceramic substrates,” in *2010 10th IEEE International Conference on Solid Dielectrics,* 2010.

[36] A. A. Abdelmalik, A. Nysveen and L. Lundgaard, “Influence of fast rise voltage and pressure on partial discharges in liquid embedded power electronics,” *IEEE Transactions on Dielectrics and Electrical Insulation,* vol. 22, pp. 2770-2779, 2015.

[37] F. Kremer and A. Schönhals, Broadband Dielectric Spectroscopy, Springer Berlin Heidelberg, 2012.

[38] “Test Interfaces for the AlphaA Modular Measurement System,” Novocontrol, Montabaur, Germany, 2023.

[39] C. Tran-Duy, “Propriétés diélectriques de liquides isolants d'origine végétale pour applications en haute tension,” 2009.

[40] M. S. Mendolia and G. C. Farrington, “Ionic mobility in macromolecular electrolytes. The failure of Walden's rule,” *Chemistry of Materials,* vol. 5, pp. 174-181, 1993.

[41] R. Bartnikas, “Dielectric Loss in Insulating Liquids,” *IEEE Transactions on Electrical Insulation,* Vols. EI-2, pp. 33-54, 1967.

[42] R. Bartnikas, “Engineering Dielectrics: Volume III Electrical Insulating Liquids,” 1994.

[43] S. LEPERT, “ÉTUDE DE DIÉLECTRIQUES LIThesis, QUIDES À TEMPÉRATUREAMBIANTE POUR L/ TOMOGRAPHffi À RAYONNEMENT X DE KAUTE ÉNERGIE,” Grenoble, 1984.

[44] W. F. Schmidt and A. O. Allen, “Mobility of electrons in dielectric liquids,” *The Journal of Chemical Physics,* vol. 52, p. 4788–4794, 1970.

[45] Q. Xue, I. Timoshkin, M. J. Given, M. P. Wilson and S. J. MacGregor, “Mobility of Charge Carriers in Dielectric Liquids,” in *2019 IEEE 20th International Conference on Dielectric Liquids (ICDL)*, 2019.

[46] D. André, “Conduction and breakdown initiation in dielectric liquids,” in *2011 IEEE International Conference on Dielectric Liquids,* 2011.

[47] L. Onsager, “Deviations from Ohm's law in weak electrolytes,” *The Journal of chemical physics,* vol. 2, p. 599–615, 1934.

[48] R. M. Hill, “Injection controlled conduction,” *Thin Solid Films,* vol. 15, pp. 369-391, 1973.

[49] “Data sheet Rhodorsil® Oils 47,” Lyon, France, 2018.

[50] R. Coelho and J. Debeau, “Properties of the tip-plane configuration,” *Journal of Physics D: Applied Physics,* vol. 4, p. 1266, September 1971.

[51] Q. Xue, I. Timoshkin, M. P. Wilson, M. Given and S. J. MacGregor, “Mobility of charge carriers in mineral oil and ester fluids,” *High Voltage,* vol. 6, p. 1040–1050, 2021.

[52] H. Reynes, C. Buttay and H. Morel, “Protruding ceramic substrates for high voltage packaging of wide bandgap semiconductors,” in *2017 IEEE 5th Workshop on Wide Bandgap Power Devices and Applications (WiPDA)*, 2017.

[53] “COMSOL Multiphysics reference manuel 5.6,” 2019.

[54] F. Breit, D. Malec and T. Lebey, “Investigations on DC conductivity and space charge in silicone gel,” in *Annual Report Conference on Electrical Insulation and Dielectric Phenomena*, 2002.

[55] J. Fuhr, “Procedure for identification and localization of dangerous PD sources in power transformers,” *IEEE Transactions on Dielectrics and Electrical Insulation,* vol. 12, pp. 1005-1014, 2005.

[56] D. König and Y. N. Rao, Partial Discharges in Electrical Power Apparatus, VDE-Verlag, 1993.

[57] L. Caliap, “Etude de l'optimisation des isolants d'un point de vue diélectrique pour les contraintes du GIS,” 2010.

[58] “8575 Photomultiplier datasheet,” Burle Technologies, Lancaster, 1989.

[59] R. G. Mertens, L. Chow, K. B. Sundaram, R. B. Cregger, D. P. Rini, L. Turek and B. A. Saarloos, “Spray Cooling of IGBT Devices,” *Journal of Electronic Packaging,* vol. 129, pp. 316-323, May 2007.

[60] J. Seyed-Yagoobi, “Electrohydrodynamic pumping of dielectric liquids,” *Journal of Electrostatics,* vol. 63, pp. 861-869, 2005.

[61] A. Castellanos, “EHD Pumping: Electrokinetic Pumping by a High Voltage Travelling Wave. Ion-Drag Pumping,” in *Electrohydrodynamics*, Vienna, 1998.

[62] J. Wu, P. Traoré, C. Louste, A. T. Pérez and P. A. Vázquez, “Heat transfer enhancement by an electrohydrodynamic plume induced by ion injection from a hyperbolic blade,” in *2014 IEEE 18th International Conference on Dielectric Liquids (ICDL)*, 2014.

[63] J. Wu, P. Traoré, C. Louste, A. T. Pérez and P. A. Vázquez, “Numerical evaluation of heat transfer enhancement due to annular electroconvection induced by injection in a dielectric liquid,” *IEEE Transactions on Dielectrics and Electrical Insulation,* vol. 23, pp. 614-623, 2016.

[64] J. Seyed-Yagoobi, B. D. Margo and J. E. Bryan, “Effect of frequency on heat transfer enhancement in temperature-induced electrohydrodynamic pumping,” *IEEE Transactions on Dielectrics and Electrical Insulation,* vol. 1, pp. 468-473, 1994.

[65] O. DIKI, “Évaluation des liquides diélectriques caloporteurs pour,” Grenoble, 2023.

[66] M. M. Rashwan, “High field electric conduction and electroluminence in dieectric liquids (Thesis),” University of Manitoba, Winnipeg, 1977.